

## University of Southampton Research Repository

Copyright © and Moral Rights for this thesis and, where applicable, any accompanying data are retained by the author and/or other copyright owners. A copy can be downloaded for personal non-commercial research or study, without prior permission or charge. This thesis and the accompanying data cannot be reproduced or quoted extensively from without first obtaining permission in writing from the copyright holder/s. The content of the thesis and accompanying research data (where applicable) must not be changed in any way or sold commercially in any format or medium without the formal permission of the copyright holder/s.

When referring to this thesis and any accompanying data, full bibliographic details must be given, e.g.

Thesis: Luis Vicente Wilches Peña (2018) "Microstructural Alterations During HPT Tests on Annealed 52100 Bearing Steel", University of Southampton, Faculty of Engineering and Physical Sciences, School of Engineering, PhD Thesis, 196 p.

Data: Luis Vicente Wilches Peña (2018) Microstructural Alterations During HPT Tests on Annealed 52100 Bearing Steel URI [\[ \]](#)





# University of Southampton

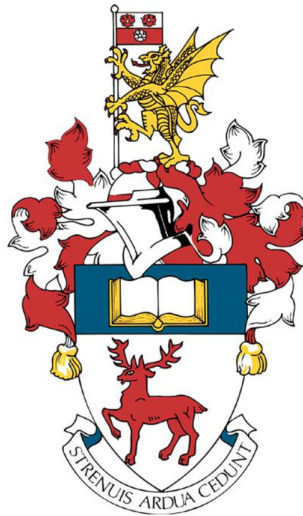
Faculty of Engineering and Physical Sciences

School of Engineering

## Microstructural Alterations During HPT Tests on Annealed 52100 Bearing Steel

by

**Luis Vicente Wilches Peña**



Thesis for the degree of Doctor of Philosophy

December 2018



# University of Southampton

## Abstract

Faculty of Engineering and Physical Sciences

School of Engineering

Thesis for the degree of Doctor of Philosophy

### **Microstructural Alterations During HPT Tests on Annealed 52100 Bearing Steel**

by

Luis Vicente Wilches Peña

White Etching Areas – WEAs have been associated with premature and catastrophic damage to rolling bearings. Severe and localized plastic deformation close to the contact surface has been suggested as one of the main drivers for WEAs formation and subsequent evolution. Similar conditions can be created by Severe Plastic Deformation (SPD) processes such as High-Pressure Torsion (HPT). HPT combines high compressive and torsional stresses to produce grain refinement on a nano scale. HPT tests are quick to perform and thus could provide an easier way to investigate the formation of white etching areas or white structures compared to both rolling contact fatigue tests and an analysis of bearings from service. Therefore, HPT has been used to study white structures in a 52100-bearing steel in this thesis. Due to the limitations on specimen hardness of the HPT equipment, AISI 52100 bearing rollers in their as received quenched and tempered service condition were annealed to reduce their hardness from 800 HV to  $180 \pm 10$  HV prior to HPT testing. After annealing, disc samples 10 mm in diameter and 1 mm thick were HPT processed under a range of pressures and number of turns. White Etching Structures - WES were found to form in two different regions in the disc samples namely on the top surface of the sample which had been in contact with the upper anvil (designated Top White Etching Areas – TWEAs) and subsurface 240 – 360  $\mu\text{m}$  from the bottom surface of the disc (designated Subsurface White Etching Areas – SWEAs). A morphological characterization was carried out on the HPT produced samples by Macroscopy (MA) and Light Optical Microscopy (LOM) and an Image Processing Program (IPP) was utilised to evaluate the %WES in relation to the pressure and strain applied during the HPT tests. Micro and

## Table of Contents

nano hardness measurements were taken of the WES and the matrix surrounding them. This was then followed by a detailed characterisation conducted using SEM / SEI / BSI to obtain information on the structure, size and shape of WES. SEM / EBSD / EDS were also utilised to evaluate features such as texture, phase distribution and chemical composition not only of the WES, but also of the material surrounding them. TWEAs covered the top surfaces of the discs as many white structures, some isolated, other more interconnected, that seemed to follow the circular tracks on the sample; they were restricted to depths of less than 100  $\mu\text{m}$  from the top surface. SWEAs varied in size and shape with radial distance, from spots with ill-defined borders (called cloud SWEAs) to well defined solid structures (called solid SWEAs). Both TWEAs and SWEAs shared a similar morphology that consisted of a fibrous / layered structure that appeared to follow patterns caused by the plastic deformation. Their hardness was approximately 24 – 46 % higher than the deformed ferritic matrix. EBSD analysis showed TWEAs and SWEAs in dark contrast in IQ images and as black regions in IPF, AP and KAM maps suggesting poor or even a total lack of indexed diffraction patterns from these areas resulting from a nanocrystalline structure. No recrystallized structures were found in the white structures. EDS analysis indicated that carbon and chromium were dragged from the carbides and dissolved in the nanocrystalline arrangement present in the TWEAs and SWEAs. EDS also revealed inclusions of aluminium with sulphur and manganese that seemed to have suffered a similar dissolution process to that observed for C and Cr. The origin of the fibres / layered structure is related to the interaction between neighbouring regions that flow under different conditions due to high strains. In the case of TWEAs, sliding of the asperities on the top anvil against the sample created heterogeneous flow conditions in small neighbouring regions and instabilities between them. For the SWEAs, the presence of discontinuities such as carbide clusters, pearlite colonies or non-metallic inclusions generated vortices that promoted instabilities in the ferritic matrix. Some of the SWEAs located at the edge of the samples could have arisen from other effects, such as the lateral friction on the vertical faces of the cavities in the anvils, flash formation due to the quasi-constrained condition of the HPT tests and the presence of a Dead Metal Zone (DMZ) at the corners of the samples. Some cracks were observed close to or inside the white structures and were caused by the differences in response of these harder areas with respect to the surrounding softer matrix during the deformation imposed by the HPT test. However, not all white structures were associated with cracks, suggesting that cracks are not necessarily a precursor to white structures. Some of the features, such as the fibrous structure, changes in carbide distribution and high hardness seen in HPT samples are similar to those observed in the WEAs located in failed rolling element bearings. This suggests that a similar phenomenon could be occurring in the vicinities of inclusions located subsurface in rolling bearings and lead to the formation of WEAs.

# Table of Contents

<b>Table of Contents .....</b>	<b>i</b>
<b>Table of Tables .....</b>	<b>vii</b>
<b>Table of Figures .....</b>	<b>ix</b>
<b>Research Thesis: Declaration of Authorship.....</b>	<b>xxiii</b>
<b>Acknowledgements .....</b>	<b>xxv</b>
<b>Definitions and Abbreviations .....</b>	<b>xxx</b>
<b>Chapter 1 Introduction .....</b>	<b>1</b>
1.1 Project overview.....	1
1.2 Thesis Structure.....	2
1.3 Aims and objectives .....	3
<b>Chapter 2 Literature Review .....</b>	<b>5</b>
2.1 Failure in rolling element bearings.....	5
2.1.1 Use Rolling element bearings.....	5
2.1.2 Steels for rolling bearings.....	6
2.2 Failures in rolling bearings .....	9
2.2.1 Rolling - Sliding Contact and Surface Fatigue.....	10
2.2.2 Microstructural changes due to RCF .....	13
2.2.3 Spalling under RCF.....	15
2.2.4 Cracks under RCF.....	16
2.2.5 White Structure Flaking.....	17
2.2.6 White Etching Areas .....	18
2.2.7 Origin of WEAs .....	22
2.3 Severe Plastic Deformation .....	23
2.3.1 The beginning of HPT and ECAP .....	25
2.3.2 Other SPD processes .....	27
2.3.3 Applications of SPD processed materials .....	28
2.4 High Pressure Torsion Test.....	29

## Table of Contents

2.4.1	The anvils .....	29
2.4.2	Strain along the radial direction .....	31
2.4.3	Strain along the axial direction .....	32
2.4.4	Interruption of plastic flow .....	34
2.4.5	Pressure .....	37
2.4.6	Hardness response.....	37
2.4.7	Microstructural evolution .....	41
2.4.8	Temperature .....	42
2.4.9	Reversal movement in HPT .....	43
2.4.10	Cracks during HPT tests .....	44
2.4.11	Slippage .....	44
2.5	HPT on steels.....	45
2.5.1	Formation, transition and fragmentation stages .....	50
2.5.2	Effect of SPD on carbide distribution.....	51
2.6	Conclusions of Literature Review .....	53
<b>Chapter 3</b>	<b>Experimental Methodology .....</b>	<b>57</b>
3.1	Annealing heat treatment.....	58
3.2	Sample extraction .....	60
3.3	Conducting SPD tests on the HPT test machine .....	60
3.3.1	Stage 1, Scoping HPT tests:.....	62
3.3.2	Stage 2, Tests for surface characterisation.....	62
3.3.3	Stage 3, Tests for determining the microstructure in the thickness direction	62
3.3.4	Stage 4, Tests for determining the roughness of the anvils .....	63
3.4	Macroscopic characterisation.....	63
3.5	Roughness measurements.....	64
3.6	Generation of circumferential surfaces.....	64
3.6.1	Stage 1, Scoping HPT tests:.....	64
3.6.2	Stage 2, Tests for surface characterisation.....	64
3.6.3	Stage 3, Tests for determining the microstructure in the thickness direction	64
3.6.4	Stage 4, Tests for determining the roughness of the anvils .....	65
3.7	LOM on circumferential and axial surfaces .....	65

3.8	IPP .....	65
3.9	Generation of axial surfaces .....	68
3.10	Hardness measurements .....	68
3.11	SEM characterisation .....	69
3.12	SEM / EBSD .....	70
3.13	SEM / EDS .....	73
<b>Chapter 4</b>	<b>General characterisation after HPT tests .....</b>	<b>75</b>
4.1	Samples condition after conducting HPT tests .....	75
4.2	LOM characterisation of top and bottom surfaces .....	78
4.2.1	Top surfaces .....	78
4.2.2	Bottom surfaces .....	84
4.2.3	Top surfaces at 6 GPa 1 turn .....	84
4.3	Compression tests on samples as a means of measuring the surface finish of the anvils .....	85
4.4	Subsurface characterisation .....	88
4.4.1	Circumferential sections .....	88
4.4.2	Axial sections .....	92
4.5	Hardness measurements .....	94
4.5.1	Microhardness profiles .....	94
4.5.2	Measurements close to TWEAs and SWEAs .....	95
4.5.3	Nano hardness maps .....	96
<b>Chapter 5</b>	<b>Advanced characterisation .....</b>	<b>101</b>
5.1	SEM / SEI characterisation of top surfaces of HPT discs .....	101
5.1.1	Ill-defined TWEAs .....	101
5.1.2	High plastic deformation and overlapping .....	102
5.1.3	Flake formation .....	103
5.1.4	Fibre / layered structures .....	104
5.2	Solid and cloud SWEAs .....	106
5.3	EBSD characterisation .....	110
5.3.1	Region 1: Annealed AISI 52100 .....	111

## Table of Contents

5.3.2	Imaging Quality Maps (IQ) .....	114
5.3.3	Auto Phase Maps (AP) .....	116
5.3.4	IPF maps .....	117
5.3.5	KAM maps .....	118
5.4	EDS characterisation .....	119
5.4.1	Carbon and Chromium content determined by EDS analysis .....	119
5.4.2	Phosphorus and Aluminium content determined by EDS analysis .....	121
5.4.3	Carbide clusters .....	123
<b>Chapter 6</b>	<b>Origin and Evolution of WES .....</b>	<b>125</b>
6.1	HPT parameters .....	125
6.1.1	Hardness saturation and number of turns .....	125
6.1.2	The influence of pressure applied .....	127
6.1.3	Slippage .....	127
6.1.4	Surface roughness of the anvils .....	128
6.2	Advanced characterisation results .....	129
6.2.1	EBS analysis .....	129
6.2.2	EDS analysis .....	130
6.3	TWEA formation .....	131
6.3.1	Fibres / layered structure formation .....	131
6.3.2	Carbide distribution .....	132
6.3.3	TWEAs reduction with number of turns and pressure .....	132
6.4	SWEA formation .....	133
6.4.1	Strain and strain rate distribution .....	133
6.4.2	SWEA formation .....	134
6.4.3	Vortices .....	134
6.4.4	Carbide clusters and inclusions .....	135
6.5	Comparison of WES and WEAs in failed bearings .....	136
<b>Chapter 7</b>	<b>Conclusions and future work .....</b>	<b>143</b>
7.1	Conclusions .....	143



7.2	Future work .....	146
7.2.1	Conduct additional HPT tests on the annealed AISI 52100 .....	146
7.2.2	Characterisation by Transmission Electron Microscopy, TEM.....	146
7.2.3	Conduct HPT tests on AISI 52100 in its quenched and tempered condition .	147
<b>References</b>		<b>149</b>



## Table of Tables

Table 2-1 Typical composition in % weight of case hardening grade steel [19].	7
Table 2-2 Typical composition in % weight of through hardening grade steel [19].	7
Table 2-3 Composition in % weight of AISI 52100 under standard ISO 683 – 17 :2014 [21].	8
Table 2-4 Common causes of bearing failures. The last row in red indicates factors and damage related to fatigue phenomenon. Adapted from [25].	10
Table 2-5. Main factors proposed to explain the beginning and growth of WEAs.	22
Table 3-1 Specified composition ranges of AISI 52100 steel in weight % [105].	59
Table 3-2 Technical details of AISI 52100 used in this study. Information provided by the supplier [105].	59
Table 4-1. Slippage in HPT tests after 1 turn. The values correspond to averages from 5 samples	75
Table 4-2. % TWEA on the top surface of samples after HPT tests under different conditions. Images correspond to the micrographs shown in Figure 1.8. TWEAs are represented as black in each case.	83
Table 4-3. Roughness measurements taken from samples discs after being pressed in the HPT test machine. Values are the average of five measurements ( $R_a \pm 0.5 \mu\text{m}$ , $R_q \pm 0.2 \mu\text{m}$ , $R_z \pm 2.1 \mu\text{m}$ )	86
Table 4-4. Profiles taken from samples after being compressed in the HPT machine	87
Table 4-5. % SWEAs as a function of strain at the midpoint of the concentric rings defined on the samples (section 3.8) of five samples processed using 3 GPa 2 turns.	91
Table 5-1. Sections taken to be analysed and WES selected for characterisation using advanced SEM techniques	110
Table 6-1. Comparison of TWEAs /SWEAs and WEAs. Material prior to transformation.	136
Table 6-2. Comparison of TWEAs /SWEAs and WEAs. Microstructural morphology	137
Table 6-3. Comparison of TWEAs /SWEAs and WEAs. Texturing	138
Table 6-4. Comparison of TWEAs /SWEAs and WEAs. Inclusions	139

## Table of Tables

Table 6-5. Comparison of TWEAs /SWEAs and WEAs. Carbide distribution .....	139
Table 6-6. Comparison of TWEAs /SWEAs and WEAs. Mechanical response .....	140
Table 6-7. Comparison of TWEAs /SWEAs and WEAs. Cracks .....	140

## Table of Figures

Figure 2-1 Rolling bearing schematic configurations. a) Elements assembled in a typical deep groove bearing. b) Different standard bearing types used according to the load requirements: 1. Deep groove single balls, 2. Steep tapered angle roller, 3. Double row balls, 4. Straight roller, 5. Pure thrust roller ball, 6. Needle roller. Adapted from [17]. .....	5
Figure 2-2 Microstructures of AISI 52100 in its delivery states. a) Spheroidized state, the small dots are carbides in a ferritic matrix.[22]. b) Hardened state: austenitised for 30 minutes at 845°C, oil quenched, and tempered 1 h at 175°C. The white dots are spheroidized cementite carbides in a tempered martensite structure [24]. .....	8
Figure 2-3 Two cracks generated by RCF. a) Crack growing from an indentation or surface defect. b) crack growing from an inclusion or internal notch. The horizontal hatching corresponds to an approximate stress distribution which can be related to the damage found inside the material. Adapted from [33]. .....	11
Figure 2-4 Pressure distribution in Hertzian contacts. a) Ellipsoidal pressure distribution from a spherical contact, b) Cylindrical pressure distribution from a cylindrical contact. Adapted from [34]. .....	12
Figure 2-5 Shear stress contour in a line contact in terms of $p_{\max}$ . The lower cylinder has infinite radius (flat condition) [36]. .....	13
Figure 2-6 Microstructural changes registered in the subsurface of the contact area in terms of the number of inner ring revolutions [39]. .....	14
Figure 2-7 Micrographs of the microstructural changes in sections transverse to the contact surface revealed by etching with Nital. a) DER in its early stage. b) Fully developed bands at 30° to the surface b. and c. bands at 80°. c) The number of cycles increases from the left to the right. Adapted from [39]. .....	14
Figure 2-8 SEM images of a spalls a) and micropitting, b) of a worn rolling element bearing affected by contact fatigue. Note the small holes or “pits” close to the cracks and spalls in b Adapted from [40]. .....	15
Figure 2-9 Typical of spalling damage during rolling contact fatigue in rolling element bearings [40]. .....	16

## Table of Figures

Figure 2-10 Damage produced by WSF in an AISI 52100 bearing inner race. The dotted lines in a) and b) indicate the cross sections showed by LOM in c) and d). The bearing in a) and c) has an outer diameter of 215 mm whilst the bearing in b) and d) has an inner diameter of 93 mm. Adapted from [48].	17
Figure 2-11 WSF in an inner ring raceway of a high-speed shaft bearing assembled in a wind turbine gearbox. a) Typical spalling produced by WSF, b) Cross section of the ring raceway taken along the dashed line showed in a). The section shows WEAs and a complex crack network extending to the contact surface. Adapted from [50].	18
Figure 2-12 SEM / SEI of a Butterfly wing formed around an $\text{Al}_2\text{O}_3$ inclusion in an AISI 52100 bearing steel. Note the two different borders, a) with crack, b) without crack [60].	19
Figure 2-13 WEAs and crack analysed using a) IQ image, b) IPF and c) KAM map. The images show long grains inside the WEAs extending from the crack to the matrix. These grains show a similar texture in b) and low average orientation angle (blue grains) in c). EBSD analysis using a step size of 150 nm. Ferrite structure was indexed prior to conducting the analysis. Adapted from [61].	20
Figure 2-14 WEAs analysed by EBSD and EDS maps. The original microstructure visible by LOM is in a), IQ map is in b), whilst the EDS – C appears in c) and EDS – Cr appears in d). No carbides were observed inside the WEAs in c) due to the dissolution of carbon in the WEAs structure. It seems that Cr was not affected by this dissolution. An IQ map reported long grains inside the WEAs Adapted from [62].	21
Figure 2-15 Classic plastic deformation processes used to shape metals that often are combined with heat treatment to refine grains. Adapted from [69].	24
Figure 2-16 Schematic drawing showing the development of microstructure during the drawing of a eutectoid steel [68].	24
Figure 2-17 A schematic drawing of the first device designed by P.W. Bridgman to test pipes. Adapted from [70].	25
Figure 2-18 Equipment to test thin discs developed by P.W. Bridgman This device would be developed to form the basis of future HPT test machines. Adapted from [71].	25
Figure 2-19 Schematic drawing of the ECAP processes defining X, Y and Z reference planes. This nomenclature is established in relation to the planes on the pressed sample [72].	26
Figure 2-20 Other SPD processes used to obtain UFG structures [74].	27

Figure 2-21 Applications of nano structured materials processed by Severe Plastic Deformation. a) implants for bone osteosynthesis made of nano structured Ti. b) Structural rod (50 mm diameter, 170 mm length) processed from ECAP billets. Adapted from [75].	28
Figure 2-22 HPT process with hydrostatic pressure and torsional stress applied to the sample disc. Adapted from [77].	29
Figure 2-23 HPT constraint conditions: a) unconstrained, b) constrained and c) quasi-constrained [78].	30
Figure 2-24 Anvils with two different alignments. a) Good alignment with relative displacements, measured by $X$ , of less than $X=25\mu\text{m}$ . b) Poor alignment with displacements more than $X=25\mu\text{m}$ . Adapted from [78].	30
Figure 2-25 Flow pattern distributions along disc diameters under an anvil misalignment of $200\mu\text{m}$ for a) $N = 1$ turn and b) $N = 5$ turns. Samples of F53 super duplex stainless steel processed using 6 GPa. Adapted from [78].	30
Figure 2-26 Shear strain and its distortion produced in a HPT sample [79].	31
Figure 2-27 Distortion produced by the shear strain at two points located on the top of a disc processed by HPT [11].	32
Figure 2-28 FEM results of the distribution of effective strain and strain rate across the axial sections of sample discs processed by HPT tests. A) Variations of strain for different sample thicknesses and number of turns. B) Variations of strain rate for different values of friction coefficients at the top and bottom anvils. Adapted from [80].	33
Figure 2-29 LOM taken from Al/Cu disc samples (axial sections) after HPT using 5 GPa and 3 turns. The images were taken at radial distances of a) 1.0 mm, b) 2.5 mm, and c) 4.5 mm. Some vortices are observed deforming the stacked Al/Cu layers. Adapted from [81].	34
Figure 2-30 An annealed oxygen – free high conductivity copper workpiece sliding against a hard steel wedge indenter at a velocity of 1 mm /s. Particle Image Velocimetry and additional software post- processing were used to determine the velocity variations in the subsurface. The red dotted circle shows a pre-existing fold. The yellow arrow indicates the sliding direction [83].	35
Figure 2-31 2D simulation of two similar bodies under sliding contact with A being slightly harder than B. A mixed layer conformed by atoms from A and B appeared between them [84].	36

## Table of Figures

Figure 2-32 Simple shear blocked locally by obstacles: a), b) schematic of the obstacles modelled. c), d) velocity fields resulting from the obstacles modelled. Adapted from [85]. .....	36
Figure 2-33 Evolution of hardness in high purity Ni samples during a HPT test under 1, 3, 5 and 9 GPa and 5 turns [86].....	37
Figure 2-34 Rectilinear grid pattern in a quarter of a disc used to create colour-coded hardness contour maps in HPT samples. The horizontal line located at the bottom of the quarter can be used to create hardness profiles across the sample diameter [78]. .....	38
Figure 2-35 Variation of hardness in Al-7075 alloy samples after HPT. A), variation of hardness with distance from the centre of the sample, b), variation in hardness with equivalent strain. The tests were conducted using 6 GPa, 1rpm and 1/8, ¼, ½, 1, 2, 5, 10 turns [87].....	39
Figure 2-36 Hardness evolution with equivalent strain for Zn after HPT using 2 GPa and 1 – 5 turns. The rotation speed was 0.5 rpm [88]. .....	40
Figure 2-37 Colour-coded contour maps of a quarter disc of a Zn–Al sample processed by HPT for a. 1 turn (3 GPa) b. 5 turns(3 GPa) c. 1 turn (6 GPa) d 5 turns (6 GPa). The legend in the bottom right corner indicates the Vickers hardness [89].In this case, the hardness tends to be higher in the centre of the HPT sample than in other places, including the sample edges. Figure 2-37 (hardness colour map) and 2-38 (Hardness – equivalent strain plot) show examples of this behaviour in a Zn-Al alloy processed using several turns [89]. The hardness decreases until reaching a stable value with higher equivalent strains. The decrease in the hardness values is related to a weakening effect, attributed to the loss of rod-shaped Zn precipitates within the Al-rich grains [90]. .....	40
Figure 2-38 Evolution of hardness vs. equivalent strain for a Zn-Al alloy after HPT using 3 GPa (1, 3, 5 turns) and 6 GPa (1, 2, 4, 5, and 20 turns) [89]. .....	41
Figure 2-39 Results of processing a Cu–Zr alloy using 6 GPa and ¼, 5 and 10 turns. The top row shows images from the centre of the sample, the bottom row corresponds to a point close to the edge of the sample. The colours represent different grain orientations [87]. .....	42
Figure 2-40 FEM prediction of the temperature distribution after 10 turns of HPT processing for pure iron. Four separate points are evaluated for comparison. Point P1 corresponds to the sample centre, P2 corresponds to a sample point close to the edge, point 3 is located inside the upper anvil and P4 is at the upper right corner of the anvil [88]. .....	43



Figure 2-41 a) Micro - cracks and b) pores found in HPT samples of a high – nitrogen stainless steel processed by 6 GPa and 1 turn [95]. .....	44
Figure 2-42 Schematic relationship between shear strength and pressure. Two main regions can be identified from the change of slope of the curve [16]. .....	45
Figure 2-43 SEM images taken at 4 mm from the sample centre after HPT using 6 GPa and a. 1/4 turn, b. 1 turn, c. 2 turns and d.5 turns [97]......	46
Figure 2-44 Hardness profile of AISI 8620 processed by HPT. Both images show an increase in hardness with distance from the sample centre, as corresponds to a <i>without recovery</i> condition. (a.) after 14 turns, (b.) after 5 turns. The original hardness without any plastic deformation is indicated by N=0 [97]......	47
Figure 2-45 Microstructural evolution of a sample of UIC 900A from a. its original condition to b. after HPT with 0.6 turns [98]. .....	47
Figure 2-46 Hardness evolution of the pearlitic rail steel UIC 900A after HPT using 5.7 GPa with 0.15 and 0.6 turns [98]. .....	48
Figure 2-47 Microstructural evolution of a commercial carbon steel UIC 860V processed by HPT using 7 GPa and at different numbers of turns: (a.) N = 0, (b.) N = 1, (c.) N = 2, and (d.) N = 3. The white arrow shows the shear orientation [11]......	49
Figure 2-48 Hardness evolution with strain ( $\gamma = 95$ or N = 1.5, $\gamma = 200$ or N = 3, $\gamma = 300$ or N = 5) for the commercial carbon steel UIC 860V. Adapted from [11]. .....	49
Figure 2-49 Effect of the number of turns on the degree of cementite dissolution in the <i>Formation</i> , <i>Transition</i> and <i>Fragmentation</i> stages. Adapted from [11]......	50
Figure 2-50 Schematic of carbon dissolution from the pearlite structures through the (a.) Formation, (b.). Transition and Fragmentation stages. Adapted from [11]. .....	53
Figure 3-1 Schematic material flow for the AISI 52100 studied in this project. The original material in its as received condition is processed and characterized through different stages (blue boxes) following the blue arrows. The product of these processes is highlighted in red text. ....	58
Figure 3-2 Schematic of the annealing heat treatment applied to the standard rollers.....	59

## Table of Figures

Figure 3-3 Details of the HPT testing machine, with the plunger and anvils used to deform the steel samples. ....	61
Figure 3-4 Images of the HPT testing machine available in the SPD Lab. a) The machine itself, b) the hydraulic unit and control system required to operate the machine.....	61
Figure 3-5 HPT sample in lower anvil. a) Before conducting HPT b) After conducting the HPT test with the sample stuck to the lower anvil. Tests conducted under 1 GPa 1 turn 1 rpm	63
Figure 3-6 Use of the <i>Analyze Particle</i> tool from <i>Image J</i> to eliminate particles according to their size. The original image appears at the left, the other images were obtained after defining a particular size. [107] .....	66
Figure 3-7 Position of the representative areas analysed by IPP Image J to determine the %WES in the HPT samples from stage 2.....	66
Figure 3-8 Top surface of a disc sample processed using 3 GPa and 1 turn. a) Micrograph taken at a radial distance of 2.5 mm from the centre. b) IPP Image J to determine the %WES in the HPT samples from stage 2 .....	67
Figure 3-9 Calculation of areas and %WES in nine concentric circles drawn on a black/white mask of a periphery montages. The radii of the circles were 3, 3.25, 3.5, 3.75, 4, 4.25, 4.5, 4.75 and 5 mm. ....	67
Figure 3-10 Example of a ring with mid – radius of 4.125 mm used to calculate the %WES in relation to the radius. Eight rings were defined to calculate the %WES along the area limited by circles of 3 and 5 mm radius. ....	68
Figure 3-11 Hardness positions taken across the sample diameter used to determine the hardness profiles. The external circumference corresponds to the sample perimeter. 36 hardness measurements were taken for each hardness profile. ....	69
Figure 3-12 Kikuchi patterns used in EBSD analysis. a). Schematic of diffraction pattern generation due to the interaction between the EB and the sample. b) Typical Kikuchi patterns on a phosphor screen [109]. ....	71
Figure 4-1. Top and bottom surface of annealed AISI 52100 samples after conducting HPT tests using 0.5, 1 GPa, 3 GPa, 6 GPa and 1 turn. Samples after tests with flash removed. Top surfaces exhibit circular grooves (except for those processed using 6 GPa) and the effects of misalignment (red arrows), whilst bottom surfaces showed a roughness pattern similar to an orange peel (enclosed with orange dotted lines). ....	76

- Figure 4-2. Montages of top and bottom surface of annealed AISI 52100 samples after conducting HPT tests using 0.5, 1 GPa, 3 GPa, 6 GPa and 1 turn. Details of the same sample after polishing (to a depth of 40  $\mu\text{m}$ ) and etching. The top surface exhibited grooves alternated by white patches. The bottom surface showed var amounts of *orange peel* pattern as a function of the pressure applied. The images were taken from samples of stage 2. LOM, 2% Nital.....77
- Figure 4-3. Details of WES structure on the top surface of a sample processed using 1 GPa 1 turn. The red rectangles show the regions detailed in the next image. a) Overlapping TWEAs (enclosed by yellow dotted line). b) Isolated TWEAs (indicated by blue arrows) c) Cracks in TWEAs and across them (blue arrows). d) Fibre / layered structures inside the TWEAs (regions enclosed by yellow dotted line), and a region of the ferritic matrix (enclosed by white dotted line). LOM Nital 2%. ....78
- Figure 4-4. Details of WES structure on the top surface of a sample processed using 1 GPa 3 turns. The red rectangles show the regions detailed in the next image. a) Elongated TWEAs due to high plastic deformation (areas enclosed by yellow dots). b) Typical abrasion grooves (indicated by blue arrows) c) Transverse brittle cracks in TWEAs (blue arrows) and loose material (enclosed by yellow dotted lines). d) Evidence of extensive plastic deformation due to sliding contact (areas enclosed by yellow dots) and the ferritic matrix (enclosed by white dotted line). The orange arrow indicates the sliding direction. LOM Nital 2%. .80
- Figure 4-5. Details of WES structure on the top surface of a sample processed using 3 GPa 1 turn. The red rectangle shows the region detailed in the next image. a) Large grooves affecting the top surface. b) Radial brittle cracks and evidence of delamination are visible inside the TWEAs (Yellow dotted lines). LOM Nital 2%.....81
- Figure 4-6. Details of WES structure on the top surface of a sample processed using 3 GPa 3 turns. The red rectangle shows the regions detailed in the next image. a) High plastic deformation and clusters of small TWEAs oriented in the sliding direction (enclosed by yellow dotted lines). b) Cracks affecting TWEAs and the ferritic matrix. LOM Nital 2%.81
- Figure 4-7. Debris produced during a HPT test (3 GPa 3 turns). a) Evidence of delamination (blue arrows) and b) grooves (yellow arrows). LOM Nital 2%.....82
- Figure 4-8. Examples of images used to calculate the % TWEAs shown in table 1.3. All samples processed correspond to Stage 2. Nital 2%.....82

## Table of Figures

- Figure 4-9. Details of the bottom surface of a sample processed by 6 GPa 1 turn. a) The red rectangle shows the region detailed in the next image. b) Details of the deformed surface ..... 84
- Figure 4-10. Details of a top surface of a sample processed by 6 GPa 1 turn. The red rectangle shows the regions detailed in the next image. a) Despite looking white, the patches on the image are asperities ground and polished during sample preparation. b) Small spheroidal carbides in the ferritic structure (enclosed by yellow dotted lines). ..... 85
- Figure 4-11. Samples after pressing by the HPT machine. a). 1 GPa, b). 3 GPa, c). 6 GPa,. The surface patterns reproduced the surface finish of the machine anvils. .... 86
- Figure 4-12. 3D reconstruction of a). top and b). bottom surface along a diameter of a samples disc pressed under 1 GPa. The roughness of the top surface is less than that of the bottom surface. Note the big flat area on the top surface, enclosed by the blue dotted line and the *orange peel* pattern on the bottom surface. .... 88
- Figure 4-13. Large cloud SWEA system located between a radial distance of 4.2 mm and the edge of a samples processed using 3 GPa 2 turns. LOM Nital 2%. .... 89
- Figure 4-14. Large solid SWEA system located between a radial distance of 4.6 mm and the edge of a samples processed using 3 GPa 2 turns. LOM Nital 2%. .... 89
- Figure 4-15. Large system of cloud and solid SWEAs linked to a crack network (blue arrows). The red rectangle shows the region detailed in figure 4-16 a). LOM 2% Nital ..... 90
- Figure 4-16. Details of large cloud and solid SWEAs. The red rectangle shows the region detailed in the next image. a). Cloud SWEAs (enclosed by yellow dotted line), and cracks (blue arrows). b.) Cloud SWEAs (enclosed by yellow dotted line) with some solid SWEAs inside (indicated by yellow arrows). LOM 2% Nital. .... 90
- Figure 4-17. TWEAs (indicated by blue arrows) and SWEAs inside the sample (indicated by yellow arrows) in a cross section of a sample processed by 3 GPa 2 turns. The red rectangles show the regions detailed in figure 4-18. Some SWEAs also appeared at the edge of the sample in another well-defined WES group (enclosed by white dotted line) LOM 2% Nital... 92
- Figure 4-18. Details of TWEAs and SWEAs in a cross section of a sample processed by 3 GPa 2 turns. a) SWEAs and cracks (indicated by blue arrows) at the edge of the sample. b) Elongated SWEA system located far from any border of the sample. c) Small and isolated SWEAs located at a radial distance of approximately 4 mm and at a depth of 200  $\mu\text{m}$  from the top

surface (Yellow arrows). d) TWEAs located at a radial distance of approximately 4 mm. LOM 2% Nital .....	93
Figure 4-19 Microhardness variations across the diameter of the disc samples after conducting HPT tests under a), 0.5 GPa, b) 1 GPa, c) 3 GPa and d) 6 GPa. The hardness of the disc sample prior to being processed by HPT was $180 \pm 10$ HV.....	94
Figure 4-20 Cloud SWEAs located at radial distances of between 3775 and 4175 $\mu\text{m}$ ; points A, C, D, E correspond to measurements on SWEAs (enclosed yellow dotted lines). Sample processed through 3 GPa 2 turns. LOM 2% Nital .....	95
Figure 4-21 Solid SWEA located at radial distances of between 4410 and 4710 $\mu\text{m}$ ; points C, D correspond to SWEAs. Sample processed through 3 GPa 2 turns. LOM Nital 2%.....	96
Figure 4-22 Top surface of a sample processed using 3 GPa 3 turns. The red rectangles show the regions detailed in figure 1.23 a), b) Images taken at increasing magnifications to localise the analysed region. LOM Nital 2% .....	97
Figure 4-23. Nano hardness map taken from the red area shown in figure 4-22 b). .....	97
Figure 4-24. Cross section of a sample processed using 6 GPa 1 turn (stage 3). The red rectangles show the regions detailed in the next image a), b). Images taken at increasing magnifications to localise the analysed region. LOM Nital 2%. .....	98
Figure 4-25 Nano hardness map taken from the red area shown in figure 4.24 b). .....	98
Figure 5-1. TWEAs and surrounding ferritic matrix with spheroidised carbides (radial distance 3.5 mm) on the top surface of a disc sample processed using 0.5 GPa 1 turn. The red rectangle shows the region detailed in (b.) Region 1 corresponds to the TWEAs, region 2 corresponds to the ferritic matrix. Elongated carbides (indicated by blue arrows) are visible in b). SEM / SEI, Nital 2% .....	101
Figure 5-2. Details of TWEAs structure on the top surface of a sample processed using 0.5 GPa 1 turn, in a region located at a radial distance of 3.5 mm. The red rectangle indicates the area shown at higher magnification in (b). a) Differences between the appearance of the deformed ferritic matrix (1) and TWEAs (2). TWEAs layers appeared to overlap (red arrows) b) High plastic deformation produced by severe sliding. SEM / SEI, Nital 2%.....	102
Figure 5-3. Formation of flakes in a TWEA located at a radial distance of 3.5 mm on the top surface of a disc sample processed by 1 GPa 1 turns. The red rectangle indicates the area shown	

## Table of Figures

- at higher magnification in b). Blue arrows in b) shows debris produced by material detaching from the flakes. SEM / SEI, Nital 2%..... 103
- Figure 5-4. Cracks and material detaching on TWEAs due to flaking failure. The detached material exposed the ferritic matrix. TWEAs located at a radial distance of 3.5 mm on the top surface of a disc sample processed by 0.5 GPa 2 turns. The red rectangle indicates the area shown at higher magnification in (b). Region 1 correspond to the exposed ferritic matrix, region 2 to a TWEA affected by flaking and cracks. SEM / SEI, Nital 2% ..... 103
- Figure 5-5. Axial section of a disc sample located at a radial distance of 4 mm processed by 1 GPa 1 turn. The red rectangle indicates the area shown at higher magnification in figure 5.6 a). Region 1 shows the ferritic matrix with spheroidised carbides, region 2 consists of TWEAs close to the top surface. The green arrow indicates the top surface of the sample. SEM / SEI, Nital 2%..... 104
- Figure 5-6. Details of the image shown in figure 5-5. The red rectangle indicates the area shown at higher magnification in (b). a) The carbide distribution in the ferritic matrix in region 1 is different to that found in the TWEAs in region 2. b) Highly deformed carbides linked to the fibrous structure in a cloud TWEA (white arrows). SEM/SEI Nital 2%..... 105
- Figure 5-7. Axial section at a radial distance of 4 mm of a disc sample processed by 1 GPa 2 turns. The red rectangle indicates the area shown at higher magnification in figure 5-6. The white dotted line encloses interconnected TWEAs present close to the top surface. Other isolated TWEAs appear at greater depths beneath the surface, at depths close to 100  $\mu\text{m}$  (yellow arrows). The green arrow indicates the top surface of the sample. SEM / SEI, Nital 2%..... 105
- Figure 5-8. Details of the image shown in figure 5-7. The red rectangle indicates the area shown at higher magnification in b). a) The depth to which TWEAs extended beneath the top surface is not regular along its length. A fibre / layered structure is visible inside the TWEAs. Deformed carbides appeared between the fibres /layers (white arrows in b)); some of these seemed to be linked to the fibre/layered structure (enclosed by yellow dotted lines in b)). SEM/SEI Nital 2%. ..... 106
- Figure 5-9. Solid WEAs (white dotted lines, region 1) and cloud SWEAs (yellow dotted line, region 2) located close to the edge of a sample processed by 3 GPa 2 turns. The red rectangle indicates the area shown at higher magnification in figure 1-10. SEM/SEI 2% Nital. 107

- Figure 5-10. Details of the SWEAs system shown in figure 5-9. Yellow dotted lines enclose clouds (region 1), whilst the white dotted lines enclose the solid SWEAs (region 2). The red rectangle indicates the area shown at higher magnification in figure 1-11. SEM/SEI 2% Nital. ....107
- Figure 5-11. Details of cloud SWEAs linked to a typical solid SWEA located at the edge of the sample. The red rectangle indicates the area shown at higher magnification in (b). a) Fibrous structure in a cloud (region 1, enclosed by a white dotted line) and solid SWEAs (region 2 enclosed by an orange dotted line). b) Deformed carbides that seem to be linked to the twisted fibrous structure in a cloud SWEA (blue arrows). SEM/SEI Nital 2%.....108
- Figure 5-12 Details of a solid SWEA located at the edge of a circumferential section of a sample processed by 3 GPa 2 turns. The red rectangle indicates the area shown at higher magnification in (b). a) Interface between the ferritic matrix (Region 1) and the SWEAs (Region 2). b). Variations of the fibre structure close to the centre of the SWEA. The orange dotted lines separate regions with significant differences in their carbide content. SEM/SEI, Vilella's reagent.....109
- Figure 5-13. Details of cloud SWEAs located at the centre of a diametral axial section of a sample processed using 3 GPa and 2 turns (white dotted line). The red rectangle indicates the area shown at higher magnification in (b). a) The fibrous structure in the cloud (blue arrows) and cracks in the solid SWEA (red arrows). b). Deformed carbides linked to the fibrous structure (yellow arrows). SEM/SEI Nital 2%. ....109
- Figure 5-14. Microstructure of the axial section of an annealed AISI 52100 roller analysed by: a) SEM / SEI, b) SEM / BSI c) Image Quality (IQ) d) Auto Phase maps (AP), e) Inverse Pole Imaging (IPF) with the Z axis as normal direction, and f) Kernel Average Maps KAM (150 nm 5°). ....111
- Figure 5-15. Axial section of a HPT sample processed using 3 GPa 2 turns. Red rectangles correspond to Regions 2 and 3, which are shown in figures 5-16 and 5-17. The blue circle shows a typical example of a SWEA located at the edge of the sample. A similar SWEA is present in Region 4. The orange arrow indicates the top surface of the sample. Montage constructed from SEM / BSI images (10 kV, x200 and 5.1 mm WD). ....112
- Figure 5-16. Isolated (blue arrows) TWEAS with ill-defined borders (yellow dotted lines) and mixed (red dotted line) TWEA types in Region 2. Blue arrows show cracks at the top surface. The orange arrow indicates the top surface of the sample. Significant regions appeared

## Table of Figures

without carbides. Montage constructed from SEM/ BSI images (10 kV, x200 and 5.1 mm WD). .....	113
Figure 5-17. Well-defined SWEA located in Region 3. The Orange arrow indicates the top surface of the sample. Montage constructed from SEM / BSI images (10 kV, x200 and 5.1 mm WD). .....	113
Figure 5-18. Well-defined SWEA located in Region 3. Orange arrow indicates the top surface of the sample. Montage constructed from SEM / BSI images 10 kV, x200 and 5.1 mm WD) images. ....	114
Figure 5-19 IQ maps taken from Regions 2, 3 and 4. White structures (TWEAs and WEAs) are easily distinguishable from the ferritic matrix because of their dark contrast.....	115
Figure 5-20 AP maps from Regions 2, 3 and 4 show as black regions without any recognized phase. The absence of carbides inside the white structures was reported by both IQ and AP maps. ....	116
Figure 5-21 IPF from Z axis (ND) taken from Regions 2, 3 and 4. A very refined structure is revealed in all regions studied after applying 3 GPa 2 turns and 6 GPa 1 turn. TWEAs and SWEAs appeared black as was observed in AP maps. IPF with CI greater than 0.1.....	117
Figure 5-22 KAM maps taken from Regions 2, 3 and 4 using a 150 nm step size and orientation angles up to 3° .....	118
Figure 5-23 Carbide distribution and WEAs in Regions 2, 3 and 4 revealed by Carbon EDS maps. Blue circles show carbide clusters in the ferritic matrix, red arrows show C trails or comet tails inside SWEAs (Image b) and c))......	119
Figure 5-24 Chromium distribution and WEAs in Regions 2, 3 and 4 revealed by Chromium EDS maps. Blue circles show carbide clusters in the ferritic matrix, red arrows show Cr trails or comet tails inside SWEAs (Image b). and c)). ....	120
Figure 5-25 EDS maps of Sulphur in Regions 2, 3 and 4. Red arrows indicate the presence of significant signals that appeared as ill – defined dots (Images a). and c).) and <i>comet tails</i> (image b).). These signals are related to the presence of inclusions inside the TWEAs and SWEAs. ....	121
Figure 5-26 EDS maps of Aluminium in Regions 2, 3 and 4. Red arrows indicate the presence of significant signals that appeared as ill – defined dots which are related to the presence of inclusions inside the TWEAs and SWEAs.....	122



Figure 5-27. SEM / BSI images of pearlite clusters in the annealed AISI 52100 microstructure (orange circles). These clusters can irrupt plastic flow during the HPT test.....	123
Figure 5-28. SEM / BSI of carbide clusters in the vicinity of the SWEAs showed in figure 5-17 (orange circles).....	123
Figure 6-1. Hardness as a function to the strain for disc samples processed using a) 0.5 GPa, b) 1 GPa, c) 3 GPa and d) 6 GPa. The regression curves correspond to the disc samples processed using 3 turns.....	126



## Research Thesis: Declaration of Authorship

Print name: Luis Vicente Wilches Peña

Title of thesis: Microstructural alterations during HPT tests on annealed 52100 bearing steel

I declare that this thesis and the work presented in it are my own and has been generated by me as the result of my own original research.

I confirm that:

1. This work was done wholly or mainly while in candidature for a research degree at this University;
2. Where any part of this thesis has previously been submitted for a degree or any other qualification at this University or any other institution, this has been clearly stated;
3. Where I have consulted the published work of others, this is always clearly attributed;
4. Where I have quoted from the work of others, the source is always given. With the exception of such quotations, this thesis is entirely my own work;
5. I have acknowledged all main sources of help;
6. Where the thesis is based on work done by myself jointly with others, I have made clear exactly what was done by others and what I have contributed myself;
7. None of this work has been published before submission or Parts of this work have been published as:
  - WANG, N. et al. Experimental and Simulation Studies of Strength and Fracture Behaviors of Wind Turbine Bearing Steel Processed by High Pressure Torsion. *Energies*, v. 9, n. 12, 2016. ISSN 1996-1073.

Signature:

Date: 20/12/2018



## Acknowledgements

I would like to express my sincere gratitude to Prof. Ling Wang who acted as the main supervisor of this project. Her commitment and enthusiasm were always a strong motivation during my PhD journey.

I am also sincerely grateful to Dr Brian Mellor, not only for his guideline as my supervisor, but also his friendship. Without his encouragement this project would not have been possible. The Way of Saint James is waiting for us...!

I would like to thank Dr Yi Huang for her constant support; her knowledge and experience with SPD processes were fundamental in the development of this project.

I would like to thank Dr Alexander Schwedt for his advice and assistance in obtaining and examining the information related to EBSD / EDS analysis

I also want to thank Mr. Dave Beckett and Ms. Heather Jones for their constant assistance and company during the endless lab hours.

To all my friends and colleagues who shared with me all the good and hard moments along this adventure, thanks for allowing me to have a second family so far from home. A special mention must go to Ning Wang, Nan Hu, Madina Omarkhan, Charles Burston-Thomas, Pedro Pereira, Brynn Dachtler, Alexander Richardson, Paul Cross, Ales Rapuc, Alvaro Sanchez, and Viktorija Smelova.

I would specially like to thank the following people, groups and institutions for their contributions to this work:

- To Dr Yi Huang and Dr Pedro Enrique Pereira for their assistance in operating the High-Pressure Torsion Test machine located in the SPD lab at the University of Southampton.
- To Dr Terry J Harvey for his help in obtaining surface roughness measurements from the Taylor Hobson Form Talysurf 120L profilometer system and the Alicona G4 Infinite Focus optical system.
- To Dr Richard Cook and Mr Behrad Mahmoodi for their help in conducting the nano indentation tests using the NanoTest Vantage nano indenter test machine (Micro Materials Ltd).
- To Dr Shunca Wang for his help in operating the JEOL JSM-6500 Scanning Electron Microscope.

## Acknowledgements

- To Mr. Alistair Clark and Mr. Nikolai Zhelev who assisted in operating the FEI/Philips XL30 ESEM Scanning Electron Microscope.
- To Prof. Joachim Mayer, who provided access to the Central Facility for Electron Microscopy – GFE at RWTH Aachen University. From this wonderful group of people, I would like to highlight my gratitude to Dr Alexander Schwedt who supported me by operating the JEOL JSM-7000F Scanning Electron Microscope and the Smart Insight / TEAM™ EBSD Analysis System (Smart Insight System from Ametek). In addition, I would like to thank Ms. Melanie Keil and Ms. Ruth Harscheidt, research technicians, who helped with sample preparation prior to SEM / EBSD / EDS characterisation.
- To Prof. Walter Martin Holweger and in his name to Schaeffler Technologies AG & Co. KG for their technical and financial support for conducting EBSD / EDS analysis.

And finally, I would want to thank the Administrative Department of Science, Technology and Innovation – Colciencias, the Medellin Higher Education Agency – Sapiencia and the British Council for sponsoring this research.

*To Esther, Carmen and Lili...*





*"As often as you can, free yourself from worldly affairs so that you may apply that wisdom which God gave you wherever you can. Remember what punishments befell us in this world when we ourselves didn't cherish learning nor transmit it to other men."*

*"Tan a menudo como puedas, libérate de los asuntos mundanos para que puedas aplicar esa sabiduría que Dios te dio donde sea que puedas. Recuerda los castigos que nos ocurrieron en este mundo cuando nosotros mismos no apreciamos el aprendizaje ni lo transmitimos a otros hombres."*

**Saint King Alfred the Great**

*"Tu fe debe ser una brillante luz para aquellos a quienes instruyes..."*

*"Your faith should be a shining light for those whom you instruct..."*

**Saint Jean-Baptiste de La Salle**

*"Cuando mira su infancia, ella también quisiera atravesar con la mirada esos años idos, para entrar al otro lado del tiempo. Al otro lado del tiempo, está la abuela..."*

*"When she's looking at her childhood, she would like to look through those years gone, to enter on the other side of time. On the other side of time, there is the grandmother..."*

**Eduardo Galeano**

*"...y se perdieron con ella para siempre en los altos aires donde no podían alcanzarla ni los más altos pájaros de la memoria."*

*"...they were lost forever with her in the upper atmosphere where not even the highest-flying birds of memory could reach her."*

**Gabriel Garcia Marquez**

*"—Bien parece —respondió Don Quijote— que no estás cursado en esto de las aventuras: ellos son gigantes; y si tienes miedo, quítate de ahí, y ponte en oración en el espacio que yo voy a entrar con ellos en fiera y desigual batalla."*

*"It is clear," replied Don Quixote, "that you are not experienced in adventures. Those are giants and if you are afraid, turn aside and pray whilst I am going to enter a fierce and unequal battle with them."*

**Miguel de Cervantes Saavedra**



## Definitions and Abbreviations

$a$	Semi-major axis of the ellipse in point contact [m] or radial distance of the cylinder in line contact [m].
$b$	Semi-minor axis of the contact ellipse [m].
$h$	Final thickness of a sample disc after HPT test [m].
$h_0$	Original thickness of a sample disc before HPT test [m].
$k$	Measurement of the local stress needed at grain boundary for transmission of plastic flow and/or for cleavage fracture [Pa].
$l$	Arc variation in relation to the angular variation and radial distance to an ideal HPT sample disc [m].
$L$	Length of an ideal cylinder in line contact to Hertzian stress contact [m].
$L_{10}$	Expected life of 90% of bearings under normal operating conditions established by the manufacturer. Also called $B_{10}$ . [revolutions].
$N$	Number of turns applied in a HPT test [turns].
$p_{prom}$	Average pressure across the spherical/cylindrical distribution in a Hertzian contact [Pa].
$p_{max}$	Maximum pressure in the spherical/cylindrical distribution in a Hertzian contact [Pa].
$r$	Distance from the centre in a HPT sample disc [m].
$R_1, R_2$	Radius of the bodies in a Hertzian contact [m].
$S_y$	Yield strength [Pa].
$\theta$	Rotational angle related to the torsional deformation applied in a HPT sample disc [rad].
$\gamma$	Shear strain

## Definitions and Abbreviations

$\varepsilon$	Equivalent or Von Mises shear strain
$\Psi, \Phi$	Angles used to define the arc of curvature of the channel intersection in a ECAP die [rad].
$\sigma$	Normal stress, true stress [Pa].
$\sigma_0$	Friction resistance for dislocation movement within the grains in the Hall – Petch equation [Pa].
$\sigma_x, \sigma_y, \sigma_z$	Principal stress components in a Hertzian contact. The letters x, y and z represent the rolling orientation, the width and the depth respectively [Pa].
$\tau_{max}$	Maximum shear stress as a function of the depth z of the contact surface [Pa]
$r_\omega, \omega$	Axis of rotation and axial vector used to describe a disclination.

---

AP	Auto Phase maps
ASB	Adiabatic Shear Bands
BSI	Back -Scattered Imaging
CI	Confidence Index
DER	Dark Etching Areas
DMZ	Dead Metal Zone
EB	Electron Beam
EBS	Electron Back-Scatter Diffraction
EB x-ray	Electron Beam X -ray source
ECAP	Equal Channel Angular Pressing
EDS	Energy-Dispersive x-ray Spectroscopy
IPF	Inverse Pole Imaging maps

IPP	Imaging Processing Program
IQ	Imaging Quality maps
IrWEAs	Irregular White Etching Areas
KAM	Kernel Average Maps
LOM	Light Optical Microscopy
MA	Macroscopy
OP – S	Colloidal Silica Polishing Suspension
RCF	Rolling Contact Fatigue
SEI	Secondary Electron Imaging
SEM	Scanning Electron Microscopy
SPD	Severe Plastic Deformation
SWEAs	Sub-surface White Etching Areas located inside of HPT disc samples
TEM	Transmission Electron Microscopy
TWEAs	Top White Etching Areas located at the top of HPT disc samples
WEAs	White Etching Areas observed in failure bearings.
WECs	White Etching Cracks associated to WEAs
WEM	White Etching Matters
WES	White Etching Structures in HPT disc samples
WD	Working Distance
WSF	White Structure Flaking



# Chapter 1 Introduction

## 1.1 Project overview

Over recent years, White Etching Areas, also known as White Etching Cracks, in bearing steels have received increasing attention due to their relationship with premature failures of rolling element bearings, especially those assembled in wind turbine gearboxes. WEAs have been linked to a catastrophic surface damage phenomenon commonly called *brittle flaking wear* [1] or *white structure flaking* (WSF) [2] that appears visible to the naked eye as smearing, cracks and macropitting. Although spalling resulting from Rolling Contact Fatigue (RCF) would normally be expected to limit bearing service life to 20 years based on the  $L_{10}$  life estimate, WEA formation and WSF can reduce this to as short as 5 - 10% of the  $L_{10}$  bearing life [2]. WEAs are a particular type of microstructure in steels, which appears to be white under Light Optical Microscopy (LOM) after etching. The white appearance is due to their higher corrosion resistance to Nital (2% nitric acid + ethanol) etch compared to the matrix that surrounds them [3].

WEAs have been related to several microstructural features in steels, such as matrix discontinuities, hydrogen concentration and adiabatic shear bands. Firstly, stress concentration from discontinuities such as non-metallic inclusions [4], porosity [5], carbide clusters [6] and pre-existing intergranular cracks [7] can alter the local stress distribution. Secondly, high hydrogen concentrations can produce embrittlement and a significant reduction in fatigue resistance [8]. Finally, adiabatic shear bands, resulting from the impact of rollers onto the rings, can lead to the propagation of micro cracks and also WEAs [9]. These microstructural features interact with the Hertzian stresses in the subsurface of the contact areas to generate localized and severe plastic deformation (SPD) conditions. This SPD could promote grain refinement and dissolution of carbides in well-defined regions. Both phenomena seem to be closely related to WEAs initiation and evolution [10].

Similar mechanisms have been suggested to explain the origin of some white microstructures encountered in pearlitic steels processed by High Pressure Torsion tests (HPT) [11]. HPT, as SPD process, is generally conducted on a thin disc sample placed between two anvils that transmit compression and high torsional stresses through the rotation of one of the anvils. The combination of compression and shear stresses can produce homogeneous microstructures with grain sizes of less than 1  $\mu\text{m}$  [12]. Although HPT differs from RCF in many ways, it can be a viable alternative to study the combined effects of compression and shear in very limited volumes. HPT tests are simple to perform and allow easy repeatability compared to both RCF tests and the analysis of field

## Chapter 1

bearings, which usually require millions of cycles to produce WEAs [13] [14], whilst HPT requires just a few minutes to process one disc. Parameters such as pressure, strain (measured as rotational displacement or turns), rotational speed and temperature can be easily controlled, allowing efficient sample processing under different conditions.

It is however important to understand the limitations of HPT tests. The slippage between anvils and discs for example, can produce unexpected changes in the samples [15] [16]. Moreover, the final hardness of discs admissible must be lower than the anvil hardness to avoid permanent damage to the anvils and the HPT test machine. To study the initiation and evolution of WEAs in a bearing steel affected by SPD conditions, the feasibility of creating White Etching Structures (WES) in an AISI 52100 bearing steel by the HPT process is described in this thesis. After successfully producing WES, the microstructural changes were examined and quantified in relation to the pressure and number of turns used during HPT tests. A detailed characterisation was also conducted by SEM / SEI / BSI and SEM / EBSD / EDS. These results were used to shed some light on the origin and evolution of white structures in AISI 52100.

## 1.2 Thesis Structure

This thesis consists of seven chapters, the first of which includes a project overview and the aims and objectives. The second chapter is a comprehensive literature review on two main topics: firstly, an overview on rolling bearing failures, especially those produced by RCF and WSF. Secondly, a review on the main features of HPT as SPD process to study the microstructural evolution of steels under extreme strains. The third chapter describes the experimental methodology utilised for the project, from disc sample preparation prior to conducting the HPT tests to the parameters employed for SEM / EBSD / EDS characterisation. The fourth chapter contains the main results of the characterisation carried out by Macroscopy, LOM and hardness measurements on an HPT processed annealed AISI 52100 bearing. The fifth chapter includes the information obtained by SEM / SEI / BSI and SEM / EBSD / EDS advanced characterisation. Chapter six consists of a general discussion on the results presented in the previous chapters. The final chapter summarizes the conclusions of this thesis and suggests future work useful to continue this line of research.



### 1.3 Aims and objectives

The aim of this project is *Identify the microstructural alterations occurring during HPT tests on annealed 52100 bearing steel*. This aim will be fulfilled by the following objectives:

- Conduct an extensive literature review on microstructural changes in materials under Rolling Contact Fatigue (RCF), White Structure Flaking (WSF) and Severe Plastic Deformation (SPD) especially HPT.
- Conduct experiments to create White Etching Structures in bearing steels by using HPT tests.
- Identify the microstructural changes produced in HPT samples by the use of optical microscopy, Scanning Electron Microscopy and Electron Backscatter Diffraction, EBSD techniques.
- Compare the microstructural changes that occur in bearing steels under RCF loading conditions with those that occur in HPT processed material and propose hypotheses to explain the mechanisms of WEAs formation in both HPT and RCF.



## Chapter 2 Literature Review

### 2.1 Failure in rolling element bearings

#### 2.1.1 Use Rolling element bearings

The term *rolling bearings* or rolling element bearings is used to describe machine components where the main load is transferred through elements in rolling rather than in sliding contact. Bearings cannot be considered as an isolated mechanical element but as a component, that means they are assembled units with relative movement between their internal parts. A typical rolling bearing component consists of an assembly of four essential parts: outer rings, inner rings, bearing elements and a separator or cage. Bearings can be classified in relation to the loads they take, as pure radial, pure thrust (or axial) and combined loads. The nature of these loads defines not only their geometry or size, but also topics such as maintenance, lubrication, tolerances and assembly sequences [17].

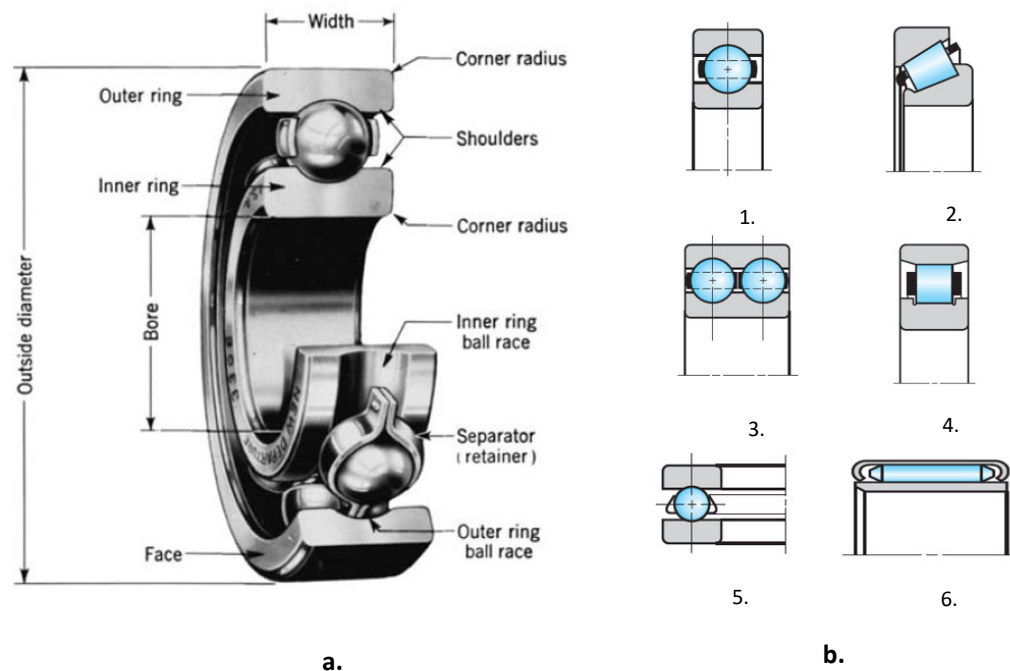


Figure 2-1 Rolling bearing schematic configurations. a) Elements assembled in a typical deep groove bearing. b) Different standard bearing types used according to the load requirements: 1. Deep groove single balls, 2. Steep tapered angle roller, 3. Double row balls, 4. Straight roller, 5. Pure thrust roller ball, 6. Needle roller. Adapted from [17].

Figure 2-1 shows the basic elements in a typical rolling ball bearing component and different standard bearing configurations used for particular load conditions [17]. The most widely used roller bearing type is the *single row deep groove ball bearing*, (figure 2-1 b)) due to its ability to take a wide range of radial and axial loads. For higher combined loads, the preferred option is the tapered angle rollers, whilst when facing higher axial loads, the double radial ball and straight roller bearings are recommended. If the application demands pure axial loads with limited assembly space, the best option is the one-way ball thrust bearings. Finally, needle bearings are selected when it is necessary to take very high radial loads with limited assembly space. These bearings represent just a small portion of the many standard configurations available, but many bearings are manufactured for special applications [17].

The life of a bearing is defined as the total number of revolutions (or hours operating at constant rotational speed) until a failure criterion is registered. The failure criterion is related to an observable damage to the contact surfaces of any element (rollers or rings). Its nature is linked to the fatigue resistance of the bearings and varies in relation to standards or commercial considerations. The minimum life of a group of bearings (also called  $L_{10}$  life or  $B_{10}$  life) is defined as the number of revolutions (or hours operating at constant speed) that 90% of a group of bearings will exceed before the failure criterions will be registered. A common  $L_{10}$  life used for many manufacturers is  $10^6$  revolutions [17].

### 2.1.2 Steels for rolling bearings

During their operative life, the bearings require a combination of high yield strength and high resistance to fatigue failure. Both properties can be obtained by increasing the hardness to values between 700 and 800 HV, with the rollers usually being 10% harder than the races [18].

#### *Case hardening grade*

These materials are basically low carbon steels (0.1 – 0.4% C) that can increase their hardness to values between 653 and 804 HV through carburizing processes. The main treatment consists of two steps, firstly exposure to high temperature 870 to 980°C in a carbon or nitrogen rich atmosphere. Then, the material is quenched and tempered to generate a hard surface but a soft core (266 – 513 HV). This combination provides high toughness and good fatigue resistance [19]. Table 2-1 summarizes the main case hardening steels used to manufacture bearings.

Table 2-1 Typical composition in % weight of case hardening grade steel [19].

Case hardening grades	%C	%Mn	%Si	%Cr	%Ni	%Mo
AISI 4320	0.20	0.55	0.22	0.50	1.82	0.25
AISI 5120	0.20	0.80	0.22	0.80		
AISI 8620	0.20	0.80	0.22	0.50	0.55	0.20
AISI 3310	0.10	0.52	0.22	1.57	3.50	
AISI 4620	0.20	0.55	0.22	1.82		0.25

*Through hardening grade*

The through hardening grade corresponds to steels capable of increasing their hardness using heat quenching and tempering heat treatments. Most current bearings are manufactured using through hardening steels. These materials are hyper eutectoid alloys with high carbon content (0.8 – 1.2%). The high carbon content provides better mechanical resistance compared to low and medium carbon steels [19]. Table 2-2 gives the main through hardening steels used to manufacture bearings and their typical chemical compositions.

Table 2-2 Typical composition in % weight of through hardening grade steel [19].

Through hardening grade	%C	%Mn	%Si	%Cr	%Ni	%Mo
ASTM A 485-1	0.97	1.10	0.60	1.05		
ASTM A 485-3	1.02	0.78	0.22	1.30		
TBS-9	0.95	0.65	0.22	0.50	0.25	0.12
SHKH15-SHDc	1.00	0.40	0.28	1.48	0.30	

*AISI 52100 Bearing steel*

The main steel from this grade is AISI 52100 (USA standard designation) due to its good mechanical properties and relatively low production cost. Around 90 % of all ball bearings in the world are made using this material [20]. This steel is called by different names depending on the national or international standard although there are not significant variations in their compositions. The main standard versions are: ISO-683-17, BS 534 -535 A99 (BSI / UK), 100Cr6 (DIN / Germany), SUJ2 (JIS / Japan) and ASTM A 295 (ASTM / USA). The chemical composition of AISI 52100 is shown in table 2-3, under standard ISO 683-17: 2014 [21].

Table 2-3 Composition in % weight of AISI 52100 under standard ISO 683 – 17 :2014 [21].

AISI 52100	%C	%Cr	%Mn	%Si	P (max)	S (max)	Mo
(ISO 683-17)	0.93 – 1.05	1.35 – 1.6	0.25 – 0.45	0.15 – 0.35	0.025	0.015	0.1

AISI 52100 usually is available in two delivery conditions, spheroidized and hardened. In the first state the material is characterized by its low hardness, between 190 and 250 HV, and its great machinability and workability. Its microstructure consists basically of primary carbides (cementite precipitates) grouped in small dots or “spheres” in a ferritic matrix (Figure 2.2 a) [22]. The microstructure of the hardened state consists of tempered martensite containing primary carbides (cementite particles) and temper carbides (called secondary or coherent carbides) and small amounts of retained austenite. These structures are obtained through a combination of quenching and tempering heat treatments [23]. The proportions of these phases can vary with the time and temperature used for tempering. The final hardness can vary between 700 and 900 HV. Figure 2-2 b) shows the microstructure of AISI 52100 in its quenched and tempered condition [24]. The typical non-metallic inclusions in AISI 52100 include manganese sulphides (MnS), aluminas ( $\text{Al}_2\text{O}_3$ ), Ca aluminates (such as  $\text{CaO } 6\text{Al}_2\text{O}_3$ ) and titanium nitrides (TiN). All of these are harder, melt at higher temperatures and are less dense than the steel. The implementation of better manufacturing processes has increased its cleanliness, improving its mechanical properties [2] [13].

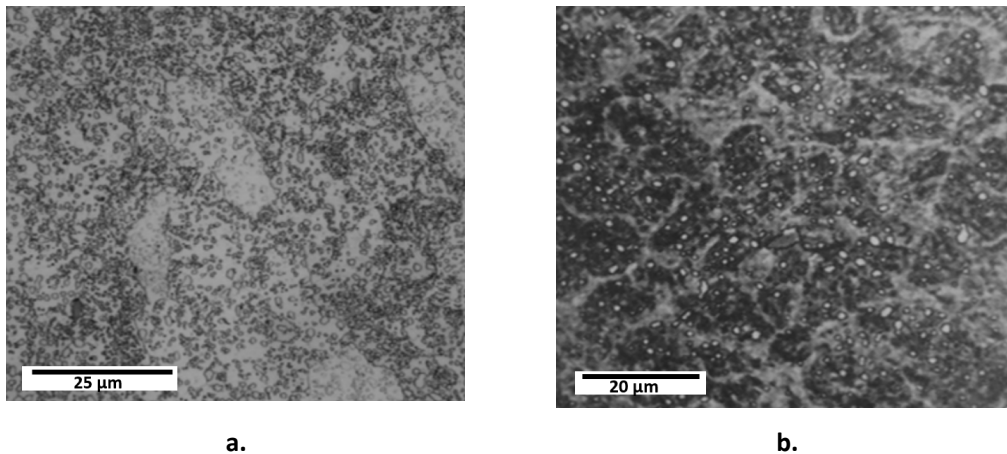


Figure 2-2 Microstructures of AISI 52100 in its delivery states. a) Spheroidized state, the small dots are carbides in a ferritic matrix.[22]. b) Hardened state: austenitised for 30 minutes at 845°C, oil quenched, and tempered 1 h at 175°C. The white dots are spheroidized cementite carbides in a tempered martensite structure [24].

## 2.2 Failures in rolling bearings <sup>i</sup>

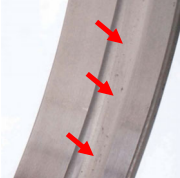

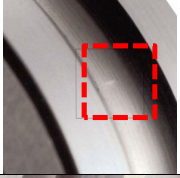
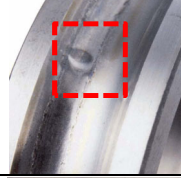

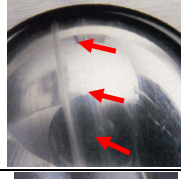
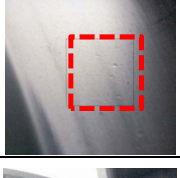

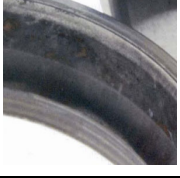



Lots of factors can lead to premature failures in rolling bearings most of these being related to poor operating environments and improper handling practices. Failure may appear as a consequence of one factor, in other cases factors may act simultaneously. For example, wear between the contact surfaces due to deficient lubrication can generate hard debris; these particles could contaminate the contact and produce denting in other areas. A similar effect can arise from the rust produced by corrosion, which can act as an abrasive in other areas, causing wear. Some of these factors and the damage associated with them are summarised in table 2-4 [25].

Good engineering practices such as adequate selection, correct assembly and regular maintenance, foresee the factors given in table 2-4 and minimize their effects. Good practice can also reduce the damage associated with fatigue phenomenon such as spalling or flaking (this is shown in the last row of table 2-4). Thus, the bearing operational life can be extended beyond the  $L_{10}$  life, thus preventing damage to other mechanical components. [26]. The fatigue phenomenon responsible for the damage to the contact surfaces is commonly called Rolling Contact Fatigue and will be discussed in the section 1.2.1.

However, over recent years another surface damage phenomenon, commonly called White Structure Flaking (WSF), has been widely reported in the technical literature as being responsible for early damage to bearings even when good engineering practice is followed. The applications affected by this phenomenon include automotive auxiliary devices [27], powertrains [28], alternators [29] compressor for fuel cell systems [30] and wind turbine rolling bearings [2].

Damage associated with WSF in wind turbine bearings usually starts within 20% of the  $L_{10}$  bearing life. However, its early diagnosis results complex due to the large variations in the speed and loads present in the wind turbines [31]. The importance of WEA flaking thus lies in its implications on operational and maintenance costs which can cause costs of around 10 % of the total wind turbine construction and installation investment. Despite the implementation of stricter design guidelines, bearing failures still occur after short service times without any preference to a particular wind turbine manufacturer [32].

Table 2-4 Common causes of bearing failures. The last row in red indicates factors and damage related to fatigue phenomenon. Adapted from [25].

<b>Misalignment</b>		<b>Overheating</b>	
Raceway ball track not parallel to raceway edges		Discoloration, annealing, thermal distortion	
<b>False brinelling</b>		<b>True Brinelling</b>	
Elliptical wear marks at each ball position due to excessive vibration		Ball indentations in raceways due to overloading	
<b>Tight fits</b>		<b>Reverse Loading</b>	
Heavy ball wear path at bottom of raceways		Balls show grooved wear bands	
<b>Contamination</b>		<b>Lubricant failure</b>	
Denting of bearing raceways and balls by hard particles		Discoloured balls and rings, excessive wear damage	
<b>Corrosion</b>		<b>Loose fits</b>	
Chemical attack		Circumferential wear due to play between moving parts, discolouration	
<b>Excessive Load</b>		<b>Fatigue failure</b>	
Premature spalled area in ball path, accelerating fatigue		Spalling or flaking of metal from contact surface	

### 2.2.1 Rolling - Sliding Contact and Surface Fatigue

When two surfaces in contact register rotational and translational motion, surface fatigue can occur. Surface fatigue is characterized by crack formation and flaking of material due to the cyclic loading of solid surfaces over many cycles. The recurring contact between asperities generates cyclic surface stresses and promotes localized fatigue on a microscopic scale. The fatigue comes from a sequence of elastic and plastic deformation, microstructural changes and crack initiation and propagation. The cracks can progress from indentations or defects in the surface and/or inclusions or notches inside the material [33]. Surface fatigue affects several mechanical systems such as rail - wheel pairs, gearboxes, cam – followers and rolling bearings. If the sliding component is less than 1% in relation to the rotational movement, the system can be analysed entirely as a



rolling condition [34]. In that case, the surface wear associated with the rotational movement receives the name of Rolling Contact Fatigue (RCF) [33].

RCF is the major surface damage mechanism in rolling bearings in service. Its influence is easily identifiable due to the typical damage feature registered in tracks and rolling elements namely spalling. Figure 2-3 shows schematics of RCF with cracks growing from surface indentations and internal notches. The first model used to analyse the effects of the rolling – sliding contact, and the surface fatigue arising from it, was proposed by Heinrich Hertz in 1880. This model is based on contact between two elastic bodies with a defined geometry in the hydrodynamic lubrication regime. The Hertzian model considers only loads normal to the contact, without sliding. Hence, the contact can be studied as a static condition. The Hertzian model has significant restrictions related to the environment and the nature of the sliding contact (i.e. the presence of external contaminants, the influence of other wear mechanisms and overloads capable of producing plastic deformation). However, this model still remains a reference for the analysis of rolling bearings, due to its strong experimental support.

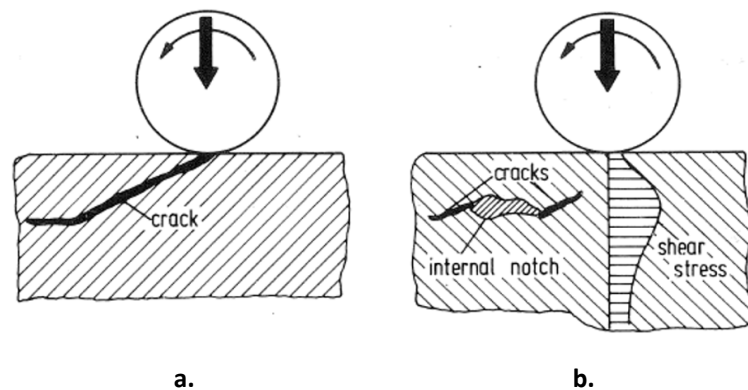


Figure 2-3 Two cracks generated by RCF. a) Crack growing from an indentation or surface defect. b) crack growing from an inclusion or internal notch. The horizontal hatching corresponds to an approximate stress distribution which can be related to the damage found inside the material. Adapted from [33].

The stresses in a contact point can be analyzed using two ideal morphological configurations: contact between two spheres (defined as a point contact) and between two cylinders (defined as line contact). Point contact generates an elliptical contact area and a semi ellipsoidal pression distribution. Line contact generates a rectangular contact area and a cylindrical pression distribution. The pressure and the stresses are defined in terms of geometrical parameters, such as the semi axis “a” and “b” of the point contact and the length L and the radius “a” of the line contact

which are represented in Figure 2-4. In both cases,  $R_1$  and  $R_2$  represent the reduced radii of the contacting bodies.

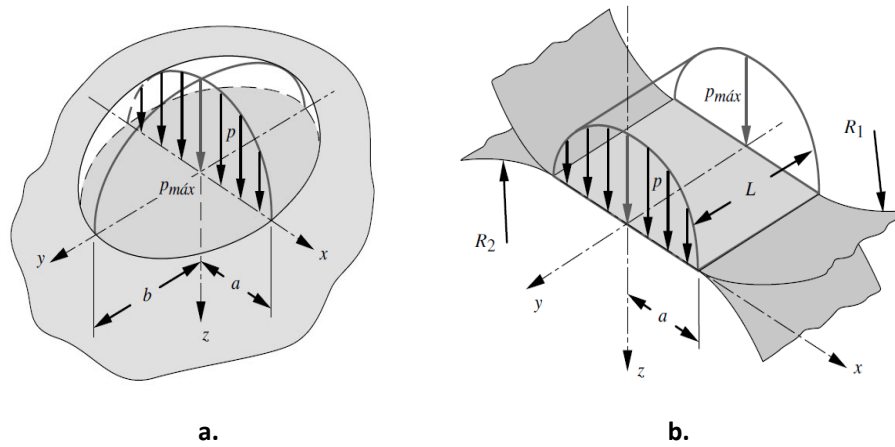


Figure 2-4 Pressure distribution in Hertzian contacts. a) Ellipsoidal pressure distribution from a spherical contact, b) Cylindrical pressure distribution from a cylindrical contact. Adapted from [34]

The normal stresses  $\sigma_x$ ,  $\sigma_y$  and  $\sigma_z$  generated by the pressure are maximum in the contact centre and decrease with the distance. In the case of a point contact, the minimum value is  $\sigma_z=0$  is at the contact border. Moreover, the maximum shear stress is registered below the centre of the contact surface. Its magnitude is equal to  $\tau_{max} = 0.34p_{max}$  at a depth of  $0.63a$ . In the case of line contact, the stresses have a similar distribution to a point contact, although the main shear stress is located at a depth of  $0.786a$  and is equal to  $\tau_{max} = 0.304p_{max}$ . A general solution of the Hertzian model for a point contact under elastic conditions is also provided by Timoshenko [35] .

The high shear stresses obtained in point and line contacts show the importance of the shear stress in the rolling contact. From these stresses, the values to produce plastic deformation can be obtained using the Tresca Criterion ( $\tau_{max} = 0.5S_y$ ):

$$\tau_{max} = 0.34p_{max} = 0.5S_y \quad (\text{For point contact}) \quad (2.1)$$

$$\tau_{max} = 0.304p_{max} = 0.5S_y \quad (\text{For line contact}) \quad (2.2)$$

Where  $S_y$  is the yield strength. Hence, plastic deformation is produced when:

$$p_{prom} \geq 1.47S_y \quad (\text{for point contact}) \quad (2.3)$$

$$p_{prom} \geq 1.644S_y \quad (\text{for line contact}) \quad (2.4)$$

These small deformations grow with each new contact cycle. Experimentally, it has been found that the average pressure approaches  $2.8S_y$ , a value higher than the obtained from Eq. 2.3 and 2.4. Hence, a small and progressive plastic deformation is registered inside the material due to the shear stress [36]. Plastic deformation invalidates the Hertzian stress distribution, hence Eq. 2.1 and 2.2 cannot be used to find the maximum shear stress in the rolling contact. An exact stress distribution is difficult to obtain due to it not being possible to define the limit between the elastic and plastic fields. A map showing the stress distribution under these conditions can however be obtained by finite element analysis [36] as shown in figure 2-5.

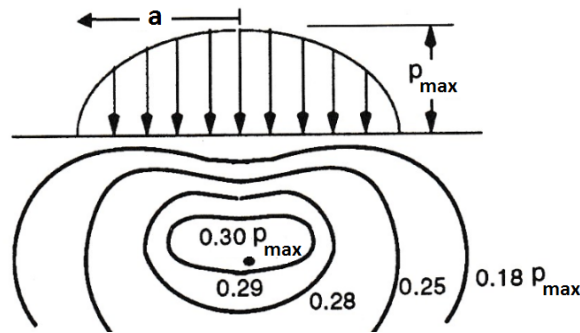


Figure 2-5 Shear stress contour in a line contact in terms of  $p_{max}$ . The lower cylinder has infinite radius (flat condition) [36].

### 2.2.2 Microstructural changes due to RCF

Microstructural changes in bearing steels, based on their different etching responses during characterization by light microscopy, produced as a result of RCF have been reported profusely since 1946. Dark etching areas (DEAs) and white etching bands (WEBs) were registered in the subsurface of the contact area after approximately  $10^7$  contact cycles (i.e. approximately after 4 months of service operation with a rotating frequency of 1 Hz) [37]. These features were located where the magnitude of the Hertzian shear stress is higher. Figure 2-6 shows a relationship between the beginning of these microstructural changes and the revolutions registered in a rolling bearing inner ring.

#### *Dark Etching Areas (DEAs):*

DEAs appear during the early rolling stages as a disperse group of dark etching patches and grow to be a large defined region surrounded by new patches. Slip marks appearing at  $45^\circ$  to the surface have been reported inside the DEAs. The DEAs dark contrast seems to be related to the number density of these marks (figure 2-7) [38]. There is no agreement about the nature of the DEAs microstructure. Possible structures include low temperature bainite, ferrite and even-tempered

## Chapter 2

martensite. DEAs have been related to micro migration of carbon atoms toward regions with high dislocation density [37]. The manufacturing processes applied to the material before this service plastic deformation can affect this process. For example, higher temperature – tempering applied during manufacture produces a lower amount of interstitial dissolved carbon. Hence, there is a lower probability of carbon migration to the dislocation sites [37].

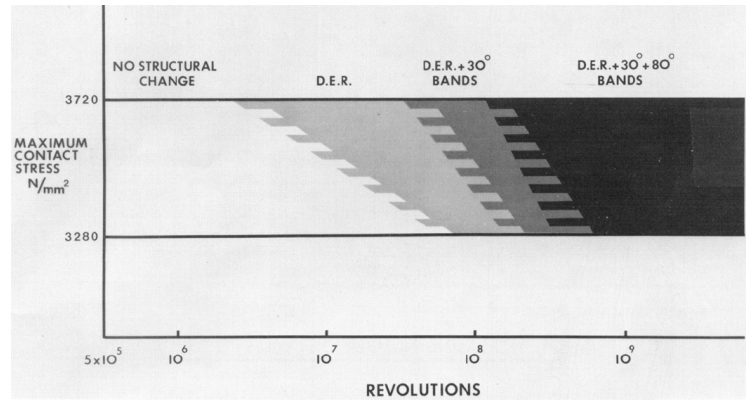


Figure 2-6 Microstructural changes registered in the subsurface of the contact area in terms of the number of inner ring revolutions [39].

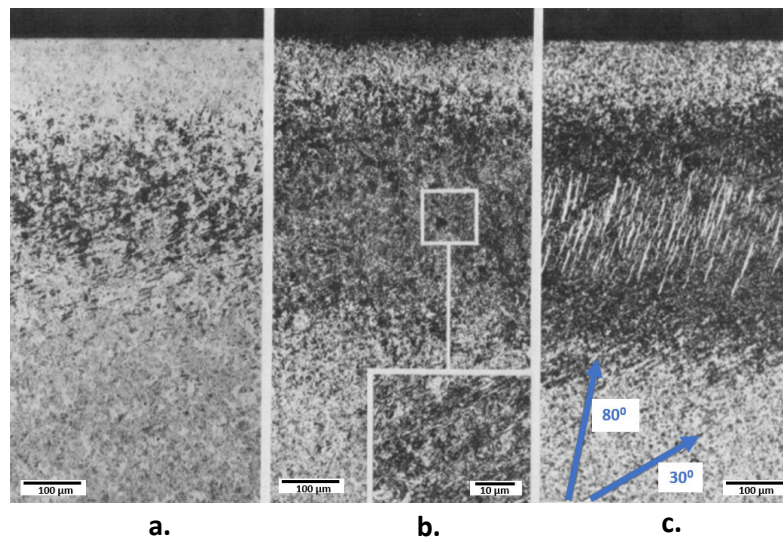


Figure 2-7 Micrographs of the microstructural changes in sections transverse to the contact surface revealed by etching with Nital. a) DER in its early stage. b) Fully developed bands at 30° to the surface b. and c. bands at 80°. c) The number of cycles increases from the left to the right. Adapted from [39].

### White Etching Bands (WEB)

WEBs develop later than DEAs and have different orientations, at first at  $20^\circ - 30^\circ$  and later at  $75^\circ - 85^\circ$  to the surface. The first orientation to appear has a thick shape, is  $2\ \mu\text{m}$  thick approximately, and there is a spacing of  $0.5\text{--}10\ \mu\text{m}$  between them. The second orientation has sizes of  $10\ \mu\text{m} \times 100\ \mu\text{m}$  long with a spacing of  $5 - 50\ \mu\text{m}$  (Figure 2.13) [37, 38]. WEBs appear  $200 - 760\ \mu\text{m}$  beneath the surface and show a maximum density at  $230 - 400\ \mu\text{m}$  from the surface. This band density tends to increase with higher contact cycles.

### 2.2.3 Spalling under RCF

The main surface damage produced by RCF is known as *spalling*, and affects all mechanical systems subjected to cyclic loads and stresses, such as gearboxes, rail track – wheel systems, cams and rolling bearings. Small notches at the surface grow in extension and depth following a fan shape pattern [40]. Spalling is a consequence of material weakened by the growth of cracks from the surface and subsurface. In the first case, the cracks are inclined at less than  $30^\circ$  to the raceway. In the second case, the cracks originate at shallow angles to the surface and end in large pits. Due to the presence of these small holes close to the spalls, this phenomenon is often called by some authors “pitting”, “frosting” or “peeling” [33]. Figure 2-8 shows two typical examples of spalling registered in a rolling element bearing. In spite of these marks being very small, they evolve quickly to produce significant damage to tracks and rollers over the  $L_{10}$  bearing lifecycle.

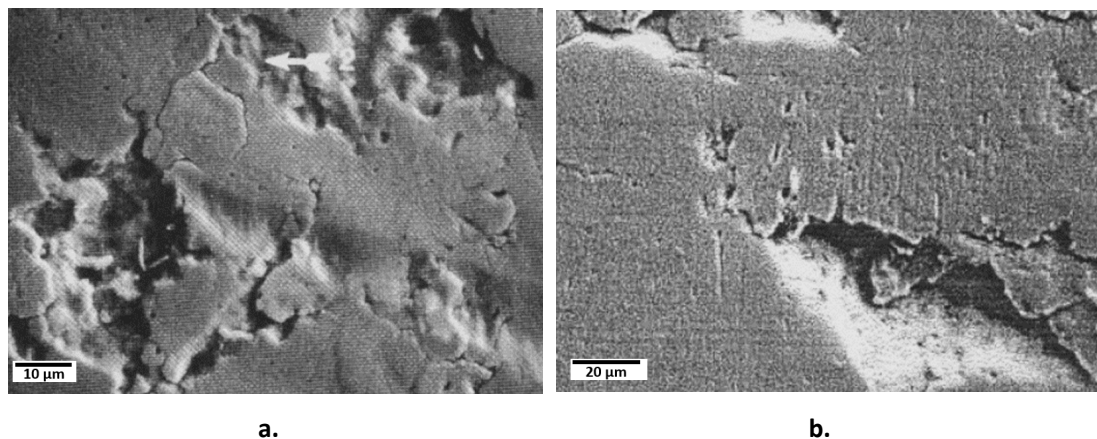


Figure 2-8 SEM images of a spalls a) and micropitting, b) of a worn rolling element bearing affected by contact fatigue. Note the small holes or “pits” close to the cracks and spalls in b Adapted from [40].

The figure 2-9 shows a classic delta shape of the pit formed by fatigue spalling in a ball bearing contact. The apex of the pit is the initiation point, usually located in a surface defect like a notch or dent. The pit grows in a fan shape, becoming wider and deeper as it grows in the direction of ball rotation. Although the delta shape is a characteristic shape of fatigue spalling, not all spalls in ball bearing have this kind of profile. Usually, temperature and noise in the bearings tend to increase, when the damage is visible to the naked eye. These conditions must be considered as a notification that a bearing replacement is needed as soon as possible [40].

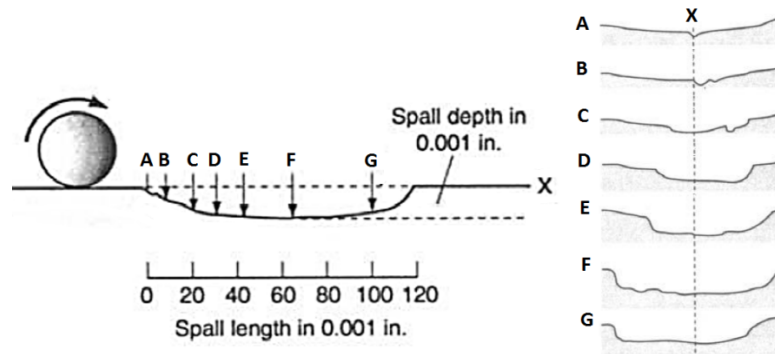


Figure 2-9 Typical of spalling damage during rolling contact fatigue in rolling element bearings [40].

#### 2.2.4 Cracks under RCF

The stresses causing cracks to propagate in RCF can arise from various sources. Cracks could grow from the hydraulic pressure of the lubricant used in the contact. The fluid trapped inside the crack is pushed every contact cycle and generates a hydraulic pressure against the crack faces [41]. Local tensile stresses combined with hydraulic pressure could also lead to crack evolution in RCF [42]. The cracks start at asperity contacts on the surface at a very early stage of RCF [33]. A similar origin from the surface has been proposed by various authors [43-45]. In 1998, A. Voskamp, one of the most prolific researchers in RCF, proposed the subdivision of spalling into three stages: shakedown, steady state and instability.

The first stage corresponds to the beginning of micro deformation near to the contact surface although it does not imply crack formation. The second stage is related to an “incubation period” where the effect of micro plastic deformation is accumulated and micro cracks initiate. Intervals of  $10^9$  cycles or more can occur without any significant change in the material. Finally, the third stage is characterized by microstructural changes such as phase transformation, changes in residual stresses and texture formation [46].



The same stages have been described by Sadeghi et al. (2009). They argued that crack initiation and propagation is preceded by work hardening and transformations of retained austenite to martensite during the first rolling stage. The second stage is characterized by a material elastic response and slow crack growth. This stage is limited by microstructural changes that lead to localized damage which itself increases the probability of further crack initiation. Finally, the third stage is marked by a decrease in yield strength and an increase in the subsurface volume affected by plastic deformation. Carbon diffusion, promoted by local temperature peaks, could activate potential slip systems, leading to softening. Radial tensile stresses and texture development promotes the growth of cracks parallel to the surface. Following this, surface damage takes place [47].

### 2.2.5 White Structure Flaking

White Structure Flaking (WSF), also called Brittle Flaking Wear, [1] appears visible to the naked eye as smearing, cracks and macropitting in the contact area and leads to significant material removal, similar to spalling damage

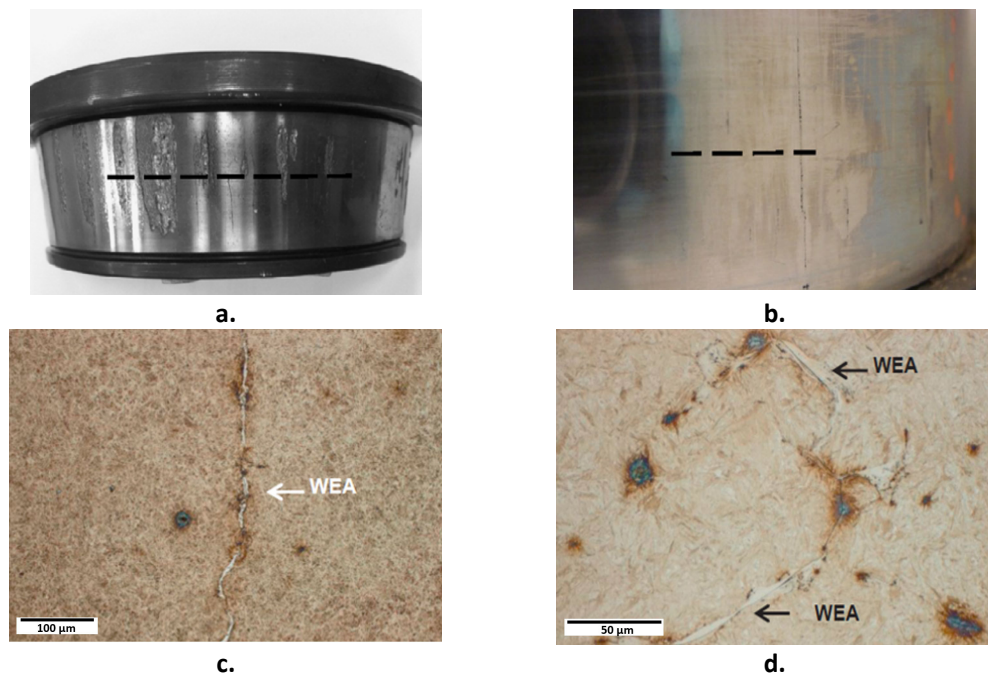


Figure 2-10 Damage produced by WSF in an AISI 52100 bearing inner race. The dotted lines in a) and b) indicate the cross sections showed by LOM in c) and d). The bearing in a) and c) has an outer diameter of 215 mm whilst the bearing in b) and d) has an inner diameter of 93 mm. Adapted from [48].

The origin of WSF has been related to a particular microstructural alteration called White Etching Areas (WEAs) that appear during the early stages of the cyclic contact [49]. Figure 2-10 and 2-11 show typical WSF linked to WEAs; its similarity to the spalling damage caused during RCF shown in Table 1.6 and Figure 1.18 should be noted.

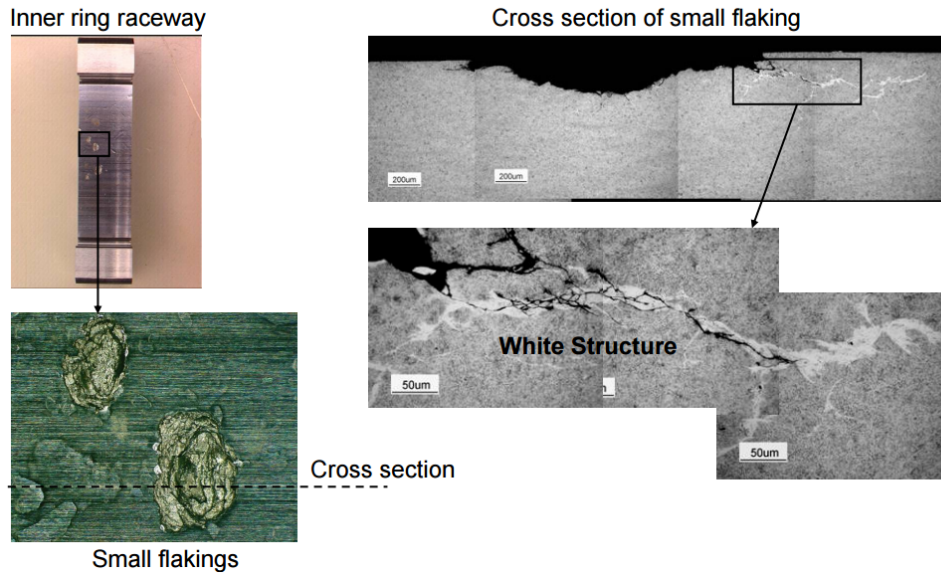


Figure 2-11 WSF in an inner ring raceway of a high-speed shaft bearing assembled in a wind turbine gearbox. a) Typical spalling produced by WSF, b) Cross section of the ring raceway taken along the dashed line showed in a). The section shows WEAs and a complex crack network extending to the contact surface. Adapted from [50].

## 2.2.6 White Etching Areas

Despite a variety of names given in the literature, such as white bands [51], light etching areas [27], White Etching Matters - WEM [1], or irregular White Etching Areas- irWEAs [52], White Etching Areas - WEAs is a term used to describe a particular type of microstructure in steels, which appear to be white under Light Optical Microscopy (LOM) after etching. The white and smooth appearance is related to their higher corrosion resistance to Nital (2% nitric acid + ethanol) etch compared to the matrix that surrounds them [3] [53].

WEAs are characterised by fibrous structure formed by nanocrystalline cubic ferrite supersaturated with carbon [54] [4] [55] [56] with grains sizes between 10 to 100 nm and with a hardness 30 – 50% higher than the bulk material [4] [54] [55] [2] [56]. WEAs often appear in combination with crack networks, suggesting mechanical incompatibilities between the WEAs and the surrounding material. This interaction has been used to support the term White Etching Cracks – WECs [57] being used to replace the term WEAs. Cracks associated with WECs tend to grow in



circumferentially or axial directions, leading to material weakening and its subsequent flaking [58] [59].

A particular morphology of WEAs resemble Butterfly Wings (BFs), this feature having at its centre a non-metallic inclusion. BFs often appear 1 – 1.5 mm from the contact surfaces and have an inclination of 45° to the surface. Their size ranges between 5 and 15  $\mu\text{m}$ . BFs are delineated by two different features, a micro crack and a gradual alteration in the microstructure without cracks. It has been postulated that residual stress combined with the shape of the interface between the inclusion and the matrix leads to the formation of the crack and butterfly wing itself [4]. Figure 2-12 shows a WEAs and a butterfly wing formed around an alumina inclusion.

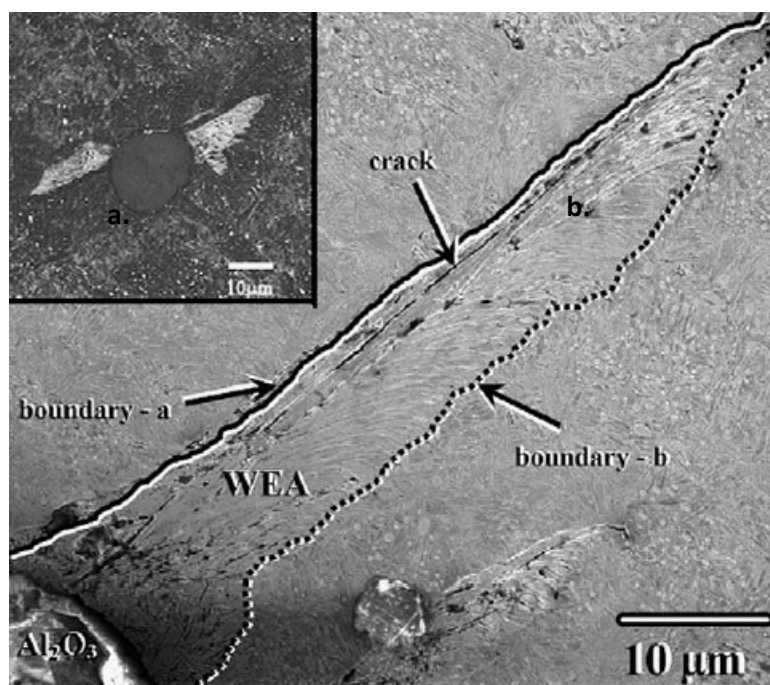
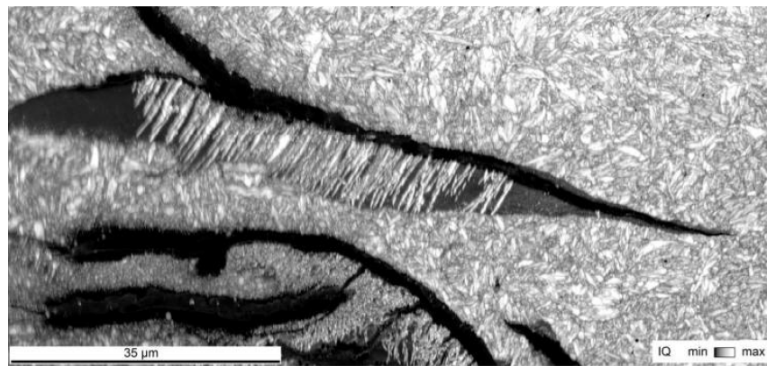
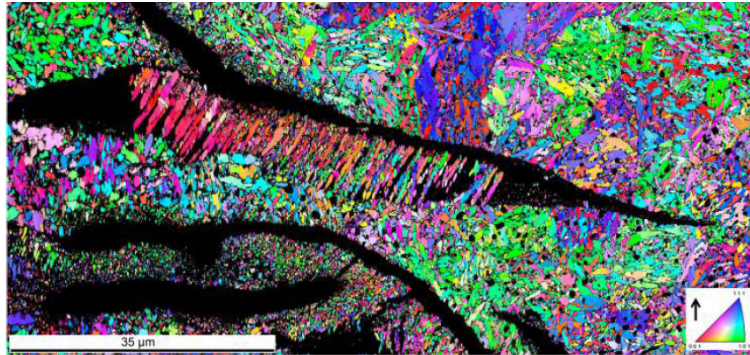


Figure 2-12 SEM / SEI of a Butterfly wing formed around an  $\text{Al}_2\text{O}_3$  inclusion in an AISI 52100 bearing steel. Note the two different borders, a) with crack, b) without crack [60].

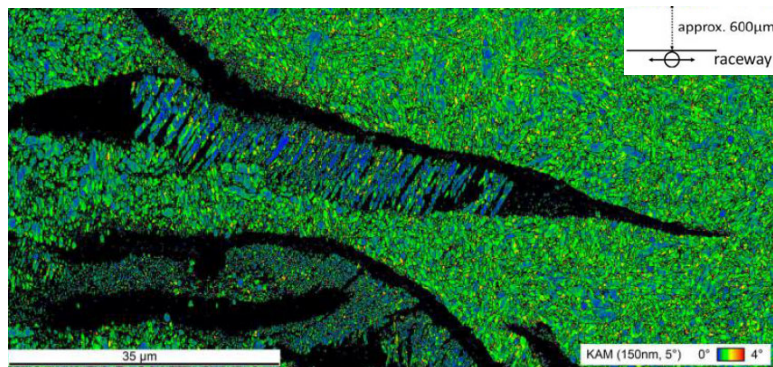
The use of SEM / EBSD techniques has revealed elongated grain structures (also called needle-shape grains due to their orientation in 2D) that appear with sharp boundaries in zones with the finest grain size. Their homogeneous texture and low average orientation registered in Inverse Pole Figures - IPF and Kernell Average Maps - KAM, suggest that a possible recrystallization process led by thermal effects, such as an annealing, is taking place.



a.



b.



c.

Figure 2-13 WEAs and crack analysed using a) IQ image, b) IPF and c) KAM map. The images show long grains inside the WEAs extending from the crack to the matrix. These grains show a similar texture in b) and low average orientation angle (blue grains) in c). EBSD analysis using a step size of 150 nm. Ferrite structure was indexed prior to conducting the analysis. Adapted from [61].

Figure 2-13 shows four maps obtained using SEM / BSI and EBSD – Image Quality Map – IQ. SEM / BSI analysis can be used to visualize the grain texture in the regions close to the WEAs. IQ images indicate the intensity of the diffraction patterns obtained from the regions analysed, well-defined microstructures being brighter. The black regions correspond to poor signal patterns from undefined nanostructures or from cracks. The coloured regions in IPF and KAM maps represent the regions with clear ferrite diffraction patterns (ferrite structure was indexed prior to conducting the analysis). [61].

EDS analysis has shown the degradation of cementite particles inside the WEAs due to carbon dissolution. Figure 2-14 presents the Carbon and Chromium distribution inside a WEAs ( c) EDS – C map, d) EDS- Cr map) together with an image taken of the same area using LOM. Thus, from these images it is possible to see how the carbon expected from the carbides has disappeared in the WEAs, but the chromium is still present. This means dissolution in the nanocrystalline structure affected preferentially the Carbon content in the spheroidal cementite. IQ image showed the presence of similar long grains inside the WEAs, as was reported in figure 2.13 [62].

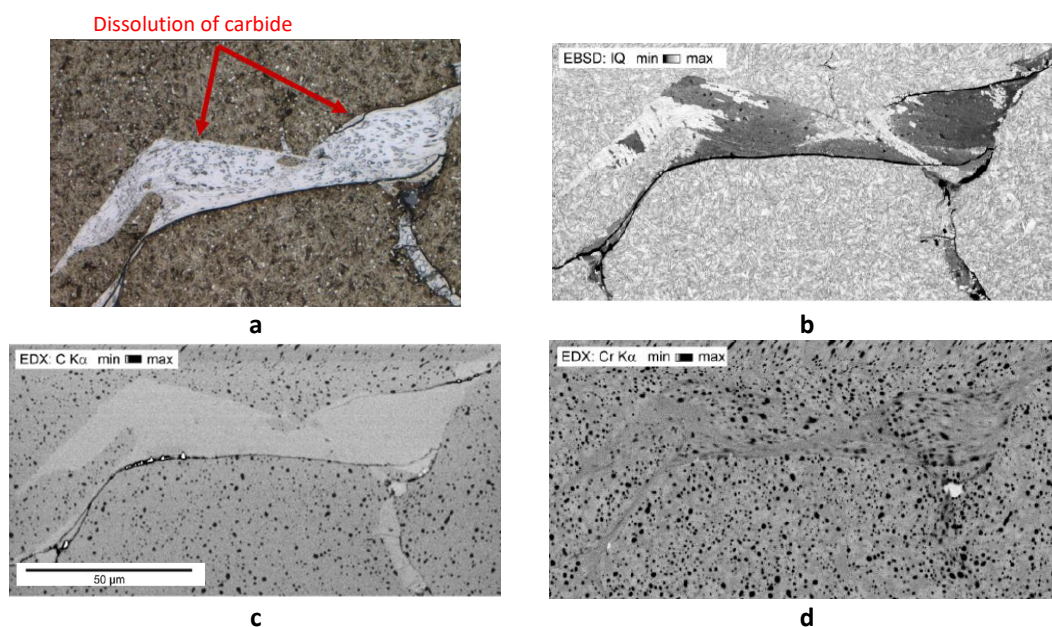


Figure 2-14 WEAs analysed by EBSD and EDS maps. The original microstructure visible by LOM is in a), IQ map is in b), whilst the EDS – C appears in c) and EDS – Cr appears in d). No carbides were observed inside the WEAs in c) due to the dissolution of carbon in the WEAs structure. It seems that Cr was not affected by this dissolution. An IQ map reported long grains inside the WEAs Adapted from [62].

### 2.2.7 Origin of WEAs

WEAs have been related to several features in the matrix that can change the stress distribution in small localized regions, however their nature is not completely understood. The main factors proposed to explain the beginning and growth of WEAs are summarized in table 2-5

Table 2-5. Main factors proposed to explain the beginning and growth of WEAs

Causes	Description
Hydrogen embrittlement	Hydrogen embrittlement can cause significant reduction in fatigue life in bearing steels. This can occur in combination with high Hertzian stresses [10].
Non – metallic Inclusions	Accumulation of localized plastic deformation in regions close to inclusions can produce WEAs in bearing steels. Cracks can grow from the matrix / inclusion interface ([4] [10].
Porosity [Gravulov 5]	Discontinuities inside the material caused by voids [5].
Carbide clusters	The high primary carbide density created during the solidification acts as stress concentrator and a carbon source that will dissolve in the matrix producing WEAs [6].
Cracks	Pre-existing intergranular micro cracks register cyclic contacts inside them [7].
Adiabatic Shear Bands	Adiabatic shear bands resulting from the impact of rollers on the ring can lead to growth and propagation of WEAs and cracks [9].
Surfacing cracks	Lubricant trapped inside surface breaking cracks is pushed into the material due to pressure, stimulating crack growth [63].

## 2.3 Severe Plastic Deformation

The combination of plastic deformation and heat treatments has been used for many centuries to control the mechanical properties of alloys through precipitation reactions, grain refinement etc. Small grains have been responsible for the good features of several products, from ancient Damascus swords to modern structural steel made by the Control Rolling Processes. In the first example, nanowire structures acting as obstacles to dislocations and crack propagation were responsible for the sword's toughness [64]. In the second example, refined grains with sizes around 5  $\mu\text{m}$  promote a good balance between strength and toughness [65]. However, only at the beginning of the 1950's was the mathematical relationship between the yield strength of a polycrystalline materials ( $\sigma$ ) and its average grain size ( $d$ ), given in Equation 2.6 [66], established by E. O. Hall and N. J. Petch.

$$\sigma = \sigma_0 + kd^{-\frac{1}{2}} \quad (2.5)$$

In this expression  $\sigma_0$  is the friction resistance for dislocation movement within the grains and  $k$  is a measure of the local stress needed at the grain boundary for transmission of plastic flow and/or cleavage fracture. The Hall – Petch relationship increased the interest in producing materials with small grains using thermomechanical methods such as the plastic deformation processes shown in figure 2-15.

These processes lead to microstructural changes such as dissolution, precipitation and phase changes as follows [67]:

- Plastic deformation compresses the dendrite arms of the cast microstructure and reduces the local diffusion distances.
- Subsequent heating provides energy to begin crystallization and thus a homogeneous microstructure develops.
- Controlled cooling allows the production of a refined microstructure often characterized by high hardness and strength.

The deformation processes can provide enough energy to start recrystallization. For example, in Fe-C alloys, recrystallization often starts during hot deformation and continues during the subsequent annealing to produce austenite grains. Finally, fine microstructures of ferrite, pearlite, and even bainite and/or martensite can be obtained from the austenite using controlled cooling [67]. However, these processes produce a significant alignment of the grains parallel to the main plastic deformation direction. Figure 2-16 shows schematically pearlite plate evolution during the drawing

of a eutectoid steel. These lamellar structures tend to follow the drawing direction and have a small orientation angle to the drawing axis [68]. Hence, the material after plastic deformation is anisotropic and has a texture.

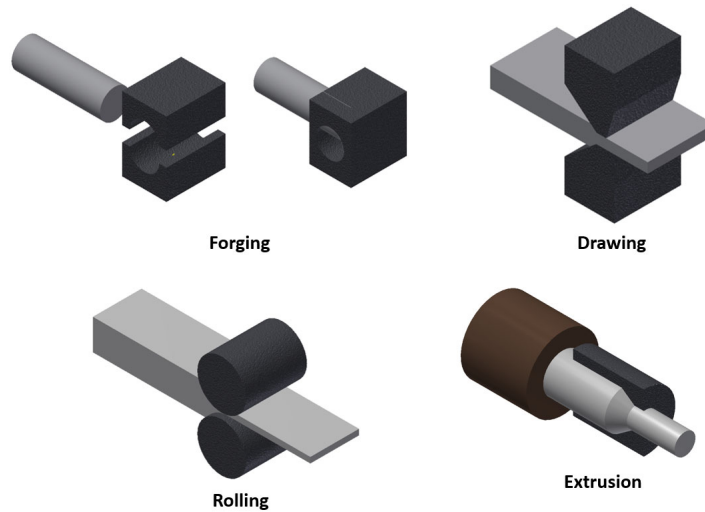


Figure 2-15 Classic plastic deformation processes used to shape metals that often are combined with heat treatment to refine grains. Adapted from [69].

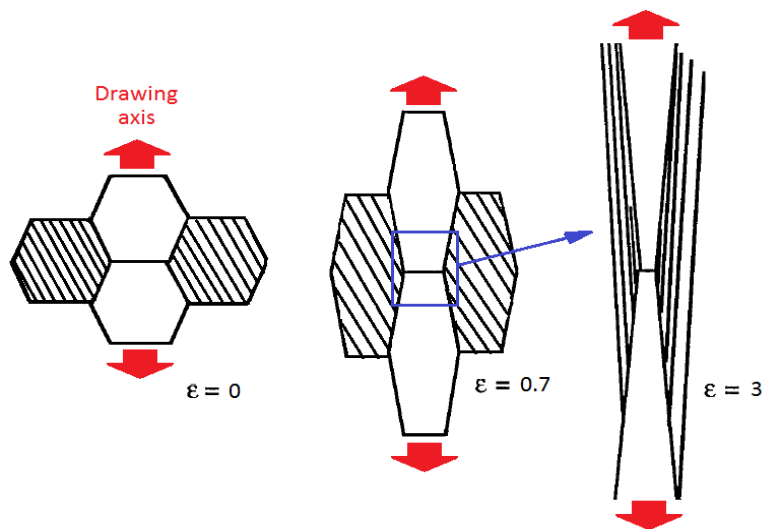


Figure 2-16 Schematic drawing showing the development of microstructure during the drawing of a eutectoid steel [68].



### 2.3.1 The beginning of HPT and ECAP

The first concept to refine grains to a nanometric scale without preferential orientation was developed by P.W. Bridgman in 1943. Bridgman designed and tested two devices study the response of polycrystalline materials to the combined action of high torsional and compressive stresses. The first equipment was built to test small pipes of AISI 1045. The ends of the pipe were fixed whilst its centre rotated due to a pulley connected to it. To avoid distortion in radial directions and preserve the original sample dimensions, a rigid rod was inserted inside the pipe (figure 2-17 ) [70].

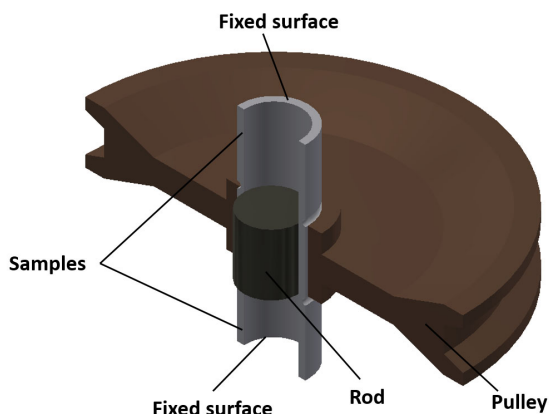


Figure 2-17 A schematic drawing of the first device designed by P.W. Bridgman to test pipes. Adapted from [70].

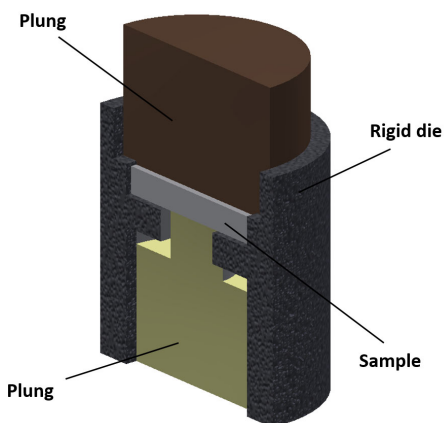


Figure 2-18 Equipment to test thin discs developed by P.W. Bridgman This device would be developed to form the basis of future HPT test machines. Adapted from [71].

The second device tested small discs of AISI 1045 using the same stress combination. The sample was assembled inside a hollow cylinder and pressed using two anvils located in the axial direction. The sample was compressed between an upper and a lower annular clamp in order to prevent warping [71] (figure 2-18). This device would be the basis of the High-Pressure Torsion method (HPT) developed during the 80s'. This process will be described in more detail in section 2.4.

Another concept developed between 1970 and 1980 by V.M. Segal and his colleagues was Equal Channel Angular Pressing or ECAP. The process consists of pushing, by a plunger, a billet with a length of between 70 to 100 mm through a channel within a rigid die. The channel has the same cross section dimensions as the sample. The extrusion produces high strain in the sample due to a change in orientation in the channel [12]. Although this method has evolved to a new and complex process, the classic configuration still continues operating nowadays without significant changes. figure 2-19 shows a simple scheme of the ECAP process.

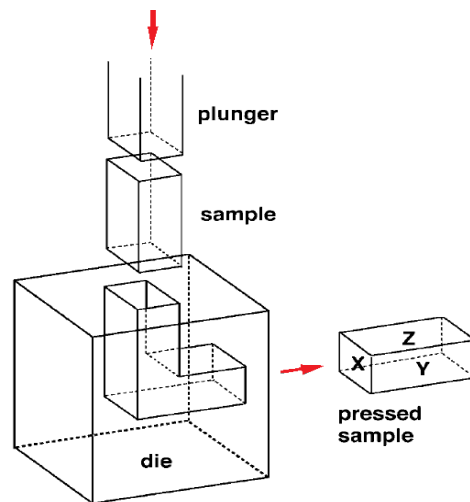


Figure 2-19 Schematic drawing of the ECAP processes defining X, Y and Z reference planes. This nomenclature is established in relation to the planes on the pressed sample [72].

Both concepts, HPT and ECAP, allow high strains to be imparted to the samples, without significant changes in their final dimensions. However, the techniques used to study the materials processed by these methods were restricted to metallography and microhardness tests for many years. A detailed examination was only possible with the development of techniques such as Electron Back Scattered Diffraction (EBSD), Energy-Dispersive X-ray Spectroscopy (EDS) or Transmission Electron Microscopy (TEM). In addition, the development of tensile tests on materials processed by ECAP or HPT enabled detailed studies of their mechanical properties. These techniques revealed the features of materials with high isotropy, controlled orientation of boundary grains, misorientation



of the grains, and refined grains on nano scales. Some of these features enable superplastic forming and provide high strength and an excellent balance of mechanical properties [12].

HPT and ECAP are the beginning of a new family of plastic deformation processes characterized by three main principles [73].

- These processes use high strains without any significant change in the overall dimensions of the work piece.
- These processes are capable of producing exceptional grain refinement using combined stresses.
- The final grains have high angles of misorientation with respect to the main strain direction.
- The final materials consist of an arrangement of nano – grains referred to as Ultrafine Grained Material (UFG).

### 2.3.2 Other SPD processes

Several techniques were subsequently following the principles established by Bridgman and Seagal. Some of these were a natural evolution from ECAP and HPT; other processes employed principles used in the metalworking industry. Figure 2-20 shows schematic diagrams of various SPD processes available nowadays.

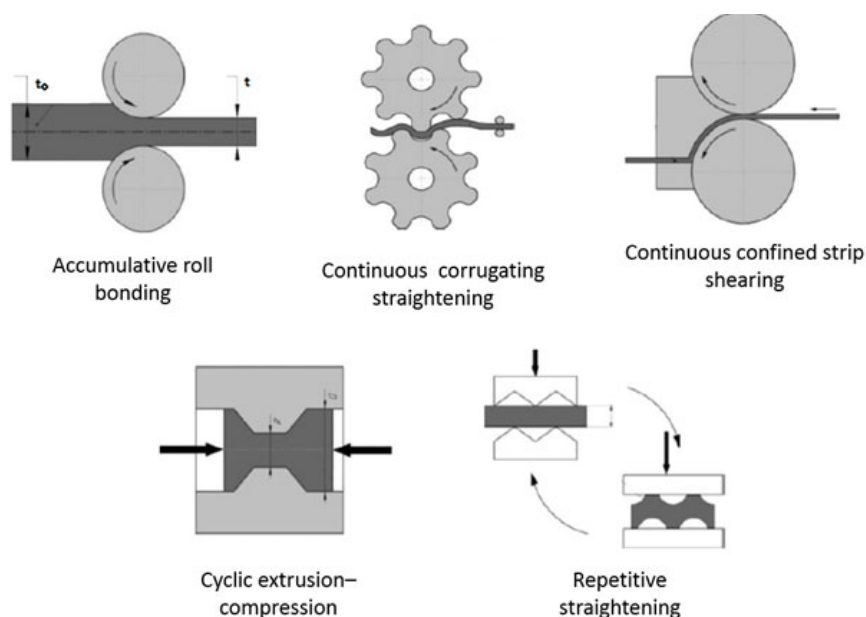


Figure 2-20 Other SPD processes used to obtain UFG structures [74].

### 2.3.3 Applications of SPD processed materials

Materials processed by SPD exhibit outstanding properties, such as high strength, ductility, thermal stability and fatigue response, compared to their coarser – grained counter parts. Their potential uses are based on two main factors: superior properties and superior machinability.

An example of their use could be for bicycle components such as gearing, pedals, shifters, rims and spokes; the experience acquired with these products could be used in specialist applications in aircraft, automobiles and boats (ref). Another good example of their applications is in the production of medical components and pieces in small lots, such as implants for bone osteosynthesis made of nano structured Ti (figure 2-21 a)).

Some nanostructure alloys processed by SPD have shown superplasticity at lower temperatures and faster rates than conventional superplastic alloys. Finally, several HPT techniques have a great potential for large scale industrial applications due to the similarities between the equipment used in SPD and conventional deformation processing. Hence, the production of bulk material useful for structural applications, such as rods processed from ECAP billets (figure 2-21) is a feasible and relative cheap alternative method of obtaining parts with exceptional mechanical properties [75].



Figure 2-21 Applications of nano structured materials processed by Severe Plastic Deformation. a) implants for bone osteosynthesis made of nano structured Ti. b) Structural rod (50 mm diameter, 170 mm length) processed from ECAP billets. Adapted from [75].

## 2.4 High Pressure Torsion Test

The High-Pressure Torsion Test (HPT) refers to a SPD process applied to metals that follows the principles established by P.W. Bridgman in 1946. HPT is used to process small disc samples with diameters in the range 10 to 15 mm and 1 mm thick [75]. The samples are placed between two anvils that transmit high pressure and torsion at the same time figure 2-22 shows a schematic of the HPT process [12].

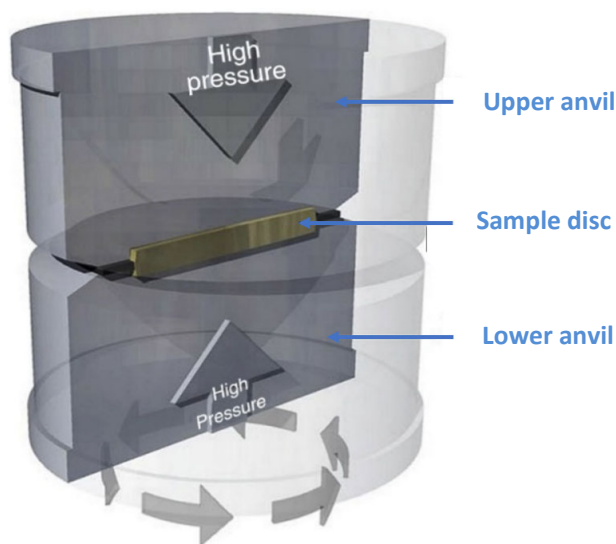


Figure 2-22 HPT process with hydrostatic pressure and torsional stress applied to the sample disc. Adapted from [77].

### 2.4.1 The anvils

The geometry of the anvils is the most important feature of the HPT test, the nature of the cavity that supports the sample between the anvils anvil alignment being especially critical. The shape of this cavity determines material lateral flow during the process. There are three possibilities, unconstrained, constrained and quasi-constrained conditions. In an unconstrained condition, the material tested is free to flow outwards, under little pressure or even no back pressure.

Under the constrained conditions, the sample is located in a cavity in the lower anvil to avoid material flow. Hence, the sample supports back-pressure. The quasi-constrained condition refers to deformation in a double cavity located in both anvils. In practice, it is difficult to get a totally constrained condition and some material flow occurs between the anvils. Figure 2-23 shows the three HPT constraint conditions [78].

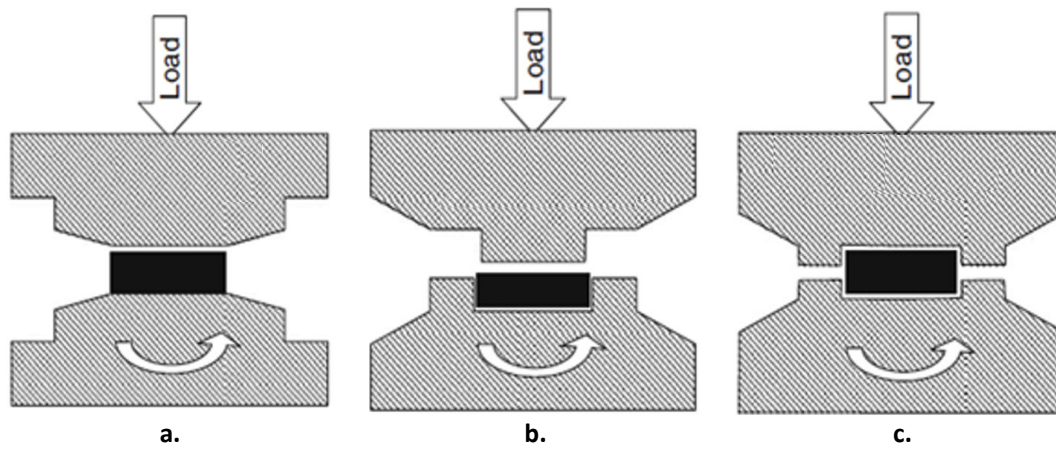


Figure 2-23 HPT constraint conditions: a) unconstrained, b) constrained and c) quasi-constrained [78].

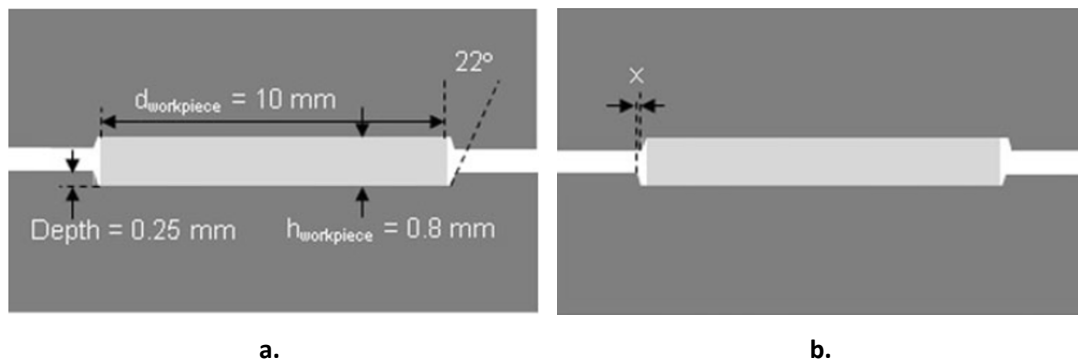


Figure 2-24 Anvils with two different alignments. a) Good alignment with relative displacements, measured by  $X$ , of less than  $X=25\mu\text{m}$ . b) Poor alignment with displacements more than  $X=25\mu\text{m}$ . Adapted from [78].

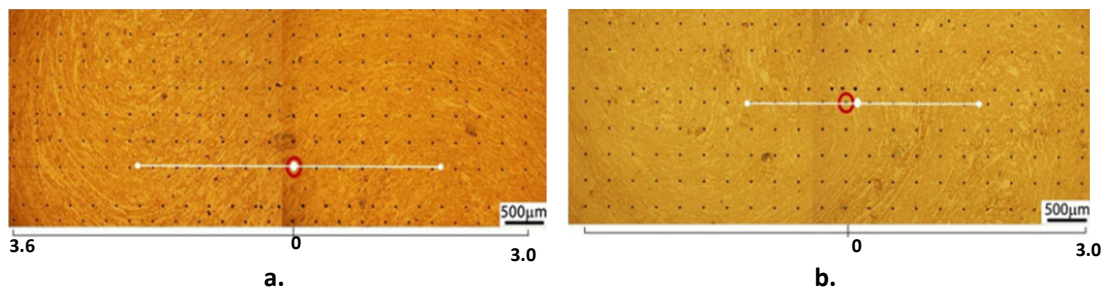


Figure 2-25 Flow pattern distributions along disc diameters under an anvil misalignment of  $200\mu\text{m}$  for a)  $N = 1$  turn and b)  $N = 5$  turns. Samples of IF53 super duplex stainless steel processed using 6 GPa. Adapted from [78].

Moreover, variations in anvil alignment can produce changes in the samples during HPT tests. A good alignment implies a sample displacement along the horizontal plane of less than 25  $\mu\text{m}$  (figure 2-24). The tests conducted using poor alignments can affect plastic flow inside the samples, especially at the edges, where flash formation takes place. Misalignment is a common problem in HPT tests. This produces double swirl flow patterns and significant variations in the hardness along the radial direction in the samples (figure 2-25). The swirl sizes tend to reduce as the number of turns increases [79].

#### 2.4.2 Strain along the radial direction

The classic model calculates the total strain in the sample discs as a function of the radial distance, rotational angle and the circular arc related to them. The model assumes the sample thickness remains constant during deformation. Figure 2-26 shows these geometrical parameters [79]. A differential arc variation ( $dl$ ) can be related to a rotational angle  $d\theta$  through the distance from the centre ( $r$ ) by:

$$dl = r * d\theta \quad (2.6)$$

The shear strain is given by,

$$d\gamma = \frac{dl}{h} = \frac{r*d\theta}{h} \quad (2.7)$$

where  $h$  is the thickness of the sample. If  $\theta = 2\pi N$ , where  $N$  is the number of revolutions, the total shear strain,  $\gamma$ , can be written as[77]:

$$\gamma = \frac{2*\pi*N*r}{h} \quad (2.8)$$

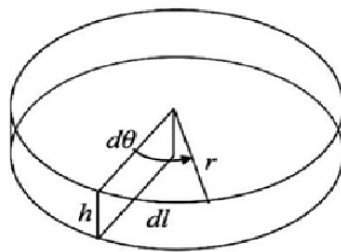


Figure 2-26 Shear strain and its distortion produced in a HPT sample [79].

Many publications use the equivalent strain,  $\epsilon$ , established by von Mises, hence it is useful to write Eq. 2.13 in terms of  $\epsilon$ :

$$\varepsilon = \frac{\gamma}{\sqrt{3}} = \frac{2 * \pi * N * r}{h \sqrt{3}} \quad (2.9)$$

Figure 2-27 shows a representation of the distortion produced by the shear strain in two points located on the top of a disc processed by HPT.

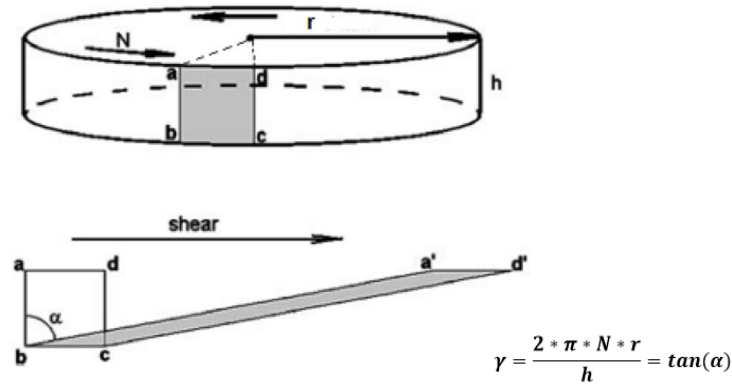


Figure 2-27 Distortion produced by the shear strain at two points located on the top of a disc processed by HPT [11].

All these expressions predict that the strain varies with radial distance, from zero at the centre of the sample disc to a maximum value at the edge of the sample. Hence, a different response will be observed across the sample discs due to the variations in the strain imposed.

### 2.4.3 Strain along the axial direction

The strain distribution in the axial direction of the disc samples also varies significantly. Figure 2-28 A) shows FEM results predicting the effective strain from HPT simulations on sample discs of 10 mm diameter for a strain hardening material [80]. The simulations were conducted under quasi – constrained conditions for samples with different thicknesses subjected to different numbers of turns. As expected, the strain increases with radial distance from the centre of the samples. The strains are symmetric with respect to the mid-plane of the samples and constant throughout the thickness except in regions close to the edge of the samples. At the upper and lower edges, a region of low strain is seen. There are regions of high strain at the edge of the sample at the mid-plane position where flash is formed. The extent of this area of localised high strain increases with sample thickness and number of turns. Figure 2-28 B) gives the strain rate predictions for a perfect plastic material modelled for various values of friction coefficient at the lateral walls of the top and bottom die impression. When the top and bottom anvils have the same values of coefficients of friction the strain rate distribution is largely symmetric with respect to the mid-plane. When the friction

coefficient is very low the plastic flow concentrates at the edges near both surfaces as in figure 2-28B a) but increasing the friction coefficient to 0.4 as in b) promotes an increase in the area of plastic flow at the edge of the disc and a decrease in the strain rate. The plastic flow then extends along the whole of the lateral wall. With further increase of coefficient of friction there is a plastic flow concentration near the mid-plane at the expense of areas near the sample surface. Figures d) and e) show the distributions of strain rate where the friction coefficients are different and for these circumstances there are differences in strain rates between the upper and lower-disc surfaces.

Plastic flow concentrates near the anvil with the lower friction coefficient, the material in contact with anvils with a higher coefficient of friction sticks to the anvil and moves as a rigid body without significant deformation. The area with the highest rate of plastic flow follows a similar trend as when both anvils have similar friction coefficients. Thus, the deformation concentrates near the surface of the disk at low friction levels and concentrates near the centre at higher friction coefficients. The results of this FEA modelling show there is a tendency for flow localization during HPT processing, Inhomogeneous plastic flow is observed near the edges of the samples. The friction between the anvil depression walls and the sample determines whether flow concentrates near the sample surface or near the sample mid-plane. Dissimilar friction coefficients at the top and bottom give rise to pronounced strain gradients with the sample thickness. This plastic flow localisation will influence the microstructural evolution of the sample discs during HPT tests

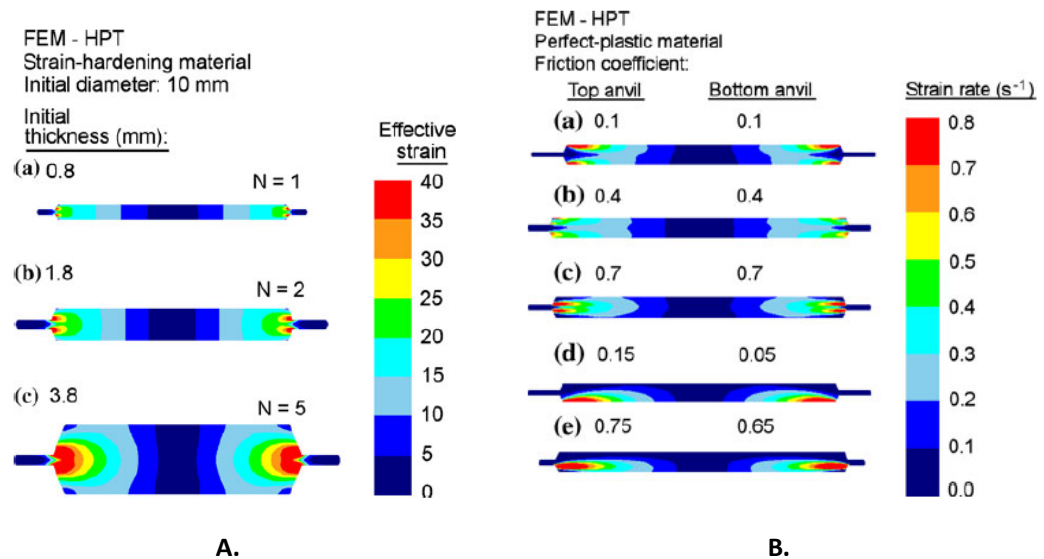


Figure 2-28 FEM results of the distribution of effective strain and strain rate across the axial sections of sample discs processed by HPT tests. A) Variations of strain for different sample thicknesses and number of turns. B) Variations of strain rate for different values of friction coefficients at the top and bottom anvils. Adapted from [80].

#### 2.4.4 Interruption of plastic flow

Plastic flow patterns that resemble swirls or vortices have been reported in the interior of disc samples in some HPT tests, suggesting that abrupt changes in the plastic flow can take place. An example of these vortex-like folds is shown in the LOM of figure 2-29 corresponding to images of an axial section of a multilayer stacked Al/Cu HPT disc (10 mm in diameter and 0.8 mm thick) taken at different radial positions [81].

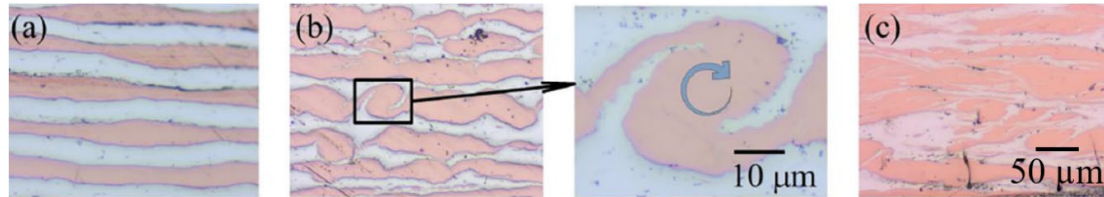


Figure 2-29 LOM taken from Al/Cu disc samples (axial sections) after HPT using 5 GPa and 3 turns. The images were taken at radial distances of a) 1.0 mm, b) 2.5 mm, and c) 4.5 mm. Some vortices are observed deforming the stacked Al/Cu layers. Adapted from [81].

Different theories have been proposed to explain the origin of these vortices, the most important of which are summarised below:

##### *Possible Kelvin–Helmholtz instabilities*

Vortices can occur in continuous fluids that suffer velocity variations where the two fluids, having sufficient velocity difference, meet at their mutual interface. These differences could occur inside the disc samples due to local shear velocity gradients between adjacent positions. Hence, complex patterns produced by Kelvin–Helmholtz instabilities could be created by the plastic flow [82].

##### *Differences between viscosity*

Folding and vortices could be caused by the layer-parallel compression of a highly viscous layer embedded in a lower viscous matrix. This model has been documented in geological systems where large length scales and millions of years are necessary to produce these patterns. However, this model can also be applied to multilayer structures under high shear stresses in a broad range of materials processed by different techniques [83].



### *Severe sliding conditions*

Folding and vortices can be created during severe sliding conditions, when a hard tool cuts a softer material or hard particles have contact with softer surfaces creating abrasive wear. The laminar flow produced during subsurface sliding of the softer material is interrupted by interaction with a hard component. Instabilities could also occur at nanoscale interfaces. Figure 2-30 shows a high-speed image taken of the sliding contact, at a velocity of 1 mm/s, between a hard steel wedge indenter and a soft annealed copper. The coloured lines show the laminar velocity condition and its change to turbulent patterns due to interaction with the indenter. A pre-existing fold is shown in the dotted red circle [83].

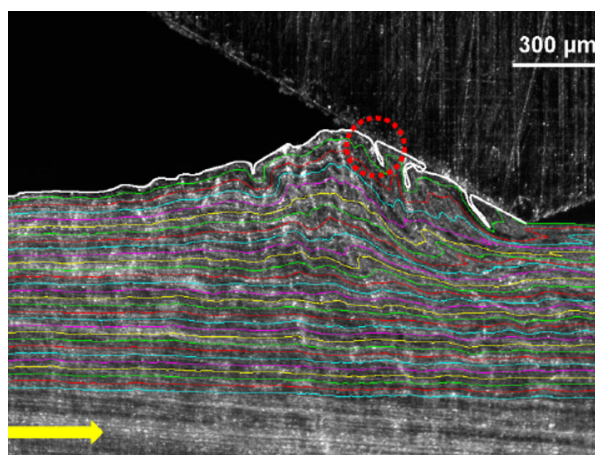


Figure 2-30 An annealed oxygen – free high conductivity copper workpiece sliding against a hard steel wedge indenter at a velocity of 1 mm /s. Particle Image Velocimetry and additional software post- processing were used to determine the velocity variations in the subsurface. The red dotted circle shows a pre-existing fold. The yellow arrow indicates the sliding direction [83].

### *Atomic interactions*

Recent FEM models based on the atomic interaction of two bodies in sliding contact have also suggested the presence of vortices at atomic scales. These vortices, that resemble the Kelvin–Helmholtz instabilities described before, seem to allow mixing at the interface between the atoms from the two bodies [84]. Figure 2-31, presents the results of a simulation of two similar bodies, A and B in sliding contact, with A (top one) being slightly harder than B. A mixed zone is clearly visible at the interface after  $10^6$  s, although the mixing is higher in the regions affected by higher vorticity (small blue arrows) [84].

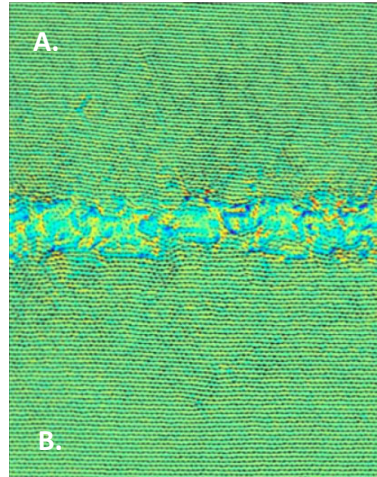


Figure 2-31 2D simulation of two similar bodies under sliding contact with A being slightly harder than B. A mixed layer conformed by atoms from A and B appeared between them [84].

#### *Local obstacles*

The interaction between the plastic flow and hard obstacles located inside the disc sample. The effect of hard particles such as lamellae and spheres blocking the shear stress can create local instabilities as shown in Figure 2-32 [85]. FEM of a small portion in an axial section of a disc sample showed how obstacles such as spheres or lamellae can cause swirls and turns, which lead to the formation of vortices at sufficiently large shear strains. The physical reason for this turbulence in a sample could arise from the presence of inclusions, with higher strength and hardness than the surrounding material, acting as obstacles.

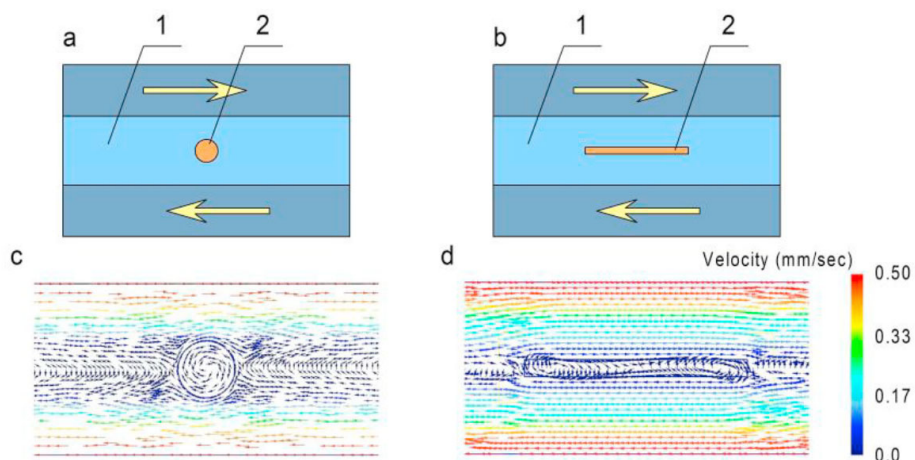


Figure 2-32 Simple shear blocked locally by obstacles: a), b) schematic of the obstacles modelled. c), d) velocity fields resulting from the obstacles modelled. Adapted from [85].

### 2.4.5 Pressure

The pressure distribution along sample discs during HPT tests is not homogeneous and depends of factors such as the material used for the anvils, the pressure used during the tests and the sample geometry. In general terms, the pressure varies with radial distance, however, the local pressure distribution at similar radial distances becomes more uniform with number of turns [16]. The pressure applied in HPT plays an important role in hardness evolution. The hardness tends to increase in value across the disc under high pressures until reaching a saturation condition. Figure 2-33 shows the results of processing high purify Ni samples under 1, 3, 6 and 9 GPa and 5 turns. A significant increase of the hardness and its homogeneity are registered with increasing pressure, particularly at 9 GPa. The hardness evolution is determined by a shearing action that takes place at a weaker area. When this initially weaker area increases its hardness, shear then takes place in another neighbouring region. The process continues throughout the HPT test until saturation occurs [86].

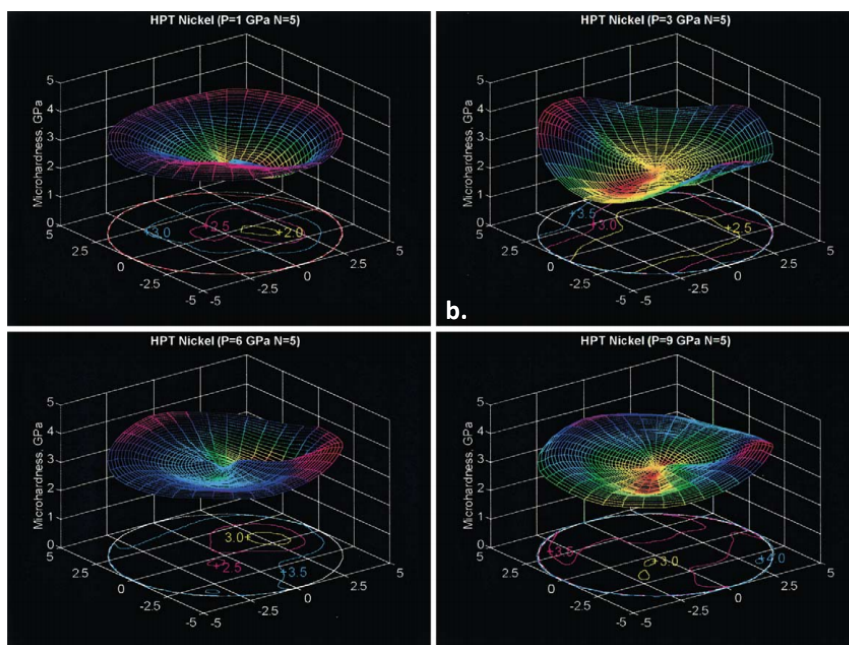


Figure 2-33 Evolution of hardness in high purity Ni samples during a HPT test under 1, 3, 5 and 9 GPa and 5 turns [86].

### 2.4.6 Hardness response

Two methods are commonly used to study the hardness response of samples after HPT tests, namely the hardness as a function of the equivalent strain applied and the hardness variation across the sample horizontal plane. In the first case, the hardness distribution is plotted versus the

equivalent strain across the sample diameter. In the work of [78] four hardness measurements separated by 0.15 mm were taken in a cruciform arrangement around the point selected and from these values the average is reported. The average hardness so determined is measured every 0.3 mm across the diameter.

In the second case, two ways can be used to visualise the results, hardness profiles across the sample diameter and hardness maps. For the hardness maps, the hardness measurements are taken along a quarter of the disc in a rectilinear grid pattern with a separation between points of 0.3 mm. A colour-code is used to assign different colours to the hardness values. If the same procedure is applied for the entire disc surface, the hardness distribution over the whole sample can be obtained [78]. Figure 2-34 shows an example of how to build a grid for hardness maps. Although Eq. 2.13 predicts an inhomogeneous hardness distribution in relation to the equivalent strain, in practice the hardness evolves with strain in three different ways. However, irrespective of how the hardness evolves, initially there is an inhomogeneous behaviour stage that occurs during the first few turns, and then the hardness stabilization occurs at high strains. The evolution of hardness observed with number of turns has been classified as *Without Recovery*, *With Recovery* and *With Weakening* [72].

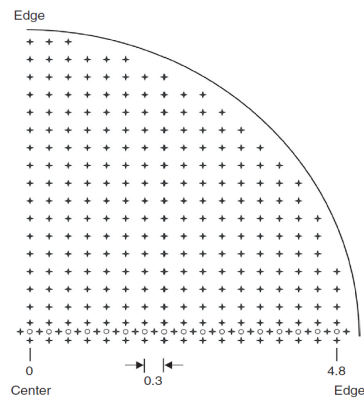


Figure 2-34 Rectilinear grid pattern in a quarter of a disc used to create colour-coded hardness contour maps in HPT samples. The horizontal line located at the bottom of the quarter can be used to create hardness profiles across the sample diameter [78].

#### *Hardness evolution Without Recovery*

In this case, the hardness is lower in the centre and tends to increase with radial position during the first few turns. At higher turns the hardness reaches a homogeneous value across the diameter [87]. Then, the hardness profiles and the colour maps tend to show similar values across the entire sample. *Without recovery* evolution can be appreciated in the plots of hardness vs equivalent strain.

In these plots the hardness increases up to a high value which is *relatively* constant after several turns.

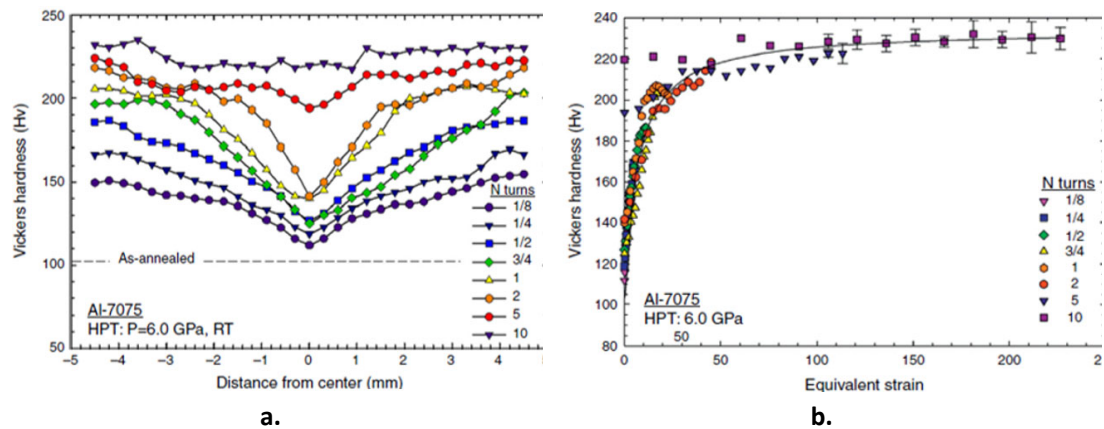


Figure 2-35 Variation of hardness in Al-7075 alloy samples after HPT. A), variation of hardness with distance from the centre of the sample, b), variation in hardness with equivalent strain. The tests were conducted using 6 GPa, 1rpm and 1/8, ¼, ½, 1, 2, 5, 10 turns [87].

This condition is commonly called *saturation* or *hardness saturation* and is related to a progressive ultrafine- grains homogenization that affects the main part of the disc samples, except some occasion the centre and its vicinities. A wide range of metal alloys, including steels, show this behaviour. Figure 2-35 shows an example of this hardness evolution. For this case, Al-7075 alloy samples were processed under 6 GPa and for different number of turns (In this case, 1/8, ¼, ½, 1, 2, 5 and 10 turns were used). The hardness measurements were taken every 0.3 mm from the centre.

#### *With Recovery hardness Evolution*

In this case, the hardness is low in the centre and follows a bell-shaped curve with a peak registered at low strains. Saturation occurs at high strains with lower hardness values than those corresponding to the bell peak. This behaviour can be explained by the high Stacking Fault Energy (SFE) of some materials. High SFE leads to easy cross – slip and rapid recovery during the HPT process. An example of this behaviour can be found in the results of HPT tests conducted on pure Zn using 2 GPa and 1-5 turns (figure 2-36) [88].

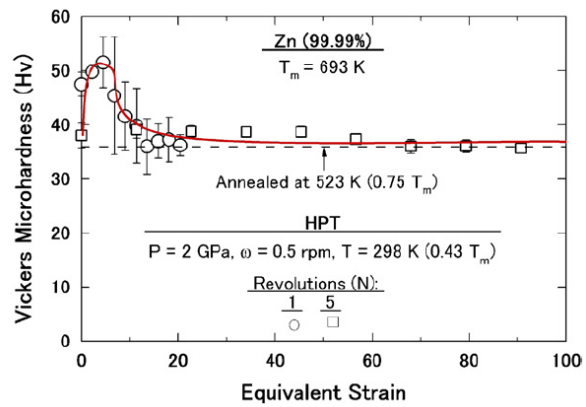


Figure 2-36 Hardness evolution with equivalent strain for Zn after HPT using 2 GPa and 1 – 5 turns. The rotation speed was 0.5 rpm [88].

*With Weakening hardness Evolution*

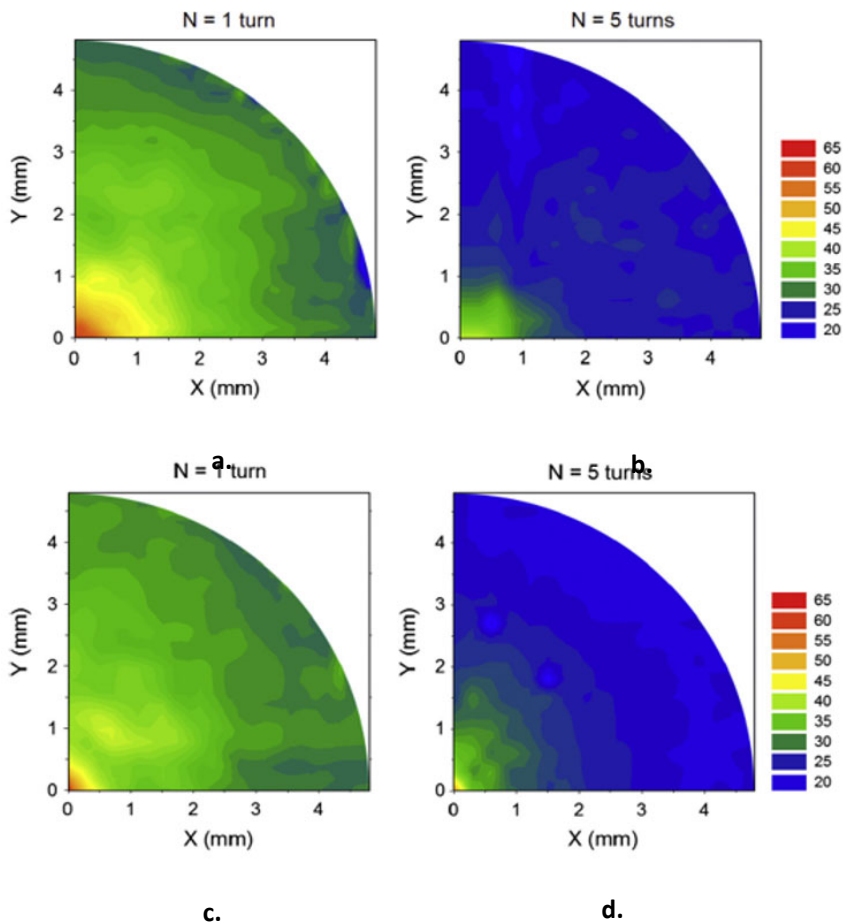


Figure 2-37 Colour-coded contour maps of a quarter disc of a Zn–Al sample processed by HPT for a. 1 turn (3 GPa) b. 5 turns (3 GPa) c. 1 turn (6 GPa) d. 5 turns (6 GPa). The legend in the bottom right corner indicates the Vickers hardness [89].



In this case, the hardness tends to be higher in the centre of the HPT sample than in other places, including the sample edges. Figure 2-37 (hardness colour map) and 2-38 (Hardness – equivalent strain plot) show examples of this behaviour in a Zn-Al alloy processed using several turns [89]. The hardness decreases until reaching a stable value with higher equivalent strains. The decrease in the hardness values is related to a weakening effect, attributed to the loss of rod-shaped Zn precipitates within the Al-rich grains [90].

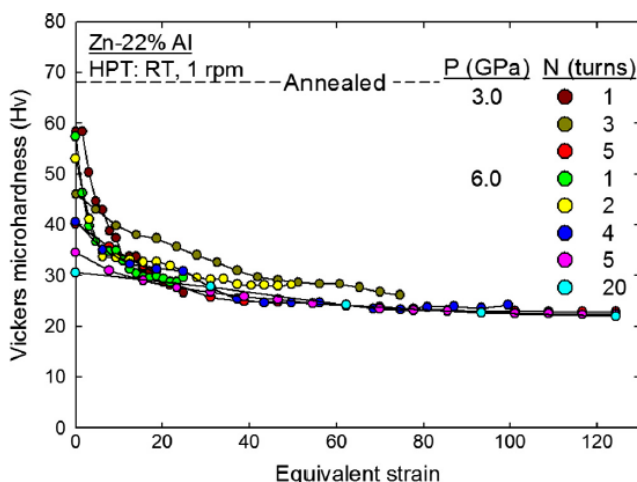


Figure 2-38 Evolution of hardness vs. equivalent strain for a Zn-Al alloy after HPT using 3 GPa (1, 3, 5 turns) and 6 GPa (1, 2, 4, 5, and 20 turns) [89].

#### 2.4.7 Microstructural evolution

Under low strains, the grain size has a significant variation across the sample diameter from bigger grains in the centre to smaller grains close to the edge. However, this difference in grain size across the sample reduces as the strain increases. Figure 2-39 shows the results after processing a Cu–Zr alloy using 6 GPa for  $\frac{1}{4}$ , 5 and 10 turns.

The top row of figure 2-39 shows images from the centre, the bottom row corresponds to the edge. The colours represent different grain orientations. In image a) the grains appear similar to the original material; in b) it is possible to see the microstructural change due to the high deformation. Grain size homogenization starts to occur from N=5 (images c) and d)) [87].

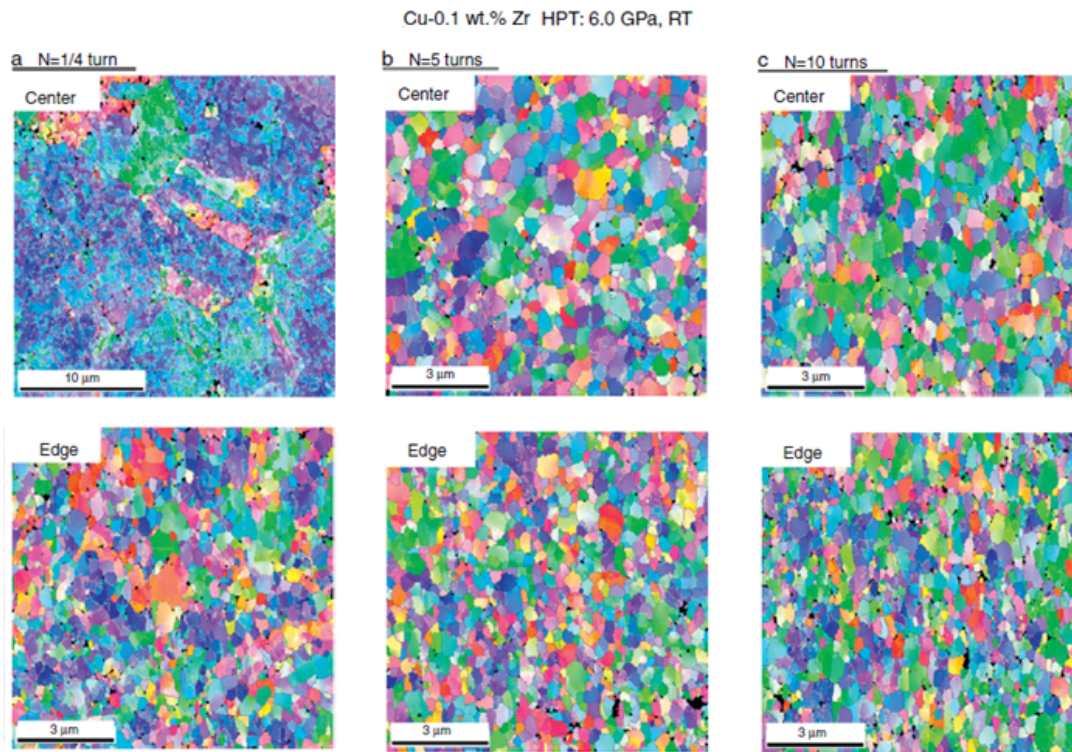


Figure 2-39 Results of processing a Cu–Zr alloy using 6 GPa and ¼, 5 and 10 turns. The top row shows images from the centre of the sample, the bottom row corresponds to a point close to the edge of the sample. The colours represent different grain orientations [87].

#### 2.4.8 Temperature

The rise in temperature registered during HPT depends on several factors such as the processing time, pressure and distance from the disc centre. However, it has been established the temperature rise in the disc sample is directly proportional to the material strength and the rate of rotation[94]. The temperature increases significantly during the early stages of HPT; however, it then levels off and reaches a steady state when there is a balance between the rate of heat generation in the sample and the rate of cooling by the anvils. Although temperature decreases with decreasing applied pressure, the most efficient way to avoid an increase in temperature is by reducing the rotational speed. In the case of high purify Fe, the temperature can increase by about 62 °C under 6 GPa, 10 turns and a speed of 1 rpm [88].



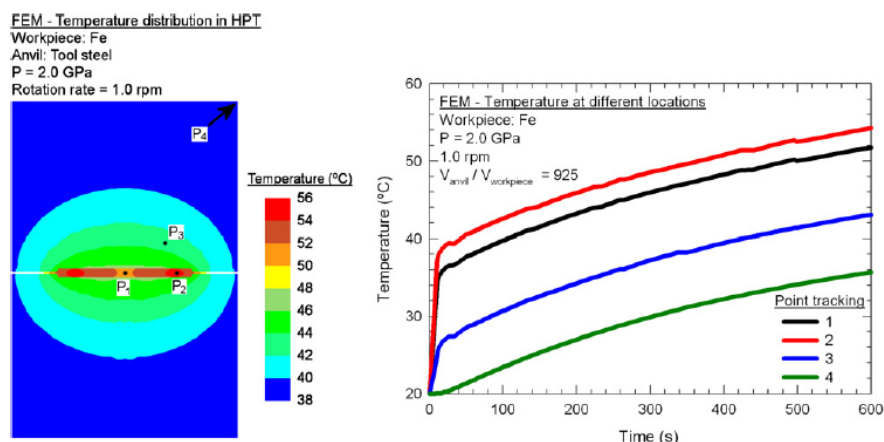


Figure 2-40 FEM prediction of the temperature distribution after 10 turns of HPT processing for pure iron. Four separate points are evaluated for comparison. Point P1 corresponds to the sample centre, P2 corresponds to a sample point close to the edge, point 3 is located inside the upper anvil and P4 is at the upper right corner of the anvil [88].

The rapid temperature increase and its subsequent stabilization are shown in the results of a FEM analysis of the sample and the anvils (figure 2-40). The evolution of four different points affected by a HPT process under 2 GPa, 10 turns and speed of 1 rpm are plotted for comparison. All points show the same behaviour, with a rapid increase during the first processing seconds and a later stabilization.

#### 2.4.9 Reversal movement in HPT

Reversal movement (called also cyclic HPT test or c-HPT to differentiate it from the classic or monotonic HPT or m-HPT) refers to a change of rotational direction in a HPT test. A simple nomenclature is used to indicate the rotational sense for c-HPT: The letter A corresponds to clockwise rotation whilst B corresponds to counter clockwise rotation.

A rotational change implies a discontinuous strain regime and a different microstructural evolution compared to m-HPT. However, the main difference between the two processes is related to the hardness evolution. The overall rate of hardness increase is quicker in samples processed by m-HPT than in those processed by c-HPT. The use of c-HPT does not affect significantly the grain refinement and the final grain size obtained in comparison to that achieved by m-HPT. However, c-HPT retards the formation of high angle boundaries when compared with m-HPT [94].

The global hardness response in c-HPT can also be classified in the three regimes described in section 2.4.6. Several c-HPT tests conducted on different materials such as Armco iron, high-purity Ni and pearlitic steel and an Al – 3% Mg – 0.2% alloy have shown lower values of hardness near the centre and higher values close to the edge, in agreement with the *without recovery stage* [96]. Other studies of hardness after c-HPT have shown hardness evolution in agreement with the recovery stages and with weakening in the case of pure Al (99%) [97] and a Zn – 22% Al eutectoid alloy respectively [94].

#### 2.4.10 Cracks during HPT tests

All SPD processes promote an increment in free volume by generating vacancies and nanovoids. These lead to the beginning of potential microdefects such as pores or micro – cracks [95] during the early strain stages, although in the case of HPT, the incidence is limited due to the high pressure applied [96]. The accumulation of these defects aids the growth of cracks.

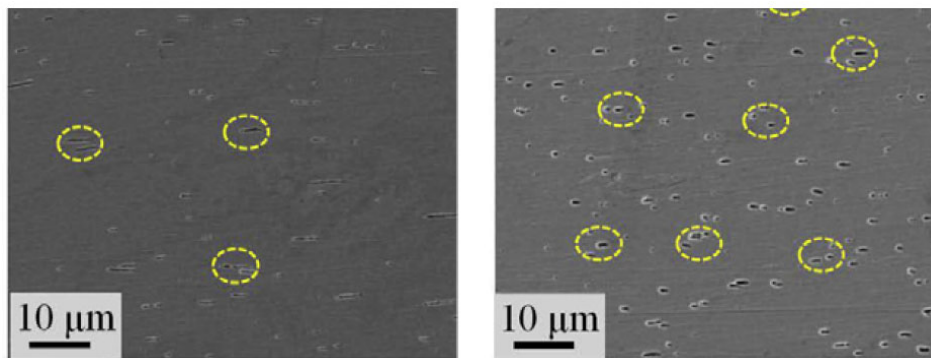


Figure 2-41 a) Micro - cracks and b) pores found in HPT samples of a high – nitrogen stainless steel processed by 6 GPa and 1 turn [95].

However, the agglomeration of non-equilibrium vacancies near different internal sinks, for instance grain boundaries or nano cracks formed by dislocation activity may sometimes produce porosity or micro – cracks, even under hydrostatic pressure conditions. To illustrate porosity development, figure 2-41 shows SEM micrographs of a high- nitrogen stainless steel processed by HPT using 6 GPa and 1 turn.

#### 2.4.11 Slippage

At low pressures, relative movement between the sample disc and the anvils may occur. This phenomenon called Slippage, has been reported by Bridgman and others since the beginning of HPT tests. Slippage has been defined as the difference between the measured torsional rotation of the disc and the rotation imposed externally by the HPT test machine. This phenomenon is linked

to the pressure applied, the strength (hardness) of the material processed and the friction coefficient between the surfaces in contact. Bridgman and others observed when the steady state shear stress was plotted against the pressure, two main regions could be identified from the change of slope of shear strength versus pressure curve (figure 2-41).

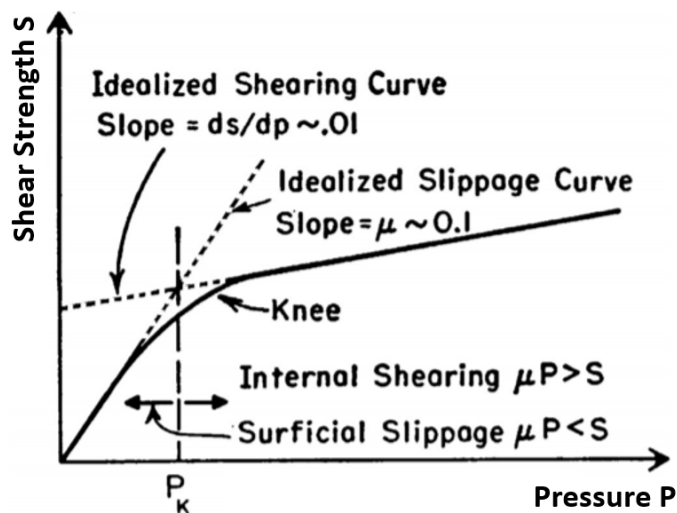


Figure 2-42 Schematic relationship between shear strength and pressure. Two main regions can be identified from the change of slope of the curve [16].

At low pressures the shear stress increases rapidly with increasing pressure. Here, the internal shear stress is below the shear yield strength and only surface slippage occurs. At higher pressures the shear stress increases slowly with increasing pressure, the internal shear stress exceeds the shear yield strength and internal plastic flow occurs. Then, the material “sticks” to the anvil and no slippage will be registered. The change in behaviour is not abrupt, a transitional region indicated as the *knee* exists.

## 2.5 HPT on steels

HPT has been used to obtain nano structures in several steels and Fe-C alloys during the last two decades. The response in each case varies due to the material composition and the manufacturing processes used to make the samples. However, some similarities resulting from the application of high strains have been established in terms of microstructural evolution and mechanical properties.

The main features in common are related to hardness saturation *without recovery* behaviour, the beginning of deformation bands, decrease in the spacing of the cementite lamellae and dissolution of carbides. In this section, the main results obtained in three different steels are summarized in

order to illustrate the common features. Significant microstructural changes under HPT in different steels

Several studies conducted on different steels have shown significant changes in the ferrite and cementite microstructures after HPT. Three of these steels have been selected here because of their similar response to the SPD process. Light Microscopy, SEM, TEM, XRD have been used to characterize these changes.

- *Low Carbon Steel AISI 8620*

In the case of a low carbon steel such as AISI 8620 processed using 6 GPa and  $\frac{1}{4}$ , 1, 2 and 5 turns, the microstructural evolution close to the edge of the samples was followed through different rotations ( $\frac{1}{4}$ , 1, 2 and 5 turns). At  $\frac{1}{4}$  turn, the microstructure is not highly deformed, although the soft ferrite grains have probably started to be deformed by dislocation subdivision. After 2 turns, the pearlite and ferrite have elongated grains, and the spacing of the cementite lamellae is reduced. (figure 2-43) [97].

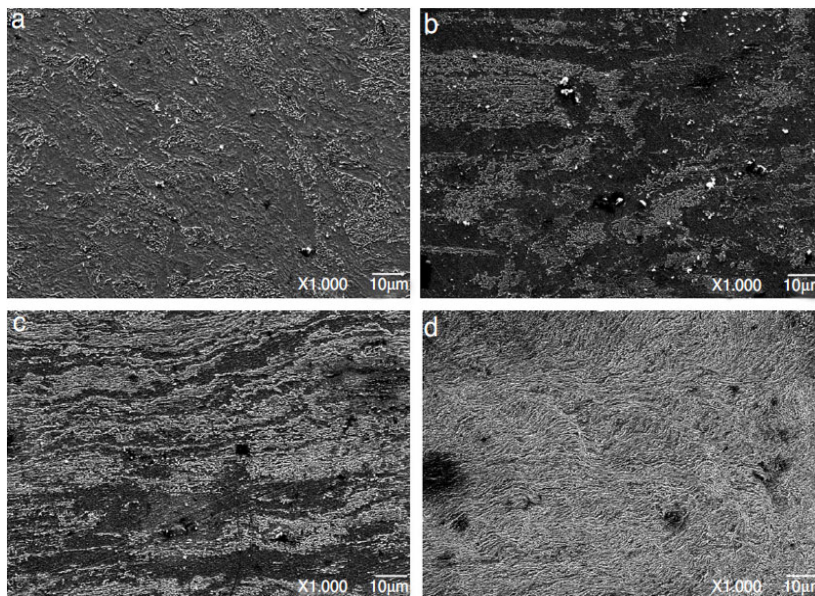


Figure 2-43 SEM images taken at 4 mm from the sample centre after HPT using 6 GPa and a.  $\frac{1}{4}$  turn, b. 1 turn, c. 2 turns and d. 5 turns [97].

Deformation bands across the ferrite structure reduce the initial cementite interlamellar distance. At 5 turns it is not possible to observe clear microstructural patterns due to the high plastic deformation and the formation of small grains. However, X-Ray Diffraction analysis suggests nanostructures are forming and dissolution of the cementite lamella is occurring [97]. The hardness after HPT tends to increase with number of turns and radial position, in agreement with the *without*

recovery condition described in section 2.4.6. Figure 2-44 shows the hardness evolution at  $\frac{1}{4}$  and 5 turns.

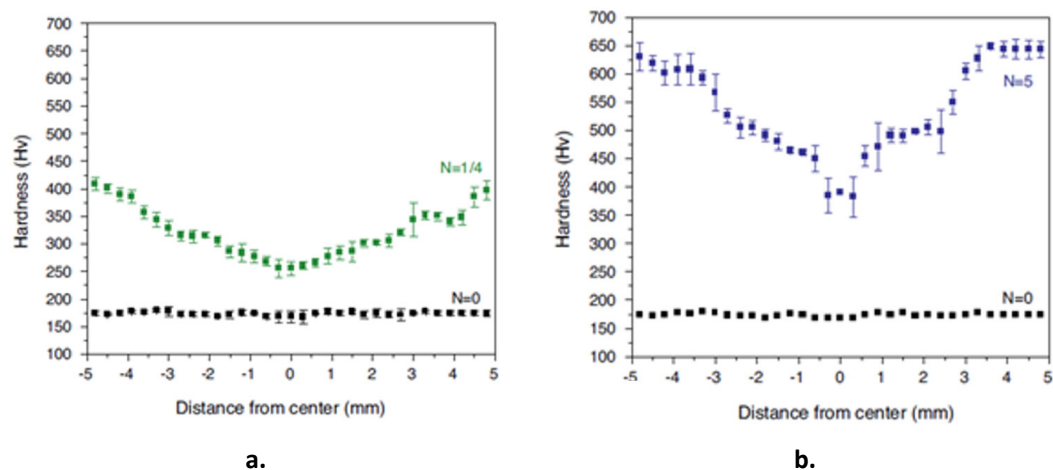


Figure 2-44 Hardness profile of AISI 8620 processed by HPT. Both images show an increase in hardness with distance from the sample centre, as corresponds to a *without recovery* condition. (a.) after 14 turns, (b.) after 5 turns. The original hardness without any plastic deformation is indicated by N=0 [97].

- *UIC 900A railway steel*

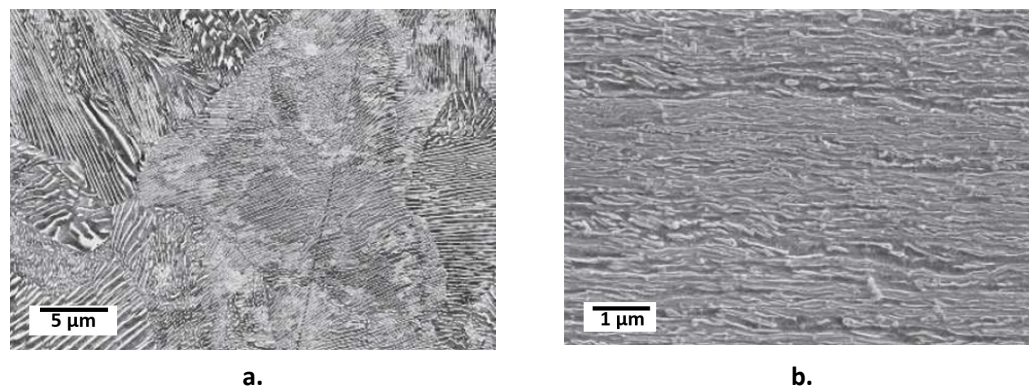


Figure 2-45 Microstructural evolution of a sample of UIC 900A from a. its original condition to b. after HPT with 0.6 turns [98].

The pearlitic rail steel UIC 900A was processed using 5.7 GPa and 0.15 and 0.6 turns. Figure 2.45 shows the microstructural evolution of this sample from its original condition to that produced by HPT with 0.5 turns [98]. The material does not show a significant change after applying HPT with 0.15 turns; the original spacing of the cementite lamellae registered before conducting the test, 300 nm, still continues. However, at 0.6 turns, deformation bands parallel to the shear plane are observed close to the sample edge, the cementite appears deformed and broken and the spacing

of the cementite lamellae is reduced to 25 nm. The pearlitic colonies present in the undeformed material are not visible at this strain. The hardness evolution shows the expected increment in relation to the higher strains. However, the saturation condition was not reached to the parameters used to these HPT tests (figure 2-46) [98].

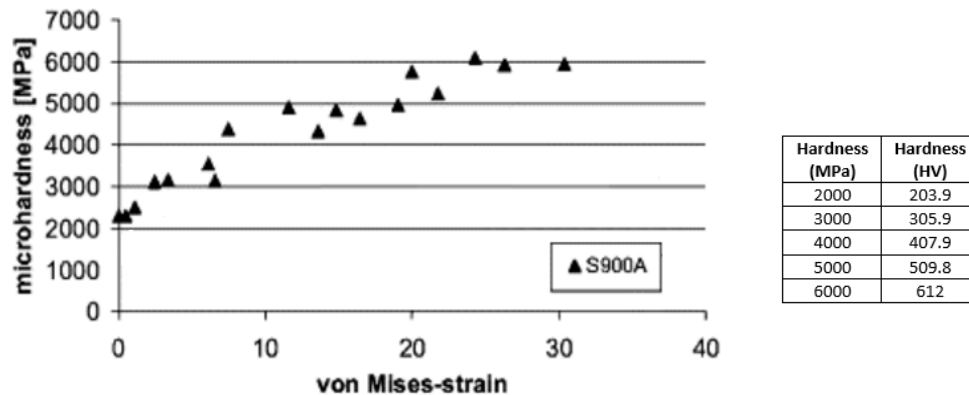


Figure 2-46 Hardness evolution of the pearlitic rail steel UIC 900A after HPT using 5.7 GPa with 0.15 and 0.6 turns [98].

#### *Commercial carbon Steel UIC 860V*

In this case the material was processed using 7 GPa and 0, 1, 2, 3, 5 turns. A reduction of the cementite lamellae spacing with strain increment was reported. However, this depended of the orientation of the cementite colonies with respect to the shear plane. If the cementite lamellae are parallel to the shear plane, the interlamellar spacing tends to decrease, but if the cementite lamellae are perpendicular to the shear plane, this spacing tends to increase. The microstructural evolution of this steel is shown in figure 2-47 after different strains ( $N = 0, 1, 2, 3$ ). If the cementite lamellae are oriented closer to the shear plane their deformation is greater (Figure 2-47 b-d) [11].

At  $N = 2$  turns, a new structure appears with grain sizes in the range 20–150 nm similar to the White Etching Areas seen in railway tracks, figure 2-47 c). These white things are found approximately 3 mm from the sample centre in regions close to the cementite colonies oriented parallel to the shear direction. At  $N=3$ , only two colonies with fine lamellar spacings were observed, with lamellae parallel and perpendicular to the shear direction (figure 2-47 d)) [11]. The hardness variation for the UIC 860V steel after HPT tests shows an increment similar to that registered in the cases of the AISI 8620 and the rail steel UIC 900A, figure 2-48.

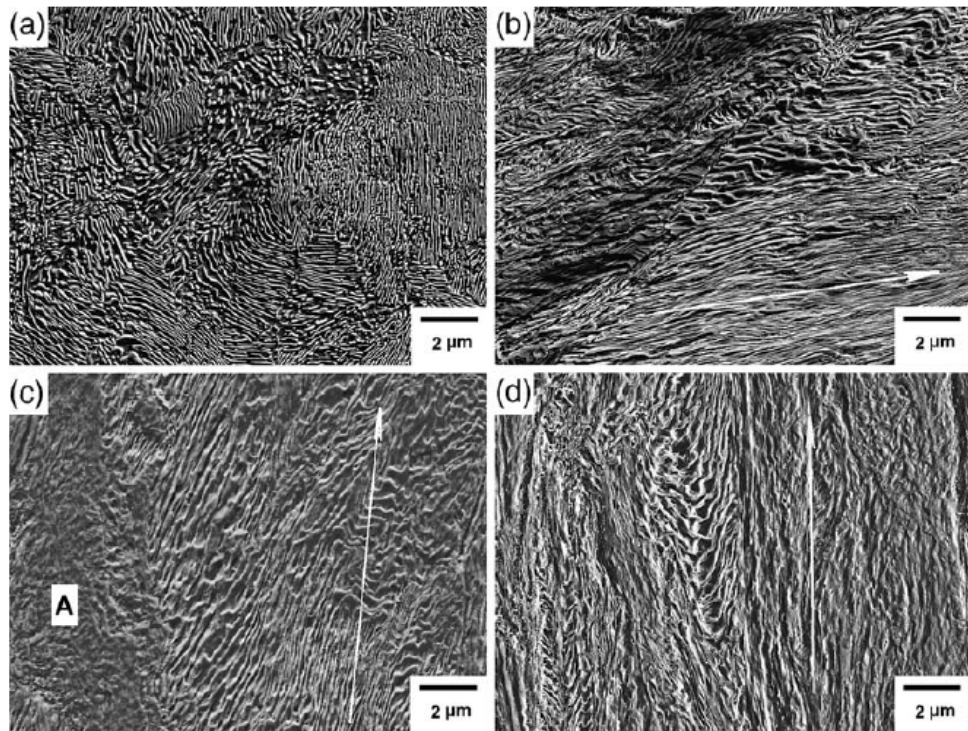


Figure 2-47 Microstructural evolution of a commercial carbon steel UIC 860V processed by HPT using 7 GPa and at different numbers of turns: (a.)  $N = 0$ , (b.)  $N = 1$ , (c.)  $N = 2$ , and (d.)  $N = 3$ . The white arrow shows the shear orientation [11].

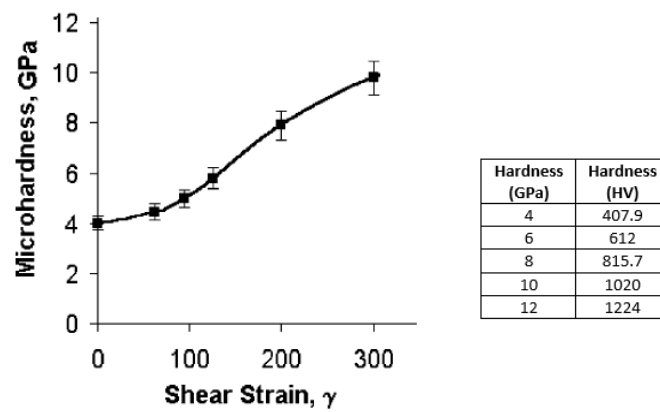


Figure 2-48 Hardness evolution with strain ( $\gamma = 95$  or  $N = 1.5$ ,  $\gamma = 200$  or  $N = 3$ ,  $\gamma = 300$  or  $N = 5$ ) for the commercial carbon steel UIC 860V. Adapted from [11].



### 2.5.1 Formation, transition and fragmentation stages

The microstructural evolution shown in these materials can be split into three different stages: *formation*, *transition* and *fragmentation* [99]. Although these stages have been defined for austenitic and ferritic stainless steels, the experimental results allow their use to classify a wide variety of steels. The *formation stage* is characterized by low strain, the beginning of cellular structures and the decrease in the interlamellar spacing of the cementite colonies oriented parallel to the shear plane [11].

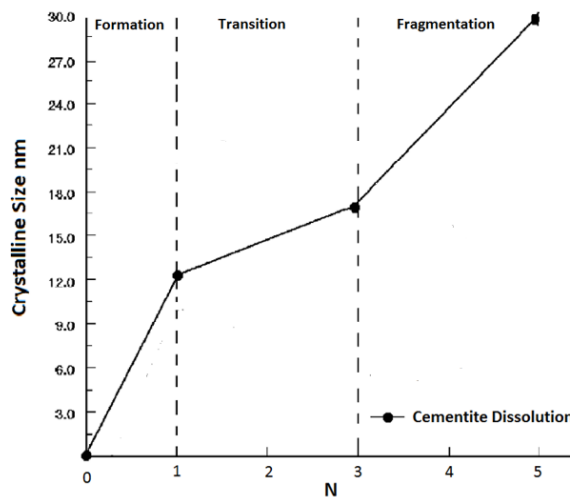


Figure 2-49 Effect of the number of turns on the degree of cementite dissolution in the *Formation*, *Transition* and *Fragmentation* stages. Adapted from [11].

The transition stage is characterized by the presence of deformation bands parallel to the shear plane. This stage corresponds to the transformation of the cellular structures to nanocrystalline structures. The nanocrystalline structures appear first in regions close to cementite lamellae oriented parallel to the shear plane, and then they spread to other regions in the material. Ivanisenko et al. include in this stage the formation of the white etching areas, characterized by nano structures enriched with carbon. The partial cementite dissolution can reach 40% approximately. The hardness increment seen during the transition stage (and the fragmentation stage as well) is related to the decrease of the interlamellar spacing of the cementite [11].

Finally, the third stage called *Fragmentation* corresponds to high strains produced by more than 5 turns. This stage is characterized by the formation of a uniform nano structure with grain sizes



around 10 nm. The absence of cementite lamellae suggests a total dissolution of the carbide in the new ferrite nano grains (figure 2-49) [11].

### 2.5.2 Effect of SPD on carbide distribution

Local microstructural changes that occur with HPT (i.e. adiabatic shear bands and white etching areas), precipitation reactions and variation of the mechanical properties (significant hardness increments) are related to carbide dissolution. These phenomena are also reported in industrial processes such as cold drawing of wire [100] and applications that involve rolling contact fatigue railway tracks [101]

In the case of rolling bearing steels, it has been suggested that white etching areas form in a region of localized plastic deformation, and the microstructural transformations registered in them possibly are a result of high dislocation density and low temperature recrystallization [102] [10, 48]. Although carbide dissolution is still not completely understood, different factors and mechanisms have been proposed to explain this phenomenon during SPD. A short description of these topics related to the effect of boundary grains and interfaces ferrite - carbides is given below.

- *Mechanisms based on the stability of ferrite – carbide interface*

Three main driving forces that lead to carbide dissolution in steel during SPD [38] are:

1. Increase of interfacial energy between carbides and matrix: Precipitate dissolution is driven by supplying an amount of energy enough to destabilise the carbides. This energy comes from cementite deformation and fragmentation that cause an increase in the Gibbs energy of the cementite [38].
2. Increase of carbon solubility in ferrite by pressure: A large hydrostatic stress increases the activity of carbon in carbides. Dissolution is assisted by the high density of dislocations generated during the plastic deformation.
3. Dislocation – carbon interaction: Since the binding energy of a dislocation with a C atom exceeds that of a Fe atoms with a carbon atom in cementite, carbon atoms tend to reside in dislocation strain fields rather than within cementite.

Carbide dissolution is also affected by the tendency of carbon to move from interstitial sites to the cores left by dislocations as a way to relax the stress created by them in their interstitial positions. Eventually, the carbon atoms pin the dislocations, stopping their free movement, in a phenomenon known as a *Cottrell Atmosphere*. Although a Cottrell atmosphere allows dissolution of carbon, the dissolution is limited. If fresh dislocations are not provided from the ferrite – carbide interface by

strain, the dislocations will remain pinned and the dissolution could stop [103] . However other ways to transport carbon have been proposed such as the mechanical effect based on “wear” between phases [11].

- *Wear effect between phases. Carbide dissolution during formation, transition and fragmentation stages*

The carbide dissolution mechanism proposed by [11] to explain the microstructural changes registered in the pearlitic steel UIC 860V after HPT tests, is very interesting due to the similarities between this steel and AISI 52100. The explanation for carbide dissolution is based on the three stages defined in section 2.5.2 (formation, transition and fragmentation [11].

The process starts with an increase of dislocations and low energy sites close to the cementite interface that promotes non-equilibrium behaviour. Then, dissolution is driven by the effect the high shear stresses involved in plastic deformation have on the deformation of phases with very different hardness, such as ferrite and cementite. The plastic deformation during HPT can be modeled as a viscous flow when the softer ferrite moves around the harder cementite. The interaction between these two phases can promote high internal strains in the cementite and severe “wear conditions” that drag the carbon from the cementite/ferrite interface. This process can explain the cementite breaking up and thinning observed when the strain increases in HPT tests applied to a pearlitic steel. This process will be more effective when the cementite lamellae are oriented parallel to the shear flow, although at high strains, all lamellae undergo the same phenomenon. However, the lamella reorientation requires time and causes a transitory decrease in the cementite dissolution rate [11].

Figure 2-50 shows schematically the mechanism proposed where carbon is dragged from the cementite lamellae in the three stages proposed in section 2.5.2. During the initial stage or *Formation* ( $N = 1$  turn) carbon jumps from the cementite (No. 1 in figure 2-50 a)). Some carbon atoms are dragged by dislocations or drift together with the flow of ferrite (No. 2 and 3 in Figure 2-50 a)). At the *Transition* stage ( $N=3$  turns) nanostructures start to form close to the cementite colonies; these are parallel to the shear plane. In these zones, the cementite starts to dissolve and structures similar to white etching areas appear (figure 2-50 b). At the *Fragmentation* stage ( $N=5$  turns) the carbon jumps across the interfacial boundary and moves with the ferrite, probably by rotation. This rotation is caused by the friction against the cementite [11].

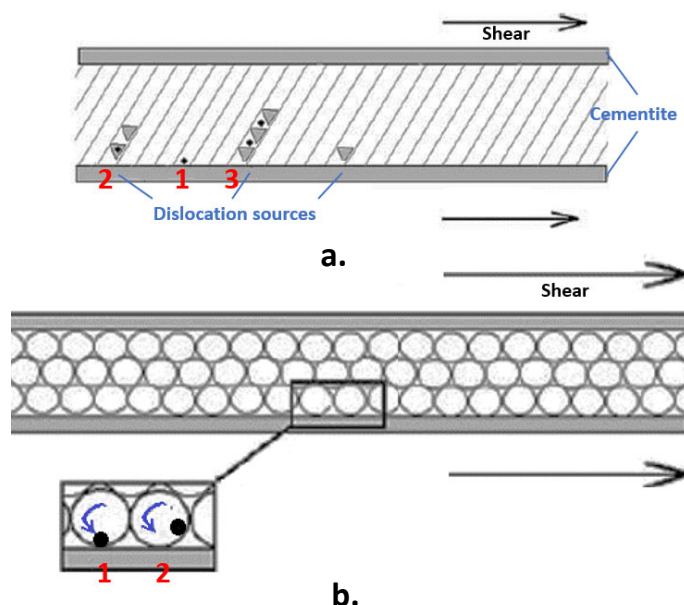


Figure 2-50 Schematic of carbon dissolution from the pearlite structures through the (a.) Formation, (b.). Transition and Fragmentation stages. Adapted from [11].

## 2.6 Conclusions of Literature Review

White Structure Flaking - WSF causes a surface damage similar to Rolling Contact Fatigue - RCF spalling. WSF occurs during the first part of the rolling bearing life cycle and can affect the entire mechanical system where the damaged rolling bearings are assembled. WSF are related to microstructural changes close to the contact surface called White Etching Areas – WEAs, their origin is related to severe plastic deformation processes caused by Hertzian shear stresses.

WEAs are characterised by fibrous structure formed by nanocrystalline cubic ferrite supersaturated with carbon and with a hardness 30 – 50% higher than the bulk material. WEAs often appear in combination with crack networks, suggesting mechanical incompatibilities between the WEAs and the surrounding material. This interaction is responsible for the crack's growth, the embrittlement and the subsequent material detachment.

Elongated grain structures, also called needle-shape grains, appeared with sharp boundaries in zones with the finest grain size. Their homogeneous texture and low average orientation suggested a possible recrystallization in them led by thermal effects. Chemical analysis via EDS confirmed the degradation of the cementite particles inside the WEAs due to carbon dissolution.

## Chapter 2

WEAs origin has been linked to different factors, all of them affected significantly by shear stresses in the subsurface of the contact surfaces Hydrogen embrittlement. These factors include the presence of Non – metallic Inclusions, porosity, carbide clusters, previous cracks, Adiabatic Shear Bands – ASB, and surfacing cracks

Similar stress and plastic deformation conditions registered under RCF conditions can be studied using High Pressure Torsion - HPT tests. HPT tests as a Severe Plastic Deformation – SPD process, combine hydrostatic pressure and shear stresses to generate ultra-grain structures in polycrystalline materials. In addition, HPT allows a record of the microstructural changes as a function of the strain applied to the samples. Materials processed by SPD exhibit outstanding properties, such high strength, ductility, thermal stability and fatigue response, compared to their coarser – grained counter parts. Their potential uses are based on two main factors: superior properties and superior machinability.

The main part of HPT tests is developed under similar parameters quasi constrained conditions, the same rotational speed (1 rpm), dry conditions and room temperature. Pressure and number of turns are the most important factors useful to reach a *saturation condition*, characterised by a homogeneous nano refined grain structure and a similar hardness response (except perhaps at the centre of the disc samples). However, other factors such as roughness of the anvils and the disc samples and the hardness of the material processed, and the anvils influence significantly the refinement grain process, especially before to reach the *saturation condition*. The combination of lower pressures, differences between roughness in disc samples and the anvils, and hardness can facilitate slippage between the disc sample and the anvils. Slippage is a difference angular displacement between top and bottom surfaces of disk samples.

Variations of the strain and strain rate distribution along axial sections of disc samples during HPT can alter the hardness response and microstructure. Different factors are involved to interrupt the plastic flow inside of the disc samples, the main important are related to the interaction of hard particles, such as inclusions, and the asperities of the anvils when the slippage take place. This interruptions resemble turbulent flows affected by Kelvin–Helmholtz instabilities.

Steels processed by HPT show a hardness increment in relation to the radial position, with higher values close to the sample edges. This behavior is commonly observed in materials *without recovery* that is for those metals that show hardness saturation after a rapid hardness increment during the first strain steps. The main microstructural changes registered in steel processed by HPT are related to the beginning of deformation bands, the decrease in the spacing of the cementite lamellae and the dissolution of carbides present in the matrix.

The nature of the boundary grains and the ferrite – carbide interface leads to carbide dissolution in eutectoid steels processed by SPD. A high dislocation density in the interfaces promotes carbide dissolution. At least three different stages can be defined to explain the microstructural evolution of steel during HPT. The first is called *Formation* and corresponds to the beginning of the formation of cellular structures and the decrease in the interlamellar spacing of the cementite colonies oriented parallel to the shear plane. The second stage or *Transition* is characterized by the presence of deformation bands parallel to the shear plane. This stage registers the transformation of the cellular structures to nanocrystalline structures. The final stage or *Fragmentation* is characterized by the formation of a uniform nano structure with grain sizes of around 10 nm and the absence of cementite lamellae.

The non-thermodynamic equilibrium between cementite and ferrite phases and the mechanical effects based on wear between phases lead to carbon diffusion from the cementite to the ferrite matrix. In the first case, the increment of dislocations and low energy sites close to the cementite interface, namely cores, allows carbon movement. In the second case, the flow of ferrite around the cementite drags carbon from the cementite during the grain refinement process. Both factors promote the total diffusion of carbon in the new nanostructure. Although this process can be used to explain the microstructural evolution in pearlitic steels, the phenomena that affect steels with a spheroidal carbide distribution such as in an annealed AISI 52100 have not been reported yet and will be studied in this thesis.

The literature review supports the use of HPT tests to study microstructural changes similar to those found in the WEAs associated with WSF. In this way the results of HPT tests on pearlitic steels has enabled theories to be established to explain the beginning and evolution of WEAs as a consequence of carbide dissolution mechanisms. However, these mechanisms cannot explain the location and develop of WEAs in spheroidal steels. This will also be studied in this research.



## Chapter 3 Experimental Methodology

The materials and techniques used in this project are detailed in this chapter. Firstly, the material preparation required to conduct the HPT tests is described in the first two sections. Following that, the parameters used in the HPT tests are presented in section 3.3. Once HPT tests had been conducted, macroscopic characterisation took place to establish possible differences between the top and bottom surfaces of the HPT disc sample. This included roughness measurements and the determination of whether any slippage had taken place between sample and anvils. A short description of these tasks is reported in sections 3.4 and 3.5.

The disc samples were then prepared for their characterisation by optical microscopy, LOM, and circumferential and axial sections generated. The different techniques used to prepare these sections are explained in section 3.6. LOM was the most useful method to identify WES due to its simplicity and low cost. However, metallography of these samples was not simple, and details are provided in section 3.7. LOM characterisation also facilitated the measurement of other features, such as hardness and % WES. Micro and nano hardness measurements were taken in different places on the studied surfaces. Details of these procedures are reported in section 3.10. The % WES on the top surface of the samples and subsurface were calculated using an Image Processing Program (IPP). The method to achieve this is described in section 3.8.

Finally, SEM was used as a platform to conduct more detailed WES characterisations. Their morphology was explored by SEI and BSI methods (section 3.11). Other microstructural features such as texture and phase distribution were studied using EBSD techniques, such as IQ, IPF and KAM maps (section 3.12). Finally, a qualitative chemical description of the WES and the areas close to them was conducted by SEM / EDS analysis (section 3.13).

Figure 3.1 summarizes the methodology used in this project as a material flow chart. The flow chart starts with the material selected for this project in its as received condition (AISI 52100 bearing steel quenched + tempered standard rollers 10 mm in diameter 14 mm long). The flow chart continues through the different stages described above, following the thick arrows, and ends showing the results obtained in red text. The thin blue arrows indicate a secondary material flow related to the characterisation of both the annealed rollers by LOM / SEM and of the debris found in the anvils cavities after conducting the HPT tests. Details of these procedures are discussed in sections 1.7 and 1.9 respectively.

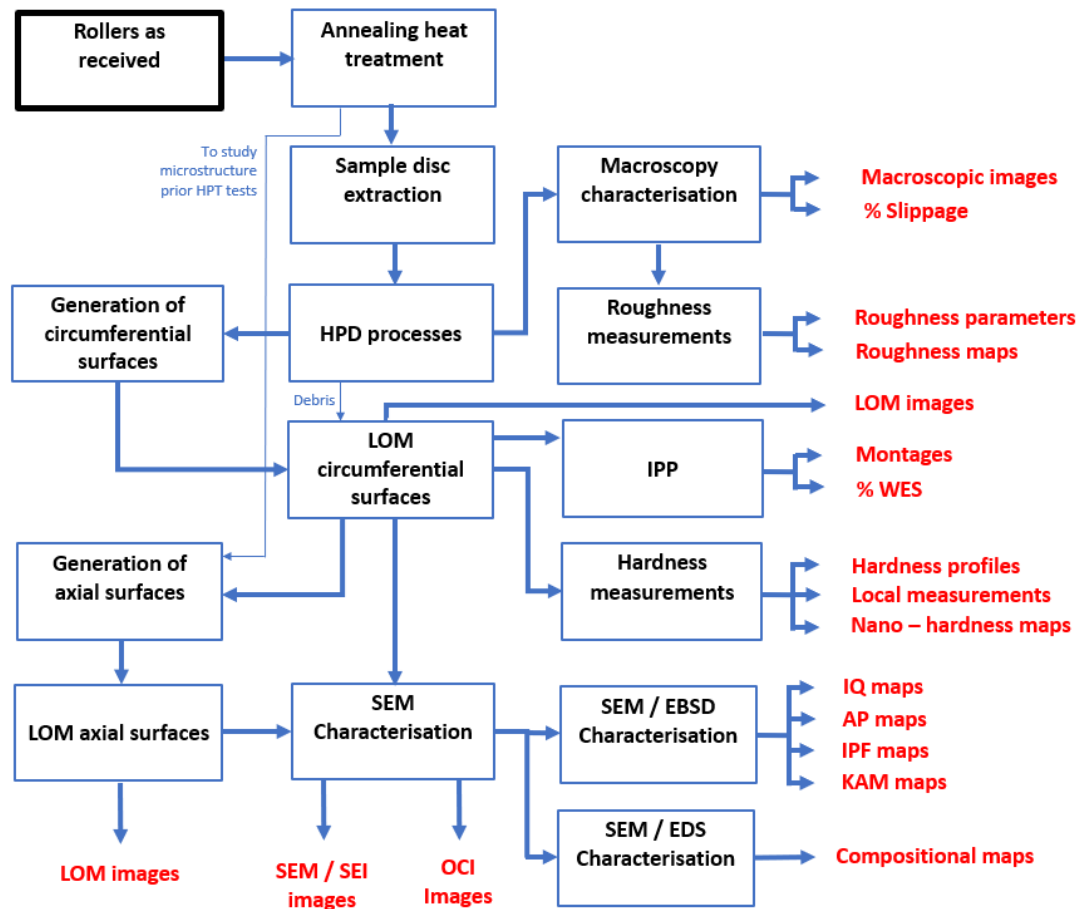


Figure 3-1 Schematic material flow for the AISI 52100 studied in this project. The original material in its as received condition is processed and characterized through different stages (blue boxes) following the blue arrows. The product of these processes is highlighted in red text.

### 3.1 Annealing heat treatment

The material selected for this study was the AISI 52100 bearing steel to British standard BSI 2S 135-2009 [104]. The steel was provided by a local company Simply Bearing Ltd. (Halton House, Greenfold Way, Leigh WN7 3XJ, UK) as standard rollers 10 mm in diameter and 14 mm long. The Vickers hardness of the rollers was measured as  $750 \pm 5$  HV (the hardness test was conducted during 15s at 200 g). Table 3-1 shows more technical information on this steel.



Table 3-1 Specified composition ranges of AISI 52100 steel in weight % [105].

% C	% Fe	% Cr	% Mn	% Si	% P	% S
0.98–1.1	96.5–97.32	1.3–1.6	0.25–0.45	0.15–0.3	0.025	0.025

Table 3-2 Technical details of AISI 52100 used in this study. Information provided by the supplier [105]

Feature	Values
Hardness	60-67 HRC / 700-900 HV
Density	7833.4 kg/m <sup>3</sup>
Tensile Strength	2.24 GPa
Yield Strength	2.03 GPa

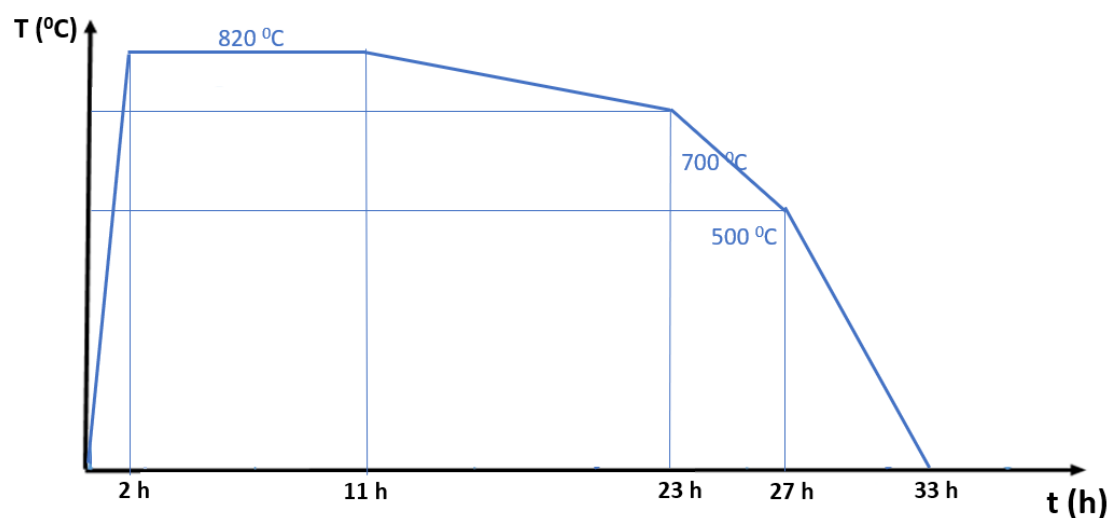


Figure 3-2 Schematic of the annealing heat treatment applied to the standard rollers.

As the maximum hardness of specimens that the HPT test machine can process is 800 HV, it was necessary to apply an annealing treatment to decrease the hardness of the rollers prior to HPT specimen preparation (figure 3-2). Annealing produces spheroidized carbides in a ferritic matrix without tempered martensite and retained austenite. This heat treatment consisted of the procedure indicated in figure 1-2 of austenitising followed by slow cooling as described in BSI standard [105]. Austenitising was carried out at  $820 \pm 10^\circ\text{C}$  for at least 6 h (in this study the rollers remained at this temperature for 9 hours). Then, the rollers were cooled to  $700^\circ\text{C}$  at a rate not greater than  $10^\circ\text{C}$  per hour by controlling the furnace set point. After that the rollers were furnace cooled to ambient temperature from  $700^\circ\text{C}$ . The annealing was conducted in air in a Carbolite CSF 1100 electric furnace.

## 3.2 Sample extraction

After this heat treatment, the roller diameter was reduced to 9.8 mm to eliminate the decarburised surface produced during annealing. The rollers were then cut into slices 1 to 1.2 mm thick using a Mecatome T210 Cutting Machine. The slices were then ground on both sides using 800 and 1200 grade silicon carbide papers to reduce their thickness to 0.8 – 0.9 mm. This reduction in thickness had two purposes, firstly, to eliminate any plastic deformation caused by the cutting process, and secondly, to reach the thickness value required for conducting the HPT tests. The weight of the samples was measured using a precision balance with a resolution of 0.001 g.

## 3.3 Conducting SPD tests on the HPT test machine

The SPD tests were conducted on a HPT machine manufactured by Riken Enterprise Co. Ltd. in Kokuraminami Ku Kitakyusyu City (Japan), available at the University of Southampton (figures 3-3 and 3-4). Basically, the HPT tests consisted of three steps: *loading, turning and finishing*. Once the sample was set up in the cavity in the bottom anvil, the *loading step* started when the machine pushed the bottom anvil against the top anvil. After 5 s of applying a pre-set pressure, the *turning step* started with the rotation of the bottom anvil against the fixed top anvil for the number of turns selected manually. Finally, the finishing step consisted of stopping the rotation and moving the bottom anvil down to extract the disc samples. The geometry of the cavities is showed in the figure 2-24.

The pressure and torsion are produced by a hydraulic unit (figure 3-4 b); if the temperature of the oil reached 30°C, the machine was stopped to protect the power source. Three pre-set pressures could be selected through buttons on the control panel of the machine: 1, 3 and 6 GPa, however, other pressure values were available by varying manually the pressure in the hydraulic unit. Thus, lower and higher pressures such as 0.5 GPa, and 8.4 GPa were possible. All disc samples were processed under the same rotational speed of the bottom anvil (1 rpm); the speed was measured manually with a chronometer. The rotational speed could be changed directly by the hydraulic unit, but this option was never used. Likewise, the HPT machine allows the rotation sense to be changed but this option was also not used. All tests were conducted rotating in an anticlockwise sense with respect to the top anvil.

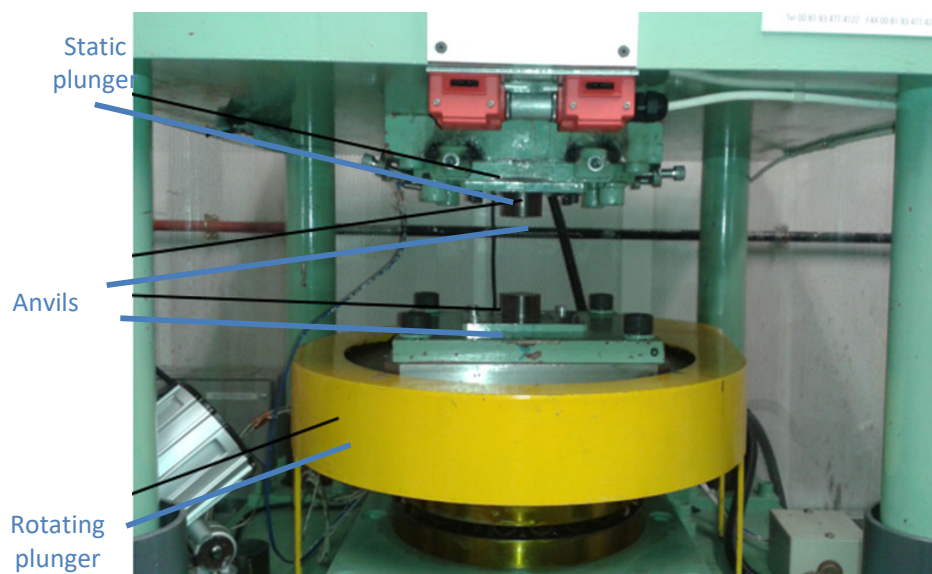
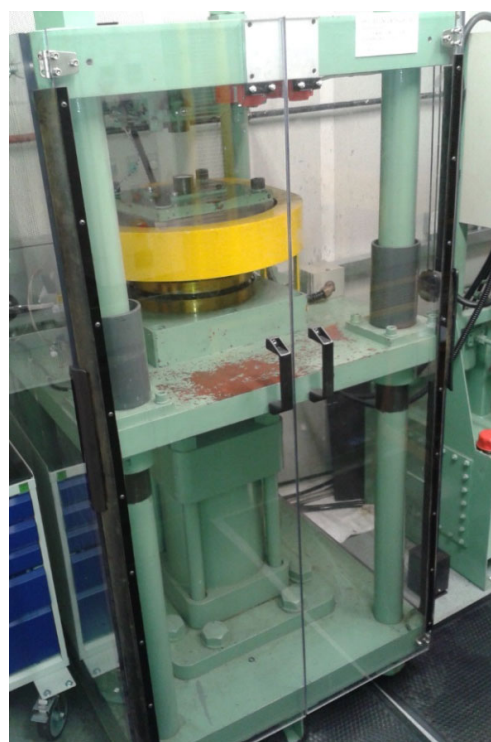


Figure 3-3 Details of the HPT testing machine, with the plunger and anvils used to deform the steel samples.



a.



b.

Figure 3-4 Images of the HPT testing machine available in the SPD Lab. a) The machine itself, b) the hydraulic unit and control system required to operate the machine.

## Chapter 3

The machine operational envelope was restricted by the highest final hardness admissible for samples which was 800 HV. This limit was set to prevent permanent damage to the anvils used to process the disc samples. After conducting some preliminary tests during *Stage 1* (see below), it was clear that the top of the operational envelope range was restricted to 6 GPa and 3 turns. Hence, all HPT tests conducted in this project were limited by these parameters. In all tests conducted, disc samples appeared stuck to the bottom anvil. Adhesive tape was used to collect any debris remaining on both, top and bottom anvils after concluding each test. Several HPT tests were conducted for the purposes detailed below:

### **3.3.1 Stage 1, Scoping HPT tests:**

HPT tests were conducted using 0.5, 1, 3, 6 GPa and 1, 2, 3 turns, at least two repeat tests were conducted for each pressure/turn combination. The purpose of these tests was to evaluate the operation of the test machine and to establish whether microstructural changes similar to the White Etching Areas observed in failed rolling bearings could be obtained. This stage was carried out following a standard practice used to study HPT samples: After retracting the bottom anvil, one side of the sample was selected for characterisation by LOM. This meant that one of the sides of the sample was slightly ground and polished to eliminate all signs of contact with the anvil. The side selected was the bottom surface of the sample.

### **3.3.2 Stage 2, Tests for surface characterisation**

HPT tests were conducted using 0.5, 1, 3, 6 GPa and 1, 2, 3 turns with two repeat tests for each pressure/turn combination. These tests were to evaluate differences between the top and bottom surfaces of the disc samples, such as slippage or morphology and to characterise the white structures revealed on the top surface of some of the HPT samples.

### **3.3.3 Stage 3, Tests for determining the microstructure in the thickness direction**

A group of HPT tests was conducted using 0.5, 1, 3, 6 GPa and 1, 2, 3 with two repeat tests for every pressure/turns combination to study white structures produced sub-surface. These samples were processed using circumferential serial sections generated from the bottom surface.

### 3.3.4 Stage 4, Tests for determining the roughness of the anvils

A sample group was processed using only pressure. The aim of these tests was to obtain a record of the anvil roughness by deforming the top and bottom surfaces of the disc samples. Compression tests under 0.5, 1, 3, 6 and 8.4 GPa were conducted.

## 3.4 Macroscopic characterisation

After conducting HPT tests the samples from stages 2, 3 and 4 were observed using a *Wild Makroskop M420* macroscope. Macroscopy was also useful to carry out the angular displacement method developed by Edalati et. al. [106] to establish the amount of slippage between samples and anvils. For these two parallel lines were drawn across the diameter of both top and bottom surfaces of the discs prior to HPT testing. After testing the angular displacement of the two lines was measured in degrees and compared with the angular rotational of the HPT machine. Any difference in the angular displacement of the lines and the machine rotation angle allows the slippage to be determined. Figure 3-5 a) reveals how the machine was set up prior to conducting a HPT test. Figure 3-5 b) shows the condition of the bottom anvil with a sample stuck to it after conducting a HPT test under 6 GPa 1 turn. The lines drawn to determine the angular displacement are visible before and after conducting the HPT test.

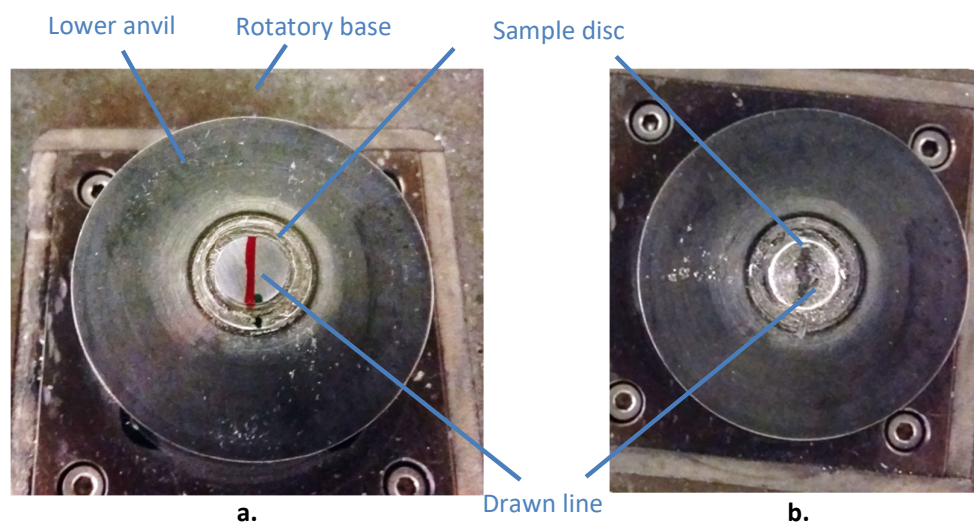


Figure 3-5 HPT sample in lower anvil. a) Before conducting HPT b) After conducting the HPT test with the sample stuck to the lower anvil. Tests conducted under 1 GPa 1 turn 1 rpm

### **3.5 Roughness measurements**

The samples from stage 4 were compressed by the HPT test machine under pressures of 1, 3 and 6 GPa to obtain an impression of the roughness of the anvils. The impressions on both top and bottom sides of the sample discs were evaluated using a Taylor Hobson Form Talysurf 120L profilometer system to obtain roughness profiles along the diameter of the disc samples. Parameters such as Ra, Rq, Rz were evaluated for all disc samples. In addition, a reconstruction of the surfaces was made using an Alicona G4 Infinite Focus optical system.

### **3.6 Generation of circumferential surfaces**

#### **3.6.1 Stage 1, Scoping HPT tests:**

Disc samples were hot mounted in Bakelite using a APA OPAL 410 mounting press. The bottom side of the samples was ground using 1200 and 4000 SiC papers until approximately 200  $\mu\text{m}$  to 360  $\mu\text{m}$  of material had been removed by grinding from the bottom sides. After grinding, the samples were polished using suspensions of 6  $\mu\text{m}$  / 1  $\mu\text{m}$  diamond pastes. Grinding and polishing were carried out using a Struers TegraPol 15 automatic machine. After evaluating different combinations, grinding pressures of 10 or 15 N were used for both 1200 and 4000 SiC papers. Polishing was carried out using 25 N for both diamond paste types. The final thickness was determined by using a Mitutoyo Micrometer, 25 mm Max Measuring Range (0.001mm, Ref. 293-821-30) to measure the thickness of the Bakelite mount, the initial thickness of the Bakelite mount before grinding having been measured previously. Thickness measurements were taken at four locations in the samples in the Bakelite mount.

#### **3.6.2 Stage 2, Tests for surface characterisation**

Disc samples were ground and polished on both their top and bottom surfaces until 40  $\mu\text{m}$  of material had been removed in order to study the differences in the roughness patterns on both surfaces. The grinding was conducted using 4000 SiC paper in an automatic machine, with 15 N pressure. Polishing was carried out with suspensions of 6  $\mu\text{m}$  / 1  $\mu\text{m}$  diamond paste and 25 N pressure.

#### **3.6.3 Stage 3, Tests for determining the microstructure in the thickness direction**

Disc samples were ground and polished in successive steps of 40  $\mu\text{m}$  from the bottom surface until 360  $\mu\text{m}$  of material had been removed so that subsurface WES could be identified for further analysis. Samples were ground using 4000 SiC papers and polished using suspensions of 6  $\mu\text{m}$  / 1

$\mu\text{m}$  diamond pastes. The grinding and polishing were carried out using a Struers TegraPol 15 machine with 10 - 15 N pressure, the polishing pressure was 25 N.

### 3.6.4 Stage 4, Tests for determining the roughness of the anvils

This sample group was not ground or polished.

## 3.7 LOM on circumferential and axial surfaces

After grinding and polishing, the surfaces were cleaned with ethanol in an ultrasonic bath, etched with 2% Nital (2ml  $\text{HNO}_3$ , 98ml ethanol) or Vilella's reagent (5ml HCl 1g picric acid, 100ml ethanol) for 5 s to reveal the white structures and the prior austenite grain boundaries. Some debris produced during HPT testes was also observed; this was cleaned and preserved between microscope slides. An Olympus 3X41 M-LED microscope with 5x, 10x, 20x, 50x and 100x objective lenses was used to examine samples.

## 3.8 IPP

Complete montages of the sample surfaces from stages 2 and 3 were constructed by photographing 10-14 images taken by LOM. For stage 3, the montages did not include images from close to the centre of the samples as WES were not present in this area. The montages were made using the *Stitching - Mosaic J* tool of the image processing program (IPP) *Image J – Flavour Fiji*. This software is a free and open source IPP inspired by IPP *NIH Image* written by Wayne Rasband in Pascal for *Macintosh Co* released in 1987. The version *Flavour Fiji* includes many plugins useful for scientific image analysis in fields such as life sciences [107].

In order to visualize the WES black/white masks were generated from the micrographs and the montages using the tool *Adjust - Threshold* of *Image J*. This tool binarises the images and produces 8 bit images using at least 16 global (histogram-derived) thresholding methods. After testing all of these thresholding methods, the default threshold method was selected to process the images as it defined better the WES. Using the grey level histograms, the grey levels were suitably adjusted so as to delineate the WES.

Once the black/white masks were generated, the new images were processed using the *Particle Analyse* tool from *Image J*. This tool provides information on particles in the images, such as size or % area (a particle is an isolated black portion in the black/white mask). The size of the particles analysed is defined by the user, setting the minimum and maximum pixel area. *Particle Analyse* was

thus used to exclude unwanted objects with respect to a specific size, for example 20, 40 and 60  $\mu\text{m}^2$  (figure 3-6).

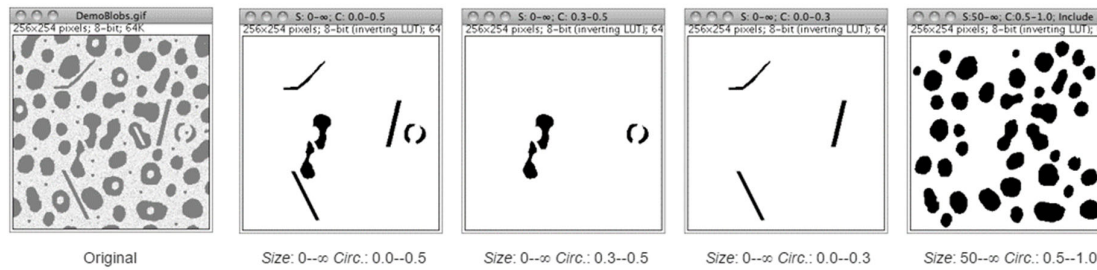


Figure 3-6 Use of the *Analyze Particle* tool from *Image J* to eliminate particles according to their size. The original image appears at the left, the other images were obtained after defining a particular size. [107]

The IPP software was also used to determine the amount of WES on the top surface of the stage 2 samples by calculating the %WES. To do this, four representative LOM images were taken every  $90^\circ$  at a radial distance of 2.5 mm. The % of black mask generated by Image J was calculated for all images, thus obtaining 4 %WES per sample. This procedure was repeated twice and hence 8 %WES were acquired from the two samples. Finally, an average of all 8 values was reported as a representative %WES for each HPT parameter combination (pressure and turns) used in stage 2. Figure 3-7 shows a schematic of the position of the selected areas used for this analysis. An example of one of these images is presented in figure 3-8.

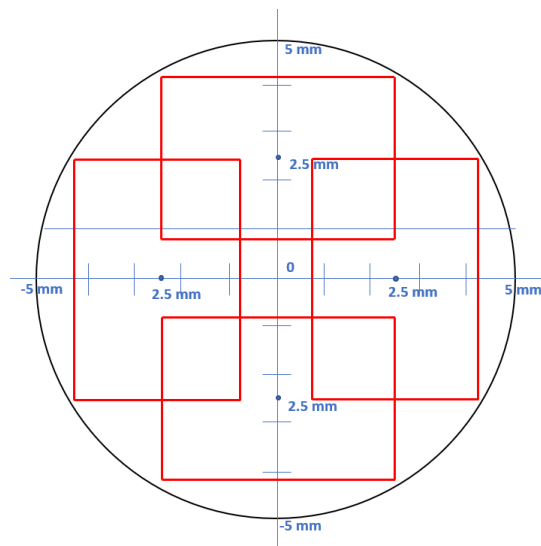


Figure 3-7 Position of the representative areas analysed by IPP Image J to determine the %WES in the HPT samples from stage 2.



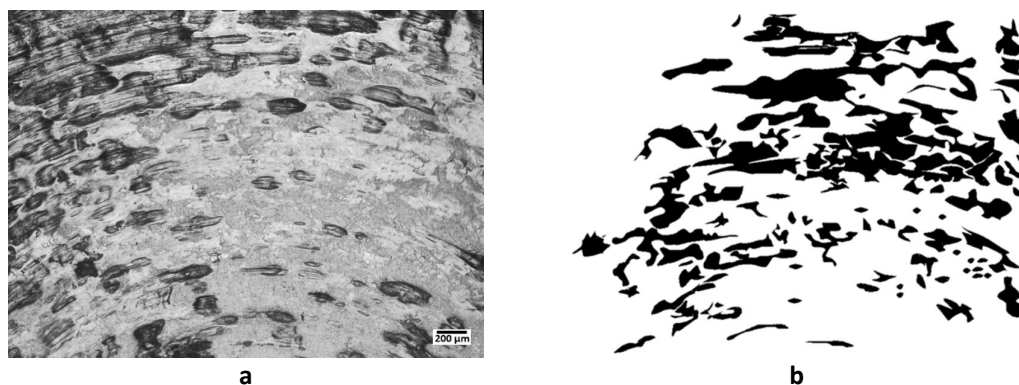


Figure 3-8 Top surface of a disc sample processed using 3 GPa and 1 turn. a) Micrograph taken at a radial distance of 2.5 mm from the centre. b) IPP Image J to determine the %WES in the HPT samples from stage 2

To analyse the influence of the strain on WES formation, the total % black area in several concentric circles drawn on the mask was calculated. Then the %WES corresponding to the next smaller circle was subtracted from the first circle analysed to define the %WES in a ring of known radius (the ring was defined by its mid radius). Circles were drawn using the macro *Circle* tool and the %WES were found using *Set Measurements* from *Image J*. Figure 3-9 shows a print screen of the areas and %WESs calculations made by *Image J*. This process generated eight rings with mid-radius position located at 3.125, 3.375, 3.625, 3.875, 4.125, 4.375, 4.625, 4.875 mm from the centre. The %WES in all rings were plotted in relation to their mid radius position and with the strain at that location. One example of a ring with mid radius 4.125 mm used in is shown as a hatched region in figure 3-10. Circles of 3 and 5 mm radius were also drawn to show the area analysed in the rings

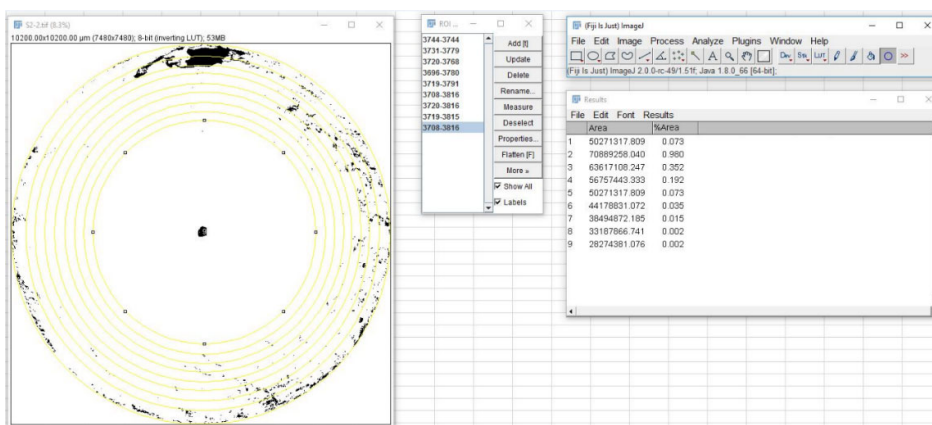


Figure 3-9 Calculation of areas and %WES in nine concentric circles drawn on a black/white mask of a periphery montages. The radii of the circles were 3, 3.25, 3.5, 3.75, 4, 4.25, 4.5, 4.75 and 5 mm.

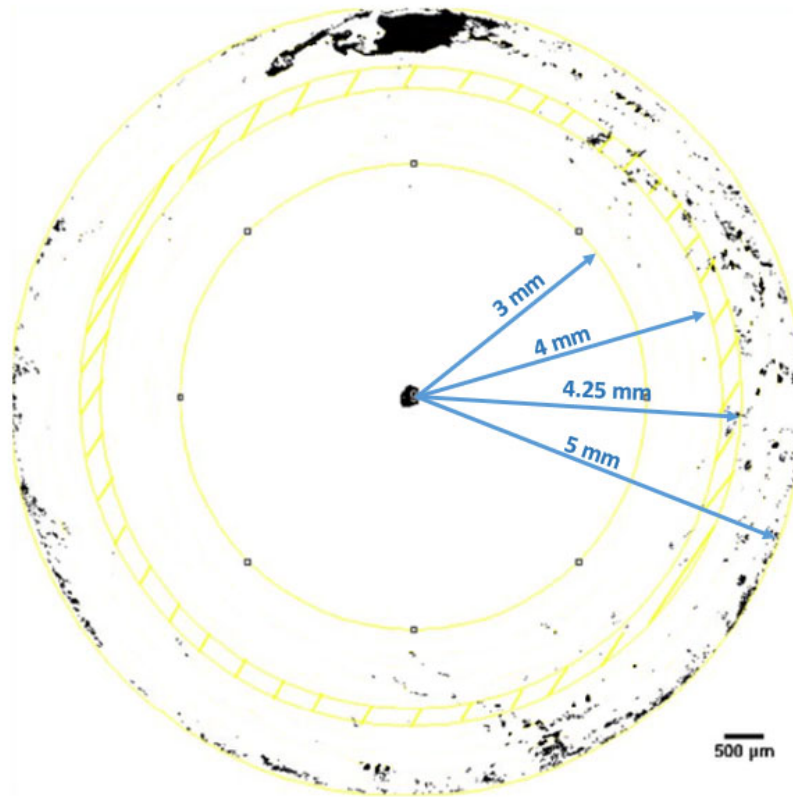


Figure 3-10 Example of a ring with mid – radius of 4.125 mm used to calculate the %WES in relation to the radius. Eight rings were defined to calculate the %WES along the area limited by circles of 3 and 5 mm radius.

### 3.9 Generation of axial surfaces

Selected disc samples from stages 2 and 3 were cut along their diameters in the axial direction to reveal WES both on the surface and subsurface. Typically, two sections from each disc cut at 90° to each other were prepared. The new surfaces were ground using 1200 and 4000 SiC papers to eliminate any plastic deformation produced during the cutting. After grinding, the axial sections were polished using suspensions of 6 μm / 1 μm diamond paste. Axial sections were also cut from the rollers in both their as received and annealed conditions for characterisation.

### 3.10 Hardness measurements

Vickers microhardness measurements were taken to determine two features: the variation of the hardness along the diameter of the disc samples and the difference of hardness of WES and the areas surrounding them. A Matsuzawa Seijki MHT-1 micro hardness tester with a Vickers indenter (100 g load for 15 s) was used. The hardness tester was calibrated by using a reference hardness

block. Firstly, the hardness profiles were determined at nine positions located every millimetre across the sample diameter. Figure 3-11 shows these positions, starting from the edge of the sample to the centre. Each hardness value reported for these positions is an average of four measurements that were taken in a cross pattern around them.

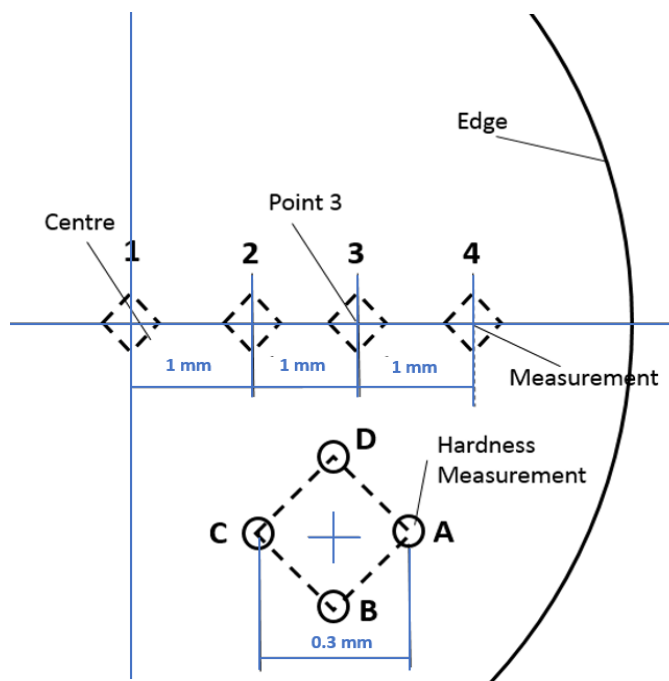


Figure 3-11 Hardness positions taken across the sample diameter used to determine the hardness profiles. The external circumference corresponds to the sample perimeter. 36 hardness measurements were taken for each hardness profile.

Other hardness values were taken in the WES and in areas near to them, using the edge of the sample as a geometrical reference. However, the position where hardness was measured was defined with respect to the centre of the sample. Their positions were obtained by using an Olympus BX51 Optical microscope (LOM) and the IPP Image J. In addition, hardness maps were constructed from measurements taken with a NanoTest Vantage, nano indenter test machine (Micro Materials Ltd). The NanoTest Analysis Mode software was used to process the data and produce the maps.

### 3.11 SEM characterisation

SEM images are obtained using two electron sources, those produced by elastic interactions between the Electron Beam (EB) and the atom structures in the sample, and those produced by the

inelastic interaction with both weakly bound conduction band electrons or outer shell valence electrons. In the first case, the EB interacts with large volumes (interaction volumes) inside the sample because of its high energy. Eventually, some electrons will be reflected or back scattered out of the specimen interaction volume. Since heavy elements (high atomic number) backscatter electrons more strongly than light elements (low atomic number), and thus appear brighter in the image (BSI), back scattered electrons are used to detect contrast between areas with different chemical compositions.

On the other hand, the electrons produced by inelastic interactions have much less energy compared to the back scattered ones and their interaction volume is significantly smaller. Cathodoluminescence radiation, x - rays and lattice vibration (heat) are also produced because of these interactions. The ejected secondary electrons are used to produce another kind of SEM image called Secondary Electron Images – SEI, which are useful for characterising the surface topography of the sample.

In this project, both BSI and SEI methods were used to characterise microstructure, crystal orientations and compositional differences. Two Scanning Electron Microscopes were used, a JEOL JSM-7000F with SEI/BSI detectors and a Smart Insight / TEAM™ EBSD Analysis System (Smart Insight System from Ametek) and a FEI/Philips XL30 ESEM with SE/BSI/GSI detectors. The same surface preparation as applied for LOM was used for samples studied by SEI, whilst BSI required two additional steps as prior polishing and etching could create surface deformation capable of interfering with the BSI (this can also interfere with EBSD /EDS analysis). Hence, the samples selected were lightly polished using a  $\frac{1}{4}$   $\mu\text{m}$  diamond suspension to remove the etched layer and then polished with 50 nm colloidal silica Polishing Suspensions (OP-S) for 5 – 8 minutes. Thus, SEM / SEI characterisation was conducted before the SEM / BSI. SEM / SEI was operated with voltages between 5 and 10 kV and working distances between 10 and 15 mm. For SEM / BSI the working distances varied between 5 and 7 mm and a relatively low accelerating voltage of 10 kV was used.

### **3.12 SEM / EBSD**

Electron Back-Scatter Diffraction, EBSD, is an advanced characterisation technique that captures and analyses electron diffraction patterns from crystalline structures. These patterns can be used to study microstructural features such as morphology or phase composition, but its main use is to determine the texture or crystallographic orientation of crystalline materials. As texture is closely linked to the mechanical response, EBSD has become a popular and powerful tool to determine the properties of a wide variety of materials, from metals and ceramics to semiconductors [108] [109]

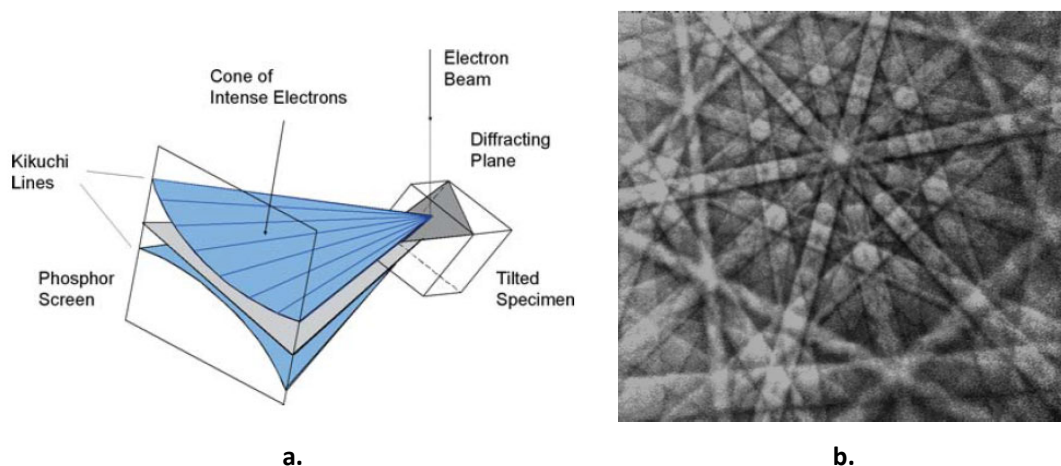


Figure 3-12 Kikuchi patterns used in EBSD analysis. a). Schematic of diffraction pattern generation due to the interaction between the EB and the sample. b) Typical Kikuchi patterns on a phosphor screen [109].

EBSD patterns are generated on a phosphor screen by backscatter diffraction of a high energy EB that interacts with regions located within 20 nm of the surface of the sample analysed. The diffraction is visible as a regular series of parallel bright bands which intersect at several points on a dark background. These lines, called Kikuchi bands, are a gnomonic projection of the crystal lattice on the flat phosphor screen [109]. Figure 3-12 a). presents a schematic of how Kikuchi patterns are formed due to interaction with the EB. The figure also shows an example of these patterns on a phosphor screen (figure 3-12 b)). The diffraction cones are the edges of the Kikuchi bands, and the plane through the centre of these cones is the gnomonic projection of the diffracting plane on the phosphor screen [109].

The lines represent the reflecting planes in the diffracting crystal volume and depend of the orientation of the crystal lattice. The line patterns indicate the symmetries of the crystal, while the width and the intensity of the bands are related to the spacing of atoms in a crystallographic plane. The angles between the bands indicate the angles between different crystallographic planes. Because of the size of the interaction volume in the sample, several crystal structures with different orientations can overlap generating different Kikuchi bands [109].

EBSD analysis is a three-step process consisting of, conversion, identification and orientation determination [109]. In the conversion step, the Kikuchi bands are converted in points or peaks in a Hough space, using a Hough Transformation. In the identification step the intensity of these peaks is compared to theoretical diffracting lattice planes; the angles between bands are also compared with theoretical values. Once the planes have been approximately identified, other similar patterns are indexed. Usually, there is more than one solution that could explain the diffraction patterns (i.e.

approximately match the diffraction patterns), so is necessary to decide which could be the best solution. A parameter called the Confidence Index (CI) is used to define the best solution. CI use a voting scheme calculated by [110]

$$CI = (V_1 - V_2)/V_{IDEAL} \quad (3.1)$$

where  $V_1$  and  $V_2$  are the number of votes for the first and second solutions and  $V_{IDEAL}$  is the total possible number of votes from the detected bands. This “voting scheme” generates values between of 0 and 1 which is used to qualify the indexing success rate. Thus, an indexing success rate can be defined as the fraction of points with a CI greater than a specified tolerance value (0.1 or 0.2 are typical). Points at grain boundaries tend to have very low CI values even though they may be correctly indexed with orientations matching either of the orientations of the grains separated by the boundary [111]. In the third step, orientation determination is based on the calculation of the orientation of the corresponding crystal lattice with respect to a reference frame. Several rotations of the image are tried by the software until the lattice orientations is determined which is then defined by Euler angles. Once the diffracted patterns have been identified, the information related to the crystal lattice can be represented assigning colours to distinguish feature variations and creating different maps:

- Image Quality maps (IQ) show the intensity of the diffracted patterns captured from the sample. They are affected by factors related to crystalline defects such as grain boundaries, high dislocation densities and localized strain. Other factors that affect IQ are discontinuities such as voids and cracks. All these factors are visible as variations in the IQ contrast, which will be brighter when the diffracted patterns are well defined [112].
- Auto Phase maps (AP): Differences between phases can also alter the intensity of the Kikuchi bands. EBSD can reveal these differences due to the diffraction pattern identification process carried out.
- Inverse Pole Imaging map (IPF) assigns colours to different texture orientations in terms of Miller vectors and planes according to a unique geometric reference expressed using three coordinate axes.
- Kernel Average Maps (KAM) provides information about local misorientation by calculating the average misorientation between each pixel and its nearest neighbors.

In this project, SEM / EBSD analysis was conducted using a JEOL JSM 7000F SEM with Backscattered (BSI) and Secondary electron (SEI) detectors. The diffraction patterns were analysed by a TEAM™ Pegasus system that provided simultaneous data collection from Electron Backscatter Diffraction - EBSD (for crystallographic analysis) and Energy-dispersive X-ray spectroscopy - EDS (for chemical analysis). The system also supported a direct correlation between the elemental content and microstructural features of the material studied.

The EBSD characterisation was carried out in two stages, an examination via SEM / BSI and then the EBSD analysis. Firstly, SEM / BSI examination was used to delimit the regions selected. The images were taken with a working distance of 5 and 7 mm (WD) and a relatively low 10 keV accelerating voltage to reveal the crystallographic orientation. Secondly, the region selected was scanned using a 15 keV accelerating voltage with probe currents of approximately 30 nA at a WD of 15 mm with different step sizes (50, 100 and 150 nm).

The data obtained was evaluated using OIM Analysis V. 7.3 software using points with a confidence index (CI) greater than 0.1. For indexing purposes, the  $\gamma$  - Fe (Austenite),  $\alpha$ -Fe (Ferrite) and Fe<sub>3</sub>C (Cementite) were chosen. No additional clean-up of the data was carried out. After data processing, Image Quality Analysis (IQ), Auto Phase maps (AP), Inverse Pole Figures (IPF), Kernel Average Misorientation (KAM) maps were generated. IPF maps were obtained to each orthogonal direction, but only the normal orientation (direction z axis) was reported. The averages in KAM maps were conducted between neighbours located at 150 nm.

### 3.13 SEM / EDS

During the inelastic scattering of the EB x-ray are produced as a continuous process or as an inner-shell ionization process. The continuous process is related to the interaction between the electrons from the EB and Coulomb field created by the atom nucleus. This interaction produces energy losses resulting in the emission of photons and electromagnetic energy. The incident beam may excite an electron in an inner shell, ejecting it from the shell and creating an electron hole. An electron from an outer, higher-energy shell then fills the hole, and the difference in energy between the higher-energy shell and the lower energy shell may be released in the form of an X-ray. The number and energy of the X-rays emitted from a specimen can be measured by an energy-dispersive spectrometer.

### Chapter 3

As the energies of the X-rays are characteristic of the difference in energy between the two shells and of the atomic structure of the emitting element, EDS allows the elemental composition of the specimen to be measured. These characteristic x-ray emissions can be detected using intrinsic Si semiconductors doped with Li. The signal produced by the detector can be expressed as spectrum or maps, according to the intensity of the signal and the element evaluated. To improve the quality of the measurements higher voltages are usually used for the EB and long count times [112].

In this project EDS analysis was conducted simultaneously with EBSD analysis using the same SEM operational parameters. Compositional maps for Carbon, Iron, Chromium, Manganese, Aluminium and Phosphorus were produced.



## Chapter 4 General characterisation after HPT tests

The results presented in this chapter were obtained after conducting HPT tests on the annealed AISI 52100. The main part of the information was obtained through metallography, MA and LOM characterisation, and consists of a large quantity of micrographs taken from the surfaces defined in sections 3.6 and 3.9. The results obtained through other activities linked to metallography and LOM such as IPP processing, roughness and hardness measurements are also included in this chapter.

### 4.1 Samples condition after conducting HPT tests

Macroscopic examination of the samples from stage 2 revealed that slippage has occurred during HPT testing. By inspecting the lines previously drawn along sample diameters, the amount of slippage in degrees after 1 turn was measured. The percentage slippage was also calculated in relation to the 360-degree corresponding to one turn of the machine. It was not possible to assess the slippage after more than one turn as the drawn lines were then no longer visible after HPT testing. Table 4-1 gives the slippage measured after HPT for 1 turn. Five measurements were taken for each test configuration using samples from stages 1, 2 and 3 (See section 3.3).

Table 4-1. Slippage in HPT tests after 1 turn. The values correspond to averages from 5 samples

HPT parameters	Slippage angle (°)	Absolute error (°)	Standard Deviation°	% Slippage
1 GPa 1 T	80.2	2.2	2.9	22.3
3 GPa 1 T	52.6	1.9	2.3	14.6
6 GPa 1 T	29.6	1.7	2.1	4.05

The top and bottom surfaces of the discs had different appearances: concentric circle tracks alternated by smooth and shiny regions appeared on the top surface, whilst a pattern similar to an *orange peel* appeared on the bottom surface (area enclosed by orange dots in figure 4-1). When higher pressures were applied, this orange peel pattern also partially appeared on the top surface; applying 6 GPa, both top and bottom surfaces exhibited this orange peel pattern over all their surface (figure 4-1).

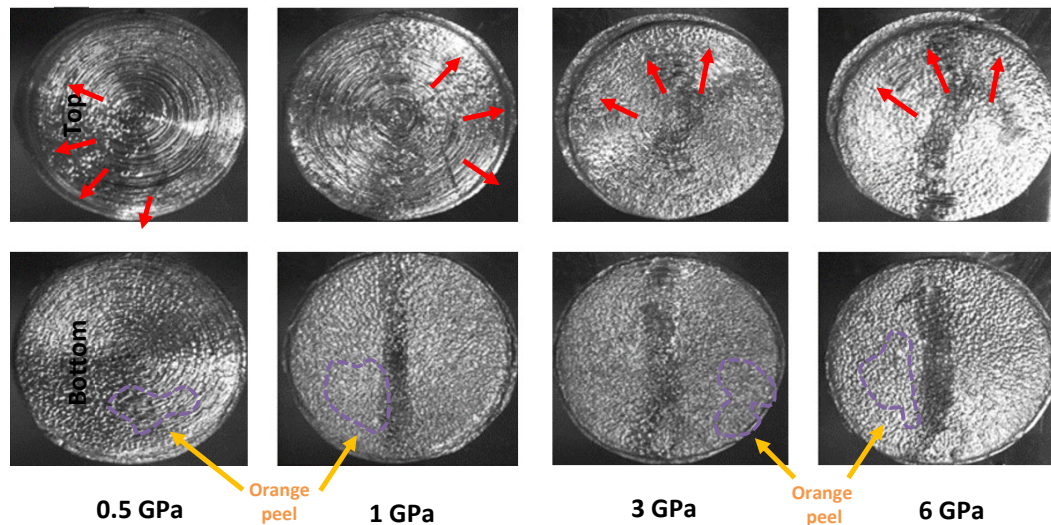


Figure 4-1. Top and bottom surface of annealed AISI 52100 samples after conducting HPT tests using 0.5, 1 GPa, 3 GPa, 6 GPa and 1 turn. Samples after tests with flash removed. Top surfaces exhibit circular grooves (except for those processed using 6 GPa) and the effects of misalignment (red arrows), whilst bottom surfaces showed a roughness pattern similar to an orange peel (enclosed with orange dotted lines).

Evidence of misalignment was found on all samples after HPT as two different circular contours were visible on their top side (red arrows in figure 4-1); the displacement of the centres of these circular contours along a common diameter indicated a slight misalignment between the anvils, the average of all the misalignment observed in the samples of figure 4-1 was 0.25 mm. Moreover, a thin extruded ribbon or flash was observed to form concentrically around the middle periphery of the disc for all samples processed, the size of this flash increasing with higher pressure and number of turns. The flash was removed by grinding using the bottom surface as a circular reference. All samples remained adhered to the bottom anvil once the HPT tests ended; some metal debris was also collected from their top at the end of the tests.

A first LOM exploration at low magnification revealed how the circular tracks referred to in figure 4-1, appeared as discontinuous grooves alternated by shiny and smooth patches that looked white under LOM after to be etched (figure 4-2). These white patches covered the main part of the top surface as a succession of concentric rings, except for a small circular area at the centre of the samples.

All samples from stage 2, after removing by grinding and polishing 40  $\mu\text{m}$  of material from their top surfaces, showed a similar white patch configuration, except for those processed under 6 GPa. Their extent and shape seemed to be related to the pressure applied during the HPT tests. For pressures of 0.5 to 1 GPa, they looked slim and elongated and affected large areas, whilst at 3 GPa their

incidence was less despite their bigger size. Figure 4-2 also shows the *orange peel* pattern observed previously which affected the bottom side of all samples processed by HPT tests. On samples processed using 6 GPa, this pattern covered the top surface as well, replacing the grooves and white patches. As these white patches are similar to WEAs observed in failed rolling bearings, they will be referred to as Top surface White Etching Areas or TWEAs. More details on the size and morphology of these changes are shown in section 4.2.1

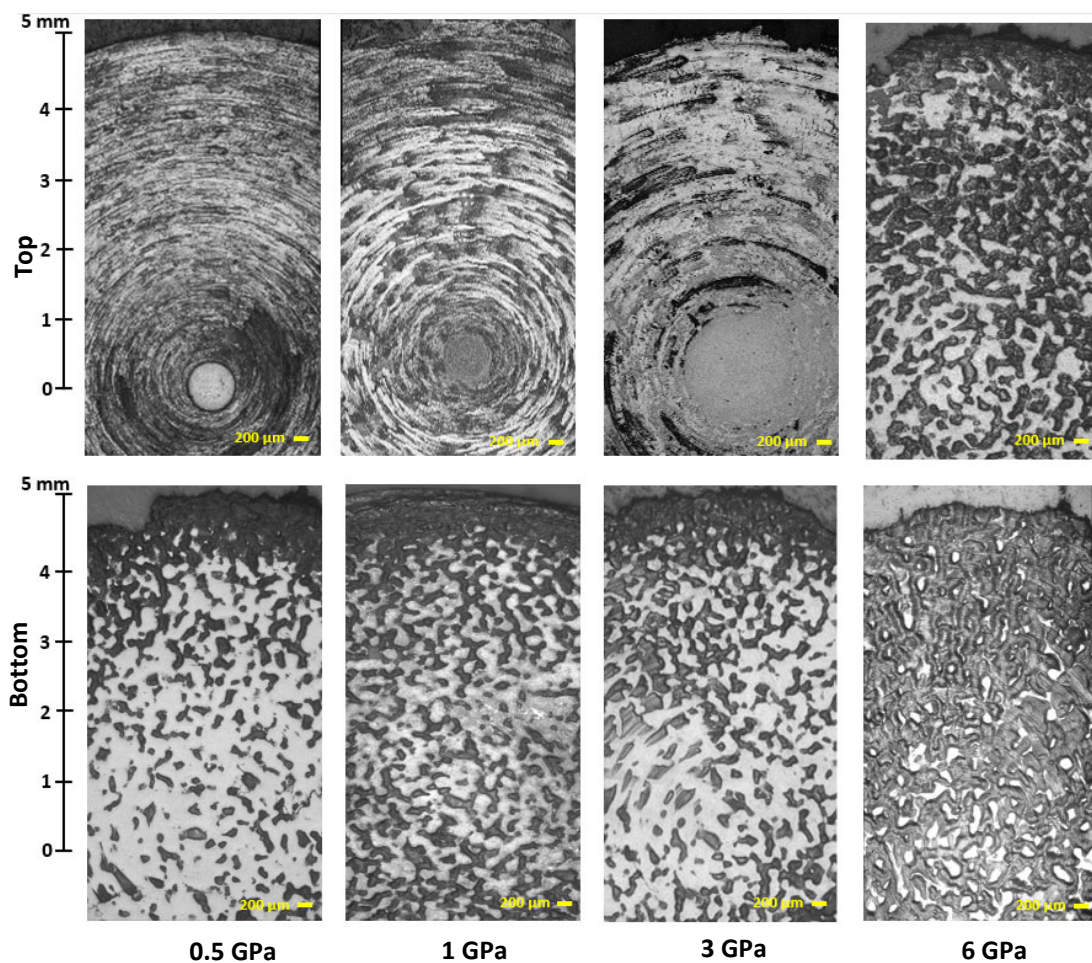


Figure 4-2. Montages of top and bottom surface of annealed AISI 52100 samples after conducting HPT tests using 0.5, 1 GPa, 3 GPa, 6 GPa and 1 turn. Details of the same sample after polishing (to a depth of 40  $\mu\text{m}$ ) and etching. The top surface exhibited grooves alternated by white patches. The bottom surface showed var amounts of *orange peel* pattern as a function of the pressure applied. The images were taken from samples of stage 2. LOM, 2% Nital.



## 4.2 LOM characterisation of top and bottom surfaces

### 4.2.1 Top surfaces

Figure 4-3 shows detailed LOM images taken at 40  $\mu\text{m}$  depth from the top surface of a samples processed using 1 GPa 1 turn. TWEAs appeared elongated and in irregular patches that seemed to follow the circular tracks on the samples. In some cases, TWEAs alternated with grooves, in other cases they overlapped them.

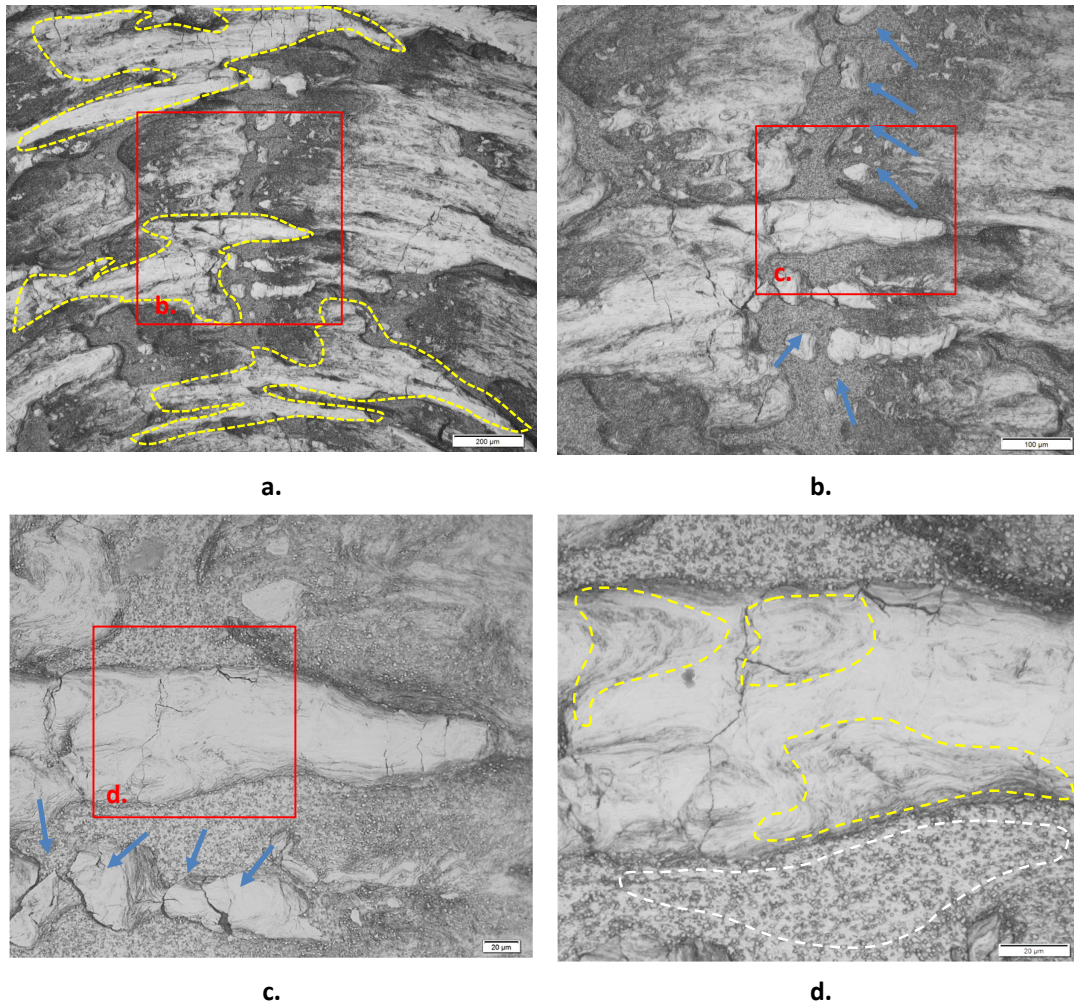


Figure 4-3. Details of WES structure on the top surface of a sample processed using 1 GPa 1 turn. The red rectangles show the regions detailed in the next image. a) Overlapping TWEAs (enclosed by yellow dotted line). b) Isolated TWEAs (indicated by blue arrows) c) Cracks in TWEAs and across them (blue arrows). d) Fibre / layered structures inside the TWEAs (regions enclosed by yellow dotted line), and a region of the ferritic matrix (enclosed by white dotted line). LOM Nital 2%.

At a radial distance of 3.5 mm, regions of higher plastic deformation were visible where TWEAs overlapped each other more, producing bigger TWEAs (figure 4-3 a) area enclosed by yellow dotted lines). In other places, small isolated TWEAs appeared, but their orientation and shape suggested that they were part of larger TWEAs located at the same radial position. (figure 4-3 b) blue arrows). Both linked and isolated TWEAs seem to be related to the high plastic deformation imposed by the rotation of the top surface of the disc against the upper anvil. Small cracks also were observed, especially close to the TWEA borders (figure 4-3 c) blue arrows). A fibre / layered structure was visible inside some TWEAs, the fibres forming a swirl or vortex pattern in some regions (figure 4-3 d). Area enclosed by yellow dotted lines). The matrix that surrounded the TWEAs and grooves appeared as a continuous ferritic phase with many small spheroidal carbides (approximately 2  $\mu\text{m}$  in diameter) that seemed to be distributed relatively uniformly at first sight. No carbides were observed inside the TWEAs by LOM (white dotted line in figure 4-3d)).

Significant changes were observed at the surfaces after applying higher strains. In a sample processed by 1 GPa 3 turns TWEAs appeared more deformed and elongated in a circular direction as observed in (figure 4-4 a). areas enclosed by yellow dotted lines). Large grooves were apparent affecting significant areas of both TWEAs and the ferritic matrix (figure 4-4 b). blue arrows). Lots of small circular grooves also appeared along all the surfaces analysed (figure 4-4 a), b) and c)). These grooves could be associated with abrasive wear produced by sliding contact between the anvil and the sample.

TWEAs contained brittle cracks oriented in a radial sense and perpendicular to the apparent sliding direction. Cracks were easily identified due to their preferential location at the leading edge of the TWEAs, where several overlapped white layers seemed to be present (blue arrows in figure 4-4 c).). The overlapped layers could originate from the sliding contact itself that dragged the layers during the HPT tests. The material loosening associated with the crack networks suggested that some TWEAs detach during the sliding contact with the anvil due to delamination (area enclosed by yellow dotted lines in figure 4.4 c).). The overlapped layers appear near to the radial cracks (enclosed by yellow lines and indicated by arrows in figure 4.4 d).), suggesting high plastic deformation and strong adhesive contact in these regions. In some regions the ferritic matrix appeared exposed and had not suffered any significant alterations to its annealed condition.

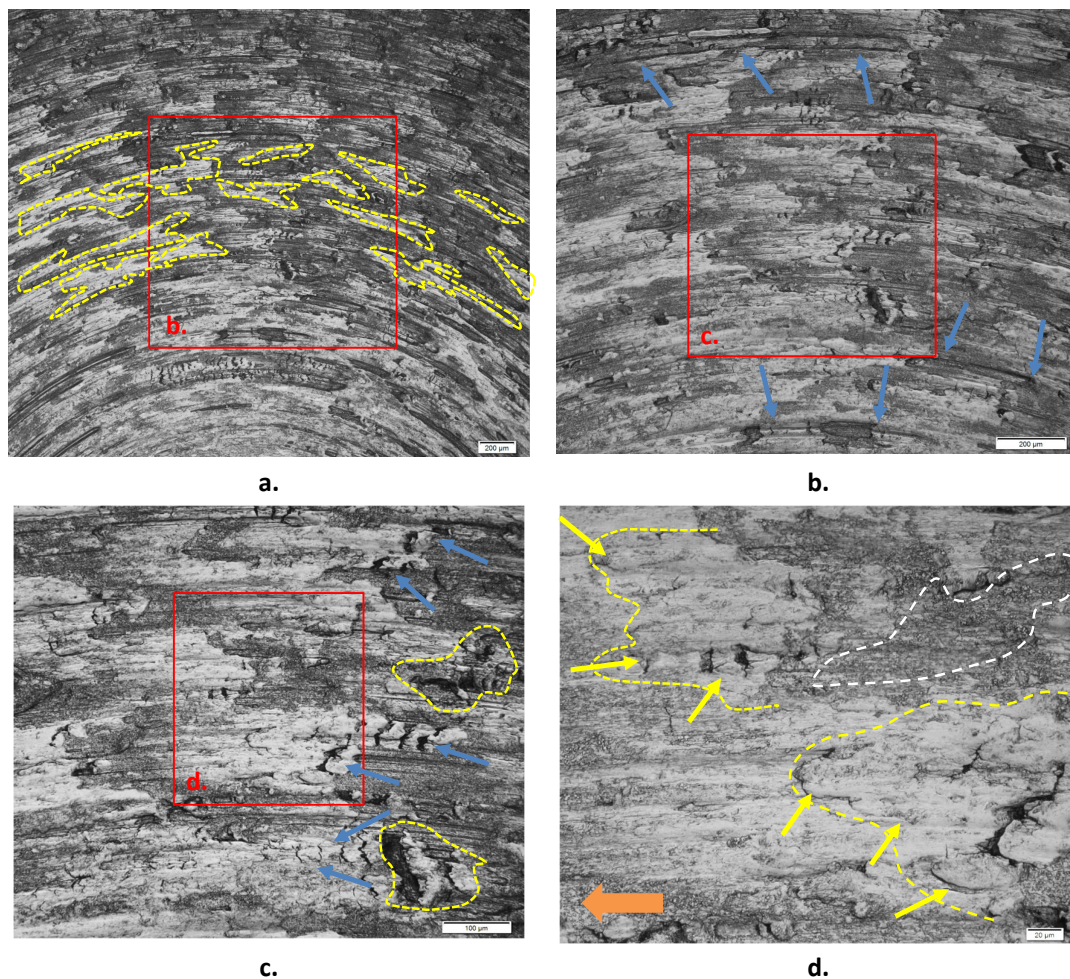


Figure 4-4. Details of WES structure on the top surface of a sample processed using 1 GPa 3 turns. The red rectangles show the regions detailed in the next image. a) Elongated TWEAs due to high plastic deformation (areas enclosed by yellow dots). b) Typical abrasion grooves (indicated by blue arrows) c) Transverse brittle cracks in TWEAs (blue arrows) and loose material (enclosed by yellow dotted lines). d) Evidence of extensive plastic deformation due to sliding contact (areas enclosed by yellow dots) and the ferritic matrix (enclosed by white dotted line). The orange arrow indicates the sliding direction. LOM Nital 2%.

The pressure imposed in the HPT test also affected the top surface of the samples during HPT tests. Figure 4-5 shows details of the top surface after being processed by 3 GPa and 1 turn. The TWEAs present had similar features to those formed under 1 GPa observed in figures 4-3 and 1-4, such as elongated shapes produced by high plastic deformation, radial brittle cracks and grooves. The grooves in the case of 3 GPa appeared larger, affecting significant areas (Blue arrows in figure 4-5 a)), it seems they were produced by an abrasive process. As was observed before, damage due to adhesion also appeared combined with that due to abrasion, although at 3 GPa there appears to be now more detachment of loosened material. (Yellow dotted lines in figure 4-5 b)).



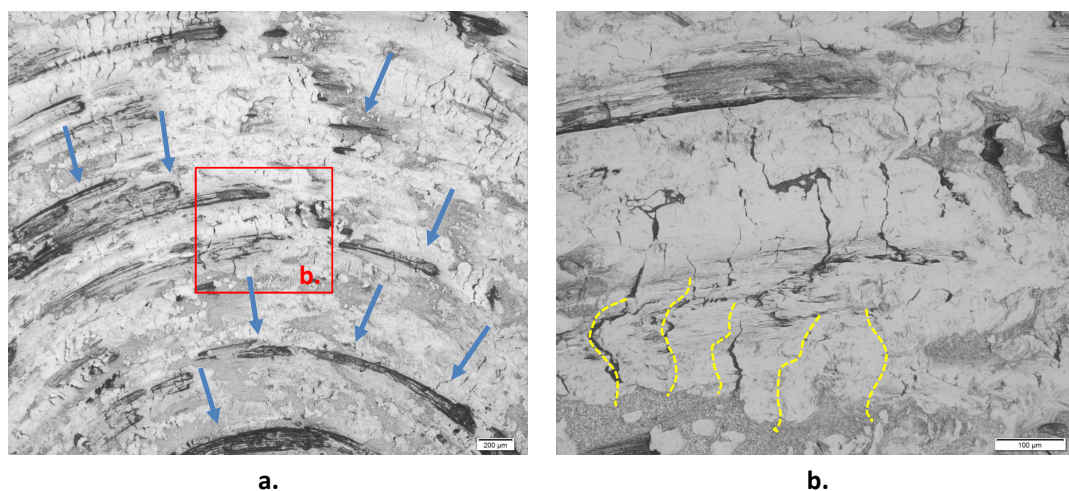


Figure 4-5. Details of WES structure on the top surface of a sample processed using 3 GPa 1 turn. The red rectangle shows the region detailed in the next image. a) Large grooves affecting the top surface. b) Radial brittle cracks and evidence of delamination are visible inside the TWEAs (Yellow dotted lines). LOM Nital 2%.

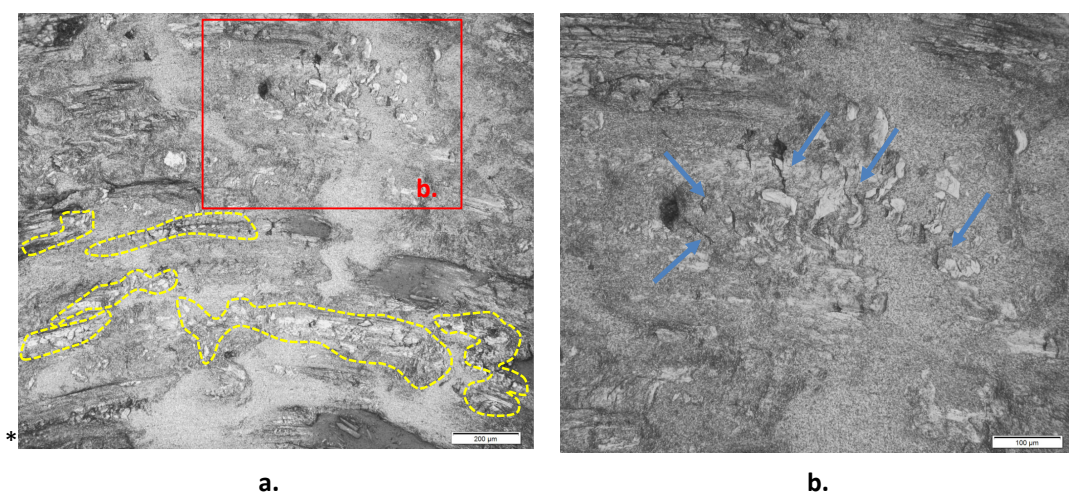


Figure 4-6. Details of WES structure on the top surface of a sample processed using 3 GPa 3 turns. The red rectangle shows the regions detailed in the next image. a) High plastic deformation and clusters of small TWEAs oriented in the sliding direction (enclosed by yellow dotted lines). b) Cracks affecting TWEAs and the ferritic matrix. LOM Nital 2%.

A dramatic reduction in the areas affected by TWEAs was noted on a more highly deformed surface where grooves were not easily visible in a sample processed through 3 GPa and 3 turns. Abrasion and adhesion combined appear to have removed the majority of the TWEAs, leaving just a few TWEA clusters oriented in the sliding direction (areas enclosed by yellow dotted lines, figure 4.6 a)). The high plastic deformation and wear not only had removed the grooves but also the cracks visible in samples produced with fewer turns, although, some of them still prevailed (Blue arrows in figure 4.6 b)).

## Chapter 4

The abrasion and adhesion eventually produced wear debris that was trapped between the contacting surfaces. Some of this debris was collected with tape after finishing a HPT test conducted using 3 GPa 3 turns. Figure 4-7 shows some of the debris which exhibited typical sliding wear features, such as high plastic deformation, delamination and grooves produced by abrasion.

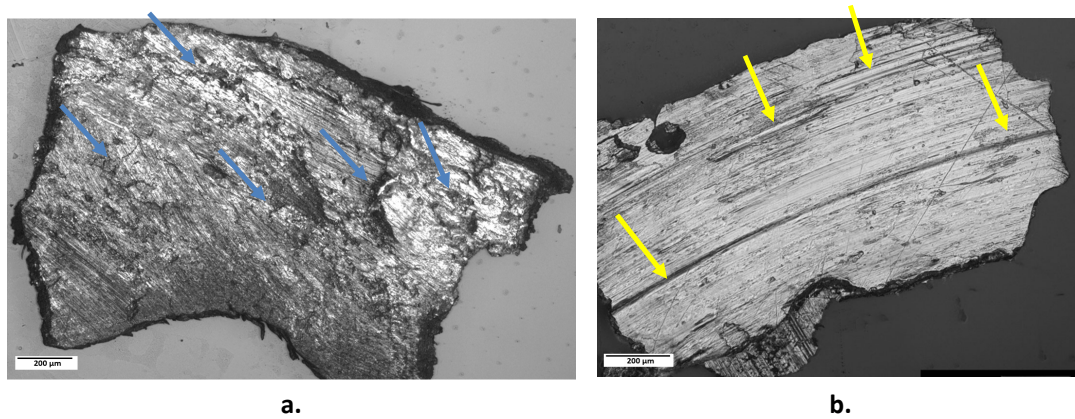


Figure 4-7. Debris produced during a HPT test (3 GPa 3 turns). a) Evidence of delamination (blue arrows) and b) grooves (yellow arrows). LOM Nital 2%.

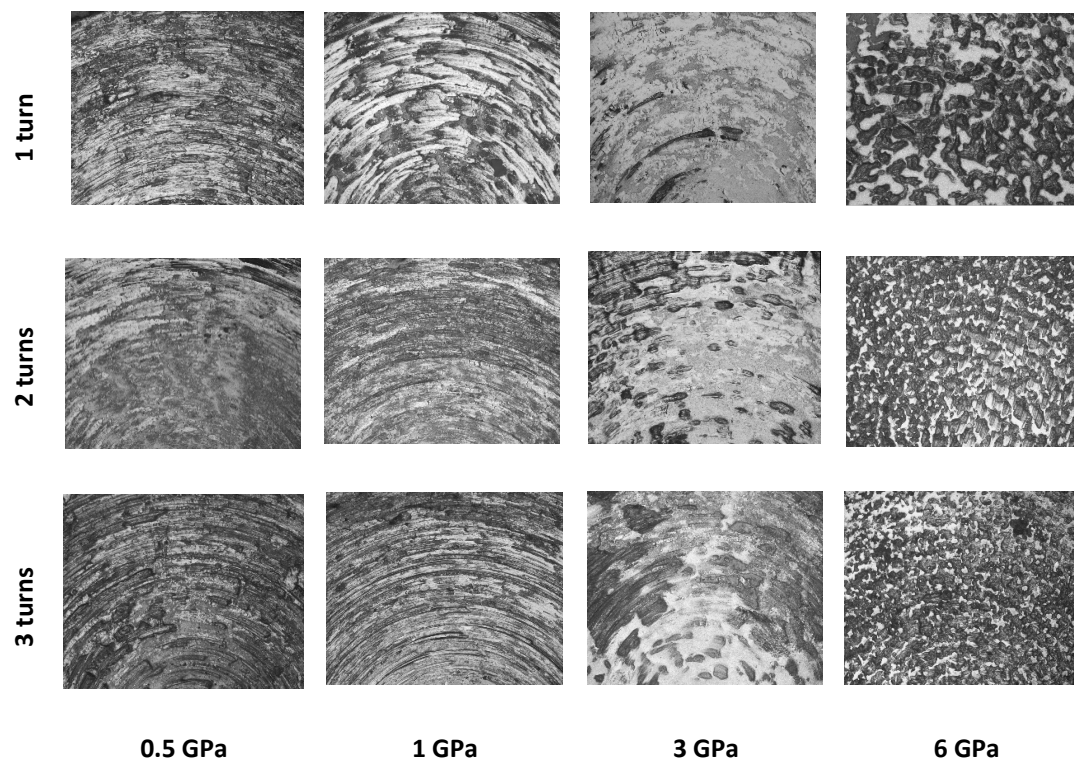











Figure 4-8. Examples of images used to calculate the % TWEAs shown in table 1.3. All samples processed correspond to Stage 2. Nital 2%.



Figures 4-8 shows that the TWEAs distribution changed with pressure and number of turns applied during HPT tests. This variation was quantified by calculating the % TWEA in representative areas using the IPP Image J. The method used (section 3.8) required eight images to be taken over the HPT samples from Stage 2; examples of these images are shown in figure 4-8 as well.

The results of these calculations are summarised in table 4-2 by black / white masks generated by IPP Image J. The highest % TWEA was registered in samples processed using 0.5 GPa 1 turn ( $75 \pm 1.2 \%$ ) and reduced with the number of turns to a very low value (around 6%). The amount of TWEAs varied more with number of turns than with pressure, but in all cases, a significant reduction was reported with increasing turns/pressure.

Table 4-2. % TWEA on the top surface of samples after HPT tests under different conditions. Images correspond to the micrographs shown in Figure 1.8. TWEAs are represented as black in each case.

	0.5 GPa	1 GPa	3 GPa	6 GPa
1 turn	 $75 \pm 1.2 \%$	 $64 \pm 1.3 \%$	 $59 \pm 1.4 \%$	$0 \%$
2 turns	 $53 \pm 1.3 \%$	 $28 \pm 2.4 \%$	 $19 \pm 2.6 \%$	$0 \%$
3 turns	 $48 \pm 1.7 \%$	 $22 \pm 2.7 \%$	 $6 \pm 2.6 \%$	$0 \%$

#### 4.2.2 Bottom surfaces

The bottom surfaces looked completely different from the top surfaces of the samples. No evidence of adhesion or abrasive wear such as grooves, delamination or brittle cracks was visible on their surfaces. However, all lower surfaces had been affected by high compressive plastic deformation which had produced impressions of the asperities present on the lower anvil in their surface. These embedded asperities extruded the soft material from the sample between the anvil asperities and so created the orange peel pattern. Figure 4-9 shows details of the orange peel pattern on the bottom surface of a sample processed by 6 GPa 1 turn. Although compressive plastic deformation is predominant on all the surfaces, small circular grooves were also visible, indicating sliding contact.

#### 4.2.3 Top surfaces at 6 GPa 1 turn

With increasing pressure, the grooves and TWEAs on the top surface started to be replaced by a pattern similar to that observed on the bottom surfaces. The orange peel pattern on the top surfaces seems to have the same origin as that responsible for its formation on the bottom side: The higher compressive pressure and thus friction progressively reduced sliding between the top disc surface and the upper anvil. Figure 4-10 shows details of the top surface of the same sample shown in figure 4-9. The top surface was also covered by the orange peel pattern, indicating that it was now stuck to the top anvil in the same way as it was stuck to the bottom anvil.

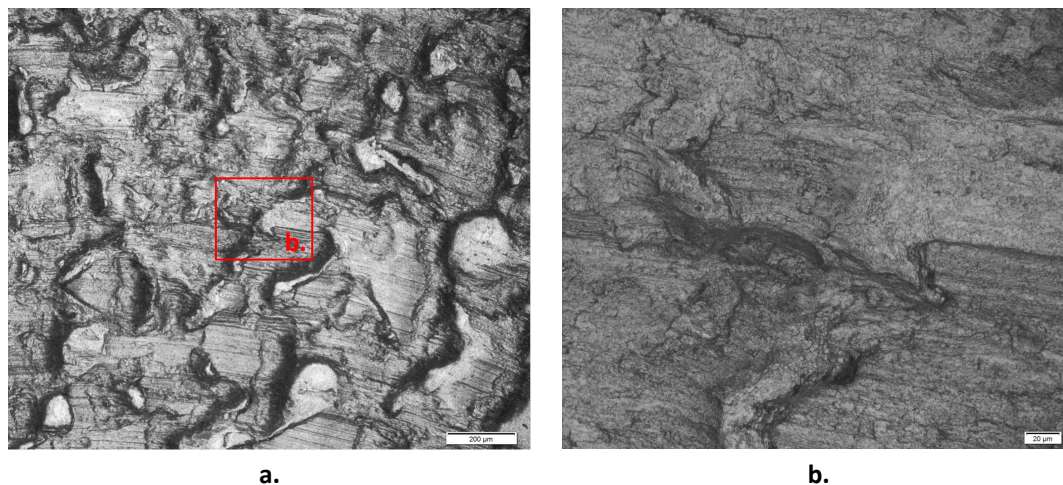


Figure 4-9. Details of the bottom surface of a sample processed by 6 GPa 1 turn. a) The red rectangle shows the region detailed in the next image. b) Details of the deformed surface

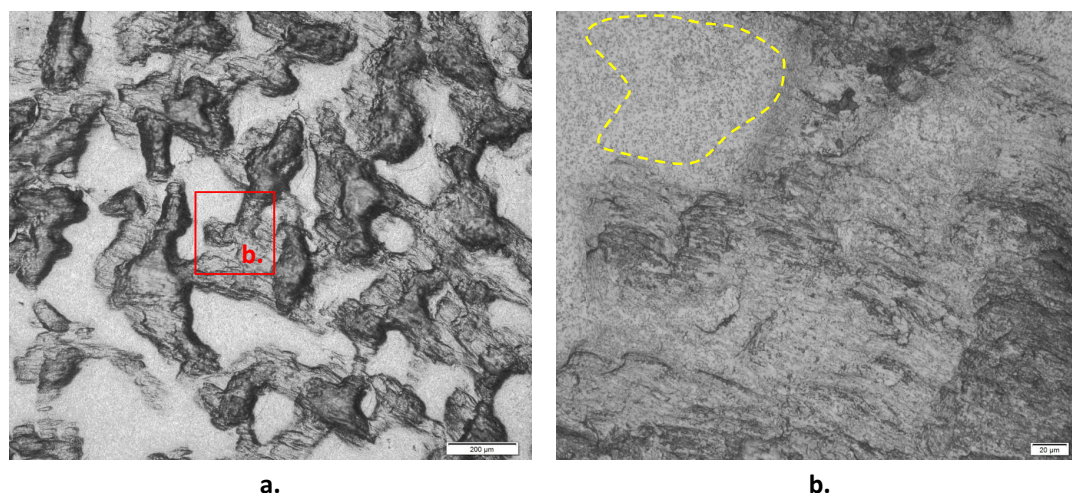


Figure 4-10. Details of a top surface of a sample processed by 6 GPa 1 turn. The red rectangle shows the regions detailed in the next image. a) Despite looking white, the patches on the image are asperities ground and polished during sample preparation. b) Small spheroidal carbides in the ferritic structure (enclosed by yellow dotted lines).

### 4.3 Compression tests on samples as a means of measuring the surface finish of the anvils

Samples from stage 4 were pressed under 1, 3 and 6 GPa using the HPT machine. The purpose of these experiments was to measure the roughness of the anvils indirectly by generating a copy of their surface finish on the samples. The surface finish of the disc surfaces so produced was measured using a contact profilometer. Images of the pressed samples are shown in figure 4-11.

The orange peel pattern was clearly visible on the bottom surface of the sample processed under 6 GPa but was only partially reproduced on the upper disc surface. The roughness measurements were made on random diameters and the results are given in table 4-3. The roughness of an unprocessed sample was also measured so as to compare it with the pressed sample. The profiles given in table 4-4 were used to calculate the roughness parameters  $R_a$ ,  $R_q$ ,  $R_y$  reported in table 4-3. The profiles exhibit higher asperity peaks and troughs on the discs in contact with the lower anvil than on the top surface in contact with the upper anvil. This indicates that the lower anvil has a higher roughness than the upper anvil. This is confirmed by the roughness parameters in table 1-3, where all values reported were higher on the bottom surface than on the top surface. Figure 4-12 presents a 3D reconstruction of the roughness along a diametral band in a sample pressed under 1 GPa. Although both, top and bottom surfaces have impressions of the asperities on the anvils, the bottom surface showed much more clearly the orange pattern described previously. Moreover, the

top surface registered a large flat area with no significant impressions, which suggests minimum contact between samples and anvil over this region.

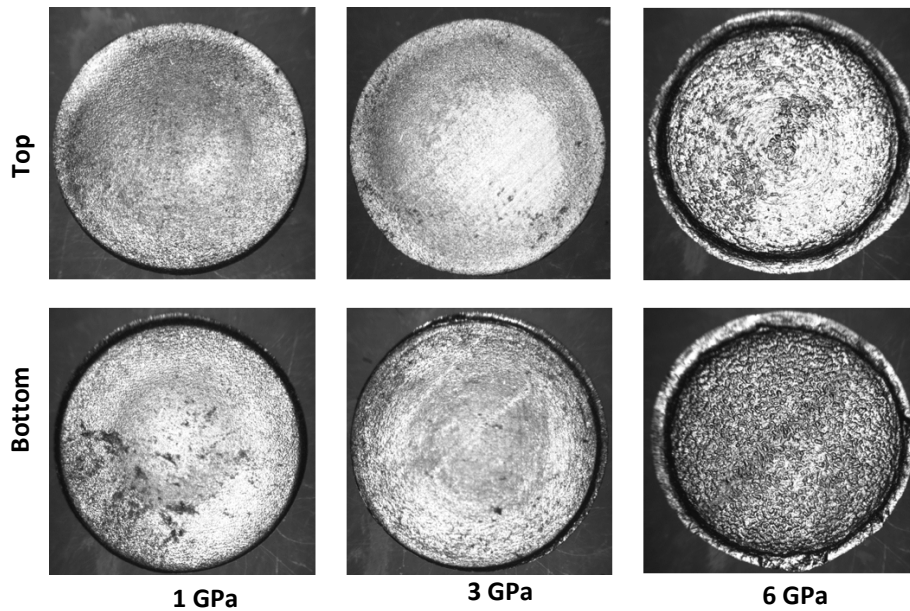
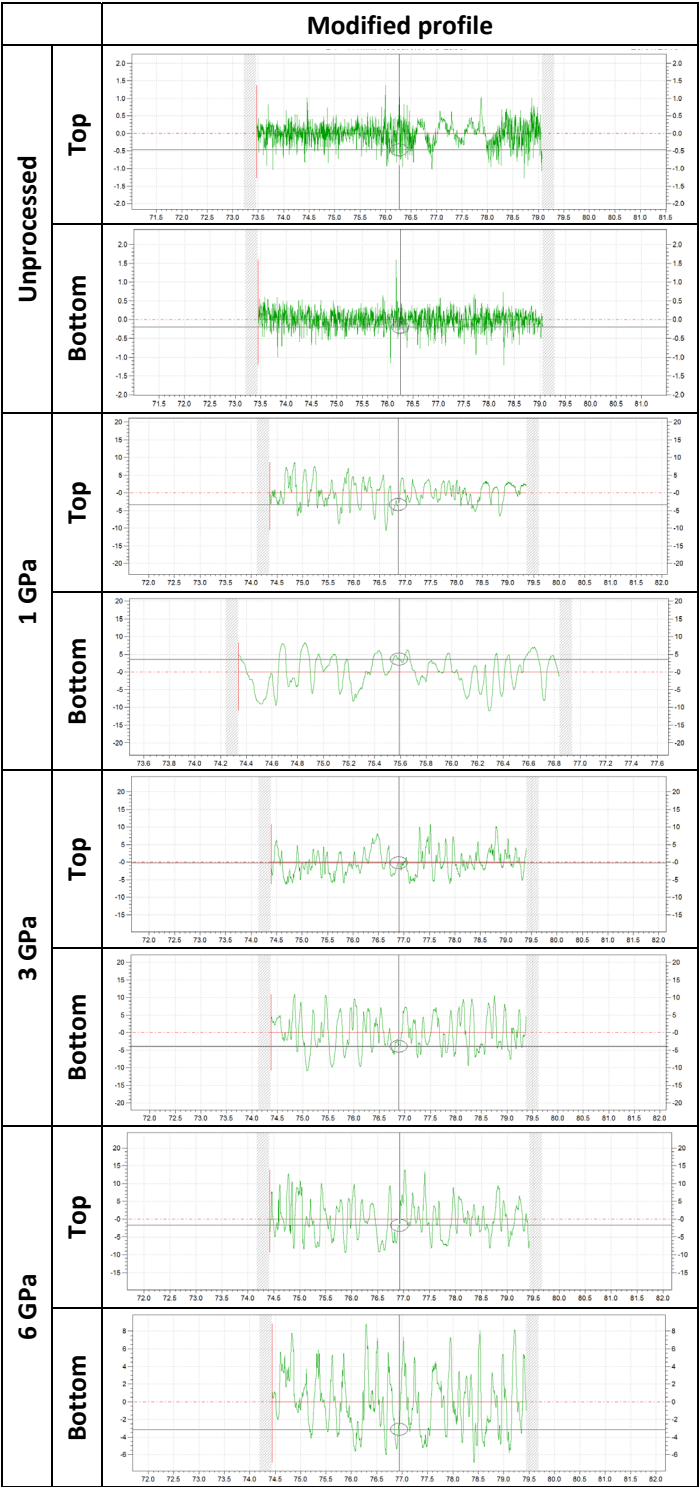


Figure 4-11. Samples after pressing by the HPT machine. a). 1 GPa, b). 3 GPa, c). 6 GPa,. The surface patterns reproduced the surface finish of the machine anvils.

Table 4-3. Roughness measurements taken from samples discs after being pressed in the HPT test machine. Values are the average of five measurements ( $R_a \pm 0.5 \mu\text{m}$ ,  $R_q \pm 0.2 \mu\text{m}$ ,  $R_z \pm 2.1 \mu\text{m}$ )

Parameter ( $\mu\text{m}$ )	Unprocessed		1 GPa		3 GPa		6 GPa	
	Top surface	Bottom surface	Top surface	Bottom surface	Top surface	Bottom surface	Top surface	Bottom surface
Ra	0.18	0.16	2.62	3.64	2.69	4.14	2.6	3.95
Rq	0.25	0.22	3.28	4.39	3.38	4.88	3.29	4.87
Rz	1.73	1.62	15.04	19.14	15.6	20.86	14.97	22.14

Table 4-4. Profiles taken from samples after being compressed in the HPT machine



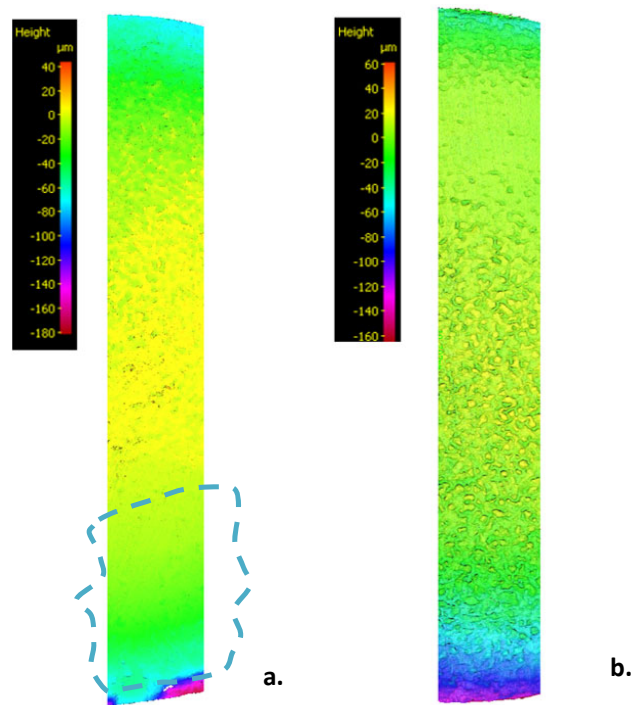


Figure 4-12. 3D reconstruction of a). top and b). bottom surface along a diameter of a samples disc pressed under 1 GPa. The roughness of the top surface is less than that of the bottom surface. Note the big flat area on the top surface, enclosed by the blue dotted line and the *orange peel* pattern on the bottom surface.

## 4.4 Subsurface characterisation

### 4.4.1 Circumferential sections

The circumferential sections generated every 40  $\mu\text{m}$  by polishing from the bottom side reported several white structures inside the samples (samples used were from stage 3). To distinguish them from the white patches located on the top surface (called TWEAs) these new structures were called SWEAs (Subsurface White Etching Areas). SWEAs appeared preferentially between 240– 360  $\mu\text{m}$  from the bottom side, the majority being located at a radial distance of between 3.5 and 5 mm. No SWEAs were found in regions located at a radial distance of less than 3 mm. In the sections examined from samples processed using 3 GPa, a significant increase in the amount of SWEAs was observed between 1 and 2 turns, but then reduced somewhat after applying 3 turns. Relatively few SWEAs were found in samples processed using 6 GPa and 1 turn.

Two SWEAs configurations were identified, those with ill-defined borders and those with more solid areas. The SWEAs with ill-defined borders had a swirled morphology and resembled spiral clouds or vortices without clear boundaries, hence they are referred to here as “cloud SWEAs”. Similarly,



to the TWEAs discussed earlier, these cloud SWEAs usually appeared overlapped by the ferritic matrix (figure 4-13). Their size also varied considerably with radial position and tended to be bigger close to the edge of the samples. Solid areas were characterised by their more well-defined borders; their size also increased with radial distance, from isolated spots located at a radial distance of 4 mm to large regions close to or at the edge of the samples (figure 4-14). In general, cloud SWEAs were not located close to the sample edges, whilst the main part of solid SWEAs was found there.

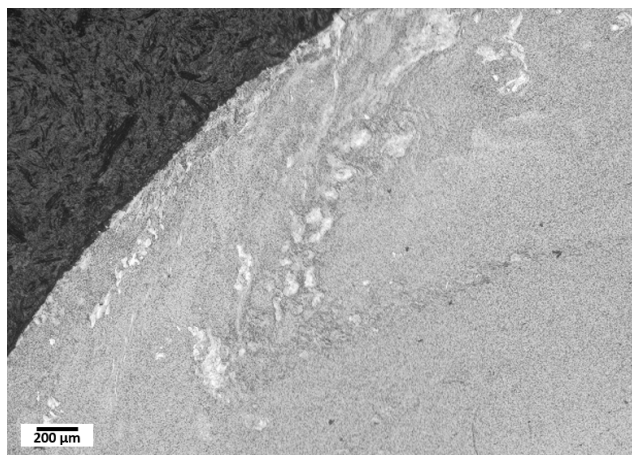


Figure 4-13. Large cloud SWEA system located between a radial distance of 4.2 mm and the edge of a samples processed using 3 GPa 2 turns. LOM Nital 2%.

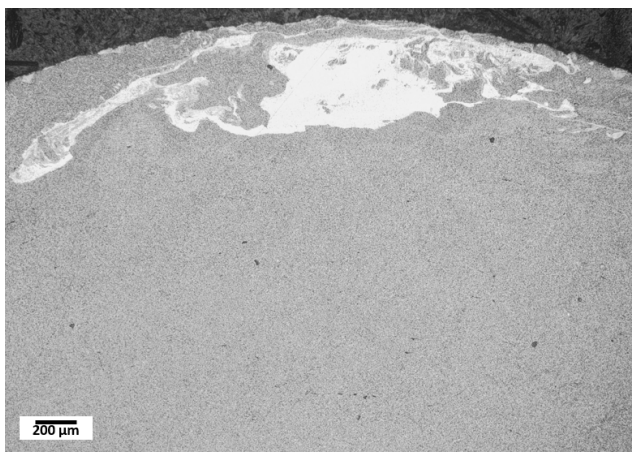


Figure 4-14. Large solid SWEA system located between a radial distance of 4.6 mm and the edge of a samples processed using 3 GPa 2 turns. LOM Nital 2%.

In other cases, cloud and solid SWEAs appeared joined in complex arrays that extended across large areas until the edge of the samples was reached. Some parts of the clouds appeared as solid, especially those located in the centre of the swirl pattern or close to the edge of the samples. These systems often appeared linked to crack networks which extended for significant distances. Details

of this kind of system are shown in figures 4-15 and 4-16. For these cases is not possible to establish a clear difference between clouds and solid structures.

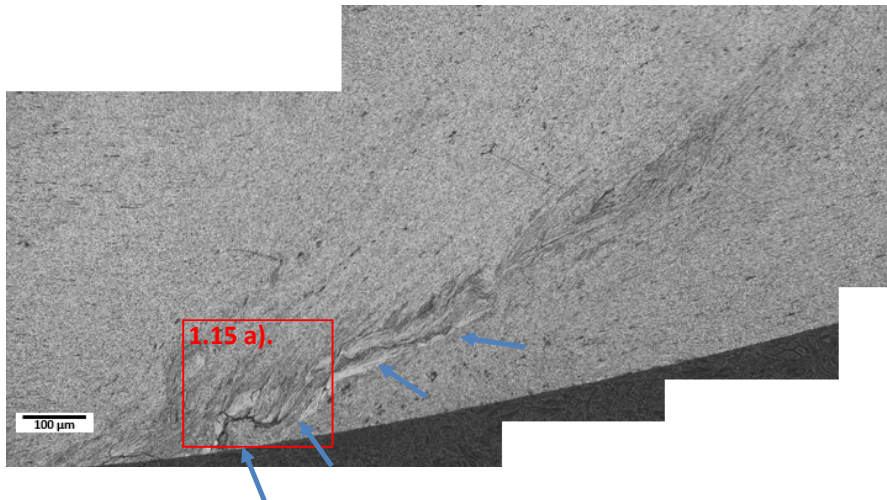


Figure 4-15. Large system of cloud and solid SWEAs linked to a crack network (blue arrows). The red rectangle shows the region detailed in figure 4-16 a). LOM 2% Nital

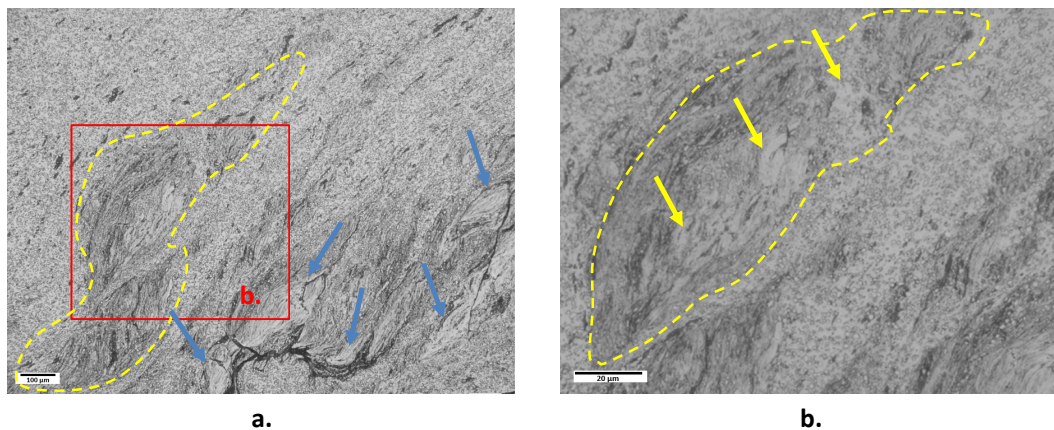
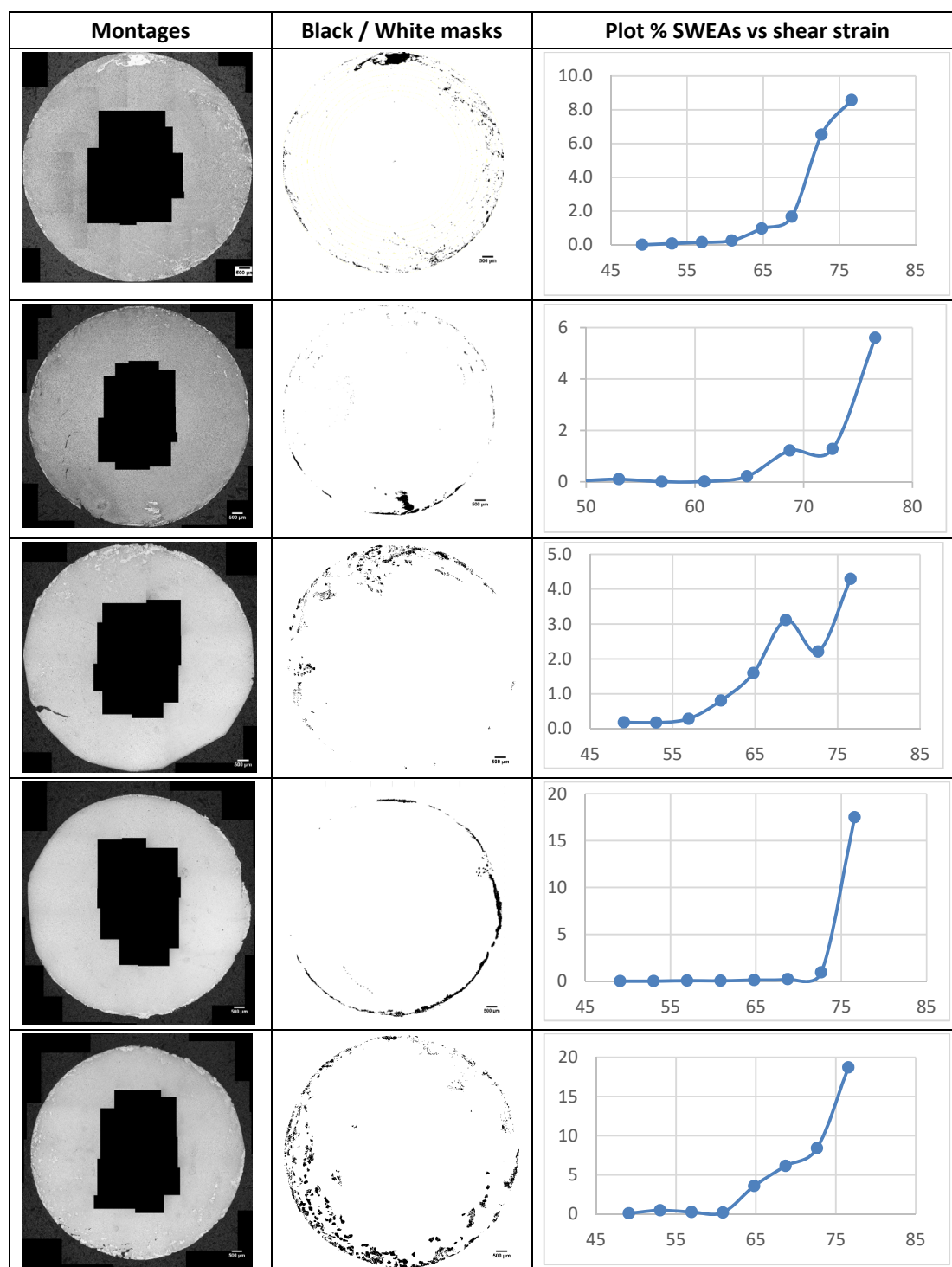


Figure 4-16. Details of large cloud and solid SWEAs. The red rectangle shows the region detailed in the next image. a.) Cloud SWEAs (enclosed by yellow dotted line), and cracks (blue arrows). b.) Cloud SWEAs (enclosed by yellow dotted line) with some solid SWEAs inside (indicated by yellow arrows). LOM 2% Nital.



Table 4-5. % SWEAs as a function of strain at the midpoint of the concentric rings defined on the samples (section 3.8) of five samples processed using 3 GPa 2 turns.



To evaluate the SWEA distribution in the samples, IPP Image J was used to calculate the % WEA with respect to the total samples area. Table 4-5 shows montages of several images taken from around the periphery of the disc and the masks generated by using the *Threshold* tool from *Image J*. The % SWEAs as a function of shear strain at the mid points of the concentric rings used to define

the measurement areas is presented in table 4-5. All plots show a similar behaviour suggesting that a relationship between % SWEAs and shear strain exists: SWEAs appeared with a shear strain of 55-66 and the majority of SWEAs was located close to the edge of the samples where the shear strain was greater than 75. No SWEAs were found at shear strains lower than 40 i.e. SWEAs were not present close to the sample centre. However, these results contain significant scatter, indicating that more factors than just shear strain are involved in SWEAs formation and distribution.

#### 4.4.2 Axial sections

A detailed microstructural characterisation by LOM on the axial sections revealed several changes inside the samples after conducting HPT tests. These changes included evidence of plastic deformation, carbide redistribution and the presence of TWEAs and SWEAs. These microstructural changes were found mainly in two regions, one close to the top surface (corresponding to the TWEAs) and another located at a depth of 240-360  $\mu\text{m}$  from the bottom side. TWEAs were located in all samples except those processed by 6 GPa. All TWEAs were located at depths of less than 100  $\mu\text{m}$  from the top surface and appeared as isolated forms with irregular sizes and shapes.

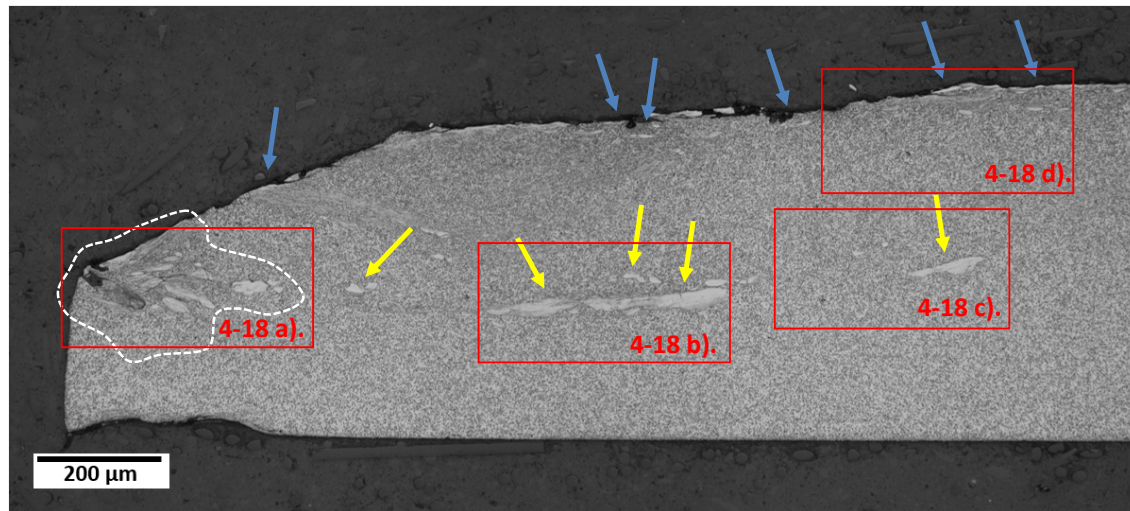


Figure 4-17. TWEAs (indicated by blue arrows) and SWEAs inside the sample (indicated by yellow arrows) in a cross section of a sample processed by 3 GPa 2 turns. The red rectangles show the regions detailed in figure 4-18. Some SWEAs also appeared at the edge of the sample in another well-defined WES group (enclosed by white dotted line) LOM 2% Nitral.

SWEAs appeared in two well defined groups, one located far from any border of the sample and another located near the sample edge. Only a few samples registered SWEAs in their cross sections, due to the random nature of the sectioning direction and the restricted parameters used to reproduce them (3 GPa 1, 2, 3 turns and 6 GPa, 1 turn). Figure 4-17 shows a cross section of a sample processed using 3 GPa and 2 turns where both TWEAs and SWEAs were visible.

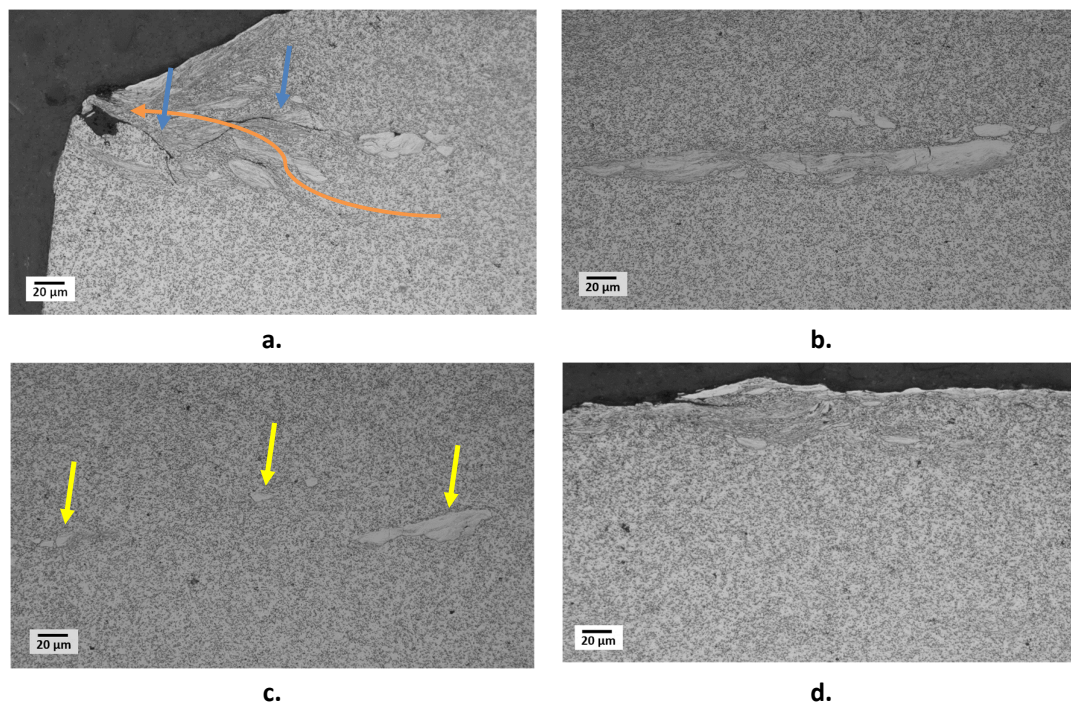


Figure 4-18. Details of TWEAs and SWEAs in a cross section of a sample processed by 3 GPa 2 turns. a) SWEAs and cracks (indicated by blue arrows) at the edge of the sample. b) Elongated SWEA system located far from any border of the sample. c) Small and isolated SWEAs located at a radial distance of approximately 4 mm and at a depth of 200  $\mu\text{m}$  from the top surface (Yellow arrows). d) TWEAs located at a radial distance of approximately 4 mm. LOM 2% Nital

Lots of the SWEAs located at the edge of the samples consisted of a fibre/ layered structure that seemed to flow towards the edge (indicated by the orange arrow in figure 4-17 a)), cracks usually appeared associated with them (blue arrows figure 4-17 a)). These SWEAs could be formed by solid and cloud SWEAs combined. Other SWEAs appeared as groups (Figure 4-17 b)) or completely isolated. Due to their location, these SWEAs could correspond to the cloud SWEAs observed in the circumferential sections. SWEAs also showed a fibre / layered structure elongated in a particular direction, in this case parallel to the top surface. Finally, TWEAs observed at the top surface consist of an arrangement of several small white structures, some of these solid, other more ill-defined. They were not connected together, but the deformed areas close to them facilitated their

identification. Some fibre / layered structures were also visible between the solid TWEAs. All TWEAs and SWEAs observed in the cross sections analysed exhibited similar features (i.e. a mixture of solid and ill-defined structures, fibre / layered structures, preferential orientations, cracks) irrespective of pressure and number of turns applied.

## 4.5 Hardness measurements

### 4.5.1 Microhardness profiles

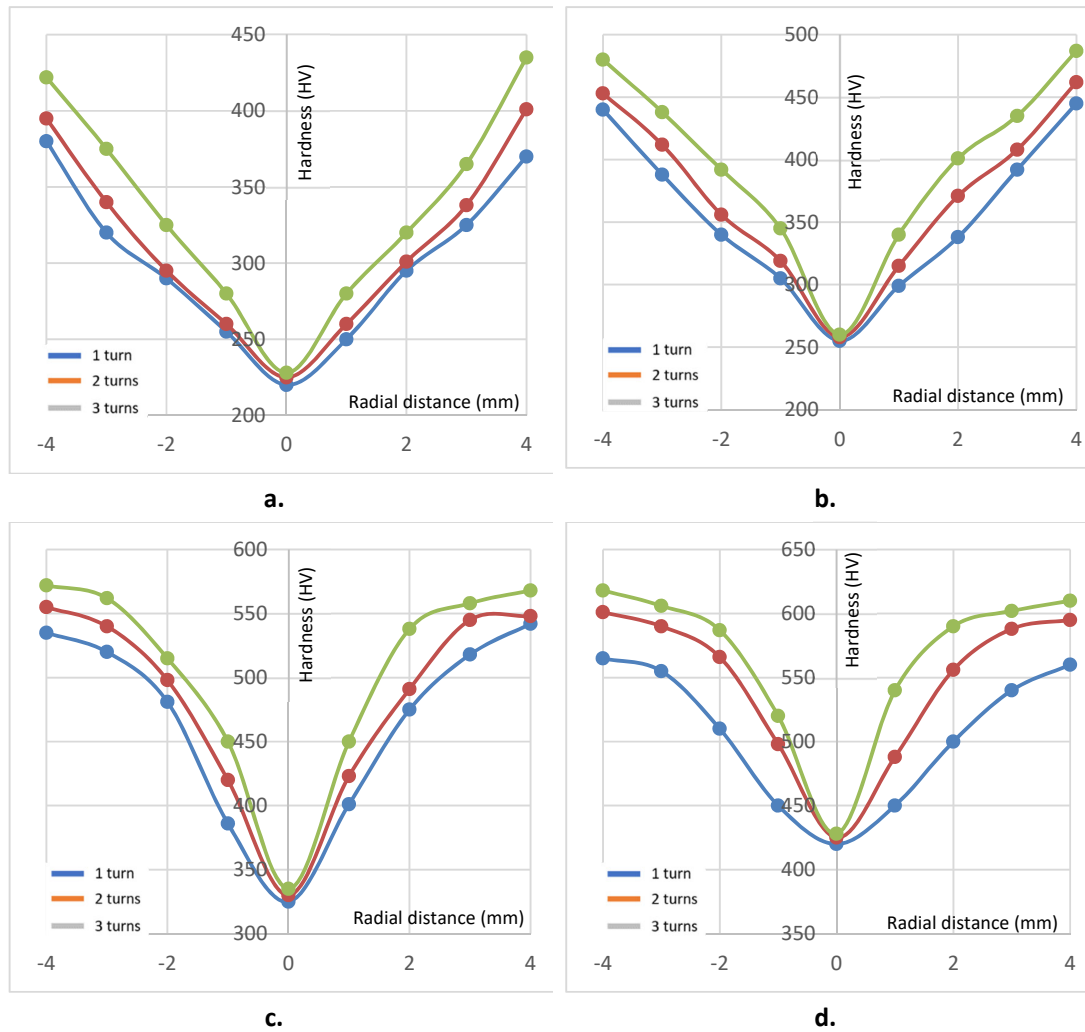


Figure 4-19 Microhardness variations across the diameter of the disc samples after conducting HPT tests under a), 0.5 GPa, b) 1 GPa, c) 3 GPa and d) 6 GPa. The hardness of the disc sample prior to being processed by HPT was  $180 \pm 10$  HV.



Micro hardness profiles are commonly used to show the variation of hardness in disc samples after conducting HPT tests. The measurements were taken using the methodology described in section 3.10 with a 100 g load on Stage 2 samples. Microhardness measurements were made on randomly selected diameters, however SWEAs were avoided and thus the microhardness values corresponding to SWEAs are not included in these measurements. Figures 4-19 shows the microhardness profiles obtained on samples processed using different HPT pressures and number of turns.

The disc samples showed a significant increase in hardness with radial distance, the values being two or three times larger at the edges than at the centres. The lowest values were at the centres of samples processed by 0.5 GPa (approximately 250 HV) and increased with the pressure applied until values close to 425 HV were obtained at the centre with 6 GPa. The hardness values also increased with pressure at other radial positions and number of turns, i.e. at other shear strain values.

#### 4.5.2 Measurements close to TWEAs and SWEAs

Hardness measurements were taken to reveal the differences between WES and the matrix that surrounded them. Measurements were taken in very localized places over circumferential surfaces evaluating TWEAs, cloud and solid SWEAs. Some of these measurements are shown in figures 4-20 and 4-21.

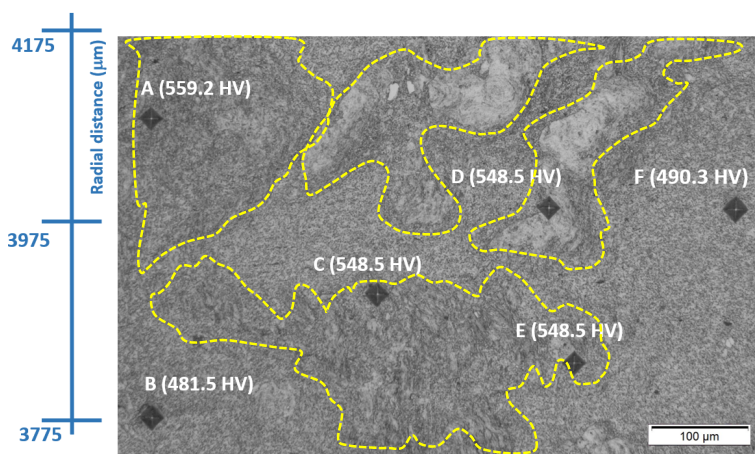


Figure 4-20 Cloud SWEAs located at radial distances of between 3775 and 4175  $\mu\text{m}$ ; points A, C, D, E correspond to measurements on SWEAs (enclosed yellow dotted lines). Sample processed through 3 GPa 2 turns. LOM 2% Nital

In Figure 1-20, Points A and E correspond to the matrix that surrounded cloud WES, whilst points B, C, D and F correspond to the hardness registered in WESs. Despite of the radial distance variations, which itself causes a difference in matrix hardness (the largest distance between the points was around 300  $\mu\text{m}$ ), cloud WES were approximately 18 % harder than the matrix close to them. Figure 1-21 shows hardness values at locations close to the interface of a solid SWEAs located between 4410 and 4710  $\mu\text{m}$  from the centre. Points A and B located in the matrix, whilst points C and D located in solid SWEAs had hardness values between 12 and 15% greater than the matrix values.

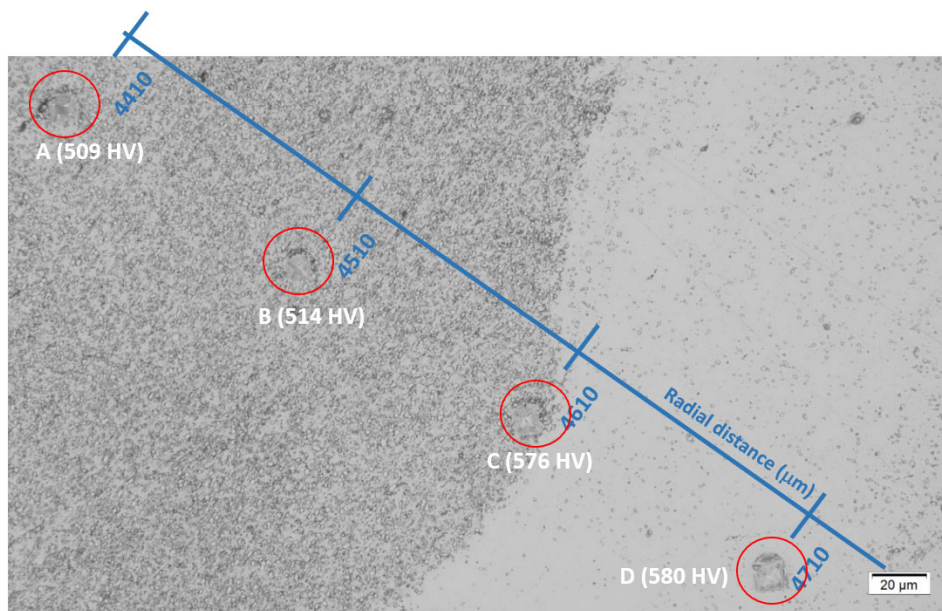


Figure 4-21 Solid SWEA located at radial distances of between 4410 and 4710  $\mu\text{m}$ ; points C, D correspond to SWEAs. Sample processed through 3 GPa 2 turns. LOM Nital 2%.

#### 4.5.3 Nano hardness maps

The hardness differences between TWEAs, SWEAs and the neighbouring matrix were evaluated in two different positions (radial distances of around 4.2 mm and 4.7 mm), one on the top surface of a sample processed by 3 GPa 3 turns, another on a cross section of a sample processed by 6 GPa 1 turn.

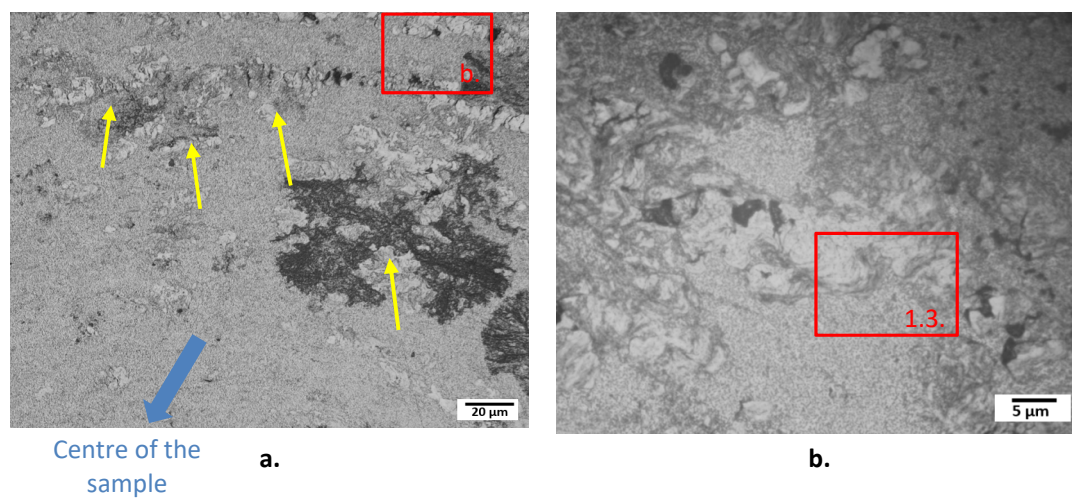


Figure 4-22 Top surface of a sample processed using 3 GPa 3 turns. The red rectangles show the regions detailed in figure 1.23 a), b) Images taken at increasing magnifications to localise the analysed region. LOM Nital 2%

The TWEAs observed in figure 4-22 were at radial distances of between 4 and 4.6 mm and appeared as isolated patches affected by wear (Yellow arrows in figure 4-22 a)). The dark patches corresponding to over-etched regions. The area analysed is visible through the red rectangle in figure 1-22 b). Figure 4-23 shows the results of the nano indentations conducted over an area of 200 x 200 μm in the region detailed in figure 4-22 b).

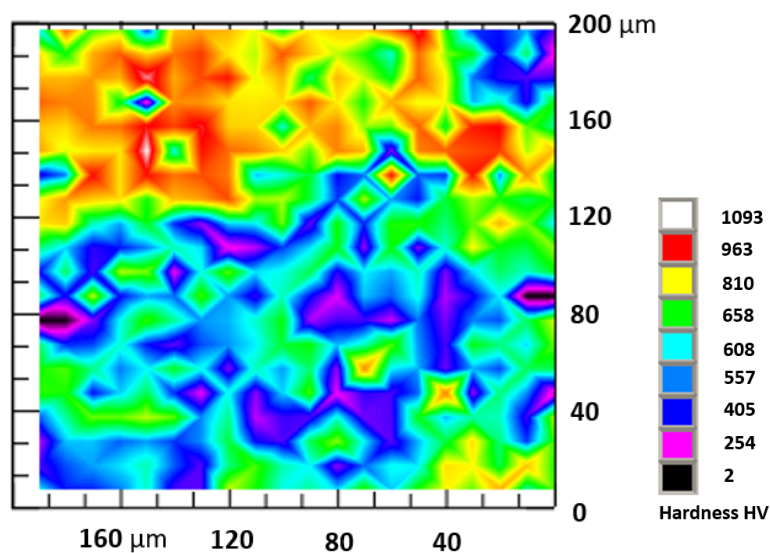


Figure 4-23. Nano hardness map taken from the red area shown in figure 4-22 b).

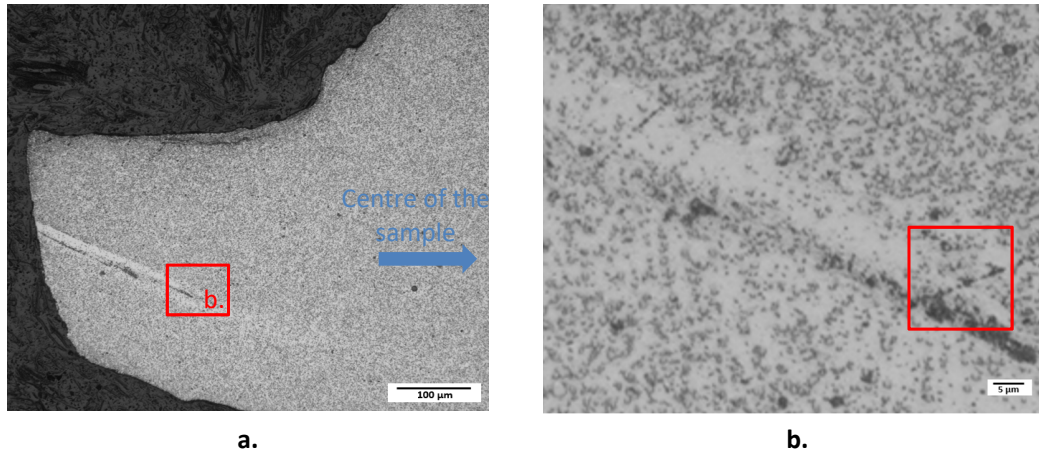


Figure 4-24. Cross section of a sample processed using 6 GPa 1 turn (stage 3). The red rectangles show the regions detailed in the next image a), b). Images taken at increasing magnifications to localise the analysed region. LOM Nital 2%.

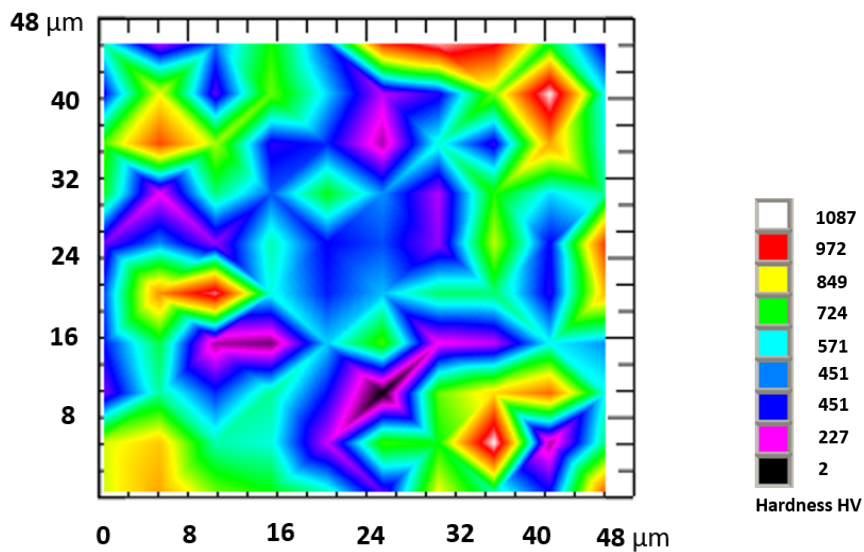


Figure 4-25 Nano hardness map taken from the red area shown in figure 4.24 b).

The SWEAs analysed were from a sample processed using 6 GPa 1 turn. They were located at the edge of the sample and consisted of an elongated structure approximately 200  $\mu\text{m}$  long without clear borders with the matrix. The dark regions correspond to over etched areas in figure 1-24 b). The area selected for nano hardness measurements is shown in figure 4-24 b). as a red rectangle. The results of these measurements are given in figure 4-25



The higher nano hardness values were easily identified as they were located at the top of the region analysed where the TWEAs were concentrated. The hardness in this region varied predominantly between 658 and 963 HV corresponding to the green, yellow and red colours in the map; there was also an isolated measurement of 1063 HV. The lower hardness values corresponded to regions occupied by the matrix and here the hardness varied predominantly between 405 and 608 HV. Figure 1-25 of a region with SWEAs showed similar hardness values to Figure 1-23, the higher hardness values corresponding to the areas affected by SWEAs. The hardness values registered in the SWEAs varied between 724 and 972 HV and thus were similar to the values observed for the TWEAs. Moreover, the significantly lower hardness values at the centre of figure 1-25 correspond to an area with an overlapped ferritic structure. The nanohardness values reported for the TWEAs and SWEAs are higher than the microhardness values shown in figures 4-20 or 4-21. The differences are a consequence of the scale of the nano and micro indents. Nano indents could be located on hard particles such as inclusions, carbides or carbide clusters so generating higher values. On the other hand, different factors could influence the lower measurements, such as indents on ferritic regions free of carbides or the lack of effective contact between the indenter and the material due to roughness variations. Micro hardness indents, on the other hand report the hardness of larger areas with mixed microstructures and so give more “averaged” values.



## Chapter 5 Advanced characterisation

This chapter reports the results of a detailed study by Scanning Electron Microscopy of both TWEAs and SWEAs in HPT disc samples. Their characterisation had three aims: firstly, to describe their morphology using Secondary Electron Imaging – SEI, secondly to explore some of their crystallographic features using Backscattered Electron Imaging – BSI, and thirdly a qualitative evaluation of their chemical composition using Energy-dispersive X-ray spectroscopy, EDS. Morphological characterisation by SEM / SEI was studied on circumferential and axial sections prepared from the HPT disc samples.

### 5.1 SEM / SEI characterisation of top surfaces of HPT discs

As was shown in chapter 4, TWEAs were observed along most of the top surface of the samples, except for a small circular region close to the centre of the sample. Their amount and distribution varied significantly with the pressure and number of turns used in the HPT tests. Despite these variations, common morphological features were observed for all TWEAs. Common features include high plastic deformation, overlapped structures, fibre / layered structures, evidence of wear due to sliding contact and a reduction in carbide content compared to the material surrounding them.

#### 5.1.1 Ill-defined TWEAs

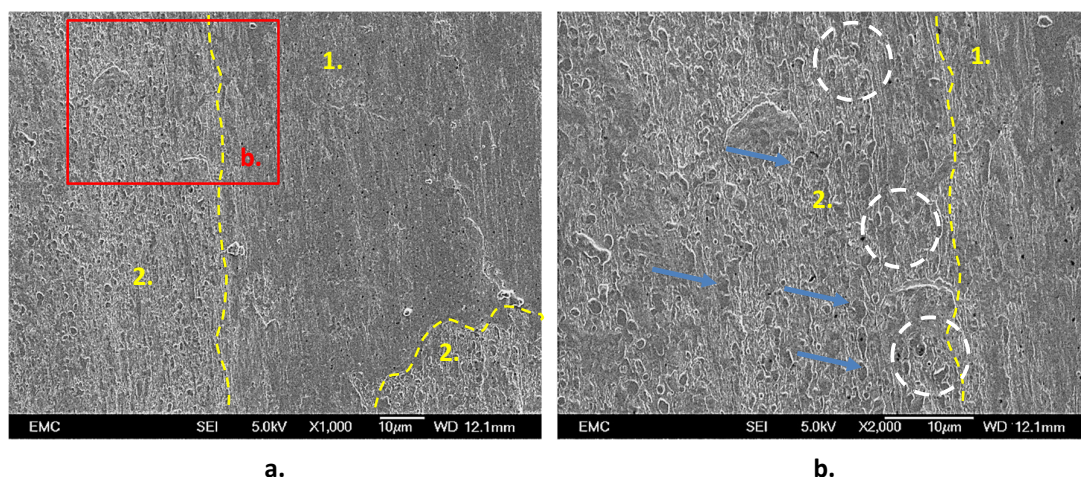


Figure 5-1. TWEAs and surrounding ferritic matrix with spheroidised carbides (radial distance 3.5 mm) on the top surface of a disc sample processed using 0.5 GPa 1 turn. The red rectangle shows the region detailed in (b.) Region 1 corresponds to the TWEAs, region 2 corresponds to the ferritic matrix. Elongated carbides (indicated by blue arrows) are visible in b). SEM / SEI, Nital 2%

In previous LOM images (figures 4-4,4-6), some TWEAs did not have clear limits with the surrounding ferritic matrix; in some areas they overlapped the ferritic matrix while in others they seemed to share part of the typical carbide distribution observed in the ferrite. Figure 5-1 shows details of one of these boundary regions, where region 1 corresponds to the TWEAs and 2 to the ferritic matrix. The carbides in the ferritic matrix in the proximity of the TWEAs appeared elongated due to plastic deformation, some of them seeming to be part of the TWEAs boundary (white dotted circles in figure 5-1 b).

### 5.1.2 High plastic deformation and overlapping

The overlapping phenomenon seemed to be caused by the sliding contact between the disc sample and the anvil, which deformed plastically the ferritic matrix and the TWEAs. This phenomenon is visible in figure 5-2 where some TWEAs located at a radial distance of 3.5 mm on the top surface of a sample processed using 0.5 GPa 1 turn are shown. The smooth surface of the TWEAs appears to be comprised of several overlapped layers stacked over each other as a result of plastic deformation. A small portion of the ferritic matrix is still visible in a), whilst deformed carbides can be seen between the layers in b).

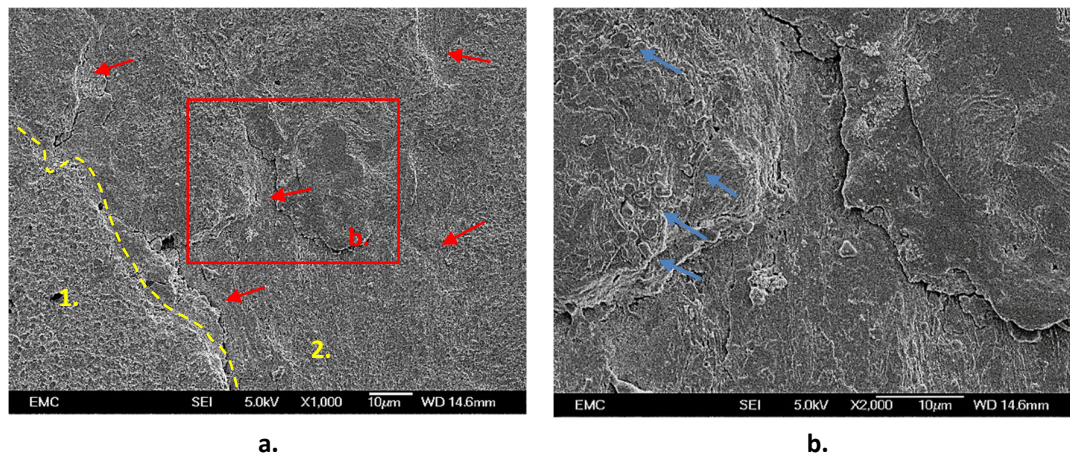


Figure 5-2. Details of TWEAs structure on the top surface of a sample processed using 0.5 GPa 1 turn, in a region located at a radial distance of 3.5 mm. The red rectangle indicates the area shown at higher magnification in (b). a) Differences between the appearance of the deformed ferritic matrix (1) and TWEAs (2). TWEAs layers appeared to overlap (red arrows) b) High plastic deformation produced by severe sliding. SEM / SEI, Nital 2%



### 5.1.3 Flake formation

Flakes were visible on TWEAs at several radial distances but were present in greater amounts when the pressure and the number of turns were higher. Flakes were formed by the high plastic deformation resulting from sliding which generated severe adhesive wear conditions.

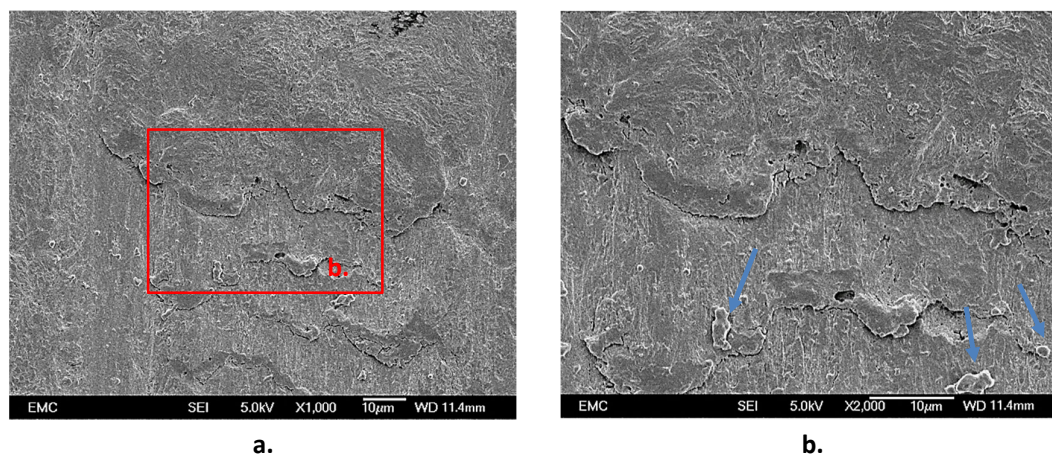


Figure 5-3. Formation of flakes in a TWEA located at a radial distance of 3.5 mm on the top surface of a disc sample processed by 1 GPa 1 turns. The red rectangle indicates the area shown at higher magnification in b). Blue arrows in b) shows debris produced by material detaching from the flakes. SEM / SEI, Nital 2%

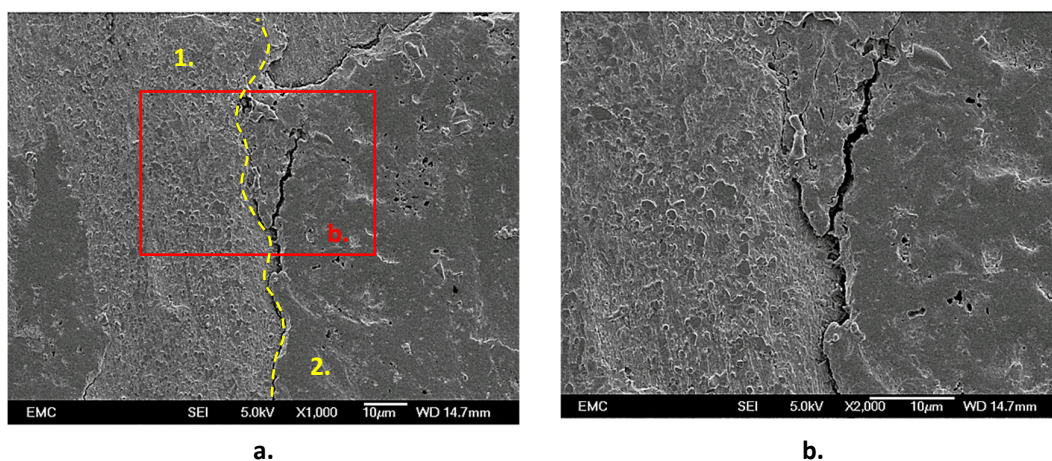


Figure 5-4. Cracks and material detaching on TWEAs due to flaking failure. The detached material exposed the ferritic matrix. TWEAs located at a radial distance of 3.5 mm on the top surface of a disc sample processed by 0.5 GPa 2 turns. The red rectangle indicates the area shown at higher magnification in (b). Region 1 correspond to the exposed ferritic matrix, region 2 to a TWEA affected by flaking and cracks. SEM / SEI, Nital 2%

Figure 5-3 shows some of these flakes on a TWEA located at a radial distance of 3.5 mm in a sample processed by 1 GPa 1 turns. Eventually, with higher pressures and number of turns, cracks form in these flakes which promotes material detachment. Figure 5-4 shows TWEAs located at a radial distance of 3.5 mm affected by cracks (region 2 in a)) in a sample processed by 0.5 GPa 1 turns. The detached material exposed part of the ferritic matrix (b).

#### 5.1.4 Fibre / layered structures

Axial sections of the HPT samples revealed that the TWEAs that form on the top surface of the samples have a fibrous / layered structure that extends parallel to the top surface as a discontinuous layer in some regions but as swirls or vortices in other places (Figures 5-5 to 5-8). This layer was restricted to a depth of less than 100  $\mu\text{m}$ . Many small white structures appeared interconnected forming complex systems close to the surface: other white structures appeared more isolated from the top surface and from other TWEAs. Although TWEAs can be distinguished easily from the ferritic matrix (white dotted lines in figure 5-5 and 5-7 indicate the boundary), their detailed shape was better revealed by SEM / BSI (figure 5-16).

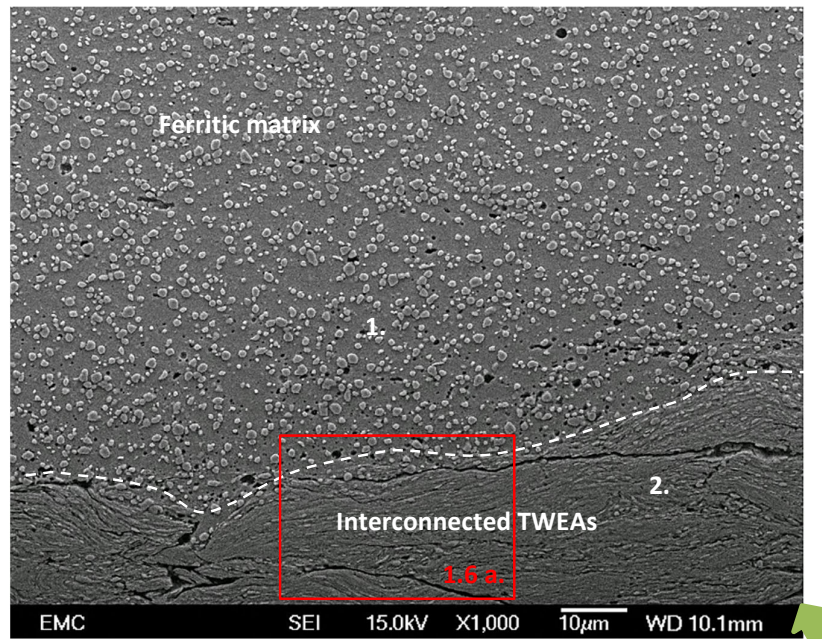


Figure 5-5. Axial section of a disc sample located at a radial distance of 4 mm processed by 1 GPa 1 turn. The red rectangle indicates the area shown at higher magnification in figure 5.6 a). Region 1 shows the ferritic matrix with spheroidised carbides, region 2 consists of TWEAs close to the top surface. The green arrow indicates the top surface of the sample. SEM / SEI, Nital 2%



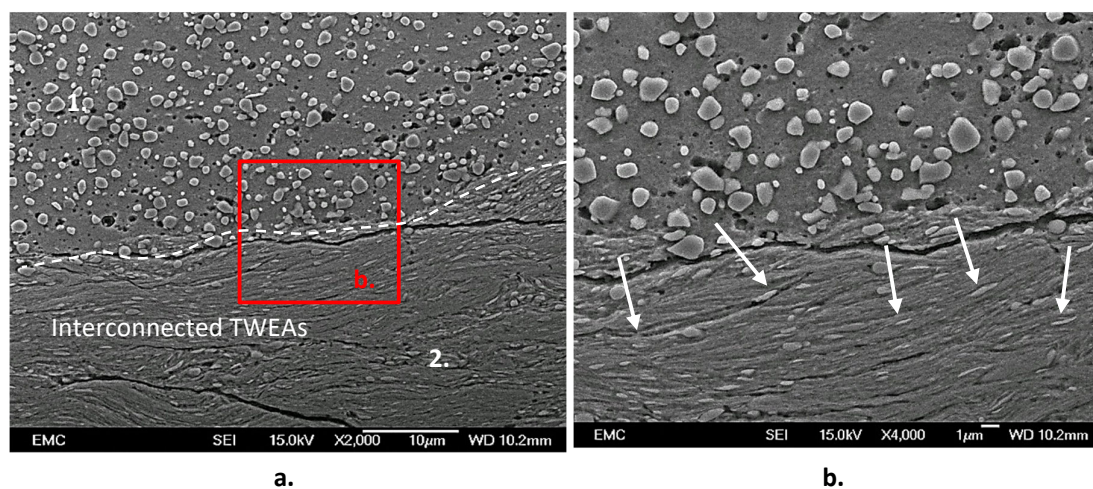


Figure 5-6. Details of the image shown in figure 5-5. The red rectangle indicates the area shown at higher magnification in (b). a) The carbide distribution in the ferritic matrix in region 1 is different to that found in the TWEAs in region 2. b) Highly deformed carbides linked to the fibrous structure in a cloud TWEA (white arrows). SEM/SEI Nital 2%.

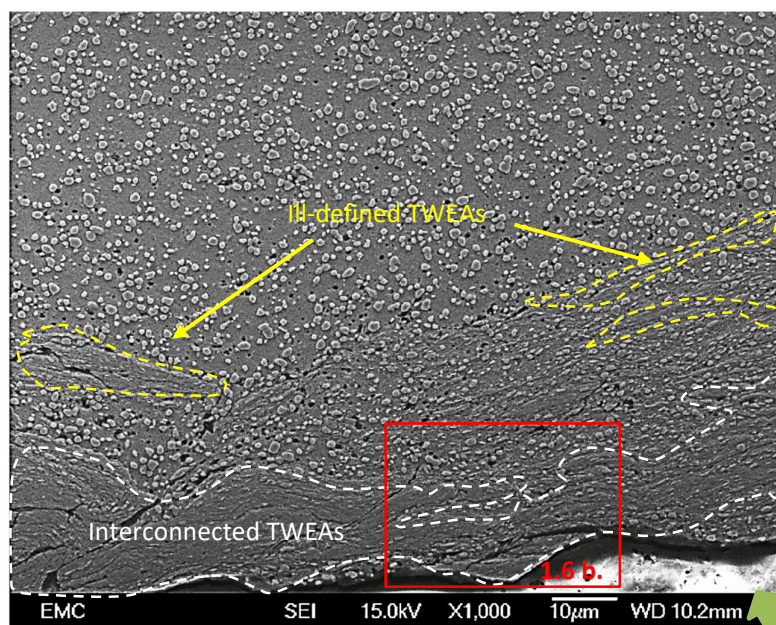


Figure 5-7. Axial section at a radial distance of 4 mm of a disc sample processed by 1 GPa 2 turns. The red rectangle indicates the area shown at higher magnification in figure 5-6. The white dotted line encloses interconnected TWEAs present close to the top surface. Other isolated TWEAs appear at greater depths beneath the surface, at depths close to 100  $\mu\text{m}$  (yellow arrows). The green arrow indicates the top surface of the sample. SEM / SEI, Nital 2%

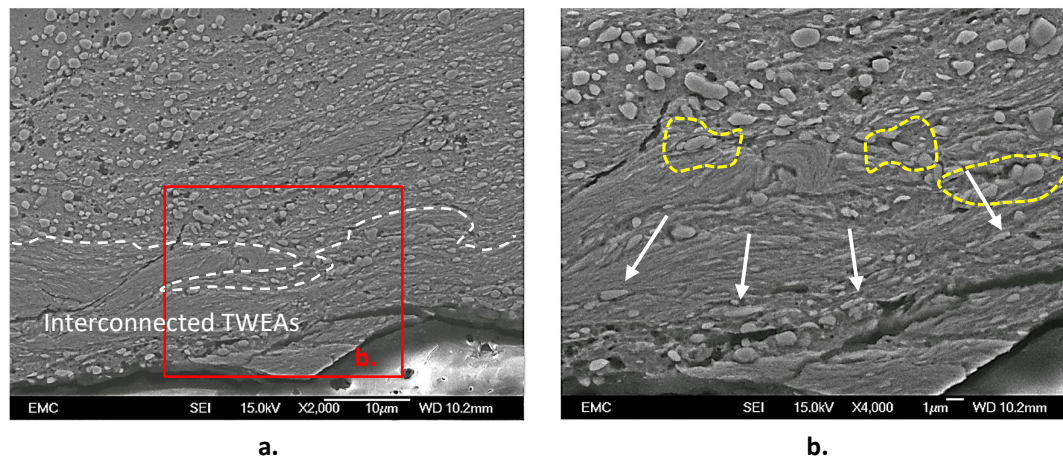


Figure 5-8. Details of the image shown in figure 5-7. The red rectangle indicates the area shown at higher magnification in b). a) The depth to which TWEAs extended beneath the top surface is not regular along its length. A fibre / layered structure is visible inside the TWEAs. Deformed carbides appeared between the fibres /layers (white arrows in b)); some of these seemed to be linked to the fibre/layered structure (enclosed by yellow dotted lines in b)). SEM/SEI Nital 2%.

In addition to the changes in the microstructure, significant variations were observed between the carbides in the ferritic matrix and in the TWEAs. Firstly, fewer carbides were observed inside the TWEAs, and their distribution between the fibres was non-uniform, compared to their relatively homogeneous distribution in the matrix (figure 5-5 and 5-6). The carbides seemed to have been dragged in the direction of the fibres, following the plastic deformation visible inside the TWEAs. Secondly the carbides in TWEAs looked smaller, elongated and fractured (white arrows in figure 5-6 b). and 5-8 b).), some of them seemed to be linked to the fibre / layered structure at different points (yellow dotted lines in figure 1.8 b)).

## 5.2 Solid and cloud SWEAs

Examination of the circumferential serial sections prepared through the cross section of the disc revealed more details of the morphology and distribution of SWEAs. Characterisation focused on a region of solid and cloud SWEAs located close to the edge of a disc sample from stage 2 (radial distance of 4.5 – 4.8 mm), processed by 3 GPa 2 turns. Figures 5-9 to 5-12 were taken from the same region studied by LOM in figure 4-15 As was highlighted for TWEAs, the features described in these figures were observed in all SWEAs identified in this thesis, no matter the pressure or number of turns used for the HPT tests.



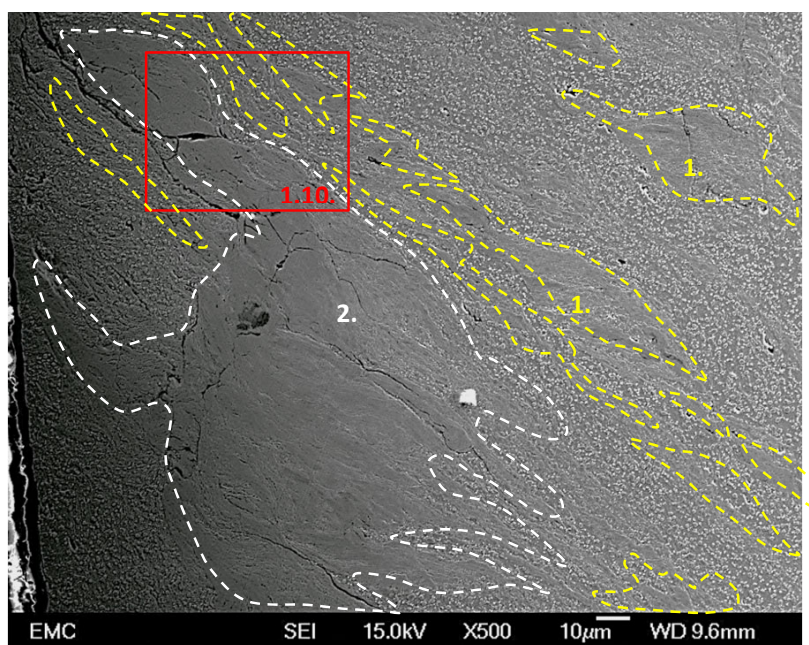


Figure 5-9. Solid WEAs (white dotted lines, region 1) and cloud SWEAs (yellow dotted line, region 2) located close to the edge of a sample processed by 3 GPa 2 turns. The red rectangle indicates the area shown at higher magnification in figure 1-10. SEM/SEI 2% Nital.

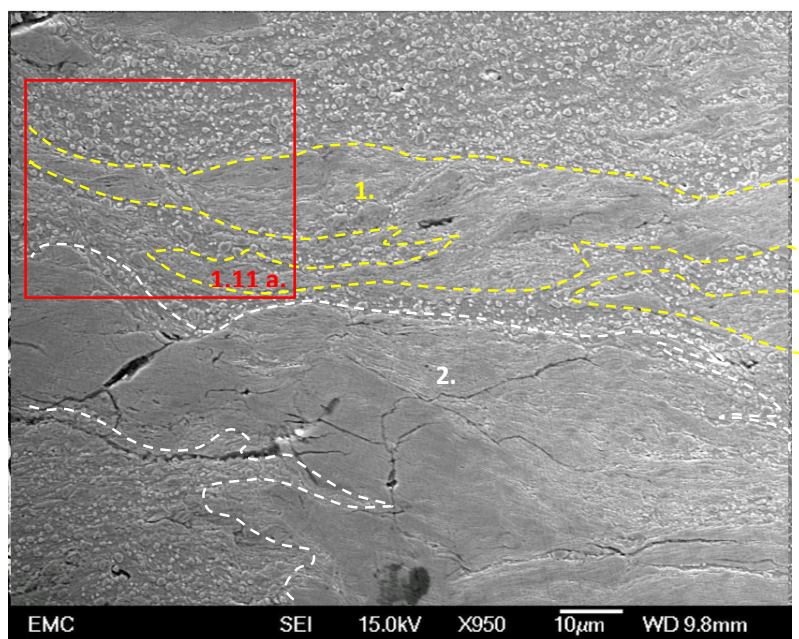


Figure 5-10. Details of the SWEAs system shown in figure 5-9. Yellow dotted lines enclose clouds (region 1), whilst the white dotted lines enclose the solid SWEAs (region 2). The red rectangle indicates the area shown at higher magnification in figure 1-11. SEM/SEI 2% Nital.

Figure 5-9 shows a general panorama of the selected SWEA system, which consisted of a solid well-defined white region located close to the edge of the sample (white dotted line, region 2) and a group of small and elongated cloud SWEAs located close by. Figures 5-10 and 5-11 present details of the same SWEA system at higher magnifications. Many cracks were located preferentially in the solid WEAs, forming an extended network. SEM images taken from the clouds and small solid SWEAs showed a twisted and folded fibrous structure that overlapped the ferritic matrix (figure 5-10 a)). The carbide distribution in the vicinity of the SWEA differs from the random distribution observed in the ferritic matrix. The carbides seemed to have been dragged by a flow force that surrounded the WES, some of the carbides appearing deformed and linked to the thin fibres (blue arrows in figure 1.11 b)).

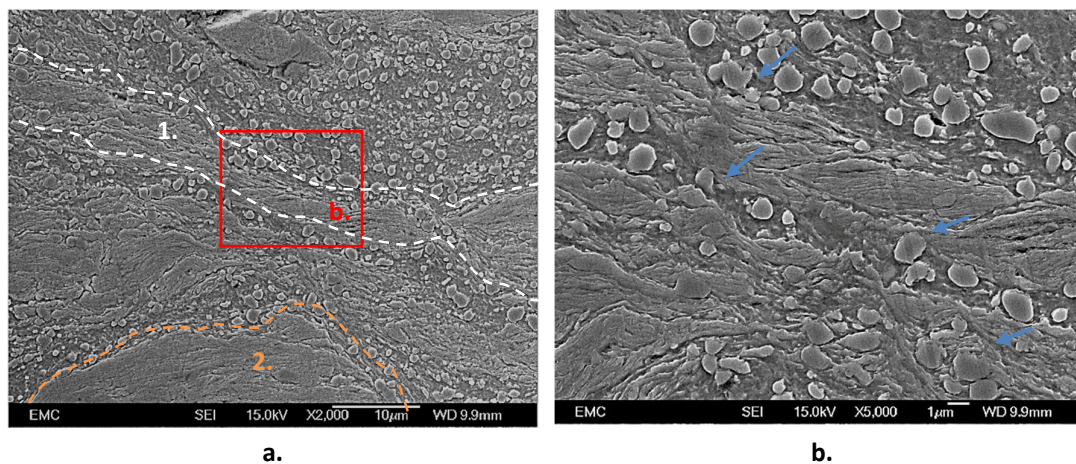


Figure 5-11. Details of cloud SWEAs linked to a typical solid SWEA located at the edge of the sample. The red rectangle indicates the area shown at higher magnification in (b). a) Fibrous structure in a cloud (region 1, enclosed by a white dotted line) and solid SWEAs (region 2 enclosed by an orange dotted line). b) Deformed carbides that seem to be linked to the twisted fibrous structure in a cloud SWEA (blue arrows). SEM/SEI Nital 2%.

Figure 5.12 presents SEM images from a solid SWEA linked to a cloud SWEA. The structure of the SWEAs looked similar to that observed in the TWEAs (figures 5.5 to 5.8). A fibrous structure has replaced the deformed matrix and the carbide content is much reduced. However, there are some differences. Firstly, the fibres tend to be thinner, more compact and bonded to each other in the SWEAs especially at locations far from the SWEA-matrix interface and the typical carbide distribution is not visible inside the fibrous structure, with only a few carbides being present (blue arrows in figure 5.12 b)). Secondly, the fibre structure is different close to the border of the SWEAs with the matrix, as compared to its centre. The fibrous structure at the centre of the SWEA looked more deformed and compacted than that observed in the TWEAs, suggesting a more significant relationship to the plastic flow imposed in this region. The orange dotted line shown in figure 5.12



b). separates both fibre structures. Thirdly, just a few carbides appeared at the centre (or core) of the SWEAs suggesting a partial or complete dissolution of the carbides inside the SWEAs.

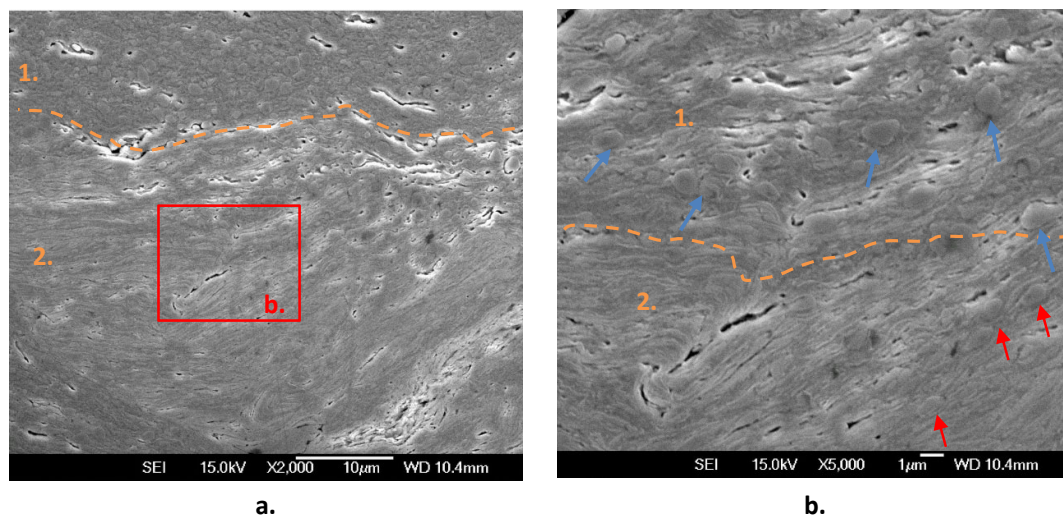


Figure 5-12 Details of a solid SWEA located at the edge of a circumferential section of a sample processed by 3 GPa 2 turns. The red rectangle indicates the area shown at higher magnification in (b). a) Interface between the ferritic matrix (Region 1) and the SWEAs (Region 2). b). Variations of the fibre structure close to the centre of the SWEA. The orange dotted lines separate regions with significant differences in their carbide content. SEM/SEI, Vilella's reagent.

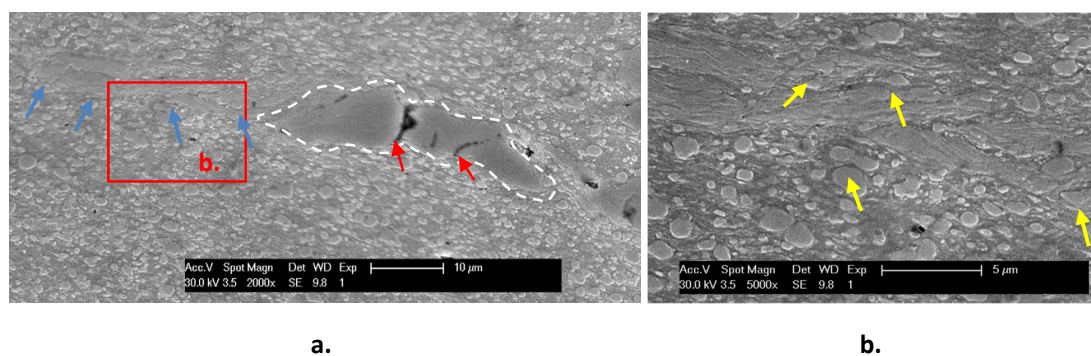


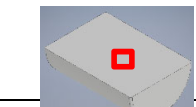

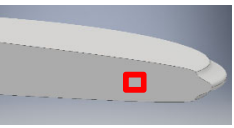
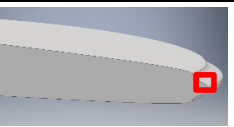
Figure 5-13. Details of cloud SWEAs located at the centre of a diametral axial section of a sample processed using 3 GPa and 2 turns (white dotted line). The red rectangle indicates the area shown at higher magnification in (b). a) The fibrous structure in the cloud (blue arrows) and cracks in the solid SWEA (red arrows). b). Deformed carbides linked to the fibrous structure (yellow arrows). SEM/SEI Nital 2%.

Finally, figure 5-13 shows images of SWEAs found in an axial section of a disc sample processed by 3 GPa 2 turns (from stage 3). This axial section was examined in figure 4-15 b) via LOM. These images basically show the same features observed in figures 1.9 to 1.12, but in a plane at right angles to the surface of the disc sample. Cloud SWEAs had a highly deformed fibrous structure with no clear boundaries and seemed to overlap the ferritic matrix. Cracks, oriented at right angles to the disc radius, were present in a small solid SWEA. (white arrows, figure 5-13 a)).

### 5.3 EBSD characterisation

EBSD characterisation was conducted on four representative regions identified in three different samples: an annealed roller (*region 1*), a sample processed using 3 GPa 2 turns (*region 2* for TWEAs and *region 3* for SWEAs) and a sample processed using 6 GPa 1 turn (*region 4* for SWEAs at the edge of the sample). These samples were selected not only because of the relative position of the TWEAs and SWEAs in the sample (at the top surface, subsurface and close to the edges of the samples) but also their size / shape. The samples used to characterise TWEAs and SWEAs correspond to those in stage 2. Table 1 summarises the regions studied.

Table 5-1. Sections taken to be analysed and WES selected for characterisation using advanced SEM techniques

Region	Sample type	Description	Position analysed	Schematic position
1	Annealed	Ferritic matrix with spheroidal carbides	Random position	
2	3 GPa 2 Turns (*)	WES on top surface, TWEAs	At top surface (within 100 $\mu\text{m}$ depth of surface) and 1.5 – 5 mm radial distance	
3	3 GPa 2 Turns (*)	WES located inside the samples, SWEAs	240-360 $\mu\text{m}$ from the bottom surface and 3.5 and 5 mm radial distances	
4	6 GPa 1 Turns	WES close to the sample edges affected by flash, SWEAs at edge	240-360 $\mu\text{m}$ from the bottom surface and 4.8 and 5 mm radial distances	

(\*) Two areas studied on the same sample

### 5.3.1 Region 1: Annealed AISI 52100

The microstructure of the AISI 52100 after the annealing heat treatment is presented in figure 5-14 using a) SEM / SEI, b) SEM / BSI, c) Image Quality, IQ d) Auto Phase maps e) Inverse Pole Imaging IPF and f) Kernel Average Maps, KAM.

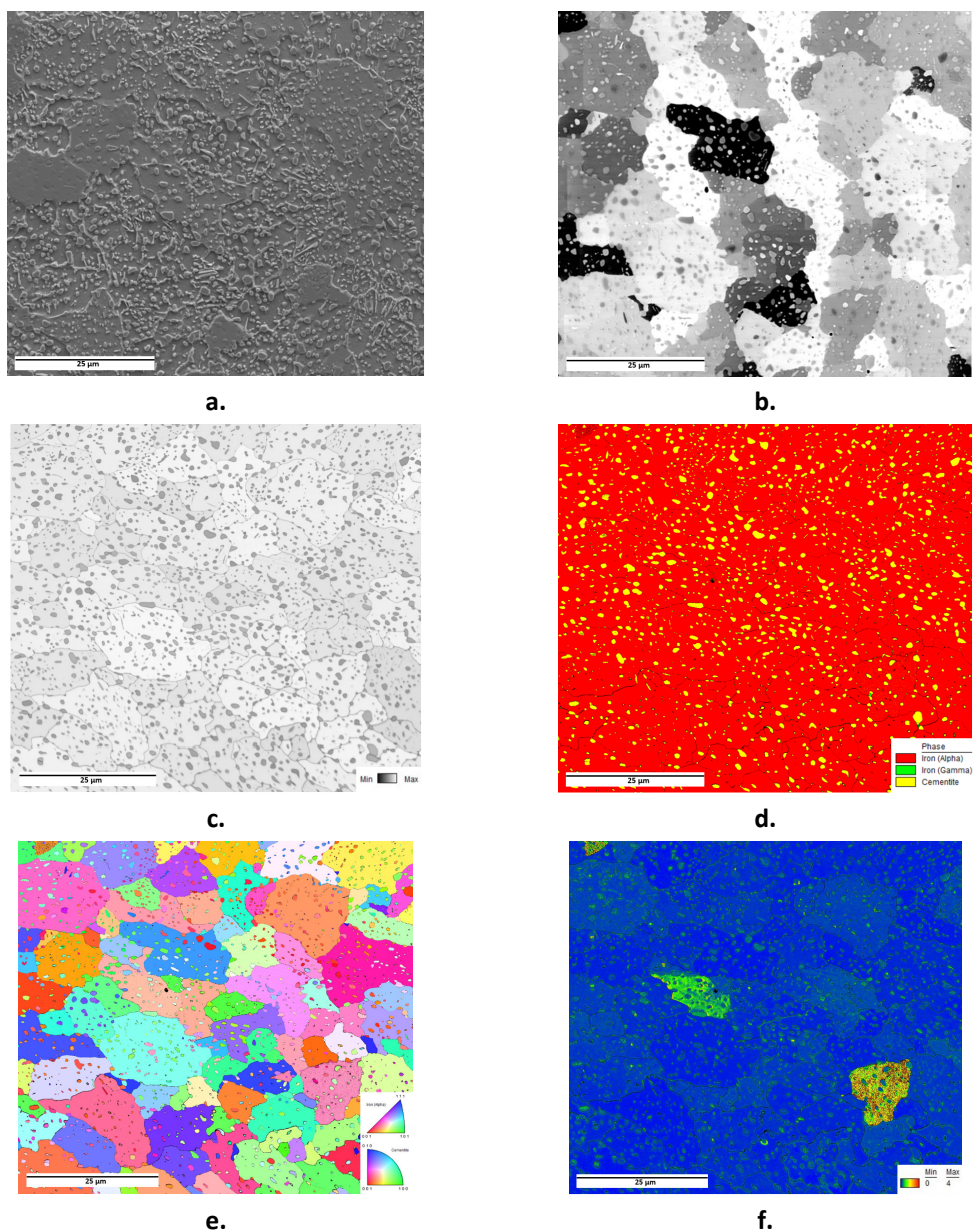


Figure 5-14. Microstructure of the axial section of an annealed AISI 52100 roller analysed by: a) SEM / SEI, b) SEM / BSI c) Image Quality (IQ) d) Auto Phase maps (AP), e) Inverse Pole Imaging (IPF) with the Z axis as normal direction, and f) Kernel Average Maps KAM (150 nm 5°).

The microstructure of the annealed AISI 52100 consisted basically of a ferritic matrix with a homogeneous distribution of spheroidal carbides of different shapes and size. Etching with Nital 2% was effective at revealing the carbides but did not reveal all the ferritic grain boundaries (figure 5-14 a)). The brightness and contrast of the images obtained by SEM / BSI can be used to study the microstructure of the samples because BSI taken at relatively low acceleration voltages detect variations in crystallographic orientation. The contrast differences allowed the size and shape of the ferritic grains and their orientation to be visualised (figure 5-14 b)). Brighter well-defined ferrite grains were observed in an IQ image, these grains exhibiting a low defect density (figure 5-14 c)). The absence of austenite was confirmed through an Auto Phase map determined using previous indexed  $\gamma$  - Fe,  $\alpha$ -Fe, and  $\text{Fe}_3\text{C}$  (figure 5-14 d)). IPF taken using the-Z axis as the normal direction, confirmed the random orientation of both phases (cementite and ferrite) (figure 5-14 e)). Finally, KAM (150 nm, 5°) image shows a very homogeneous microstructure free from significant changes in the average internal grain orientations (figure 5-14 f)).

An artefact is present in the KAM image where three ferritic grains appeared in a different colour compared to the rest of the grains in the image. All images in figure 5-14 exhibit a relaxed microstructure with a low defect density and no preferential crystallographic orientations. Preliminary SEM / BSI examination

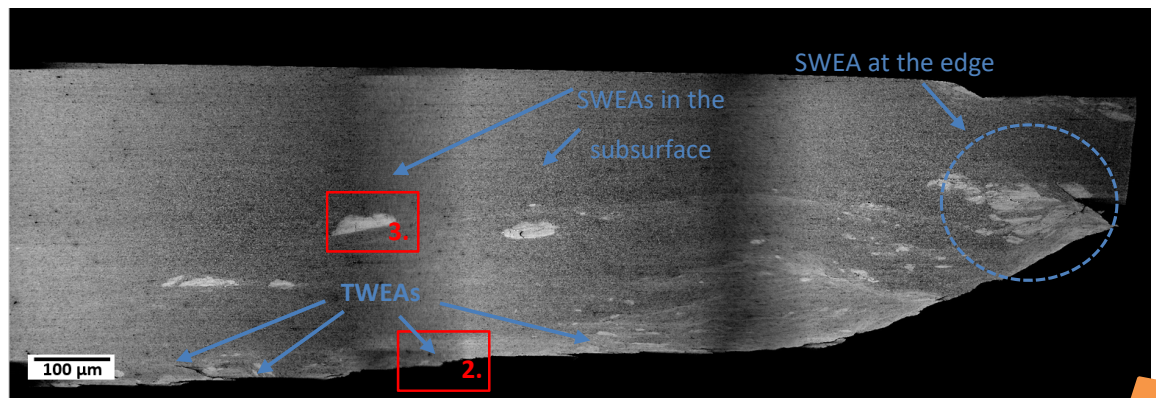


Figure 5-15. Axial section of a HPT sample processed using 3 GPa 2 turns. Red rectangles correspond to Regions 2 and 3, which are shown in figures 5-16 and 5-17. The blue circle shows a typical example of a SWEA located at the edge of the sample. A similar SWEA is present in Region 4. The orange arrow indicates the top surface of the sample. Montage constructed from SEM / BSI images (10 kV, x200 and 5.1 mm WD).

Figures 5-15 to 5-17 show SEM / BSI images taken from Regions 2, 3 and 4 illustrating various features of the WEAs. Firstly, TWEAs in Region 2 (figure 5-15) did not form a continuous or homogeneous structure close to the top surface; they appeared as small and bright patches, scattered parallel to the top surface and at a radial distance of 1.5 – 5 mm. Some of these patches



appeared isolated and well defined (blue arrows in figure 5-15), but others seemed to be overlapped by the matrix that surrounds them and had ill-defined borders (yellow dotted lines in figure. 5-16). A third TWEAs group could be distinguished as a mixture of these two types and extended across large areas.

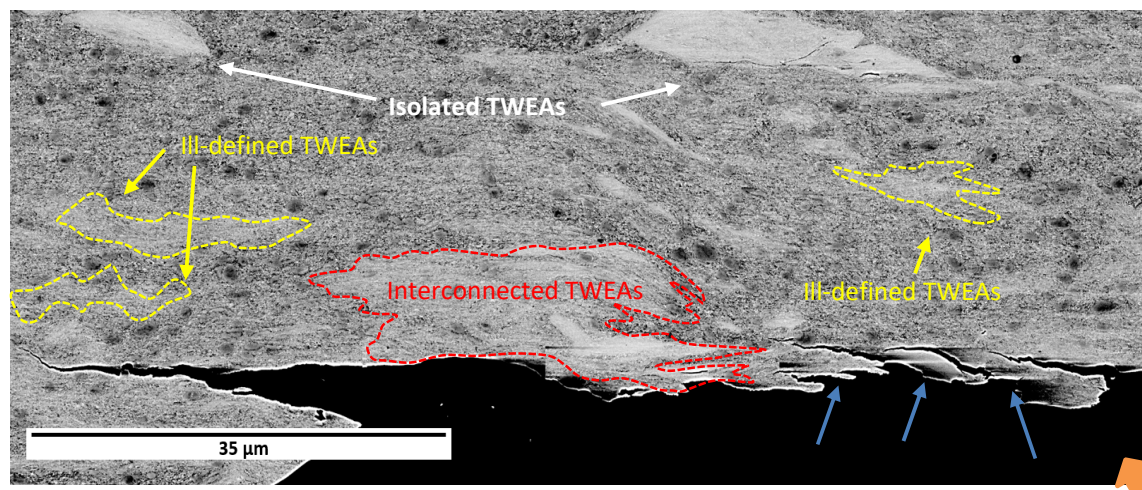


Figure 5-16. Isolated (blue arrows) TWEAs with ill-defined borders (yellow dotted lines) and mixed (red dotted line) TWEA types in Region 2. Blue arrows show cracks at the top surface. The orange arrow indicates the top surface of the sample. Significant regions appeared without carbides. Montage constructed from SEM/ BSI images (10 kV, x200 and 5.1 mm WD).

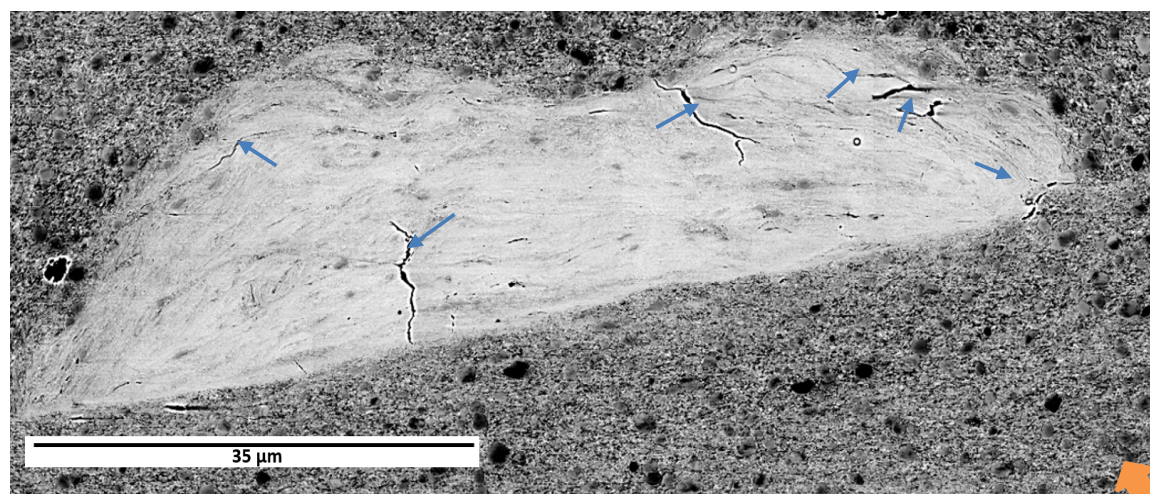


Figure 5-17. Well-defined SWEA located in Region 3. The Orange arrow indicates the top surface of the sample. Montage constructed from SEM / BSI images (10 kV, x200 and 5.1 mm WD).

Figure 5-16 shows a well-defined SWEA located in the subsurface of the HPT sample (Region 3). A fibrous structure affected by high plastic deformation is visible inside the SWEA where some cracks were also present with different orientations (blue arrows in figure 5-17). Finally, Region 4 is shown in figure 5-18 and is revealed to consist of a mixture of well-defined and ill-defined SWEAs similar to the TWEA systems described in figure 5-16. A *fibre / layered* structure is visible inside the white structures; this had a preferential direction that seemed to be related to the plastic flow at the edge of the sample caused by the HPT tests. The presence of cracks was widespread in this case and they appeared to follow the preferential direction exhibited by the *fibre / layers* (blue arrows in figure 5-18)

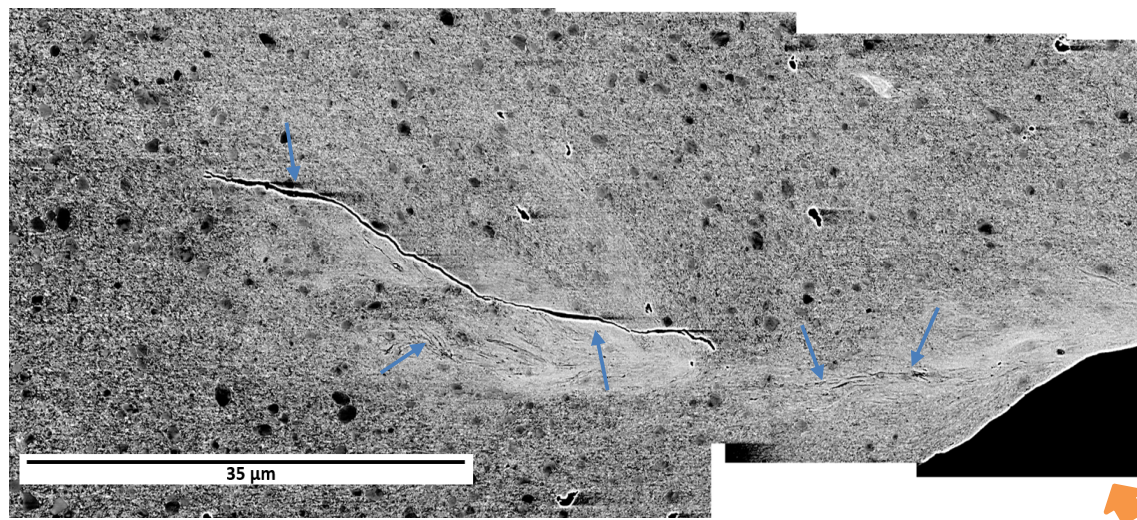


Figure 5-18. Well-defined SWEA located in Region 3. Orange arrow indicates the top surface of the sample. Montage constructed from SEM / BSI images 10 kV, x200 and 5.1 mm WD) images.

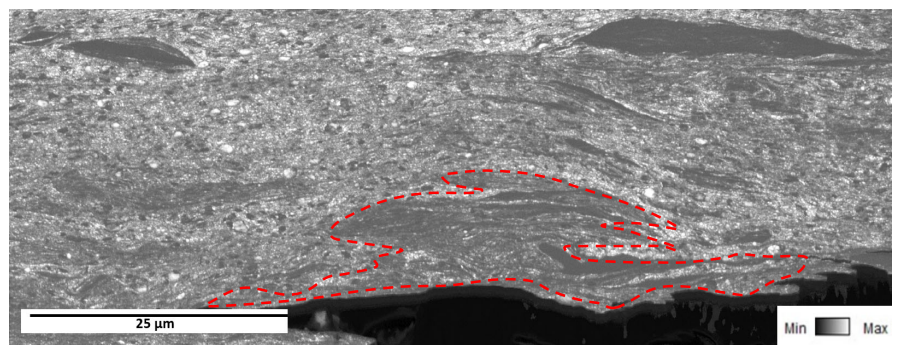
### 5.3.2 Imaging Quality Maps (IQ)

Figures 5-19 to 5-21 present the Image Quality (IQ) maps corresponding to Regions 2, 3 and 4. The dark regions observed in IQ correspond to the white structures, whilst the brighter regions correspond to the ferritic matrix. The dark regions derive from the absence of clear diffraction patterns from the structures present in these regions. Large discontinuities such as cracks, as observed in all regions (blue arrows) can also disturb the diffraction responses. The differences in the contrast revealed modifications in the ferritic matrix as well, not only in the vicinities of the WEAs, but also in other areas analysed.

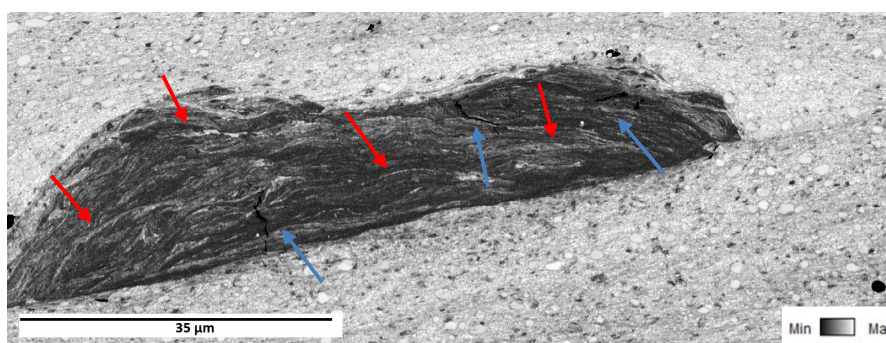
The alterations included bigger overlapped areas than those revealed by SEM / BSI images (dark contrast), flow patterns affecting the white structures (Regions 2 and 3) and slight variations in the



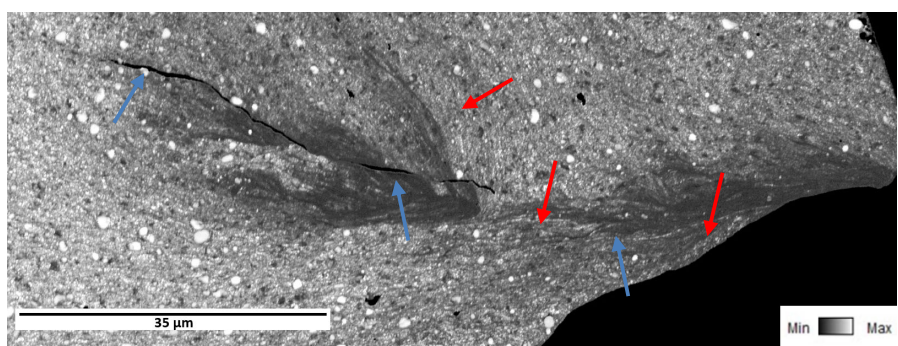
contrast of the matrix possibly related to localised plastic deformation. The plastic flow patterns were also visible inside some SWEAs, where a fibrous structure appeared here stacked to form several parallel layers.



a.



b.



c.

Figure 5-19 IQ maps taken from Regions 2, 3 and 4. White structures (TWEAs and WEAs) are easily distinguishable from the ferritic matrix because of their dark contrast.

### 5.3.3 Auto Phase Maps (AP)

The AP maps showed the cementite and ferrite distribution. The poor quality obtained in the white structures in IQ maps is visible in the AP maps as black regions. Inside these black areas some ferritic *fibre / layers* were visible, indicating signals corresponding to ferrite structures figure 5-20 b). Overall, the carbide distribution in the ferritic matrix looked homogenous except for some isolated clusters. No carbides were revealed inside any white structure.

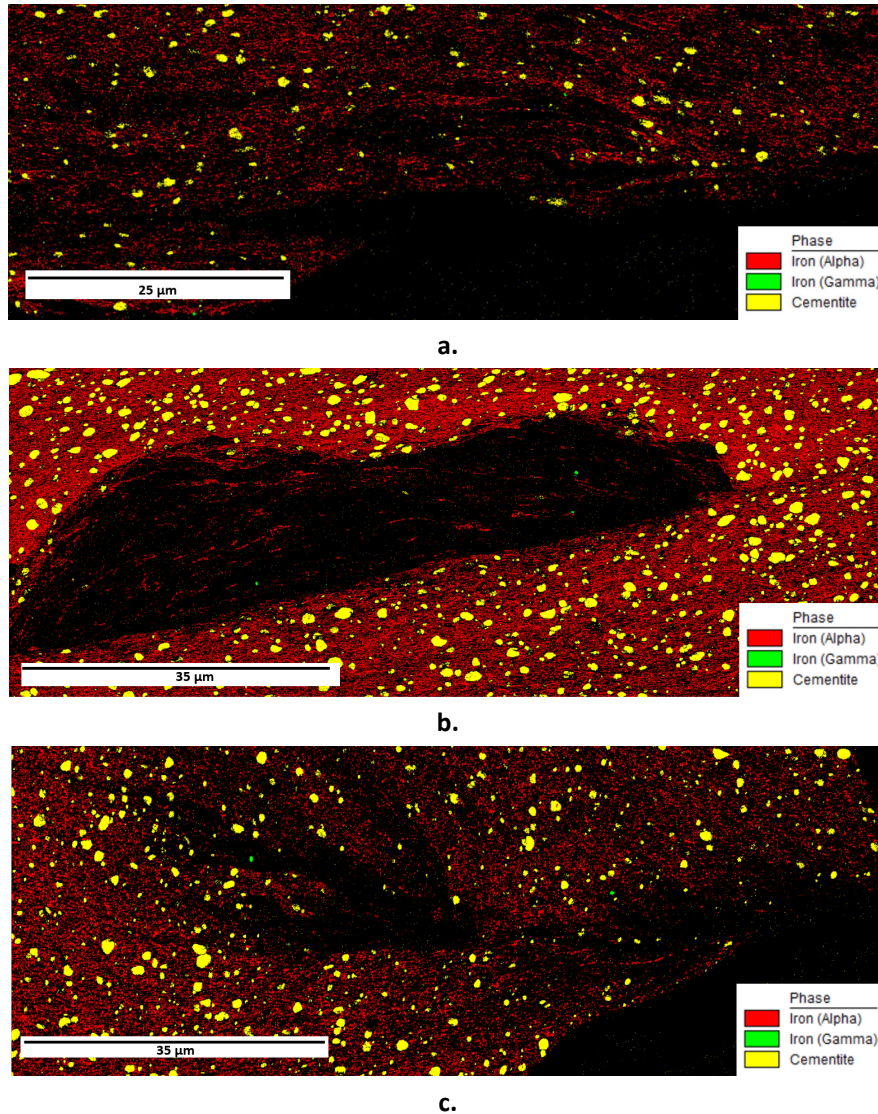


Figure 5-20 AP maps from Regions 2, 3 and 4 show as black regions without any recognized phase. The absence of carbides inside the white structures was reported by both IQ and AP maps.



### 5.3.4 IPF maps

The IPF maps show the matrix has a very refined ferritic grain structure containing the spheroidal carbides (figure 1.21 a), b), c)). Both phases, ferrite and cementite reported heterogeneous crystallographic orientations in relation to the Normal *Direction* or Z axis used as orthogonal reference. Similarly, to the AP maps given in figure 5-20, TWEAs and SWEAs appear in figure 5-21 as black areas because of the lack of clear diffraction patterns from them.

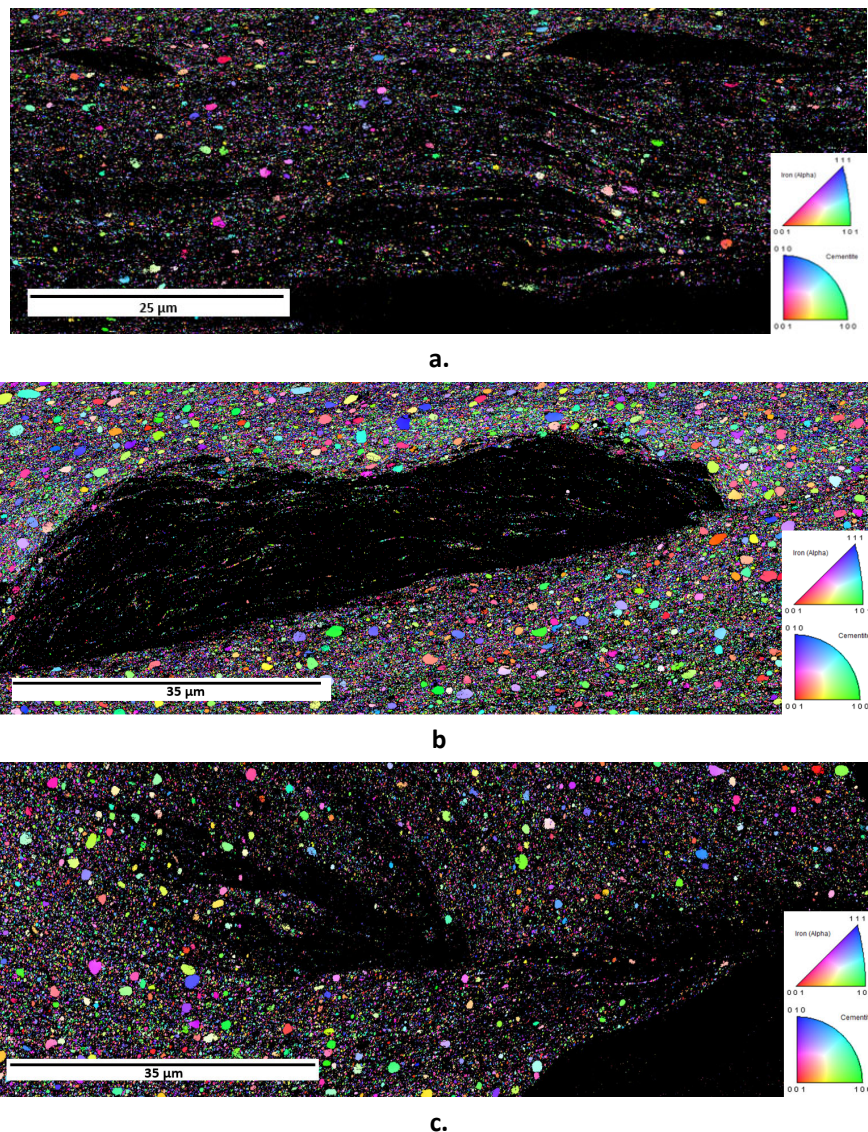


Figure 5-21 IPF from Z axis (ND) taken from Regions 2, 3 and 4. A very refined structure is revealed in all regions studied after applying 3 GPa 2 turns and 6 GPa 1 turn. TWEAs and SWEAs appeared black as was observed in AP maps. IPF with CI greater than 0.1

### 5.3.5 KAM maps

The KAM maps showed how the average misorientation that a pixel has with its nearest neighbours was very similar in all structures analysed. No higher or lower misorientation angles were consistently registered in Regions 2, 3 and 4. TWEAs and SWEAs appeared black as shown in Figures 5.22.

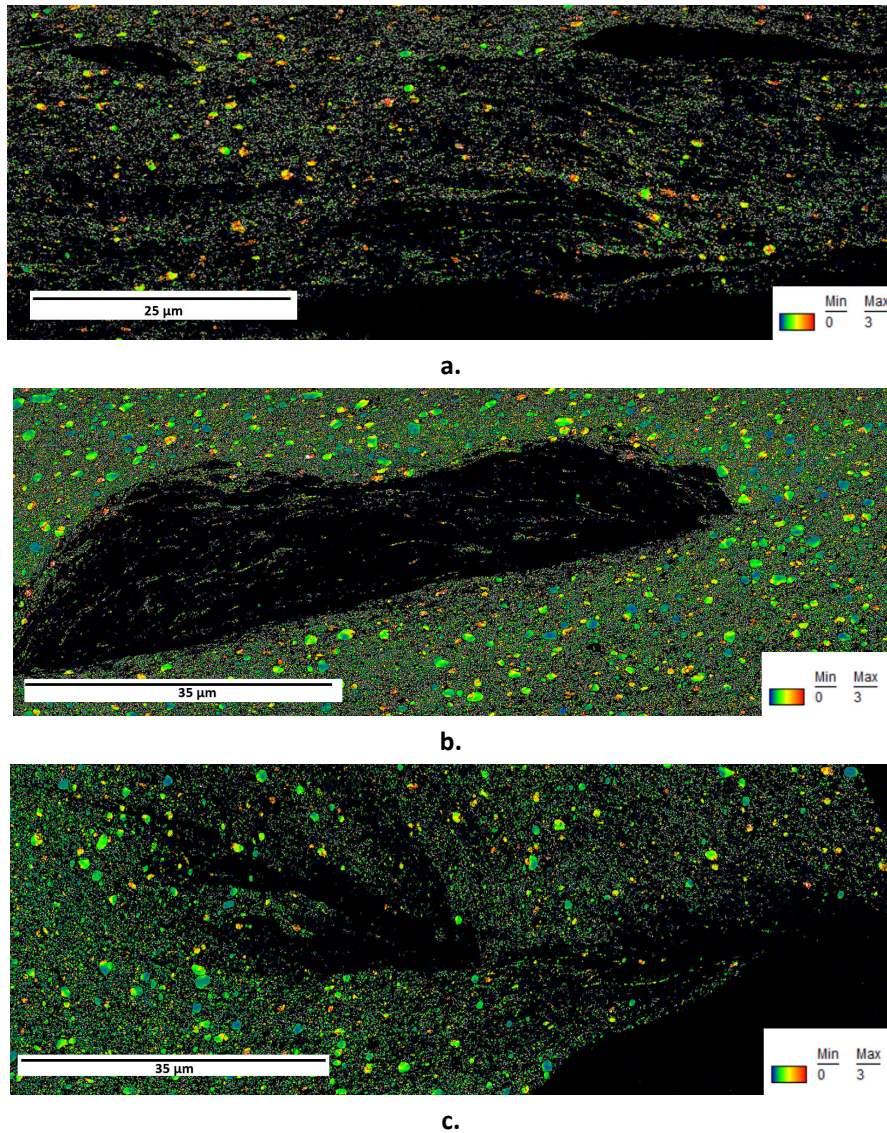


Figure 5-22 KAM maps taken from Regions 2, 3 and 4 using a 150 nm step size and orientation angles up to 3°



## 5.4 EDS characterisation

### 5.4.1 Carbon and Chromium content determined by EDS analysis

Figure 5-23 and 5-24 summarise the results of EDS analysis for Carbon and Chromium in Regions 2, 3 and 4. Analysis of both elements is important in understanding the evolution of carbides during HPT tests.

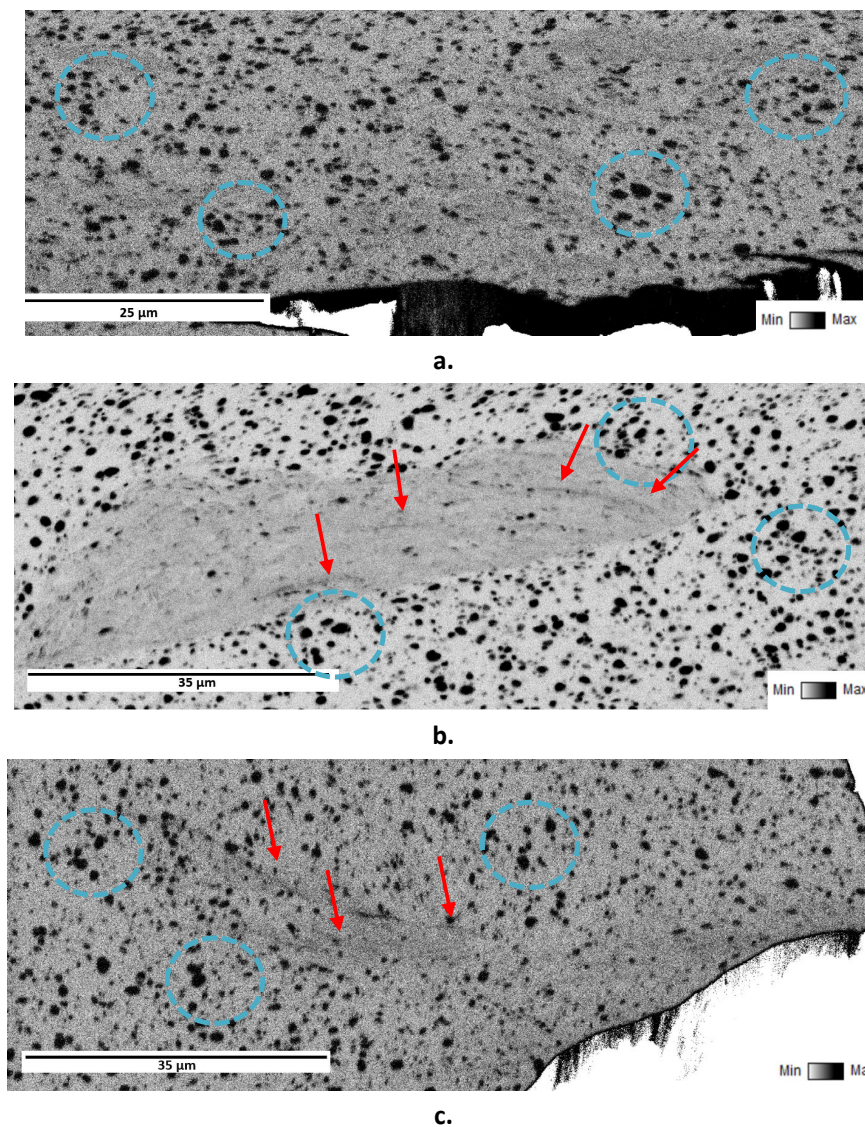


Figure 5-23 Carbide distribution and WEAs in Regions 2, 3 and 4 revealed by Carbon EDS maps. Blue circles show carbide clusters in the ferritic matrix, red arrows show C trails or comet tails inside SWEAs (Image b) and c)).

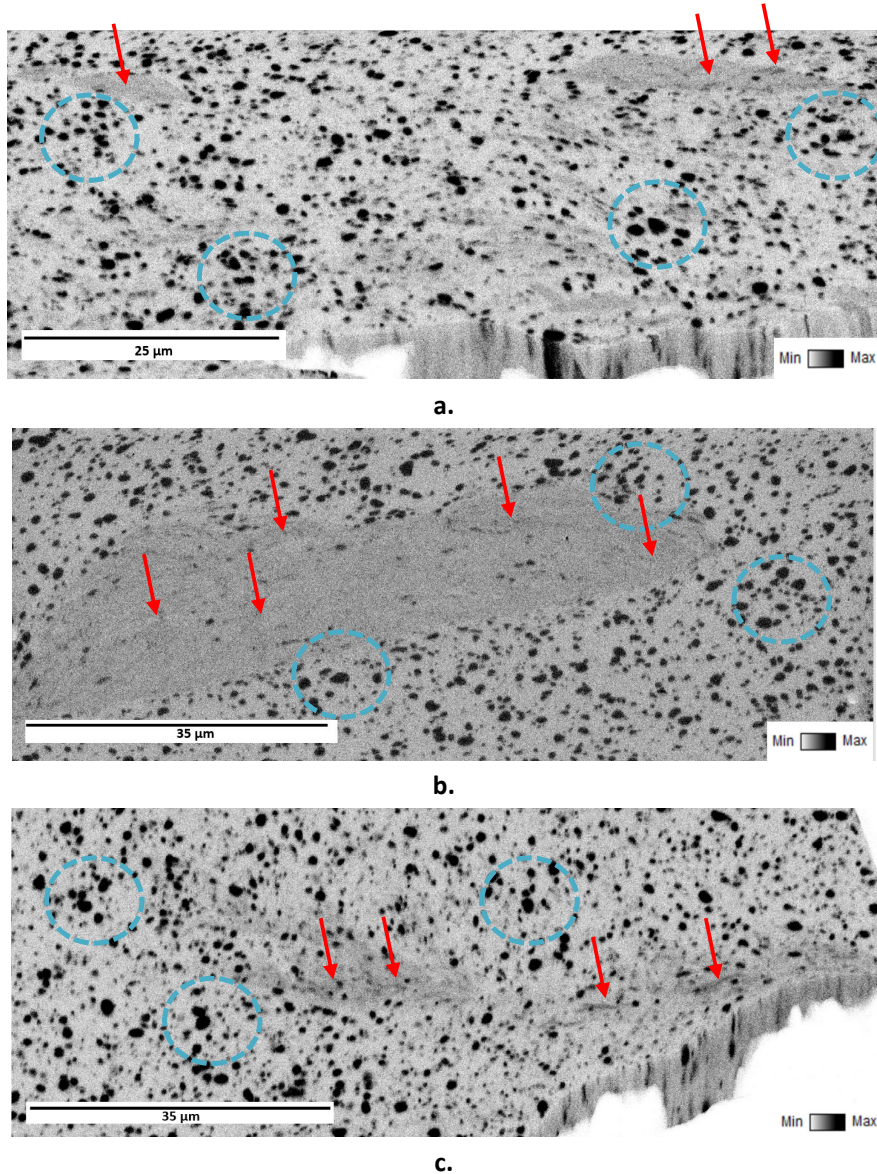


Figure 5-24 Chromium distribution and WEAs in Regions 2, 3 and 4 revealed by Chromium EDS maps. Blue circles show carbide clusters in the ferritic matrix, red arrows show Cr trails or comet tails inside SWEAs (Image b). and c)).

Although spherical carbides appeared dispersed in all directions, some clusters were visible in different areas (blue dotted circles). The WES were visible because of their different contrast compared to the ferritic matrix, indicating that they had a slightly higher C and Cr content than the matrix surrounding them. A significant reduction in the number of the spheroidal carbides was observed in the WES, especially those located in Regions 2 and 3. The carbides that remained in these WES were smaller compared to those located in the matrix, others seemed to flow in the same direction as the *fibre / layers* described in figure 5-19, leaving behind an ill-defined trail similar to a *comet tail*. These *comet tails* extended for significant distances and linked other small carbides



(Red arrows in figures 5-23 and 5-24). A similar phenomenon was visible in the Cr – EDS map, but with less intensity.

#### 5.4.2 Phosphorus and Aluminium content determined by EDS analysis

EDS analyses conducted in Regions 2, 3 and 4 reported signals from aluminium and sulphur as ill – defined dots in very localized areas inside the white structures. The study of these elements is important in understanding the role of inclusions in the evolution of TWEAs and SWEAs during HPT tests.

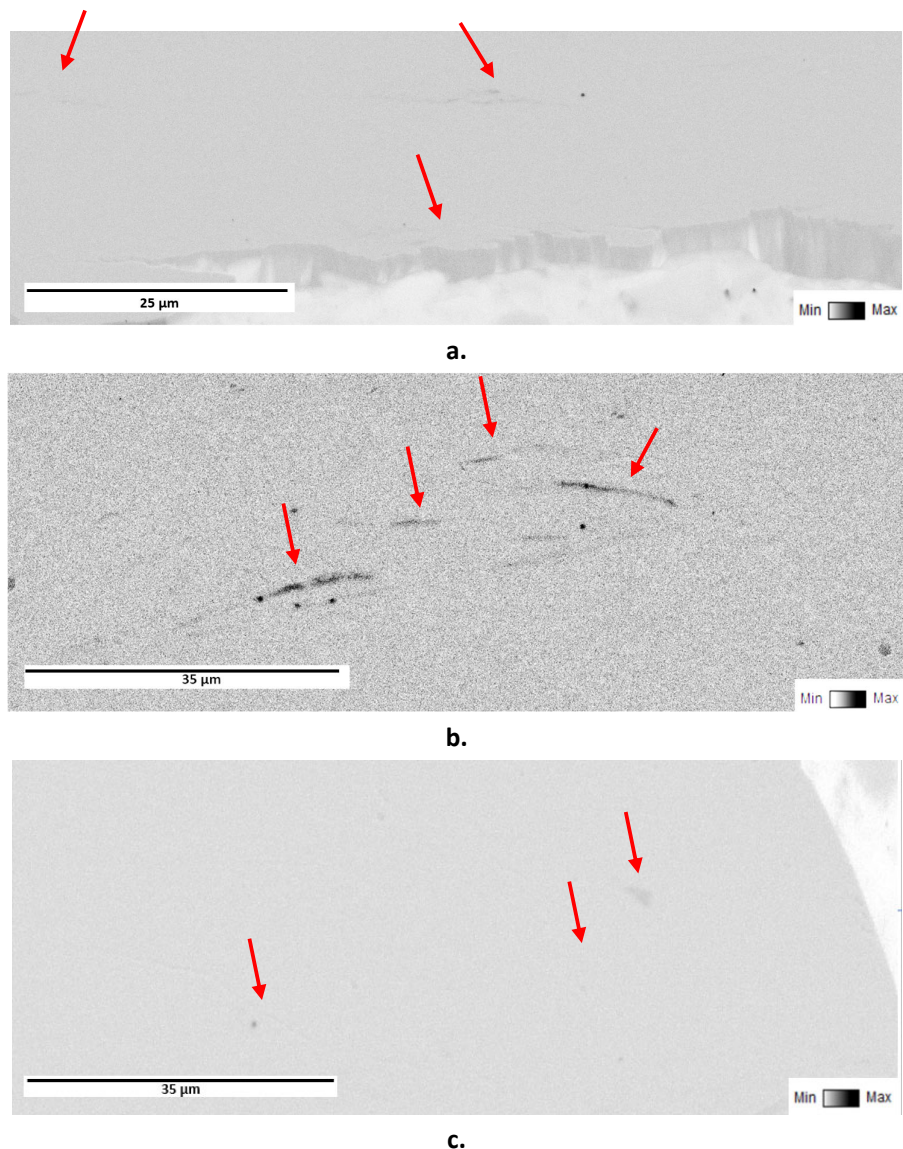


Figure 5-25 EDS maps of Sulphur in Regions 2, 3 and 4. Red arrows indicate the presence of significant signals that appeared as ill – defined dots (Images a). and c).) and *comet tails* (image b).). These signals are related to the presence of inclusions inside the TWEAs and SWEAs.

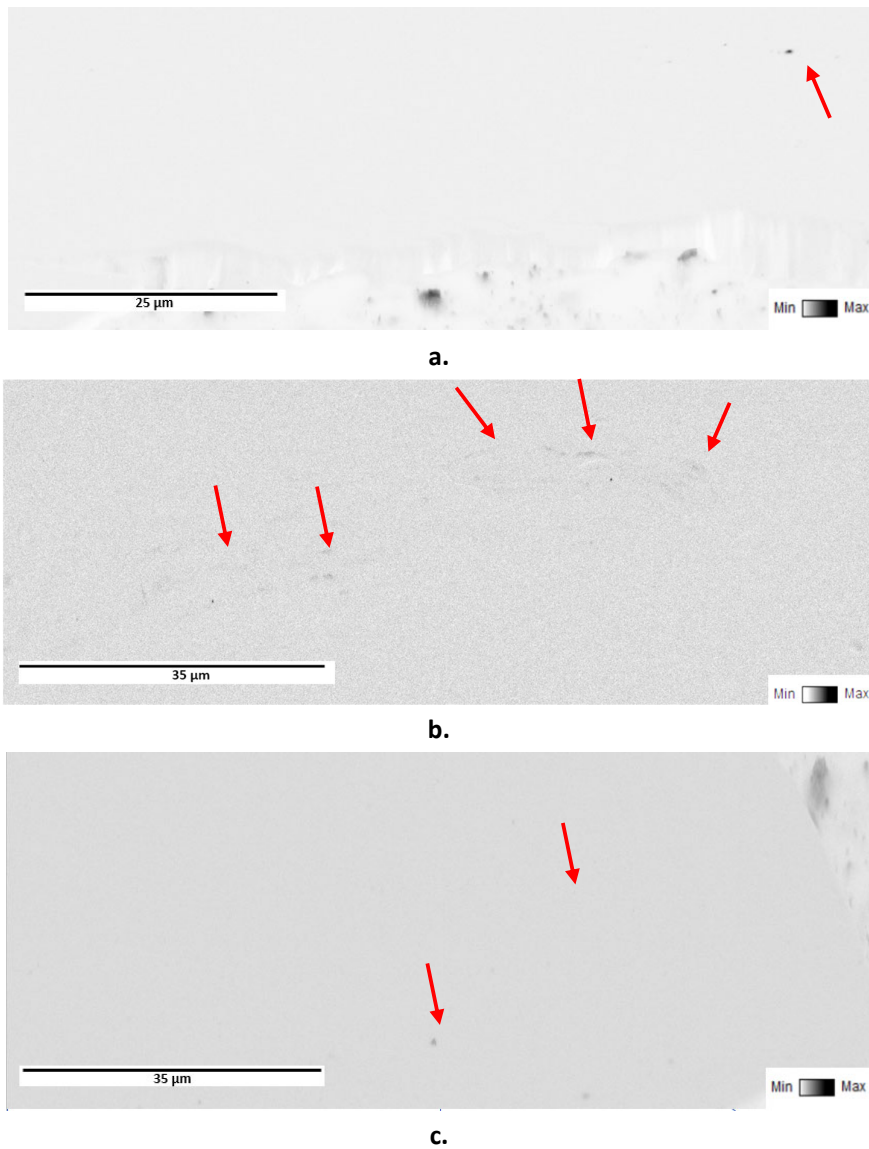


Figure 5-26 EDS maps of Aluminium in Regions 2, 3 and 4. Red arrows indicate the presence of significant signals that appeared as ill – defined dots which are related to the presence of inclusions inside the TWEAs and SWEAs.

The Sulphur and Aluminium EDS analyses conducted in Regions 2, 3 and 4 reported signals from Aluminium and Sulphur as ill – defined dots in very localized areas inside the white structures. These dots appeared linked to the *comet tails*, similar to those observed for Carbon and Chromium in figure 5-24 b). The dots correspond to dual-phase inclusions of Aluminium with Sulphur and Manganese commonly found in AISI 52100 steel. These inclusions could have a significant role in the initiation of the white structures, as they would interrupt plastic flow inside the samples during the HPT tests.



### 5.4.3 Carbide clusters

The long austenisation heat treatment time and the uniform and very slow cooling applied during annealing produced large ferritic grains, a relatively homogeneous carbide distribution and the total absence of austenite. However, some pearlitic structures were visible as parallel lamellae clusters in the material prior to be processed through HPT. (blue circles in figure 1-27 a). These cluster could be related to the origin of the carbide clusters observed after to conduct the HPT tests showed in figure 1-28.

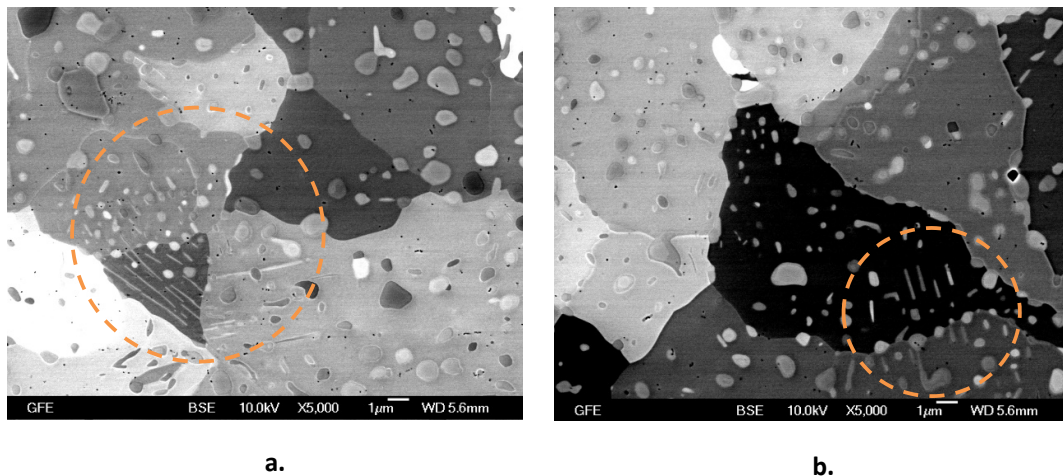


Figure 5-27. SEM / BSI images of pearlite clusters in the annealed AISI 52100 microstructure (orange circles). These clusters can irrupt plastic flow during the HPT test.

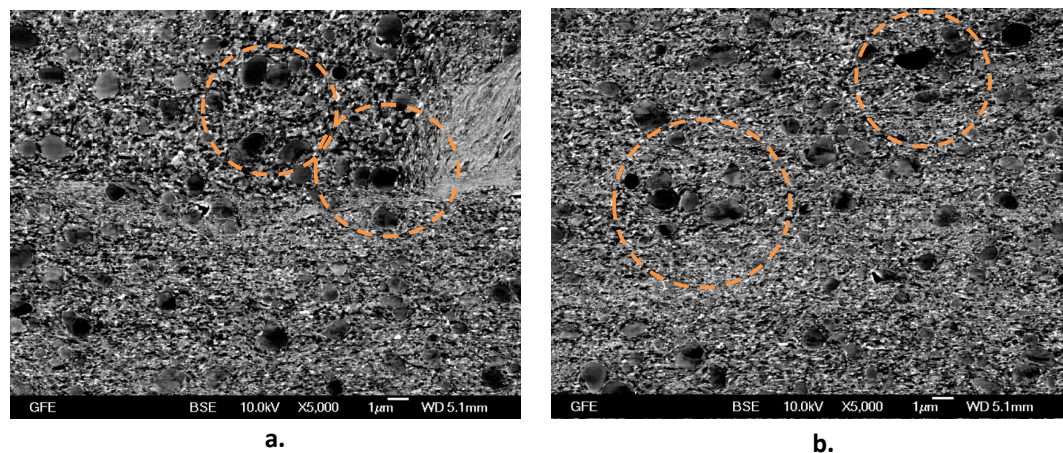


Figure 5-28. SEM / BSI of carbide clusters in the vicinity of the SWEAs showed in figure 5-17 (orange circles).



## Chapter 6      Origin and Evolution of WES

Based on the results obtained from the experimental work in this thesis and those presented in the literature review, different topics related to the microstructural evolution of annealed AISI 52100 in HPT tests are discussed in this chapter. Five main topics are considered in separate sections namely: the relevance of the parameters used for the HPT tests, some considerations on the results obtained from the SEM / BSI / EBSD / EDS characterisation, considerations on the formation of both TWEAs and SWEAs in disc samples, and finally, a comparison of the white structures observed in HPT tests and those found in failed rolling bearings (or WEAs).

### 6.1      HPT parameters

The knowledge accumulated over recent decades on SPD processes, has allowed the development of highly efficient methods to refine polycrystalline grains to nano metre scales. These advances have provided not only better machinery and tools to be used for the processes, but also suitable parameters to obtain ultrafine grain sizes efficiently. In this context, HPT has been one of the most prolific information sources on SPD processes, due to its long history and simplicity. Although no standard procedures have been established for HPT processes, a consensus is recognized by many researchers on the parameters necessary to produce ultrafine grains. However, these guidelines were not entirely adequate for the current research and this is discussed below:

#### 6.1.1      Hardness saturation and number of turns

Saturation in HPT tests implies hardness stabilization and material homogenization to produce an ultrafine grain size structure over the main part of the disc sample (except in some cases at the centre). This saturation is easily identifiable when the hardness measured at different radial distances is plotted against strain. For steels, the hardness shows a rapid increase with low strains, followed by an asymptotic tendency at very high number of turns (similar to that shown in Figure 2-35). To evaluate the effect of the strain imposed in the HPT tests conducted on the annealed AISI 52100 steel, the hardness was plotted against the shear strain using the data provided in figure 4-19. These plots presented in figure 6-1 showed significant scatter, except for the disc samples processed under 6 GPa. Logarithmic regression curves were also fitted to the data obtained from the HPT tests using 3 turns and the correlation coefficients are given in figure 6-1. A higher correlation coefficient was obtained for tests conducted at higher compressive stresses.

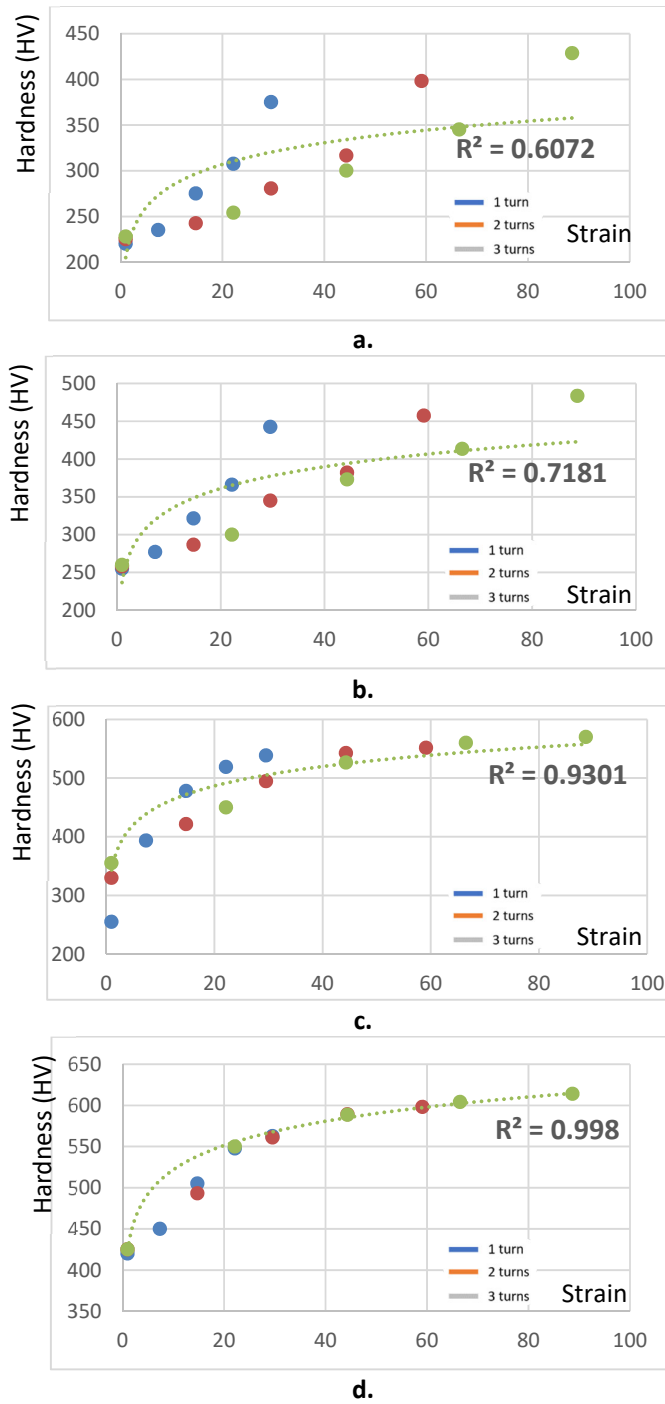


Figure 6-1. Hardness as a function to the strain for disc samples processed using a) 0.5 GPa, b) 1 GPa, c) 3 GPa and d) 6 GPa. The regression curves correspond to the disc samples processed using 3 turns.

The samples processed using 6 GPa and 3 turns showed very good agreement with similar curves reported for *without recovery* materials (see section 2.4.6). The curves in Figure 6.1 indicate that the most efficient way to process the annealed disc samples was using 6 GPa. Increase in processing pressure and number of turns (strain) led to higher hardness values and so to a more pronounced grain refinement [113]. Despite this, the hardness values did not show stabilization, suggesting that 3 turns were not enough to reach saturation and therefore, a complete nano grain refinement over the disc sample has not been reached.

### 6.1.2 The influence of pressure applied

To guarantee a successful HPT test, the cavities in the anvils must be fully filled with the disc sample material. To do this, the disc samples are deformed by the preliminary compressive stress applied before the rotation. The disc samples reproduce not only the size and shape of the cavities but also the roughness of their surfaces. If the friction force generated by the pressure is not enough to prevent movement between the anvil surfaces and the top and bottom sides of the disc samples during torsion, slippage between anvils and samples will occur. To avoid these problems, a minimum pressure equivalent to at least three times the yield strength of the material processed must be applied [113]. Taking the annealed 52100 steel yield strength as 427 HV from the correlation [114]:

$$Y_s = -90.7 + 2.876Hv \quad (6.1)$$

It's clear that this value is lower than three times the yield strength to pressures such as 0.5 and 1 GPa. Thus, these pressures are not the best options to process the annealed material. At 3 and 6 GPa, the ratio of compressive stress to yield strength is higher than three (7.14 and 14.29 times respectively), however, as was shown in Chapter 4, rotational movement between the disc sample and the anvils (slippage) was still registered in samples processed using 3 and 6 GPa. (See figure 4.-1 and table 4-1) However, as HPT progresses the hardness and thus yield strength of the steel increases and TWEAs form and hence a higher pressure might be then necessary to avoid slippage. In addition, other factors might also be important namely the roughness of the disc samples and the anvils.

### 6.1.3 Slippage

TWEAs only appeared on the top surface of the samples where slippage took place. This suggests that TWEAs could have formed as a consequence of the sliding taking place between the top surface of the disc and the anvil. Thus, to understand the origin of TWEAs, it is necessary to study slippage evolution. At the beginning of the HPT tests, the pressure imposed embedded the anvil asperities

in both top and bottom surfaces of the samples. Once torsion is applied the top surface of the sample in contact with the non-rotating anvil rotates but the anvil asperities slip producing grooves and deform the top surface (except for samples processed using 6 GPa). Thus, the circular patterns alternated by smooth and shiny areas were formed. Similar configurations have been reported as a usual feature on samples affected by slippage [115]; in this case, the frictional stress generated at the surface by the torsion in the HPT test is below the shear yield strength of the sample, thus the disc will not deform, and slippage occurs. Localized plastic flow takes place because of asperities sliding and the circular pattern features observed on the sample surface are formed. When the pressure is increased, the frictional stress at the surfaces will also increase and at certain point it will exceed the shear yield strength producing *sticking* between the surfaces in contact. In other words, this occurs when the friction is high enough to ensure that the surfaces are “stuck” to each other. Hence, the circular patterns reduce significantly until they disappear, whilst plastic flow begins inside the sample and the slippage starts to reduce [116] [117]. Significant % slippage reductions have been reported experimentally in Al, Cu and Fe when pressures are increased from 2 to 6 GPa. In the annealed AISI 52100 steel samples studied here the % slippage also reduced significantly as the pressure increased from 1 to 6 GPa (see table 4.1). The transition from slippage to plastic flow inside the sample is gradual, and both phenomena, slippage and sticking usually appeared together in different proportions [118]. To avoid slippage, a relatively high roughness of the anvils (approximately 30  $\mu\text{m}$  Ra) has been recommended [16].

#### 6.1.4 Surface roughness of the anvils

Nevertheless, the process described above cannot be used to explain the interaction between the bottom surface of the samples which reproduced the anvil roughness in all cases, generating the *orange peel* patterns. A similar behaviour has been described in a previous study, where the roughness of the anvils used to process stainless steels was carefully characterised [118]. Based on this examination it was concluded that the orange peel impression occurred on the lower surface of the disc because the roughness of the bottom anvil was higher than the top anvil. To demonstrate whether this was the case here, some sample discs were pressed using the HPT test machine under 1, 3 and 6 GPa to obtain an impression of the roughness of the anvils. The results of these measurements are summarised in table 4-3 and figure 4-11. The top surfaces of the disc samples in contact with the non-rotating top anvil had smaller values of all roughness parameters evaluated (Ra, Rq, Rz) than the lower surfaces in contact with the rotating anvil. figure 4-11 also shows that some parts of the top surface, arrowed, had no impression of the anvils indicating that over some areas of the sample there was no contact between anvil and sample. Regarding the latter, it

important to highlight the procedure used to prepare the disc samples prior to conducting the HPT tests.

After cutting the disc samples from the annealed rollers, the disc samples were ground on both sides using 800 and 1200 grade silicon carbide papers to reduce their thickness to 0.8 – 0.9 mm. Although sample thickness was measured several times during the grinding processes by a micrometre, it was not possible to guarantee that the thickness across all the sample was completely uniform and thus that the top and bottom sample surfaces were completely parallel to each other. Although the variations in thickness were very small, less than approximately 60  $\mu\text{m}$  (table 4-4), this variation could be enough to create areas that did not have contact with the anvil asperities at lower pressures. At higher pressures, the deformed material finally contacted all the anvil asperities eliminating these flat areas where there was no contact with the anvils.

The lower roughness of the top anvil could act to produce lower frictional forces between the top anvil and the top surface of the disc and thus aid slippage and the possible generation of TWEAs. However, because the bottom surface of the anvil has a higher roughness ( $R_z$  results particularly close to 30  $\mu\text{m}$ ), the pressures applied were sufficient to generate a significant real contact area and hence, with higher frictional forces, slippage did not occur on the bottom disc surface.

## **6.2 Advanced characterisation results**

### **6.2.1 EBSD analysis**

Several details of the microstructure of TWEAs and SWEAs and their relationship with the ferritic matrix that could not be ascertained by LOM and SEM / SEI images were revealed through EBSD analysis. Firstly, SEM / BSI revealed how the initially relaxed ferritic grains (figure 5-14) were replaced by a very refined and deformed structure without clear grain boundaries (figures 5-16 to 5-18). However, these images showed multiple grey tones, suggesting variations in orientation of the ferrite grains as SEM / BSI images are sensitive to crystallographic orientation at lower voltages. The carbide distribution also looked different after HPT, some of the carbides appeared in clusters, whilst other areas appeared free from carbides. This carbide distribution could result from the plastic flow generated during the HPT tests that dragged the carbides. However, the most significant feature is the clear difference between the matrix and its carbides and the white structures visible in figures 5-16 to 5-18.

Both TWEAs and SWEAs were more visible in the IQ maps where they appeared clearly differentiated from the matrix due to their darker contrast (using the qualitative grey scale cited at the bottom right corner in the IQ images of figure 5-19). IQ showed that these dark regions



extended over significant areas with different configurations namely *fibre / layers* that seemed to be stacked close to the top of the surface (region enclosed by the red dotted line in figure 5-19 a)) and swirls (vortices) resembling the patterns produced in turbulent flow (*fibre / layers* inside the white structure in the IQ image in figure 5-19 b)).

The grey scale in the IQ images indicates the intensity of the diffraction patterns obtained from Regions 1 to 4 defined in figures 5-16 to 5-18 respectively, the brighter and clearer regions resulting from areas with well-defined diffraction patterns [119]. Many factors can influence these IQ maps, for example the proximity of grain boundaries, high dislocation contents and lattice distortion produced by plastic deformation. This can lead to the superposition of the signals generated from individual crystal lattices and thus produce poor diffraction patterns. Moreover, other factors such as nanocrystalline structures and defects such as cracks can produce the total absence of indexed diffraction patterns [111] [62]. Hence, the dark contrast observed in the WEAs can be a consequence of one or more of these factors.

However, the WES also appeared as black areas in AP, IPF and KAM, suggesting a total lack of indexed diffraction patterns from these areas resulting from a nanocrystalline structure (figures 5-20, to 5-22). Thus, this is also the most likely explanation for the findings from the IQ maps. In addition, AP maps showed small ferritic *fibre / layers* inside the WES. Fibres were more visible in Region 3 (figure 5-20 b)), corresponding to a well-defined SWEA. AP images also showed clear differences between the ferritic matrix and the carbides, compared to the SEM / EBSI and IQ images. Despite the new ferritic grain sizes being less than 2  $\mu\text{m}$ , it was possible to obtain information on their texture through IPF and KAM maps (figures 5-21, 5-22). IPF confirmed the well-refined condition of the ferritic matrix and the absence of any preferential orientation in the ferritic grains, both features previously observed in SEM / BSI. In addition, the average misorientation between each pixel and its nearest neighbours in the KAM maps, suggest homogeneous and low misorientation angles (figure 5-22). These results indicate the lack of relaxed new grains produced by recrystallization [120] [121].

### 6.2.2 EDS analysis

The large decrease in the amount of carbides inside the WES registered in SEM / BSI images was confirmed by EBSD and EDS analyses. All EBSD maps from the WES registered a significant reduction in the cementite patterns detected in them, whereas the EDS signals taken from the same areas indicated a carbon and chromium redistribution (figure 5-23 and 5-24). The changes observed in the remaining carbides such as size reduction and their elongated shapes, suggest a progressive degradation. This degradation is visible as *comet tails* extending with the *fibre / layer* structure

following the plastic flow direction. Thus, carbon and chromium are dragged from the carbides and dissolved in the nanocrystalline arrangement present in the white structures. As carbon has a lower atomic number than chromium, this diffusional process is more visible in the Carbon EDS maps. Figures 5-23 and 5-24 also showed how the dissolved carbon and chromium are distributed throughout the entire white structure. The darker contrast of the ferritic matrix registered in both EDS maps indicates that the carbon and chromium content is slightly higher in the white structures than in the matrix.

## 6.3 TWEA formation

### 6.3.1 Fibres / layered structure formation

Sample axial sections revealed how TWEAs form on the top surfaces as an arrangement of many small white structures distributed without a particular pattern. Some of these formed complex systems over significant areas, other appeared isolated from the top surface and from other white structures (figures 4-18 d), 5-7, 5-15, 5-16). In all cases, TWEAs were located at depths less than 100  $\mu\text{m}$ . TWEAs consisted of a fibrous / layered structure that extended parallel to the top surface in some regions but containing swirls or vortices in other places. The origin of the fibres / layers seems to be related to the strain and plastic flow caused by the interaction between anvil asperities and the sample surface during slippage. As their geometry was not regular, anvil asperities could create heterogeneous flow conditions in very localized places causing small neighbouring regions to flow under different conditions, generating *interactions* between them. As a result, the *interactions* could produce shear instabilities, atomic scale mixing, and the generation of nano eddies or vortices at the sliding interfaces [88] [87]. As a consequence, the interface between the neighbouring regions could change to nano fibres / layers with different mechanical properties [120]

The nature of these fibres / layers in the annealed AISI 52100 is not completely understood but could be related to transformation mechanisms observed under SPD conditions, such as segregation and diffusion of interstitial elements through “non-equilibrium” grain boundaries [121] the formation of high density dislocation clusters (called by some authors dislocation cores) and even the generation of new structures by dynamic recrystallization [11]

As slippage progressed, new fibres / layers were formed and stacked over each other. Different flow conditions could appear between the deformed matrix and the stacked fibres, recreating new heterogeneous flow conditions. Thus, the process described above could take place several times until structures at a micro scale are produced. An example of these phenomena can be observed in figures 5-7 to 5-8, 5-16 and 5-19 a) where the stacking fibre /layered structure is easily visible in

regions close to the top surface. The differences between the mechanical properties of these new fibrous / layered structures (the TWEAs have a higher hardness than the ferritic matrix) and the ferritic matrix could also explain the beginning of small cracks around the fibres / layered structures. The soft ferrite could tend to flow more easily around the TWEAs than through them (figure 5-8). This movement could continue until the interface cannot support the flow and the excess energy accumulated is liberated through crack formation.

At higher strains, bigger vortices appeared affecting ever larger regions. The vortices by themselves could provide more conditions where more *interactions* take place to generate new fibres / layers and so extend the TWEAs. The nature of these bigger vortices is not related directly to the atomic interaction and will be discussed later for the SWEAs case. However, voids and cracks could progress creating bigger crack networks on a micro scale and are possibly responsible for the detachment of significant portions of the deformed surface.

### 6.3.2 Carbide distribution

The changes in the carbides between the deformed ferritic matrix and the TWEAs are significant. Firstly, fewer carbides were observed inside the TWEAs and their distribution between the fibres was non-uniform, compared to the relative homogeneous distribution in the matrix (figure 5- to 5-8). Secondly the carbides in the TWEAs were smaller, elongated and looked fracture (Figure 5-6). Based on these observations, it would appear that the shear stress produced by the slippage was responsible for the transformation of the ferrite matrix and the carbides located close to and inside the TWEAs. This transformation could include grain refinement and diffusion of carbon from the carbides to the matrix, as a part of a dynamic recrystallization process in regions close to the surface. Similar transformations have been considered to explain the formation of white layers in AISI 52100 by hard turning and drilling machining processes [122] [123] [124] at temperatures below any phase transformation, i.e. without static recrystallization promoted by high temperatures.

### 6.3.3 TWEAs reduction with number of turns and pressure

Apparently, the amount of TWEAs decreased when the number of turns was increased, as was shown in table 4-2 and with increase in compressive stress applied. The decrease in TWEAs resulted from two main causes, wear and slippage reduction. In the first case, material detached from the top sample surface due to its rotation with respect to the top anvil because of severe sliding wear. It is clear that TWEAs have higher hardness than the matrix, but less than the anvil asperities. If these asperities slide against the TWEAs after one or more turns, they could detach these areas

eventually producing wear debris that becomes trapped between the surfaces in contact, generating a three body wear system [125] Figure 4-7 shows some of the debris collected from the top anvil after conducting HPT tests, classic sliding wear features appear on their surfaces as has been reported by [126]. Moreover, the reduction in slippage caused by the increase of pressure influenced directly TWEA formation. This phenomenon is visible on samples processed using 6 GPa, where both top and bottom sides reproduced the roughness of the anvils as an orange peel pattern without TWEAs.

## 6.4 SWEA formation

### 6.4.1 Strain and strain rate distribution

Equation 2.14 predicts the strain in HPT tests is constant throughout the thickness of the sample discs but changes linearly with radial distance [12]. Thus, no significant variations in the mechanical properties or microstructure should be expected in the thickness direction, i.e. on surfaces of axial sections. This model has good experimental support when the materials have reached a saturated condition, usually after applying high pressures and several turns, however significant differences appear when low strains are imposed. Some studies in Mg, Al,  $Zr_3Al$ , iron and pearlitic steels have shown dissimilarities in terms of hardness distribution and microstructure on the axial sections of samples which suggests a non-homogeneous strain distribution inside the samples and changes in the plastic flow [113] [127-129]. Moreover, FEM simulations have reported concentration of the strain at the centre of the diametral axial section, with the highest values at the edge. The strain rate also appeared greater in this region, with values increasing with radial distance [80] [130] [131].

It is clear the annealed AISI 52100 samples did not show a homogeneous strain distribution after being processed by HPT. The parameters used to conduct the HPT tests did not allow a completely refined grain structure with similar mechanical properties to be achieved everywhere. On the contrary, the samples showed microstructural changes across the whole thickness, such as evidence of localised high plastic deformation in the ferritic matrix, cracks and the formation of the subsurface white structures (SWEAs). These SWEAs seem to be located parallelly to the top or bottom surfaces at a radial distance of 3.5 – 5 mm (figure 4-17).

Considering that the high plastic flows, expressed as higher strain rates, allow conditions to generate white structures (as was discussed for the TWEAs case), the concentration of SWEAs at the edge of the samples could be justified [80] [129]. However, the plastic flow at the edge of the sample can vary significantly due to other complex factors, such as the friction against the vertical cavity walls [130], the friction between the flash and anvils outside the anvil cavities [131] or the

formation of Dead Metal Zones (DMZs) [132]. Hence, the study of plastic flow in this region is complex.

#### 6.4.2 SWEA formation

Figures 5-11 and 5-13 shows SEM /SEI images from a solid linked to cloud SWEAs. These images were from a region close to the edge of a sample processed using 3 GPa 2 turns. The SWEA structure looks similar to that observed in the TWEAs case (see figure 5-6). A fibrous structure has replaced the deformed matrix and the carbide content is much reduced inside it. However, there are some differences. Firstly, the fibres tend to be thinner, more compact and bonded to each other in the SWEAs especially at locations far from the SWEA matrix interface. Secondly, just a few carbides appeared inside the SWEA cores suggesting a partial or complete dissolution of the carbides inside the SWEAs. Thirdly, the SWEA fibrous structure looked more deformed and bonded, suggesting a higher incidence of *turbulence* flow. The interaction between regions that flow under different conditions discussed for the TWEAs case could be present for the SWEAs as well, supporting the same transformation mechanisms (diffusion of carbon, the formation of high-density dislocation clusters and possible dynamic recrystallization). However, in this case, two factors replace the interaction of asperities on the anvil and sample. Firstly, the edge of the samples suffers from a *border effect*, where there are several factors that can alter the plastic flow of the material. Secondly, the interaction with *strong obstacles* such as inclusions or carbide clusters can promote vortex generation and with them the beginning of fibres between neighbour regions affected by different plastic flow conditions.

#### 6.4.3 Vortices

According to FEM simulations [80] [129], the same strain rate is registered over all the axial section at the same radial distance (except in regions very close to the edges i.e. at maximum radial distances) but decreases towards the centre of the sample. But the plastic flow was not organised. Unusual flow patterns such as swirls or vortices and tracks of *local turbulence* have been found previously in high-purity aluminium and a Zn–22%Al eutectoid alloy processed by HPT. The patterns resembled the vortices associated with Kelvin–Helmholtz instabilities in fluids, which could occur where there are local shear velocity gradients between adjacent positions. Despite the similarities between both phenomena, Kelvin–Helmholtz instabilities require inertial forces in rapidly flowing low viscous fluids at high Reynolds numbers. However, plastic flow in metals has a very small Reynolds number because of the high viscosities and the very low flow velocities. Thus, Kelvin–Helmholtz instabilities do not appear to explain these *turbulence* patterns [82].

Some authors have suggested that their origin is linked to dislocation-mediated plastic flow, with suitably oriented slip systems. Subsequent folding could be explained by the inhomogeneity of plasticity on polycrystalline surfaces which favours bulge formation on a scale of the grains [133]. However, the vortices observed are much larger than any grains, suggesting that another factor must be related to their evolution. An interesting alternative to explain the formation of vortices in a deformed material under simple shear is the presence of constituents that generate local blocking of the shear deformation. FEM simulations supported by experiments have shown how the local blocking of the shear causes rotation around *strong obstacles*, which leads to the formation of vortices at a sufficiently large shear strain [81] [85] [134]. The nature of these *strong obstacles* is highly interesting, because they could define not only the size of the vortices but also their position.

SEM images taken from cloud and small solid SWEAs found in different annealed AISI 52100 samples processed by HPT show a twisted and folded fibrous structure that overlapped the ferrite matrix (figure 5-10 to 5-13). The carbide distribution in the SWEAs vicinity differs from the random distribution observed in other ferritic matrix regions unaffected by the SWEAs. The carbides seemed to have been dragged from the matrix by a flow force that surrounded the WEAs. Some carbides appeared deformed and linked to the coil fibres (figures 5-11 b) and 5-13b). From these images, it is possible to affirm that cloud SWEAs have features similar to the turbulence patterns described previously, thus, their origin could be linked as well. However, the nature of the *strong obstacles* present in the annealed 52100 samples are not clear but could be associated with carbide clusters, pearlite colonies or non-metallic inclusions.

#### 6.4.4 Carbide clusters and inclusions

The characterisation of the annealed AISI bearing steel prior to being processed by HPT tests revealed the presence of pearlitic structures grouped in very well-defined clusters. Their origin is a result of an incomplete transformation of the cementite lamellae into spheroids during cooling from the annealing temperature. Due to their shape, size and proximity, the pearlitic lamellae can distort the neighbouring matrix acting as a stress concentrator capable of interrupting plastic flow during HPT tests. In addition, the proximity of the ferrite and cementite lamellae and the long contact area between them can facilitate carbon diffusion [11]. Figure 5-27 shows two examples of pearlitic clusters found in Region 1 corresponding to the annealed AISI 52100 prior to being processed by HPT. Other carbide clusters were observed in all regions analysed after to conduct HPT tests, some of them are visible in the figure 5-28.

Moreover, EDS analyses conducted in Regions 2, 3 and 4 reported signals from aluminium and sulphur as ill – defined dots in very localized areas inside the white structures. These dots appeared

linked to the *comet tails*, similar to that observed for carbon and chromium in Figure 5-26). The dots correspond to dual-phase inclusions of aluminium with sulphur and manganese. These inclusions could have a significant role in the initiation of the white structures, as they would interrupt plastic flow inside the samples during the HPT tests. Non-metallic inclusions have also been suggested to play a role in the initiation of WEAs in failed bearings [137 - 139]. They might not only act as stress concentrators but also interact with the plastic flow and help to generate WEAs.

## 6.5 Comparison of WES and WEAs in failed bearings

Table 6-1. Comparison of TWEAs /SWEAs and WEAs. Material prior to transformation.

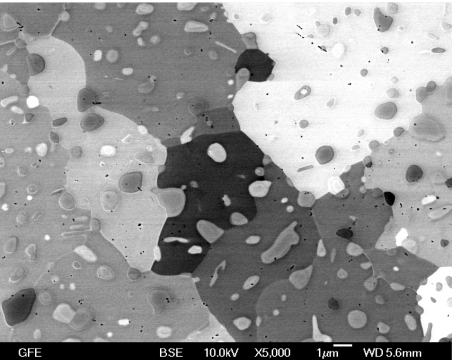
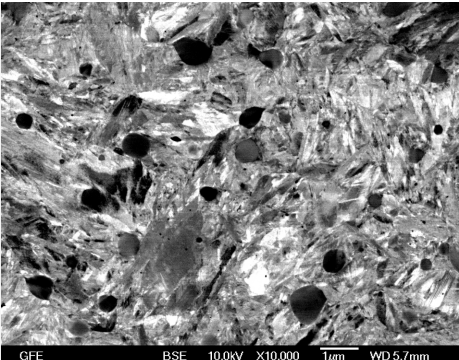
WES	WEAs
<p><b>Heat treatment:</b> Annealed condition  <b>Original hardness:</b> <math>180 \pm 10</math> HV  <b>Microstructure:</b></p> <p>Prior austenite grain boundaries, ferritic matrix containing spheroidal carbides (cementite) distributed relatively uniformly. [104]</p>  <p>GFE BSE 10.0kV X5,000 1µm WD 5.6mm</p>	<p><b>Heat treatment:</b> Quenched + tempered  <b>Original hardness:</b> 700 – 900 HV  <b>Microstructure:</b></p> <p>Tempered martensite with small amounts of retained austenite, primary carbides (cementite particles), and temper carbides (secondary or coherent carbides). [23]. Phase proportions can vary with tempering parameters</p>  <p>GFE BSE 10.0kV X10,000 1µm WD 5.7mm</p>



Table 6-2. Comparison of TWEAs /SWEAs and WEAs. Microstructural morphology

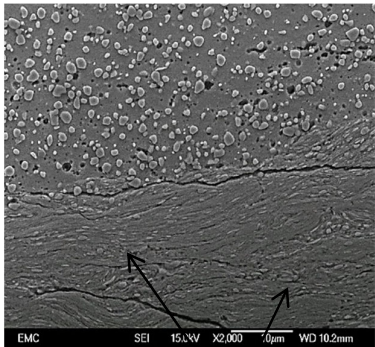
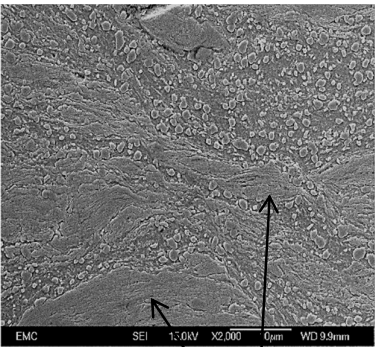
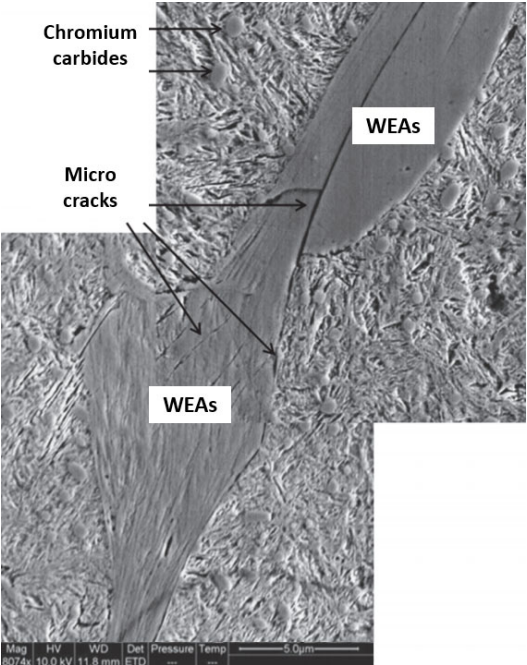
WES	WEAs
<p data-bbox="363 308 867 504">Fibre / layered structures that looked affected by the plastic flow. Some cracks appeared with the same orientation as the fibres, others at the interface between the matrix and within the TWEAs / SWEAs</p> <div data-bbox="444 554 816 940"><p data-bbox="646 915 711 940">TWEAs</p></div> <div data-bbox="444 974 816 1360"><p data-bbox="639 1335 704 1360">SWEAs</p></div>	<p data-bbox="889 308 1438 436">Aligned / fibrous morphology with micro-cracks throughout the WEAs oriented along the length of the WEAs and along the interface between the matrix and WEAs</p> <div data-bbox="919 611 1443 1272"><p data-bbox="959 632 1057 680">Chromium carbides</p><p data-bbox="976 772 1040 821">Micro cracks</p><p data-bbox="1276 722 1341 747">WEAs</p><p data-bbox="1073 999 1138 1024">WEAs</p><p data-bbox="919 1247 1289 1272">Mag HV WD Det Pressure Temp 5.0µm 2024x 10.0 kV 11.8 mm ETP</p></div> <p data-bbox="889 1310 1084 1339">Adapted from [3]</p>

Table 6-3. Comparison of TWEAs /SWEAs and WEAs. Texturing

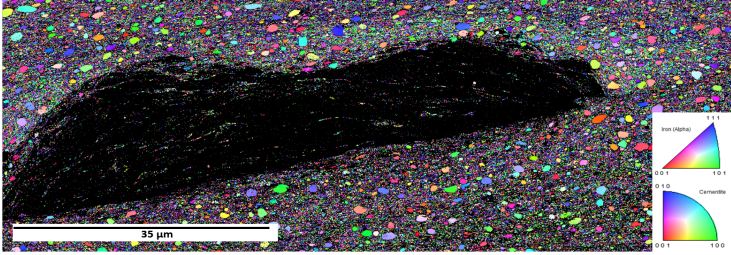
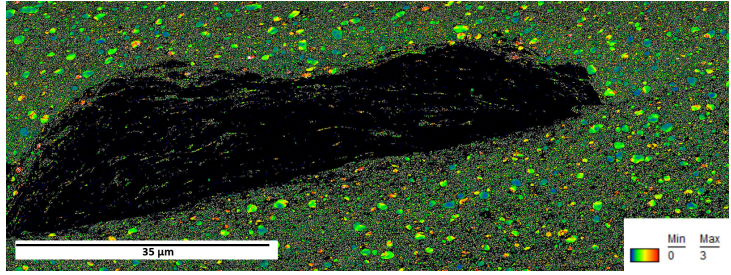
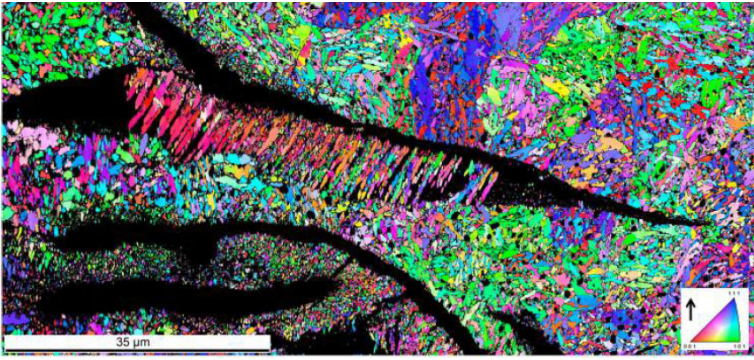
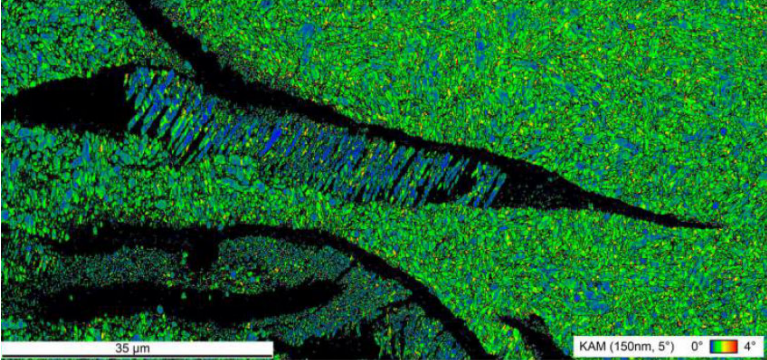
WES	<p>Poor diffraction patterns (black regions) indicate nano structures in SWEAs.            Ferritic grains exhibit the same size and shape features.            No preferential orientation of grains in the vicinities of the SWEAs.            No recrystallized structures.</p> <p><b>IPF</b> z axis</p>  <p><b>KAM</b></p> 
WEAs	<p>Poor diffraction patterns (black regions) indicate nano structures in WEAs.            Different grain structures appeared inside WEAs            Blue regions in KAM indicates recrystallization close to cracks</p> <p><b>IPF</b> z axis</p>  <p><b>KAM</b></p>  <p>Adapted from [61]</p>



Table 6-4. Comparison of TWEAs /SWEAs and WEAs. Inclusions

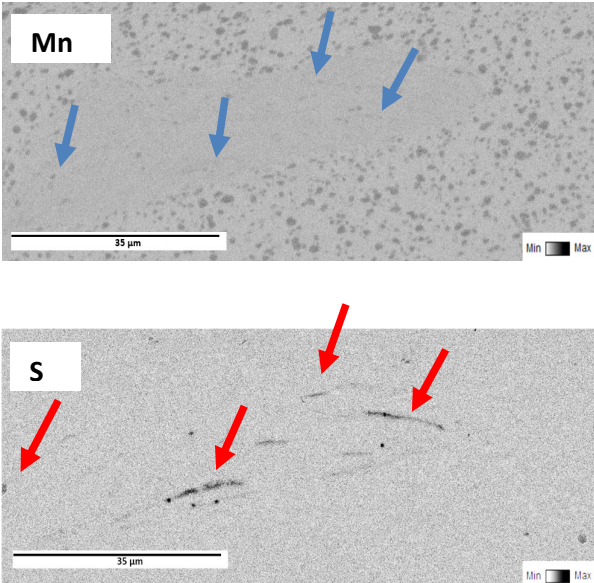
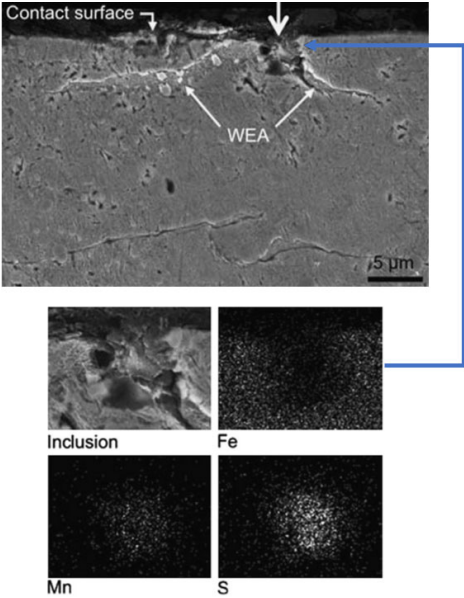
WES	WEAs
<p>MnS inclusions appeared inside TWEAs and SWEAs, they interrupt plastic flow creating vortices. Arrows indicate inclusions</p>	<p>MnS inclusions appeared close to WEAs and cracks, they act as stress concentrators</p>
	
	<p>Adapted from [8].</p>

Table 6-5. Comparison of TWEAs /SWEAs and WEAs. Carbide distribution

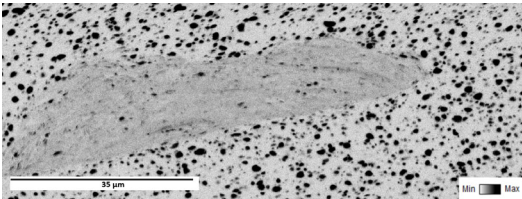
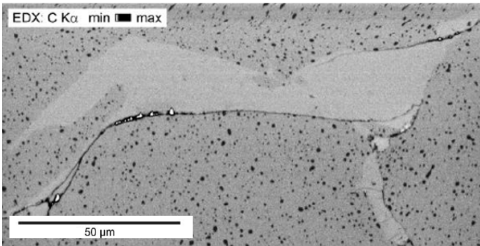
WES	WEAs
<p>Absence of carbides inside of the TWEAs / SWEAs. Carbon diffuses into the TWEAs / SWEAs nano grain structure, increasing their carbide content.</p>	<p>Absence of carbides inside of the TWEAs / SWEAs A diffusional carbon process take place, but the final carbon content inside of WEAsel is less than the registered to the matrix</p>
	
	<p>Adapted from [62]</p>

Table 6-6. Comparison of TWEAs /SWEAs and WEAs. Mechanical response

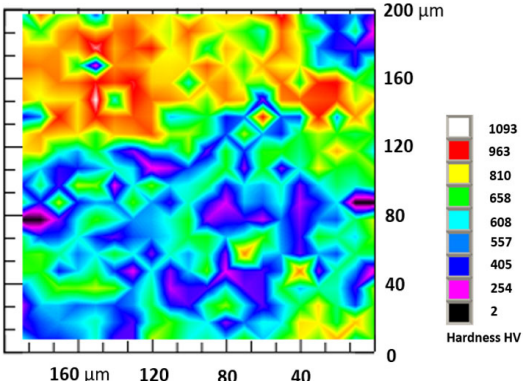
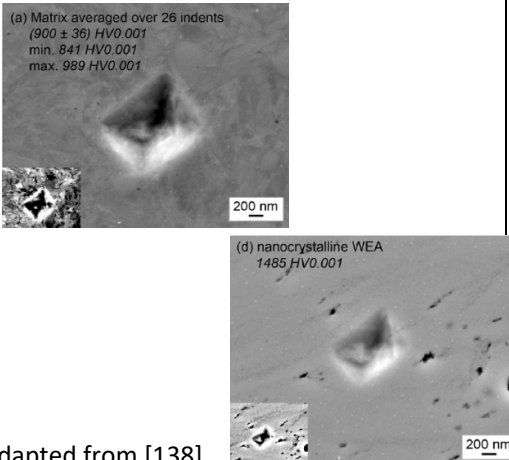
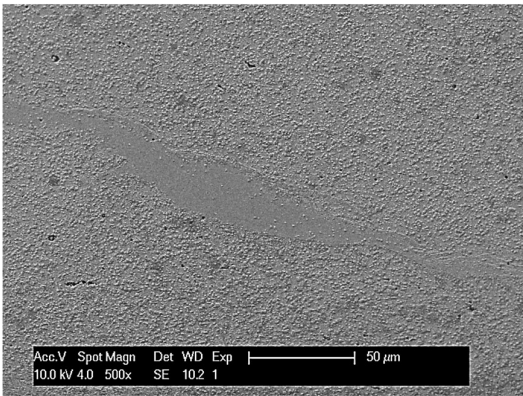
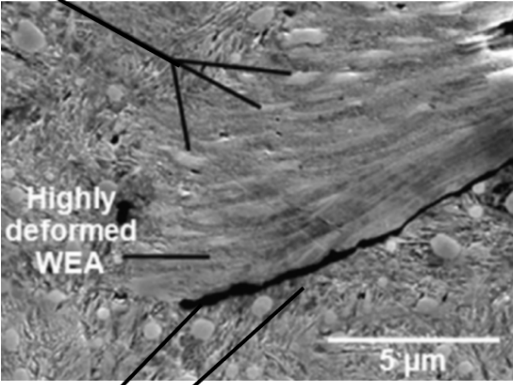
WES	WEAs
<p>Nanoindentation shows that the white structures can exceed by 24 - 46 % the hardness of the ferritic matrix</p> 	<p>Nanoindentation shows that the white structures can exceed by 65 % the martensitic matrix hardness</p>  <p>(a) Matrix averaged over 26 indents (900 ± 36) HV0.001 min. 841 HV0.001 max. 989 HV0.001</p> <p>(d) nanocrystalline WEA 1485 HV0.001</p> <p>Adapted from [138]</p>

Table 6-7. Comparison of TWEAs /SWEAs and WEAs. Cracks

WES	WEAs
<p>Apparently, there are some SWEAs without cracks in their vicinity as illustrated in this image of SWEAS located at the edge of a sample processed by 6 GPa 1 turn</p> 	<p>Cracks usually appeared close to the WEAs</p>  <p>Deformed carbides</p> <p>Highly deformed WEA</p> <p>Cracks</p> <p>Adapted from [1380]</p>

The white etching regions found in HPT tests on annealed 52100 strongly resemble those found in WEAs from rolling contact fatigue in failed bearing. However, two features are different. Firstly, cracks are not always associated with the white etching areas in HPT tests. This may arise because the high compressive stresses present in HPT might well affect the propensity for crack formation.

This could indicate that cracks are not necessarily a precursor to white etching areas, rather white etching areas form before cracks. Secondly, recrystallized grains are not found in the SWEAs and TWEAs produced by HPT but are present close to crack boundaries in WEAS in rolling contact fatigue. It is suggested that rubbing of the crack surfaces caused by the cyclic shear stresses in RCF could lead to the generation of sufficient heat to locally increase the temperature to a value sufficient for recrystallization to occur. As rubbing of cracks does not take place in HPT as there are no cyclic shear stresses hence recrystallized grains are not found in SWEAs and TWEAs in HPT.



## Chapter 7 Conclusions and future work

This chapter presents the conclusions from this study related to white etching areas found in annealed AISI 52100 processed by HPT. In addition, some future work that could be undertaken as a follow up to this study is described in section 7.2.

### 7.1 Conclusions

1. Several HPT tests were conducted on annealed AISI 52100 bearing steel to study the microstructural changes developed under SPD conditions and to generate *white etching structures* similar to the WEAs found in rolling bearings affected by WSF. Different combinations of pressures (0.5, 1, 3, 6 GPa) and number of turns (1, 2, 3) were used to produce these *white etching structures*. All tests were conducted at ambient temperature, under non-lubricated condition and with the same rotational speed (1 rpm). In addition to the expected grain refinement of the annealed structure, two white structure groups were observed, one at the top surface of the disc samples (designated Top White Etching Areas – TWEAs) and the other located subsurface, at a depth of between 240 – 360  $\mu\text{m}$  from the bottom surface of the disc samples (designated Subsurface White Etching Areas – SWEAs).
2. The HPT tests conducted on the annealed AISI 52100 were influenced significantly by the hardness of the material prior to the tests, the hardness of the anvils and the roughness and integrity of the circumferential surfaces in contact. These factors are usually not important in HPT tests when materials are processed using higher strains and pressures or when the initial hardness is low. The effect of these factors was evident in three ways:
  - As the maximum hardness of the samples tested in HPT cannot exceed that of the anvils, in order to prevent their damage, and the steel samples strain harden during testing, the strain imposed in HPT is limited. If the final hardness of the steel is to be less than 800 HV the maximum strain that can be imposed in the samples is limited to a value of less than that produced by the combination of 3 turns and a radial distance of 5 mm ( $\gamma = 88.7$  using Eq. 2.1). This level of strain was not sufficient to reach a saturation condition, which meant that a homogeneous ultrafine – grain size microstructure and similar hardness were not obtained throughout the whole sample.
  - As an AISI 52100 bearing steel exhibits a *non-recovery response*, the evolution of hardness with strain can be approximated by a logarithmic curve. The best correlation of the hardness data to this logarithmic curve was obtained in samples processed using 6 GPa, suggesting that this pressure, rather than a lower one, was more suitable to



obtain an ultrafine – grain structure by HPT. Unfortunately, the hardness limitations on the anvils meant that processing the material beyond three turns was not possible.

- Evidence of slippage between the top surface of the sample and the anvil was observed after conducting the HPT tests. Grooves and TWEAs were visible as circular patterns on the top surface of the sample. In addition, the relative angular displacement measured between sample and anvils after the test was larger at lower pressures. Slippage was caused by two factors: Firstly, low pressures cannot ensure “sticking” between the top sample surface and the top anvil because of the relatively high hardness of the 52100 steel; secondly, the surface finish on the top anvil was smoother than that of the bottom anvil, which resulted in less contact between anvil asperities and the top surface of the disc samples from the compression and thus less friction. As a result, sliding occurred between the top surface of the disc and the anvil producing abrasion and adhesive damage, whilst the bottom surface of the disc in contact with the rougher anvil where more friction was present, remained “stuck” to it and reproduced its surface finish.

3. TWEAs covered the top surface of the samples as many white structures, some isolated and other more interconnected that seemed to follow the circular tracks on the sample. Axial sections of samples showed TWEAs as an arrangement of small white structures distributed with no particular pattern at depths of less than 100  $\mu\text{m}$ . SWEAs, on the other hand, varied in size and shape with radial distance, from spots with ill-defined borders to well defined solid structures. The regions with ill-defined borders, which looked similar to swirled clouds (*cloud* SWEAs), appeared in various regions in random patterns. *Solid* SWEAs appeared largely at the edge of the samples. TWEAs and SWEAs shared a similar morphology, which consisted of a *fibrous / layered* structure that seems to follow patterns imposed by the plastic deformation.

4. SEM / SEI / BSI and SEM / EBSD / ESD revealed details of the microstructure of the disc samples after conducting the HPT tests:

- SEM / BSI revealed that the ferritic matrix had a very refined and deformed structure without clear grain boundaries. The carbide distribution was altered by the plastic flow generated during the HPT tests; it dragged them, creating carbide clusters.
- IPF confirmed the well-refined condition of the ferritic matrix and the absence of any preferential orientation of the ferritic grains, whilst the average misorientation between each pixel and its nearest neighbours in the KAM maps, suggests

homogeneous and low misorientation angles. No recrystallized structures were observed in the matrix or inside the TWEAs and SWEAs.

- TWEAs and SWEAs appeared with dark contrast in IQ images, and as black regions in IPF, AP and KAM maps. This suggests poor or even a lack of indexed diffraction patterns from these areas resulting from a nanocrystalline structure. IQ showed the *fibrous / layered* structure seemed to be stacked close to the top surface or formed swirls (vortices) subsurface that resemble the patterns produced by turbulent flow.
- EDS analysis indicated that carbon was dragged from the carbides and dissolved in the nanocrystalline arrangement present in TWEAs and SWEAs. A slight increase of the carbon and chromium content in the white structures compared to the surrounding matrix was observed, supporting the dissolution process described. EDS also revealed inclusions of aluminium with sulphur and manganese, inside of TWEAs and SWEAs.

5. TWEAs and SWEAs shared similar features, such as a fibrous / layered internal structure, higher hardness compared to the deformed ferritic matrix that surrounds them and the absence of the carbide distribution observed in the matrix. Different drivers were identified to explain their origin. In the case of TWEAs, the sliding of the asperities on the top anvil against the sample created heterogeneous flow conditions in small neighbouring regions and instabilities between them. The origin of SWEAs is related to similar instabilities but created by interruptions of the plastic flow due to different factors: vortex formation around inclusions in highly strained regions of the sample, and the influence of Dead Metal Zones, DMZ, lateral friction and flash formation at their edges. Plastic flow around carbide clusters could also be a source of instabilities. The local shear instabilities produce atomic scale mixing and nano eddies or vortices at the sliding interfaces. They transformed the material into a nano *fibre / layered* structures with different properties. Although the nature of these *fibres / layered* structures is not completely understood, it could be related to similar transformation mechanisms observed under SPD conditions, such as the diffusion of carbon or the formation of high-density dislocation clusters. Some cracks appeared close to the TWEAs and SWEAs, but not all of them exhibited cracks. As HPT progressed, new *fibres / layered* structures were formed and stacked over each other. The differences between the mechanical properties of these new *fibres / layered* structures and the matrix surrounding them could also explain the initiation and growth of small cracks around them. However, not all TWEAs or SWEAs registered cracks, suggesting that white structures appeared first, and then cracks developed. TWEAs were produced by adhesion and abrasion produced by severe sliding between the top surface of the disc and the top anvil.

6      TWEAs and SWEAs shared similar features to WEAs produced by rolling contact fatigue, such as the fibrous structure formed by nano grains, carbon and chromium dissolution, a link with inclusions and a higher hardness than the surrounded matrix. These similarities suggest that the same phenomena responsible for the formation of SWEAs could also be responsible for the formation of WEAs, i.e. plastic flow in well localized regions (close to an inclusion or carbide cluster) creating instabilities between neighbour regions. However, two features are different. Firstly, it seems cracks are not always associated with the white etching areas in HPT tests. This may well be a consequence of the high compressive stresses present in HPT tending to prevent crack initiation and growth. This suggests that cracks could be not necessarily a precursor to white etching areas, rather white etching areas might form before cracks. Secondly, recrystallized grains are not found in the SWEAs and TWEAs produced by HPT but are present close to crack boundaries in WEAs in rolling contact fatigue. Rubbing of the crack flanks caused by the cyclic shear stresses in rolling contact fatigue could lead to a local increase in temperature that was sufficient to cause recrystallisation to occur. As rubbing of crack flanks does not take place to the same degree in HPT as there are no cyclic shear stresses, hence recrystallized grains are not found in SWEAs and TWEAs.

## 7.2      **Future work**

Based on the limitations faced during the HPT tests and the characterisation of the annealed AISI 52100, three main tasks are proposed as future research:

### 7.2.1      **Conduct additional HPT tests on the annealed AISI 52100**

Additional HPT tests on the annealed AISI 52100 bearing steel using 3 and 6 GPa and greater than 3 turns should be conducted until the saturation condition is reached. Characterisation using the same techniques as the present study (LOM, SEM /SEI / BSI, SEM /EBSD /EDS) should then be conducted on these samples to establish a comprehensive description of the transformations in the steel until complete nano grain refinement is reached. This tasks requires the use of anvils with hardness over 1000 HV.

### 7.2.2      **Characterisation by Transmission Electron Microscopy, TEM**

Despite of all the information provided in this thesis, the techniques used were not able to characterise the structure at nano scales. TEM would be a useful technique to use to study different features, such as lattice parameters, dislocation density variations in regions of interest. This information would permit a greater understanding of the carbon and chromium dissolution

processes taking place inside the TWEAs and SWEAs and the role of the inclusions and asperities in promoting localised plasticity and the formation of the white structures.

### **7.2.3 Conduct HPT tests on AISI 52100 in its quenched and tempered condition**

Despite the similarities observed between TWEAs / SWEAs in annealed 52100 and WEAs in failed bearings, both materials are different in terms of microstructure and hardness. Thus, it would be interesting to perform HPT tests on the quenched and tempered material. This would require the use of a HPT machine with harder anvils. The samples so produced could then be studied using the techniques of the present work together with TEM.



## References

- [1] M.N. Kotzalas, G.L. Doll, Tribological advancements for reliable wind turbine performance, *Philosophical Transactions of the Royal Society A: Mathematical, Physical and Engineering Sciences* 368(1929) (2010) 4829.
- [2] M.H. Evans, White structure flaking (WSF) in wind turbine gearbox bearings: effects of 'butterflies' and white etching cracks (WECs), *Materials Science and Technology* 28(1) (2012) 3-22.
- [3] A. Greco, S. Sheng, J. Keller, A. Erdemir, Material wear and fatigue in wind turbine Systems, *Wear* 302(1) (2013) 1583-1591.
- [4] A. Grabulov, U. Ziese, H.W. Zandbergen, TEM/SEM investigation of microstructural changes within the white etching area under rolling contact fatigue and 3-D crack reconstruction by focused ion beam, *Scripta Materialia* 57(7) (2007) 635-638.
- [5] A. Grabulov, Fundamentals of Rolling Contact Fatigue, PhD theses, University of Delft - TU, (2010).
- [6] G. Guetard, I. Toda-Caraballo, P.E.J. Rivera-Díaz-del-Castillo, Damage evolution around primary carbides under rolling contact fatigue in VIM-VAR M50, *International Journal of Fatigue* 91 (2016) 59-67.
- [7] M. Paladugu, R. Scott Hyde, White etching matter promoted by intergranular embrittlement, *Scripta Materialia* 130 (2017) 219-222.
- [8] M.H. Evans, A.D. Richardson, L. Wang, R.J.K. Wood, Effect of hydrogen on butterfly and white etching crack (WEC) formation under rolling contact fatigue (RCF), *Wear* 306(1) (2013) 226-241.
- [9] L. Junbiao, Investigation on the Mechanisms of White Etching Crack (WEC) Formation in Rolling Contact Fatigue and Identification of a Root Cause for Bearing Premature Failure, *Wear* 364-365 (2016) 244-256.
- [10] M. Evans, White Etching Crack (WEC) Investigation by Serial Sectioning, Focused Ion Beam and 3-D Crack Modelling, *Tribology International* 65 (2013) 146-160.

## References

- [11] Y. Ivanisenko, W. Lojkowski, R.Z. Valiev, H.J. Fecht, The mechanism of formation of nanostructure and dissolution of cementite in a pearlitic steel during high pressure torsion, *Acta Materialia* 51(18) (2003) 5555-5570.
- [12] T.G. Langdon, Twenty - five years of ultrafine-grained materials: Achieving exceptional properties through grain refinement, *Acta Materialia* 61(19) (2013) 7035-7059.
- [13] H.K.D.H. Bhadeshia, Steels for bearings, *Progress in Materials Science* 57(2) (2012) 268-435.
- [14] J. Jelita Rydel, I. Toda-Caraballo, G. Guetard, P.E.J. Rivera-Díaz-del-Castillo, Understanding the factors controlling rolling contact fatigue damage in VIM-VAR M50 steel, *International Journal of Fatigue* 108 (2018) 68-78.
- [15] A. Vorhauer, R. Pippan, On the homogeneity of deformation by high pressure torsion, *Scripta Materialia* 51(9) (2004) 921-925.
- [16] K. Edalati, Z. Horita, A review on high-pressure torsion (HPT) from 1935 to 1988, *Materials Science and Engineering: A* 652 (2016) 325-352.
- [17] R. Budynas, Shigley's mechanical engineering design, 10 ed., McGraw-Hill Education, New York, NY USA, (2015).
- [18] I. Hutchings, Tribology Friction and Wear of Engineering Materials, St. Edmundsbury Press, London, 1992.
- [19] H. Burrier, Bearing Steels, *Encyclopedia of Materials: Science and Technology*, Elsevier Ltd. The Netherlands – (2011). 501-506.
- [20] B. Hamrock, Ball Bearing Lubrication, John Wiley & Sons Inc., New York - USA, (1981).
- [21] ISO, Heat-treated Steels, Alloy Steels and Free-cutting Steels, Part 17: Ball and roller bearing steels, European Committee for Standardization - CEN, Brussels, Belgium, (2014).
- [22] D. Sorgente, Laser Hardening of a AISI 52100 Bearing Steel with a Discrete Fiber Laser Spot. *Proc. SPIE* 8963, San Diego, Ca, USA – (2014).
- [23] A. Olver, The Mechanism of Rolling Contact Fatigue: An Update, *Proc. IMechE* 219(J) (2005) 313-330.



- [24] A. Benscoter, Carbon and Alloy Steels, Metals Handbook Ninth Edition Vol. 9 Metallography and Microstructures, American Society for Metals, Metals Park, Ohio - USA, (1985)167-196.
- [25] Schaeffler Technologies, Bearing Failures Causes and Cures.  
[https://www.schaeffler.com/remotemedien/media/\\_shared\\_media/08\\_media\\_library/01\\_publications/barden/brochure\\_2/downloads\\_24/barden\\_bearing\\_failures\\_us\\_en.pdf](https://www.schaeffler.com/remotemedien/media/_shared_media/08_media_library/01_publications/barden/brochure_2/downloads_24/barden_bearing_failures_us_en.pdf), January2018,  
 (accessed 06/04/18.2018).
- [26] FAG Rolling Bearings Ltd. [http://www.lezaji.com/download/FAG\\_tehnicke\\_informacije.pdf](http://www.lezaji.com/download/FAG_tehnicke_informacije.pdf),  
 October 2009 (accessed April 2017).
- [27] K. Tamada, Occurrence of Brittle Flaking on Bearings Used for Automotive Electrical Instruments and Auxiliary Devices, Wear 199 (1996) 245-252.
- [28] N. Kino, K. Otani, The influence of hydrogen on rolling contact fatigue life and its improvement, JSAE Review 24(3) (2003) 289-294.
- [29] Y. Murakami, M. Naka, A. Iwamoto, G. Chatell, Long Life Bearings for Automotive Alternator Applications, SAE technical paper series, 950944. International Congress and Exposition Detroit, Mi, USA (1995).
- [30] K. Iso, Rolling Bearing, Rolling Bearing for Fuel Cell, Compressor for Fuel Cell System and Fuel Cell Systems, in: U.S.P.P. Application (Ed.) NSK LTD., USA, (2006)
- [31] R. Zimroz, Diagnostics of Bearings in Presence of Strong Operating Conditions Non-Stationarity—A Procedure of Load-Dependent Features Processing with Application to Wind Turbine Bearings, Mechanical Systems and Signal Processing 46 (2014) 16–27.
- [32] A. Ragheb, Wind Turbine Gearbox Technologies, Fundamental and Advanced Topics in Wind Power, Rijeka, Croatia (2011).
- [33] K. Zum Gahr, Microstructure and Wear of Materials, Elsevier Science Publisher B.V, Amsterdam, The Netherlands, (1987).
- [34] R. Norton, Machine Design: An Integrated Approach, Pearson Education, Inc, New York, USA, (2011).
- [35] S. Timoshenko, Theory of Elasticity, Mc Graw- Hill Book Company, York, Pa - USA, (1951).
- [36] K. Ludema, Friction, Wear, Lubrication, CRC Press Inc., Boca Raton, Fl - USA, (1996).

## References

- [37] A. Voskamp, Material Response to Rolling Contact Loading, *Journal of Tribology* 107 (1985) 359-366.
- [38] Kang, Rolling Contact Fatigue in Bearings: A Multiscale Overview, *Materials Science and Technology*, 28, (2012) 44-45
- [39] H. Swahn, Martensite Decay During Rolling Contact Fatigue Ball Bearings, *Metallurgical Transactions A* 7A (1976) 1099-1110.
- [40] W. Glaeser, Contact Fatigue, *ASM Handbook, Volume 19 Fatigue and Fracture*, ASM Handbook Committee, Russell Township, Ohio - USA, (1996) 331-336.
- [41] Way, Referenced in Zum Gahr, 1987, (1935).
- [42] Keer, Referenced in Zum Gahr 1987, (1982).
- [43] H. Gang, Spall Initiation and Propagation due to Debris Denting, *Wear* 201 (1996) 106-116.
- [44] C. Chue, Pitting Formation under Rolling Contact, *Theoretical and Applied Fracture Mechanics* 34 (2000) 1-9.
- [45] C. Chue, The effects of Strain Hardened Layer on Pitting Formation During Rolling Contact, *Wear* 249 (2001) 109–116.
- [46] A. Voskamp, Fatigue and Material Response in Rolling Contact, in: H.H.B. Green (Ed.), *Bearing Steels: Into 21st Century*, ASTM STP 1327, Barr Harbor, PA - USA, (1998).
- [47] F. Sadeghi, A Review of Rolling Contact Fatigue, *Journal of Tribology* 131 (2009) 1-14.
- [48] A. Greco, Material Wear and Fatigue in Wind Turbine Systems, *Wear* 302 (2013) 1583–1591.  
{2}
- [49] M. Evans, White structure Flaking (WSF) in Wind Turbine Gearbox Bearings: Effects of 'Butterflies' and White Etching Cracks (WEC), *Materials Science and Technology* 28(1) (2012) 3-22.  
{3}
- [50] N. Uyama, The Mechanism of White Structure Flaking in Rolling Bearings. Wind Turbine Tribology Seminar, Wind and Water Power Program U.S. Department of Energy NREL. Broomfield CO, USA, (2011).

- [51] H. Muro, N. Tsushima, Microstructural, microhardness and residual stress changes due to rolling contact, *Wear* 15(5) (1970) 309-330.
- [52] R. Errichello, Wind Turbine Tribology Seminar, US department of Energy, Wind and Water Power Program, Broomfield, Colorado, USA, (2011).
- [53] Y.-S. Su, S.-X. Li, S.-Y. Lu, X.-D. Shu, Deformation-induced amorphization and austenitization in white etching area of a martensite bearing steel under rolling contact fatigue, *International Journal of Fatigue* 105 (2017) 160-168.
- [54] H. Harada, T. Mikami, M. Shibata, D. Sokai, A. Yamamoto, H. Tsubakino, Microstructural Changes and Crack Initiation with White Etching Area Formation under Rolling/Sliding Contact in Bearing Steel, *ISI International* 45(12) (2005) 1897-1902.
- [55] A. Grabulov, R. Petrov, H.W. Zandbergen, EBSD investigation of the crack initiation and TEM/FIB analyses of the microstructural changes around the cracks formed under Rolling Contact Fatigue (RCF), *International Journal of Fatigue* 32(3) (2010) 576-583.
- [56] J.H. Kang, P.E.J. Rivera-Díaz-del-Castillo, Carbide dissolution in bearing steels, *Computational Materials Science* 67 (2013) 364-372.
- [57] W. Solano-Alvarez, E.J. Pickering, M.J. Peet, K.L. Moore, J. Jaiswal, A. Bevan, H.K.D.H. Bhadeshia, Soft novel form of white-etching matter and ductile failure of carbide-free bainitic steels under rolling contact stresses, *Acta Materialia* 121 (2016) 215-226.
- [58] M.H. Evans, L. Wang, R.J.K. Wood, Formation mechanisms of white etching cracks and white etching area under rolling contact fatigue, *Proceedings of the Institution of Mechanical Engineers, Part J: Journal of Engineering Tribology* 228(10) (2014) 1047-1062.
- [59] R. Errichello, R. Budny, R. Eckert, Investigations of Bearing Failures Associated with White Etching Areas (WEAs) in Wind Turbine Gearboxes, *Tribology Transactions* 56(6) (2013) 1069-1076.
- [60] A. Gravulov, EBSD Investigation of the Crack Initiation and TEM/FIB Analyses of the Microstructural Changes around the Cracks Formed under Rolling Contact Fatigue (RCF), *International Journal of Fatigue* 32 (2010) 576-583.
- [61] A.M. Diederichs, A. Schwedt, J. Mayer, T. Dreifert, Electron microscopy analysis of structural changes within white etching areas, *Materials Science and Technology* 32(16) (2016) 1683-1693.

## References

- [62] M. Oezel, A. Schwedt, T. Janitzky, R. Kelley, C. Bouchet-Marquis, L. Pullan, C. Broeckmann, J. Mayer, Formation of White Etching Areas in SAE 52100 Bearing Steel under Rolling Contact Fatigue – Influence of Diffusible Hydrogen, (2018).
- [63] W. Holweger, M. Wolf, D. Merk, T. Blass, M. Goss, J. Loos, S. Barteldes, A. Jakovics, White Etching Crack Root Cause Investigations, Tribology Transactions 58(1) (2015) 59-69.
- [64] W. Kochmanna, Nanowires in Ancient Damascus Steel, Journal of Alloys and Compounds (2004) 372, L15–L19.
- [65] I. Tamura, Thermomechanical Processing of High-Strength Low-Alloy Steels, Butterworth-Heinemann London, UK, (1998).
- [66] R. Armstrong, 60 Years of Hall-Petch: Past to Present Nano-Scale Connections, Materials Transactions 55(1) (2014) 2 - 12.
- [67] A. Khare, Open-Die Forging, ASM Handbook Vol. 14 Forming and Forging, ASM Handbook Committee, Russell Township, Ohio - USA, (1993), 96-141.
- [68] D. Lesuer, Influence of Severe Plastic Deformation on the Structure and Properties of Ultra High Carbon Steel wire, NATO Advanced Research Workshop, Laurence Libermore National Laboratory, Moscow, (1999), 1-13.
- [69] S. Kalpakjian, Manufacturing, Engineering & Technology, Pearson Prentice Hall, Upper Saddle River, NJ - USA, 2006.
- [70] P. Bridgman, On Torsion Combined with Compression, Journal of Applied Physics 14, 273 (1943)
- [71] P. Bridgman, The Effect of Hydrostatic Pressure on Plastic Flow under Shearing Stress, Journal of Applied Physics 17, 692 (1946)
- [72] K. Suehiro, Change in Magnetic Property of Cu-6.5 mass %Co Alloy through Processing by ECAP, Materials Transactions 49(1) (2008) 102-106.
- [73] R. Valiev, Producing Bulk Ultrafine-Grained Materials by Severe Plastic Deformation, JOM (2006) 58: 33
- [74] Y. Estrin, Extreme Grain Refinement by Severe Plastic Deformation: A Wealth of Challenging Science, Acta Materialia 61 (2013) 782-817.

- [75] Y.T. Zhu, T.C. Lowe, T.G. Langdon, Performance and applications of nanostructured materials produced by severe plastic deformation, *Scripta Materialia* 51(8) (2004) 825-830.
- [76] JMR&T, Enhancement in Mechanical Properties of a  $\beta$ -titanium Alloy by High-Pressure Torsion, *Journal of Materials Research and Technology*, 2013.
- [77] A. Zhilyaev, Evolution of Microstructure and Microtexture in FCC Metals During High-Pressure Torsion, *Journal of Materials Science* 42 (2007) 1517–1528.
- [78] Y. Huang, An Evaluation of the Shearing Patterns Introduced by Different Anvil Alignments in High-Pressure Torsion, *Journal of Materials Science* 49 (2014) 3146–3157.
- [79] E. Zeynali, Comparing Plastic Deformations Produced by HPT and ECAP Processes Using the Finite Element Analysis Method, *International Journal of Mechanics and Applications* 2(1) (2012) 20-24.
- [80] R.B. Figueiredo, M.T.P. Aguilar, P.R. Cetlin, T.G. Langdon, Analysis of plastic flow during high-pressure torsion, *Journal of Materials Science* 47(22) (2012) 7807-7814.
- [81] R. Kulagin, Y. Beygelzimer, Y. Ivanisenko, A. Mazilkin, B. Straumal, H. Hahn, Instabilities of interfaces between dissimilar metals induced by high pressure torsion, *Materials Letters* 222 (2018) 172-175.
- [82] Y. Cao, M. Kawasaki, Y.B. Wang, S.N. Alhajeri, X.Z. Liao, W.L. Zheng, S.P. Ringer, Y.T. Zhu, T.G. Langdon, Unusual macroscopic shearing patterns observed in metals processed by high-pressure torsion, *Journal of Materials Science* 45(17) (2010) 4545-4553.
- [83] N.K. Sundaram, Y. Guo, S. Chandrasekar, Mesoscale Folding, Instability, and Disruption of Laminar Flow in Metal Surfaces, *Physical Review Letters* 106001, 109(10) (2012).
- [84] D.A. Rigney, S. Karthikeyan, The Evolution of Tribomaterial During Sliding: A Brief Introduction, *Tribology Letters* 39(1) (2010) 3-7.
- [85] H. Hahn, High Pressure Torsion: from Laminar Flow to Turbulence, *IOP Conference Series: Materials Science and Engineering* 012045,194(1) (2017)
- [86] A. Zhilyaev, Experimental Parameters Influencing Grain Refinement and Microstructural Evolution During High-Pressure Torsion, *Acta Materialia* 51 (2003) 753–765.

## References

- [87] S. Sabbaghianrad, An Examination of the Saturation Microstructures Achieved in Ultrafine-Grained Metals Processed by High-Pressure Torsion, *The Journal of Materials Research and Technology* 3(4) (2014) 319–326.
- [88] Edalati, Significance of Homologous Temperature in Softening Behavior and Grain Size of Pure Metals Processed by High-Pressure Torsion, *Materials Science and Engineering A* 528 (2011) 7514–7523.
- [89] Seong Cho, Microstructural Evolution and Mechanical Properties in a Zn–Al Eutectoid Alloy Processed by High-Pressure Torsion, *Acta Materialia* 72 (2014) 67–79.
- [90] Chuan, Strain weakening and superplasticity in a Bi-Sn eutectic alloy processed by high-pressure torsion, *Materials Science and Engineering* 63 (2014) 1-9.
- [91] R. Figueiredo, Using Finite Element Modeling to Examine the Temperature Distribution in Quasi-Constrained High-Pressure Torsion, *Acta Materialia* 60 (2012) 3190–3198.
- [92] D. Orlov, Role of Strain Reversal in Grain Refinement by Severe Plastic Deformation, *Materials Science and Engineering A* 499 (2009) 427–433.
- [93] Kawasaki, Significance of Strain Reversals in a Two-Phase Alloy Processed by High-Pressure Torsion, *Materials Science and Engineering A* 527 (2010) 7008–7016.
- [94] M. Kawasaki, Effect of Strain Reversals on the Processing of High-Purity Aluminum by High-Pressure Torsion, *J Mater Sci* 45 (2010) 4583–4593.
- [95] F. Dong, Strength, Damage and Fracture Behaviors of High-Nitrogen Austenitic Stainless, *Scripta Materialia* 96 (2015) 5–8.
- [96] K. Masaaki, Developing Grain Refinement and Superplasticity in a Magnesium Alloy Processed by High-Pressure Torsion, *Materials Science and Engineering A* 488 (2008) 117–124.
- [97] D. Marulanda, Microstructural Evolution and Microhardness in a Low Carbon Steel Processed by High-Pressure Torsion, *Journal Materials Research and Technology* 4(3) (2014) 344–348.
- [98] F. Wetscher, TEM Investigations of the Structural Evolution in a Pearlitic Steel Deformed by High-Pressure Torsion, *Metallurgical and Materials Transactions* 1963 37A (2006)
- [99] Y. Ivanisenko, Formation of Submicrocrystalline Structure in Iron and its Alloys after Severe Plastic Deformation, *NanoStructured Materials* 6 (1996) 433-436.

- [100] M. Zelin, Microstructure Evolution in Pearlitic Steels During Wire Drawing, *Acta Materialia* 50 (2002) 4431–4447.
- [101] W. Lojkowski, Nanostructure Formation on the Surface of Railway Tracks, *Materials Science and Engineering A* 303 (2001) 197–208.
- [102] A. Barrow, Nanoprecipitation in bearing steels, *Acta Materialia* 59 (2011) 7155–7167.
- [103] J. Kang, Carbide Dissolution in Bearing Steels, *Computational Material Science* 67 (2013) 364–372.
- [104] BS 2S 135: 1977 1% Carbon – Chromium Steel Billets, Bars, Forging and Parts (Limiting Ruling Section 25 mm), BSI Standard Publication, London, (2009).
- [105] Simply-Bearing, Authorised Precision Ball and Roller Distributors in the UK, AISI 52100 Chrome Steel Needle Roller Data Sheet. [https://simplybearings.co.uk/shop/files/52100\\_roll.pdf](https://simplybearings.co.uk/shop/files/52100_roll.pdf) April 2015, (accessed 03/04/2015).
- [106] K. Edalati, Z. Horita, T.G. Langdon, The significance of slippage in processing by high-pressure torsion, *Scripta Materialia* 60(1) (2009) 9–12.
- [107] W. Rasband, Image J, National Institutes of Health, University of Wisconsin, Madison, Wisconsin, USA, (2009).
- [108] A. Schwartz, Electron Backscatter Diffraction in Materials Science, 2 ed., Springer Science+Business Media, 233 Spring Street, New York, NY, USA, (2009).
- [109] D. Stojakovic, Electron Backscatter Diffraction in Materials Characterization, Processing and Application of Ceramics 6(1) (2012) 1–13.
- [110] S. Suwas, Experimental Determination of Texture Crystallographic Texture of Materials. *Engineering Materials and Processes*, Springer, London, UK, (2012).
- [111] S. Wright, M. Nowell, EBSD image quality mapping, *Microsc. Microanal.* 12, 72–84, (2006).
- [112] J. Goldstein, Scanning Electron Microscopy and X- Ray Microanalysis, 3rd ed., Springer Science+Business Media, New York, NY, (2003).
- [113] A. Hohenwarter, A. Bachmaier, B. Gludovatz, S. Scheriau, R. Pippan, Technical parameters affecting grain refinement by high pressure torsion, (2009).



## References

- [114] E.J. Pavlina, C. Vantyne, Correlation of Yield Strength and Tensile Strength with Hardness for Steels, 2008.
- [115] Y. Cao, Y.B. Wang, R.B. Figueiredo, L. Chang, X.Z. Liao, M. Kawasaki, W.L. Zheng, S.P. Ringer, T.G. Langdon, Y.T. Zhu, Three-dimensional shear-strain patterns induced by high-pressure torsion and their impact on hardness evolution, *Acta Materialia* 59(10) (2011) 3903-3914.
- [116] D. Kuhlmann-Wilsdorf, B.C. Cai, R.B. Nelson, Plastic flow between Bridgman anvils under high pressures, *Journal of Materials Research* 6(12) (1991) 2547-2564.
- [117] R.E. Riecker, L.C. Towle, Shear Strength of Grossly Deformed Cu, Ag, and Au at High Pressures and Temperatures, *Journal of Applied Physics* 38(13) (1967) 5189-5194.
- [118] Y. Huang, A. Al-Zubaydi, M. Kawasaki, T.G. Langdon, An overview of flow patterns development on disc lower surfaces when processing by high-pressure torsion, *Journal of Materials Research and Technology* 3(4) (2014) 303-310.
- [119] O. Kazuhiro, Advances in Gas Turbine Technology, in: E. Benini (Ed.), *Advances in Gas Turbine Technology*, Intech Open, London, UK, (2011).
- [120] H.J. Kim, S. Karthikeyan, D. Rigney, A simulation study of the mixing, atomic flow and velocity profiles of crystalline materials during sliding, *Wear* 267(5) (2009) 1130-1136.
- [121] X. Sauvage, G. Wilde, S.V. Divinski, Z. Horita, R.Z. Valiev, Grain boundaries in ultrafine grained materials processed by severe plastic deformation and related phenomena, *Materials Science and Engineering: A* 540 (2012) 1-12.
- [122] J.G. Li, M. Umemoto, Y. Todaka, K. Tsuchiya, Nanocrystalline structure formation in carbon steel introduced by high speed drilling, *Materials Science and Engineering: A* 435-436 (2006) 383-388.
- [123] S.B. Hosseini, T. Beno, U. Klement, J. Kaminski, K. Rytberg, Cutting temperatures during hard turning—Measurements and effects on white layer formation in AISI 52100, *Journal of Materials Processing Technology* 214(6) (2014) 1293-1300.
- [124] L. Zhou, G. Liu, X.L. Ma, K. Lu, Strain-induced refinement in a steel with spheroidal cementite subjected to surface mechanical attrition treatment, *Acta Materialia* 56(1) (2008) 78-87.

- [125] Z. Gahr, *Microstructure and Wear of Materials*, Elsevier Science Publisher B.V., Amsterdam, The Netherlands, (1987).
- [126] W. Hong, W. Cai, S. Wang, M.M. Tomovic, Mechanical wear debris feature, detection, and diagnosis: A review, *Chinese Journal of Aeronautics* 31(5) (2018) 867-882.
- [127] D. Geist, C. Rentenberger, H.P. Karnthaler, Extreme structural inhomogeneities in high-pressure torsion samples along the axial direction, *Acta Materialia* 59(11) (2011) 4578-4586.
- [128] R.B. Figueiredo, T.G. Langdon, Development of structural heterogeneities in a magnesium alloy processed by high-pressure torsion, *Materials Science and Engineering: A* 528(13) (2011) 4500-4506.
- [129] R.K. Figueiredo, M. Langdon, T., An Evaluation of Homogeneity and Heterogeneity in Metals Processed by High-Pressure Torsion, *Acta Physica Polonica A* 3 (2012) 425-429.
- [130] R.B. Figueiredo, P.R. Cetlin, T.G. Langdon, Using finite element modeling to examine the flow processes in quasi-constrained high-pressure torsion, *Materials Science and Engineering: A* 528(28) (2011) 8198-8204.
- [130] Y. Song, M. Chen, B. Xu, D. Gao, J. Guo, L. Xu, Z. Wang, H.S. Kim, Effects of Friction and Anvil Design on Plastic Deformation during the Compression Stage of High-Pressure Torsion, *Korean J. Met. Mater.* 54(11) (2016) 831-837.
- [131] Y. Song, W. Wang, D. Gao, E.Y. Yoon, D.J. Lee, H.S. Kim, Finite element analysis of the effect of friction in high pressure torsion, *Metals and Materials International* 20(3) (2014) 445-450.
- [132] D.J. Lee, E.Y. Yoon, L.J. Park, H.S. Kim, The dead metal zone in high-pressure torsion, *Scripta Materialia* 67(4) (2012) 384-387.
- [133] N. Beckmann, P.A. Romero, D. Linsler, M. Dienwiebel, U. Stolz, M. Moseler, P. Gumbsch, Origins of Folding Instabilities on Polycrystalline Metal Surfaces, *Physical Review Applied* 064004. 2(6) (2014)
- [134] R. Kulagin, Y. Beygelzimer, Y. Ivanisenko, A. Mazilkin, H. Hahn, Modelling of High-Pressure Torsion using FEM, *Procedia Engineering* 207 (2017) 1445-1450.

## References

- [135] B. Gould, A. Greco, K. Stadler, X. Xiao, An analysis of premature cracking associated with microstructural alterations in an AISI 52100 failed wind turbine bearing using X-ray tomography, *Materials & Design* 117 (2017) 417-429.
- [136] T. Bruce, H. Long, R.S. Dwyer-Joyce, Threshold Maps for Inclusion-Initiated Micro-Cracks and White Etching Areas in Bearing Steel: The Role of Impact Loading and Surface Sliding, *Tribology Letters* 66(3) (2018) 111.
- [137] H.A. Al-Tameemi, H. Long, R.S. Dwyer-Joyce, Initiation of sub-surface micro-cracks and white etching areas from debonding at non-metallic inclusions in wind turbine gearbox bearing, *Wear* 406-407 (2018) 22-32.
- [138] V. Šmeļova, A. Schwedt, L. Wang, W. Holweger, J. Mayer, Microstructural changes in White Etching Cracks (WECs) and their relationship with those in Dark Etching Region (DER) and White Etching Bands (WEBs) due to Rolling Contact Fatigue (RCF), *International Journal of Fatigue* 100 (2017) 148-158.
- [139] T. Bruce, E. Rounding, H. Long, R.S. Dwyer-Joyce, Characterisation of white etching crack damage in wind turbine gearbox bearings, *Wear* 338-339 (2015) 164-177.
-